
Universidade de Aveiro Departamento de Electrónica,
2007 Telecomunicações e Informática

Ruben Soares Luís

PROJECTO E OPTIMIZAÇÃO DE TÉCNICAS DE ROTEAMENTO E DISPOSITIVOS ÓPTICOS

DESIGN AND OPTIMIZATION OF OPTICAL ROUTING TECHNIQUES AND DEVICES

Universidade de Aveiro
2007
Departamento de Electrónica,
Telecomunicações e Informática

Ruben Soares Luís

PROJECTO E OPTIMIZAÇÃO DE TÉCNICAS DE ROTEAMENTO E DISPOSITIVOS ÓPTICOS

DESIGN AND OPTIMIZATION OF OPTICAL ROUTING TECHNIQUES AND DEVICES

dissertação apresentada à Universidade de Aveiro para cumprimento dos requisitos necessários à obtenção do grau de Doutor em Engenharia Electrotécnica, realizada sob a orientação científica do Dr. António Luís Jesus Teixeira, Professor Auxiliar do Departamento de Electrónica, Telecomunicações e Informática da Universidade de Aveiro e do Dr. Paulo Miguel Nepomuceno Pereira Monteiro, Professor Associado do Departamento de Electrónica, Telecomunicações e Informática da Universidade de Aveiro.

Apoio financeiro do POCTI/POSC no âmbito do III Quadro Comunitário de Apoio.

Apoio financeiro da FCT e do FSE no âmbito do III Quadro Comunitário de Apoio.

To my supervisors,
António Teixeira, and Paulo Monteiro

Jury

president

Full Professor at Universidade de Aveiro

Doctor Josep Joan Prat Gomá
Full Professor at Universitat Politècnica de Catalunya

Doctor José Antonio Lázaro Villa
Associate Professor at Universitat Politècnica de Catalunya

Doctor Mário José Neves de Lima
Invited Assistant Professor at Universidade de Aveiro

Doctor Paulo Miguel Nepomuceno Pereira Monteiro
Associate Professor at Universidade de Aveiro

Doctor António Luís Jesus Teixeira
Assistant Professor at Universidade de Aveiro

acknowledgment

It is extremely important for me to recognize the good deeds that people have done for me and for the successful completion of this work. These include their time, effort, caring and collaboration. I have been immensely enriched by all the valuable lessons I have learned from so many people. I simply cannot find the words to express the depth of my gratitude and appreciation. Without diminishing all the contributions received along these last few years, I will acknowledge some of the most significant.

To my scientific supervisor, Professor Doctor António Teixeira. His contagious creativity and enthusiasm have been a driving source of inspiration, leading me to strive for originality. To my co-supervisor, Professor Doctor Paulo Monteiro. With his remarkable insights and constructive attitudes he has more than once guided me through tortuous paths. The success of this endeavor would not have been achieved without the tireless devotion of these two great men. With all my heart, I thank them for believing in me, even when I no longer did. To my dearest friend and colleague, Doctor Daniel Fonseca. He has been a devoted companion, always and insistently challenging me to improve. I am deeply grateful for the hundreds of hours of vivid discussions, the meticulous reviews and, more importantly, his warm and caring support. I would also like to acknowledge the support of my dear and unforgettable friends, Fábio Costa, Fernando Fonseca and Jorge Epifânio. To the Optical Communications Research group of Nokia Siemens Networks in Portugal, where I had the privilege of working with an incredible group of wonderful and talented persons. Although all have contributed to this work, I will indulge myself by naming a few: Silvia Pato, for her patience in putting up with me daily; Rui Morais, for his insight; Rui Meleiro, for his spirit; José Pina, for his brilliance; João Pedro, for his rigor; Lara Pellegrino for her attitude; Ana Ferreira, for her smile; and Tiago Silveira, for his overwhelming sense of team. To all, I am grateful for shared ideas, mutual support and collaboration that I have found uncommon in other research groups. Finally, I am grateful to Sandra Bulhões and my family, which although distant, have never been absent.

This work has been supported by Nokia Siemens Networks and Fundação para a Ciência e Tecnologia, under grant SFRH/BDE/15542/2005.

palavras-chave

sistemas de monitorização óptica, histogramas assíncronos, conversão de comprimento onda, modulação cruzada de fase, espelho de fibra não-linear, não-linearidades intra-canal, modulação cruzada de fase intra-canal, mistura de quatro ondas intra-canal.

resumo

Este trabalho apresenta três estudos principais acerca do desenvolvimento e aplicação de sistemas de monitorização óptica avançados com base na análise de histogramas assíncronos, conversão de comprimento de onda de sinais de débito elevado e o impacto das não-linearidades das fibra ópticas em sistemas utilizando técnicas avançadas de transmissão. Mostra-se que a comparação de histogramas assíncronos com histogramas de referência pode ser usada para extrair informação a respeito da qualidade e do ruído que afecta o sinal em análise. O método proposto é validado através de simulação numérica e experiência.

Um modelo analítico para a computação das limitações em frequência da modulação cruzada de fase (XPM) em conversores de comprimento de onda de fibra é proposto e validado através de simulação numérica até frequências de modulação acima de 1 THz. O modelo proposto permite a derivação de regras de engenharia para o dimensionamento de conversores de comprimento de onda compostos por espelhos de fibra não linear. O dimensionamento de um novo filtro para a optimização da conversão da XPM em modulação de intensidado é proposto e validado por simulação numérica.

O impacto das não-linearidades na transmissão em fibra óptica de sinais de banda lateral única a 10 Gb/s com compensação de dispersão concentrada é avaliado através de simulação numérica. Mostra-se que as não-linearidades intra-canal levam a severa degradação do desempenho. A degradação de sinais de chaveamento por desvio diferencial de fase (DPSK) a 40 Gb/s devida a XPM com sinais de chaveamento por desvio de amplitude herdados de sistemas anteriores é também analisada. Uma análise bomba-sonda mostra que a degradação do sinal resulta da modulação de intensidade induzida por XPM. Este resultado permite a derivação de um modelo para estimar a probabilidade de erro dos sinais DPSK degradados por XPM. Finalmente, é apresentada uma abordagem analítica baseada em pequenas perturbações para o estudo de não linearidades intra-canal em fibra óptica em sinais com razão de extinção finita. Este estudo permite a identificação de duas novas formas de degradação tomando a forma de impulsos entre diferentes símbolos e fluctuações temporais e de amplitude.

keywords

optical monitoring systems, asynchronous histograms, wavelength conversion, cross-phase modulation, nonlinear optical loop mirror, intra-channel nonlinearities, intra-channel cross-phase modulation, intra-channel four-wave mixing

abstract

This work presents three main studies regarding the development and application of advanced optical monitoring systems based on the analysis of asynchronous amplitude histograms, the wavelength conversion of ultra-high bit-rate signals, and the impact of fiber nonlinearities in systems employing advanced transmission techniques. It is shown that asynchronous amplitude histograms may be numerically compared with reference histograms to extract information regarding quality and the noise degrading the signal under analysis. The proposed method is validated through numerical simulation and experiment.

An analytical model to compute the frequency limitations of cross-phase modulation (XPM) in all-optical fiber wavelength converters is proposed and validated using numerical simulation at modulation frequencies exceeding 1 THz. The proposed model allows deriving engineering rules for the dimensioning of wavelength converters using nonlinear optical loop mirrors. A novel filter design to optimize the conversion of XPM-induced phase modulation in intensity modulation is proposed and validated using numerical simulation.

Numerical simulation is used to evaluate the impact of fiber nonlinearities in the transmission of 10 Gb/s single sideband signals in links using concentrated electrical or optical dispersion compensation. It is shown that, intra-channel fiber nonlinearities severely degrade the performance. The degradation of 40 Gb/s differential phase-shift-keying (DPSK) signals due to XPM with legacy amplitude-shift keying signals is also analyzed. Pump-probe analysis show that the signal degradation results from XPM-induced intensity modulation. This allows deriving and validating a novel analytical model to estimate the bit-error probability of the XPM-degraded DPSK signals. Finally, an analytical small-perturbations approach to the study of intra-channel fiber nonlinearities in signals with finite extinction ratio is presented. It allows the identification of two new forms of degradation taking the form of impulses between symbols and amplitude and temporal jitter.

Table of Contents

List of Figures

List of Tables

List of Symbols

a_c	Attenuation of the carrier phase shifting filter.
A_{eff}	Effective area of a fiber section.
α	Fiber attenuation parameter.
α_{th}	Adjustment constant for the asynchronous histogram analysis proposed by Shake et al.
B	Bit-rate.
B_{in}	Bandwidth of the instantaneous power of the input signal.
B_o	Bandwidth of an optical receiver filter.
B_{oc}	Bandwidth of the detuned optical filter for cross-phase-modulation-based wavelength conversion.
B_r	Bandwidth of an electrical receiver circuitry.
B_{ref}	Reference bandwidth for the calculation of an optical signal-to-noise ratio
B_{XPM}	Cross-phase-modulation cut-off frequency.
$B_{XPM,req}$	Required cross-phase-modulation cut-off frequency.
β and β'	Fiber propagation constant in linear and nonlinear transmission regimes, respectively.
β_2	Group velocity dispersion parameter.
$\Delta\beta_{nmp}$	Phase matching condition for four-wave mixing.
c	Speed of light in vacuum.
$C_{PM-PM,GVD}$	Conversion factor due to group velocity dispersion in a fiber.
$C_{PM-PM,SPM}$	Conversion factor due to self-phase modulation in a fiber.
C_{pre} and C_{pos}	Dispersion pre-compensation and post-compensation, respectively.

d_F	Degeneracy factor of four-wave mixing.
d_{sp}	Walkoff parameter.
dz	Infinitesimal segment of fiber.
δf	Offset of the detuned filter for XPM-based wavelength conversion, with respect to the average probe channel frequency.
Δ	Width of the bins of an asynchronous histogram.
$\Delta\phi_{XPM}$	Differential XPM-induced phase modulation.
Δi_d	Electrical current fluctuations resulting from cross-phase modulation.
Δi_ϕ	Electrical current fluctuations resulting from the cross-phase modulation-induced phase modulation.
Δi_p	Electrical current fluctuations resulting from the cross-phase modulation-induced intensity modulation.
$\Delta\mu$	Difference between the nominal levels for the mark and space symbols in an asynchronous histogram.
Δp_{XPM}	Differential XPM-induced intensity modulation.
D	Dispersion parameter.
D_{ac}	Accumulated dispersion.
D_s and D_p	Dispersion parameters of the fiber at the probe and pump wavelengths, respectively.
D_{res}	Total residual dispersion of a link.
EOP	Eye opening penalty.
f	Frequency.
ϕ_c	Phase shift imposed by a carrier phase shifting filter.
ϕ_s	Phase shift of a probe channel.
ϕ_{SPM}	SPM-induce phase shift
ϕ_{XPM}	XPM-induced phase shift.
g	Gain of an optical amplifier in linear units.
γ	Nonlinearity coefficient of the fiber.

h	Plank constant.
h_{eq}	Impulse response of the equivalent sampling filter.
$h_{EST,i}$	Estimated histogram of a signal.
$h_{MEA,i}$	Measured histogram of a signal.
$h_{OMS,i}$	Histogram of the noise generated within an optical monitoring system.
$h_{REF,i}$	Reference histogram of a signal.
$h_{SIG,i}$	Theoretical histogram of a signal in the absence of noise.
$h_{SIG1,i}$ and $h_{SIG0,i}$	Components of the theoretical histogram of a signal in the absence of noise, corresponding to the mark and space symbols, respectively.
H_{CPSF}	Transfer function of the carrier phase shifting filter.
H_{eq}	Transfer function of the equivalent sampling filter.
H_{EDC}	Transfer function of the electrical dispersion compensation filter.
$H_{\phi,GVD}$	Transfer function of the equivalent linear model for the cross-phase modulation-induced phase shift, considering the contribution of group velocity dispersion.
$H_{\phi,SPM}$	Transfer function of the equivalent linear model for the cross-phase modulation-induced phase shift, considering the contribution of self-phase modulation.
$H_{\phi,XPM}$	Transfer function of the equivalent linear model for the cross-phase modulation-induced phase shift.
H_o	Low-pass equivalent transfer function of an optical filter.
H_r	Transfer function of an electrical receiver filter.
H_T	Transfer function of a Hilbert transformer.
η	Conversion efficiency.
η_{nmp}	Four-wave mixing efficiency.
η_{req}	Required conversion efficiency.
i_d	Electrical current after photo-detection.

$\overline{I}_s$	Average electrical current.
κ	Q-factor correction factor due to non-ideal sampling.
L	Fiber length.
L_{eff}	Effective length of a fiber.
λ	Wavelength.
λ_s and λ_p	Probe and pump wavelengths, respectively.
μ_1 and μ_0	Nominal levels for the mark and space symbols of a binary signal, respectively.
$\mu_{1,\text{avg}}$ and $\mu_{0,\text{avg}}$	Average levels for the mark and space symbols in an asynchronous histogram, respectively.
$\mu_{1,k}$ and $\mu_{0,k}$	Nominal levels for the k-th mark and space symbols of a binary signal, respectively
n	Noise component of a generic signal in the time domain.
n_0	Refractive index of an optical fiber in linear transmission regime.
n_2	Coefficient of the nonlinear refraction index of an optical fiber.
n_{ref}	Refractive index of an optical fiber.
n_{sp}	Spontaneous emission noise factor of an optical amplifier.
N_b	Number of bins on an asynchronous histogram.
N_{ch}	Number of channels in a WDM system.
N_{sp}	Power spectral density of the amplified spontaneous emission noise generated by an optical amplifier.
υ	Optical frequency
$osnr$	Optical signal-to-noise ratio, in linear units.
$osnr_{EST}$	Estimated optical signal-to-noise ratio of a signal, in linear units.
$OSNR_{EST}$	Estimated optical signal-to-noise ratio of a signal, in decibel.
$osnr_{REF}$	Optical signal-to-noise ratio of a reference signal, in linear units.
$OSNR_{REF}$	Optical signal-to-noise ratio of a reference signal, in decibel

$osnr_{SIG}$	Actual optical signal-to-noise ratio of a signal, in linear units.
$OSNR_{SIG}$	Actual optical signal-to-noise ratio of a signal, in decibel.
p_{SIG}	Probability density function of a signal.
P_{CW}	Average power of a continuous wave signal.
P_e	Bit-error probability.
$P_{e,XPM}$	Bit-error probability of a differential phase shift keying signal degraded by cross-phase modulation.
P_{FWM}	Power of a wave generated by four-wave mixing.
P_{out}	Instantaneous power at the output of a wavelength converter.
P_p	Instantaneous pump power.
P_{peak}	Peak power.
$P_{peak,req}$	Required peak power.
q	Q-factor in linear units
q_{avg}	Average Q-factor, in linear units.
q_{eq}	Equivalent Q-factor measured using a non-ideal sampling system, in linear units.
s	Information component of a generic signal in the time domain.
s_{01} and s_{10}	Space-to-mark and mark-to-space transitions, respectively.
S_n	Power spectral density of the noise component of a generic signal in the frequency domain.
σ_1 and σ_0	Standard deviation of the noise components associated with the mark and space symbols of a binary signal, respectively.
$\sigma_{1,k}$ and $\sigma_{0,k}$	Standard deviation of the noise components associated with the *k*-th mark and space symbols of a binary signal, respectively.
$\sigma_{1,\text{avg}}$ and $\sigma_{0,\text{avg}}$	Average standard deviation of the noise components associated with the mark and space symbols of an asynchronous histogram, respectively.
$\sigma_{\Delta i,XPM}$	Standard deviation of the differential electrical current fluctuations induced by cross-phase modulation.

$\sigma_{EST,1}$ and $\sigma_{EST,0}$	Estimated standard deviations of the noise components associated with the mark and space symbols of a binary signal, respectively.
$\sigma_{EST}(a_i)$	Estimated standard deviation of the noise component associated with the current level a_i.
$\sigma^2_{\min}$	Variance of the signal-independent noise components after detection.
σ^2_n	Variance of the noise samples after an ideal sampling system.
$\sigma^2_{n,eq}$	Variance of the noise samples after a non-ideal sampling system.
$\sigma_{OMS}(a_i)$	Standard deviation of the noise component associated with the current level a_i and generated within an optical monitoring system.
$\sigma_{REF}(a_i)$	Standard deviation of the noise component associated with the current level a_i from a reference signal.
$\sigma_{SIG}(a_i)$	Standard deviation of the noise component associated with the current level a_i from a signal under analysis.
$\sigma_{XPM,P}$	Standard deviation of the cross-phase modulation-induced intensity fluctuations.
t	Time.
T	Symbol period.
T_a	Sampling period.
t_r	Transition time of a non-return-to-zero signal.
τ_{in} and τ_{out}	Pulse-width of the input and output impulses of a wavelength converter, respectively.
τ_{XPM}	Pulse-width of the XPM-induced phase impulses.
u_{conv}	Complex envelope of a wavelength converted signal, using four-wave mixing.
u_s	Complex envelope of the probe channel.
u_{signal}	Complex envelope of an optical signal.
u_{out}	Complex envelope of the probe channel at the output of the PM-IM converter
u_{pump}	Complex envelope of a pump signal.
u_{ref}	Complex envelope of the reference signal in a NOLM.

u_{reg}	Complex envelope of a regenerated signal, using four-wave mixing.
υ	Optical frequency
υ_{mnp}	Optical frequency of an optical wave generated by four-wave mixing of the optical waves located at the frequencies υ_m, υ_n and υ_p.
υ_0	Zero dispersion optical frequency.
v_{gp} and v_{gs}	Group velocities of the pump and probe signals, respectively.
ω	Angular Frequency.
ω_o	Optical angular frequency.
x_k	Generic succession of samples with integer index, *k*.
X_μ	Variation of the difference between symbols of an asynchronous histogram between consecutive measurements.
$X_{\sigma 1}$	Variation of the standard deviation of the noise component on the mark symbol of an asynchronous histogram between consecutive measurements.
Ψ	Sampling impulse.
z	Fiber coordinate.
z_0	Point of zero accumulated dispersion in a link.

List of Acronyms

A

ADC: Analog-to-Digital Converter

AOWC: All-Optical Wavelength Converter

ASE: Amplified Spontaneous Emission

ASK: Amplitude Shift Keying

B

BER: Bit-Error Ratio

BOF: Bismuth Oxide-based Fiber

BPS: Bandwidth of Phase-Shift

C

CPSF: Carrier Phase Shifting Filter

CSRZ: Carrier Suppressed Return-to-Zero

CW: Continuous Waveform

D

DCE: Dispersion Compensating Element

DD: Direct Detection

DGD: Differential Group Delay

DI: Delay Interferometer

DPSK: Differential Phase Shift Keying

DQPSK: Differential Quadrature Phase Shift Keying

DSB: Double Sideband

DSF: Dispersion Shifted Fiber

E

EAH: Estimated Amplitude Histogram

EAM: Electro-Absorption Modulator

ECL: External Cavity Laser

EDC: Electrical Dispersion Compensation

EDFA: Erbium Doped Fiber Amplifier

ELM: Equivalent Linear Model

EOP: Eye Opening Penalty

F

FBG: Fiber Bragg Grating

FEC: Forward Error Correction

FM: Frequency Modulation

FSK: Frequency Shift Keying

FWC: Fiber Wavelength Converter

FWHM: Full-width at Half Maximum

FWM: Four-Wave Mixing

G

GVD: Group Velocity Dispersion

H

HN-DSF: Highly Non-linear Dispersion Shifted Fiber

HT: Hilbert Transformer

I

IFWM: Intra-channel Four Wave Mixing

IM: Intensity Modulation

IM-DD: Intensity Modulation-Direct Detection

IR: Invention Report

ISI: Inter-Symbol Interference

IXPM: Intra-channel Cross-Phase Modulation

M

MAH: Measured Asynchronous Histogram

MD: Monitor Diode

MZM: Mach-Zehnder Modulator

N

NOLM: Nonlinear Optical Loop Mirror

NRZ: Non-Return-to-Zero

NZDSF: Non-Zero Dispersion Shifted Fiber

O

OIM: Optical Impairment Monitor

OMS: Optical Monitoring System

OPM: Optical Performance Monitor

OSA: Optical Spectrum Analyzer

OSNR: Optical Signal-to-Noise Ratio

P

PDF: Probability Density Function

PM: Phase Modulation

PM-IM: Phase Modulation-to-Intensity Modulation

PMD: Polarization Mode Dispersion

PSD: Power Spectral Density

R

RAH: Reference Asynchronous Histogram

RF: Radio Frequency

RTD: Resonant Tunnelling Diode

RZ: Return-to-Zero

S

S&H: Sample and Hold

SOA: Semiconductor Optical Amplifier

SCR: Signal-to-Crosstalk Ratio

SDH: Synchronous Digital Hiearchy

SPM: Self-Phase Modulation

SSB: Single Sideband

SSFM: Split-Step Fourier Method

SSMF: Standard Single-Mode Fiber

SSNR: Signal-to-Sampling Noise Ratio

T

TF: Transmission Fiber

TW: TrueWave

V

VOA: Variable Optical Attenuator

W

WDM: Wavelength Division Multiplexing

WP: Waveguide Photodetector

X

XGM: Cross-Gain Modulation

XPM: Cross-Phase Modulation

Chapter 1. Introduction

1.1. Context

Communications have conquered a preponderant role in the ever more technologically involved society, actively influencing the way of life of each individual and community. The use of digital communications resources such as telephony, television or internet has become commonplace in everyday life. In fact, the demand for bandwidth resources greatly surpassed all expectations, rapidly exhausting the resources made available by network operators. To maintain availability of capacity, network operators were required to evolve not only the access networks supporting broadband requirements, but also the core optical networks, improving capacity and flexibility.

Core optical networks have seen a dramatic evolution since the development of erbium doped fiber amplifiers (EDFA) in the 1990's and the subsequent deployment of wavelength division multiplexed (WDM) systems, which multiplied the capacity of optical links. However, the incredible expansion of mobile communications and services in the first decade of the 21st century has quickly consumed this newfound capacity, leaving operators once again without the ability to respond to traffic demands. The deployment of high capacity WDM links is currently considered trivial and the real challenges lie in the deployment of fully meshed dynamic optical networks. Optical transmission standards have also evolved significantly to a point where the standardization of multi-channel

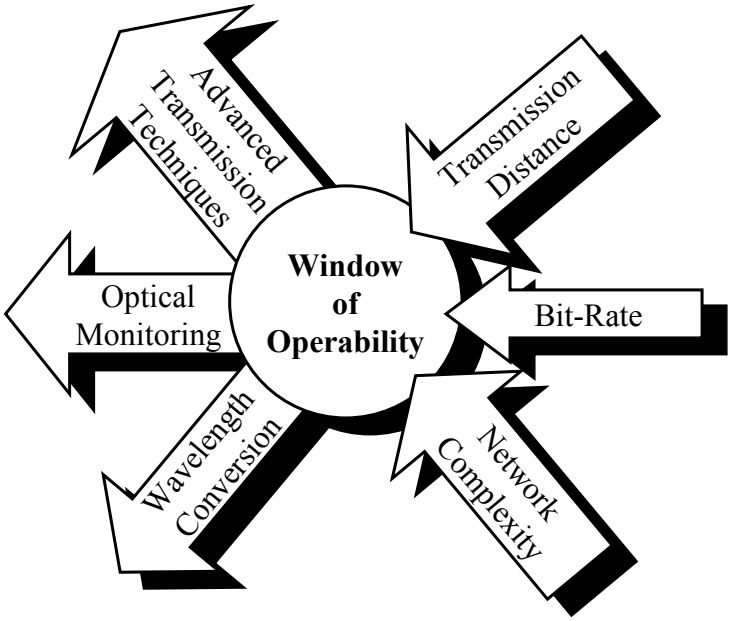

Fig. 1.1. Window of operability.

systems operating at bit-rates exceeding 100 Gb/s per channel is under discussion [Duelk, 2005], [Nakamura, 2006]. It now falls within the responsibility of researchers to devise solutions that allow the development of optical transmission systems capable of operating in such networks and at such bit-rates. Hence the work presented in this dissertation intends to contribute to that purpose.

1.2. Motivation

Current optical networks operate in a fairly static mode within well defined specifications [Willner, 2006]. It is assumed that the parameters that condition the network such as number, bit-rate and path of optical signals; transmission distances or even traffic matrix change slowly in time and within a restricted range. This range corresponds to the window of operability, as illustrated in Fig. 1.1. This concept was developed for the first time by Chraplyvy and Tkach in [Chraplyvy, 1990] and further discussed in [Kilper, 2004]. In the latter reference, Kilper defends the notion that, as the capacity of the optical network increases, the window of operability is closed due to physical constrains such as fiber nonlinearity, noise in optical amplifiers, or simply the limited traffic capacity of the transmission systems. New technology developments try to re-open the window of operability, allowing the advancement of optical communications networks.

In recent years, the main requirements of network operators have been to reduce the overall cost of optical transmission systems while simultaneously extend their capacity and range. This pushes the systems requirements to a limit where it is indispensable to maintain the operational conditions of power, noise, wavelength or dispersion within an increasingly reduced window of operability. For such cases, Willner and Kilper proposed the development of ubiquitous optical monitoring as a fundamental step in the evolution of optical networks [Willner, 2006], [Kilper, 2004]. Optical monitoring systems (OMS) can enable the effective operation of optical transmission systems in the limits of their capabilities, extending the use of the window of operability to its maximum. The initial OMS where used mostly for supervision purposes, allowing the operator to identify and locate failures of the optical links to act accordingly. However, the advent of dynamic networks, where optical paths may be changed automatically, brought the need to automate the response of the transmission systems to changes in the network. This has led to the development of impairment compensation systems controlled by locally installed OMS. One may foresee that in the near future, with the increasing complexity of the architecture of optical networks, OMS may no longer be used only to control locally installed impairment compensating systems but also to control remotely installed compensation systems. Furthermore, the advancement of telecommunications management systems using impairment constrain based routing may allow the use of OMS to achieve a ubiquitous evaluation of the optical performance in a network [Tomkos, 2004]. This would bring novel network functionalities, such as dynamic redirection of traffic through specific paths in the network, according to their instantaneous capability to provide the required quality.

Nevertheless, optical monitoring alone is insufficient to ensure dynamic interconnectivity in a network. The latter requires also a substantial increase of capacity as the number of wavelengths in WDM networks determines the number of independent optical paths available. Although this number may be large enough to fulfill the required information capacity, it often is not large enough to support a large number of nodes. As a simple example, a ring network with N nodes requires a minimum of $N \cdot (N-1)/2$ wavelengths to secure a protected optical path between every two nodes. This yields 28 wavelengths for a ring with 8 nodes but increases to 120 wavelengths for a ring with 16 nodes. As such, typical commercial WDM transmission systems using a limited number of wavelengths have limitations on the number of configurable optical paths. One method of

overcoming this limitation is to convert signals from one wavelength to another. The benefit of wavelength conversion varies with network architectures and traffic patterns [Zang, 2000], [Yoo, 1996]. Wavelength conversion may be performed by converting the signal to the electrical domain and reconverting the signal to the optical domain in a different wavelength. All-optical wavelength conversion is also possible, using the nonlinear behavior of optical components to convert a signal from one wavelength to another. Typically, optical components pose less bandwidth restrictions to the processed signals than electrical components. For this reason, and with the steady increase of the bit-rates of the transmitted signals, all-optical wavelength conversion has been considered an essential function of future all-optical networks operating at ultra-high bit-rates [Elmirghani, 2000]. Several types of optical components have been considered for application in all-optical wavelength converters (AOWC). The fundamental criteria for the choice of the optical component are the inherent nonlinearity and the response time [Elmirghani, 2000]. The most common proposals for AOWC in the literature use semiconductor-optical amplifiers (SOA) or optical fibers [Öhlén, 2000]. SOA typically present a strong nonlinearity in the presence of intense optical fields, with the advantage of increased sensitivity due to power gain, often dispensing further optical amplification to achieve reasonable output powers [Leuthold, 2004]. However, SOA tend to have a slow response to variations of the optical field, due to the opto-electronic recombination processes that occur within the semiconductor material. However, several techniques can be used to compensate the slow response of SOA, such as specialized optical filtering or operation in interferometric structures [Leuthold, 2004]. This has allowed the successful demonstration of SOA-based AOWC operating at bit-rates as high as 320 Gb/s [Liu, 2007]. In the case of conventional optical fibers, the nonlinear response is typically weaker than SOA. Hence optical amplification is usually required for fiber-based AOWC. Nevertheless, the nonlinear response of optical fibers is nearly instantaneous, allowing operation at remarkably high bit-rates [Perlin, 2002]. Furthermore, the development of highly nonlinear fibers has boosted significantly the research of this form of AOWC [Holmes, 1995]. As examples, experimental demonstration of optical time-domain demultiplexing using a fiber-based AOWC at bit-rates as high as 1.28 Tb/s has been presented in [Nakazawa, 2000], making this type of wavelength converters highly desirable for medium term application in all-optical networks. Fiber-based AOWC make

use of well known nonlinear phenomena such as four-wave mixing (FWM) and cross-phase modulation (XPM). In the prior case, the FWM-generated waves resulting from the nonlinear interaction between the original signal and one or more high power continuous waveform (CW) signals [Inoue, 1992: 1]. This allows generating replicas in phase and intensity of the original signal. However, AOWC using FWM have significant limitations regarding the relative wavelengths of the input and output signals, which in a general way restrict the operability [Elmirghani, 2000]. AOWC using XPM are significantly more flexible by imprinting the phase of a CW signal with the information carried on the intensity of the original signal [Elmirghani, 2000]. This allows an arbitrary choice of the wavelength of the output signal regardless of the wavelength of the input signal. The final output signal is produced by converting the phase modulation imprinted on the CW signal in intensity modulation. Given their flexibility, XPM-based fiber AOWC have been considered as the most promising technology for wavelength conversion at ultra-high bit-rates. The main disadvantage of AOWC using XPM is the need to have intensity modulated input signals. However, phase modulated signals may also be handled using phase-to-intensity conversion prior to the AOWC, as recently proposed in [Matsumoto, 2007].

Despite the strong investments realized in the fields of optical monitoring and all-optical wavelength conversion, system manufacturers have not yet applied the full potential of these techniques to commercial systems. Instead, the main developments in optical transmission systems in recent years have regarded advanced optical transmission techniques. These bring a direct opening of the window of operability with advanced modulation techniques to handle noise, fiber dispersion and nonlinearity. A number of advanced optical modulation formats have attracted increased attention. Some of these formats carry information through amplitude shift keying (ASK), but also modulate the optical phase in a non-information-bearing way in order to enhance the robustness to fiber dispersion and/or nonlinearities. Advanced optical transmitters using techniques based on electronic pre-distortion [Killey, 2005] and single sideband (SSB) modulation [Sieben, 1999] have been proposed, allowing the reduction or even suppression of optical dispersion compensation. However, this leads to strong nonlinear inter and intra-channel interactions, as shown by Essiambre et al. in [Essiambre, 2006]. Optical phase modulation formats such as differential phase shift keying (DPSK) have also resurfaced in the recent

years [Gnauck, 2005]. In fact, the most recent transmission distance records have been achieved using DPSK modulation formats e. g. [Charlet, 2003], among others. Currently, DPSK systems have reached sufficient maturity for deployment in commercial long and ultra-long haul optical communications networks at bit rates exceeding 40 Gb/s. One of the main obstacles to the deployment of such systems in currently installed infrastructure is the nonlinear interaction with legacy ASK signals [Rohde, 2000]. Finally, when considering advanced transmission techniques, one must account for the advancements in the study of fiber nonlinearities in the transmission of signals at ultra-high bit-rates. For such systems, Essiambre et al. have demonstrated the dominant degradation due to intra-channel nonlinearities such as intra-channel cross-phase modulation (IXPM) and intra-channel four-wave mixing (IFWM) [Essiambre, 2002].

Given this analysis, one may infer that currently the main constrains to the window of operability are based on the required increase of transmission distance and bit-rate and the required advancements in network complexity, as illustrated in Fig. 1.1. Furthermore, these constrains may be relieved by developments in the fields of optical monitoring, wavelength conversion and advanced transmission techniques. Hence the development of these three areas is the motivation of the following work, aiming to expand the window of operability of optical networking systems in the future.

1.3. Structure and Objectives

This work intends to present innovative techniques for the design and optimization of optical routing techniques and devices. As described in section 1.1, the focus of the work falls in the development of optical monitoring systems, as fundamental enabling systems for optical networks; the improvement of all-optical wavelength conversion techniques, essential for the effective operation of transparent optical networks at ultra-high bit-rates; and the study of the impact of fiber nonlinearities in systems employing advanced optical transmission techniques. As such, Chapter 2 contains a description of the basic concepts regarding optical monitoring techniques and systems. The presented work proposes a classification of OMS according to their purpose and method of analysis of the optical systems and impairments. It also includes a review of the reference works in this field available in the literature and a study of fundamental techniques to monitor power, noise and dispersion in optical systems. Chapter 2 also intends to introduce the main

concepts behind the optical monitoring techniques using the analysis of asynchronous histograms, with a review of other works on this topic available so far, and an evaluation of the advantages and disadvantages of each technique. Chapter 3 intends to demonstrate the applicability of the analysis of asynchronous histograms as a practical means to implement OMS. The limitations imposed by sampling systems with limited bandwidth are addressed, deriving a simplified method to estimate the Q-factor measurement error in such cases. Two techniques to counter these limitations are proposed and validated using numerical simulation. Chapter 3 also presents a novel method to analyze asynchronous histograms using reference asynchronous histograms. The novel method is experimentally demonstrated, allowing a reasonable evaluation of optical signal-to-noise ratio (OSNR) with relaxed requirements for the monitoring system.

To contribute for the improvement of fiber XPM-based AOWC, Chapter 4 presents a study of the mechanisms of fiber nonlinearity behind such systems. This chapter also includes a study of fiber FWM-based AOWC, for comparison purposes. Chapter 5 intends to present a study of the bandwidth limitations of fiber XPM-based AOWC operating at ultra-high bit-rates. Analytical expressions are derived to compute the XPM cut-off frequency, taking into account the impact of walkoff, group velocity dispersion (GVD) and self-phase modulation (SPM) in optical fibers. The analytical model is validated using numerical simulation considering signals with modulation frequencies in the THz range. Applicability of the analytical models is demonstrated by deriving expressions for the physical design of fiber-NOLM wavelength converters, which are validated through numerical simulation. Chapter 5 also presents a study of a hypothetical ideal phase modulation-to-intensity modulation (PM-IM) converter for application in fiber XPM-based AOWC. This theoretical device would allow the use of all the available energy in the wavelength converter to produce an intensity modulated output signal. Practical implementation of the ideal PM-IM converter is discussed and analyzed using numerical simulation.

To contribute to the development of advanced transmission techniques, Chapter 6 presents a study of the impact of fiber nonlinearities in three distinct types of systems. We begin by addressing the operation of 10 Gb/s SSB systems in links without dispersion compensation, employing electrical dispersion pre-compensation. It is shown, for the first time to the author's knowledge, that the impact of intra-channel fiber nonlinearities plays a

significant role in the optimum dispersion management scheme. Numerical simulations are used to demonstrate that the optimum transmission regime in such systems resembles the pseudo-linear transmission regime observed by other authors at higher bit-rates. Chapter 6 also includes an innovative approach to the problem of nonlinear interactions in WDM systems employing mixed modulation formats. The particular case of 40 Gb/s DPSK signals impaired by XPM due to 10 Gb/s ASK channels is considered using a pump-probe analysis for the first time. Numerical simulations demonstrate that the analysis of the XPM-impact may be reduced to the analysis of the XPM-induced intensity modulation (IM), similarly to the case of intensity modulation-direct detection (IM-DD) systems. This result is used to derive a simple analytical model for the XPM-induced bit-error ratio (BER) degradation. To complete the study of advanced transmission techniques, Chapter 6 presents an analytical description of the intra-channel nonlinearities in signals with finite extinction ratio. This approach uses a small-perturbations model to describe two new forms of nonlinear interactions between mark symbols and the space level within the signal. The magnitude of these interactions is compared with the well known degradations induced by IFWM and IXPM, showing that the former easily surpass the latter. Furthermore, it is shown that the new interactions are responsible for significant changes in the optimum dispersion management scheme, in agreement with simulation works by other authors.

1.4. Main Contributions

The main contributions of this work may be summarized as follows:

- Development of a simple approach to handle the impact of the frequency limitations of sampling systems on the analysis of the performance of optical signals using of asynchronous histograms. This approach allowed a substantial reduction of the bandwidth requirements for these systems, without loss of accuracy (Chapter 3);
- Development of an asynchronous histogram analysis method to estimate Q-factor, that simultaneously accounts for frequency limitations of the sampling system, GVD-induced distortion and optical or electrical filtering of the signal (Chapter 3);
- Development and experimental demonstration of an asynchronous histogram analysis method based on the numerical processing of reference histograms acquired from the signal under analysis in a calibration stage, to estimate the OSNR. The novel method

is applicable to arbitrary modulation formats and tolerant to perturbations introduced by the OMS. (Chapter 3);

- Development and validation through numerical simulation of a novel analytical model for the characterization of the XPM-frequency limitations in fiber-XPM AOWC (Chapter 5);
- A study of the impact of the XPM-frequency limitations on the design of fiber-nonlinear optical loop mirror (NOLM) wavelength converters operating at ultra-high bit-rates (Chapter 5);
- Study of the characteristics required for a theoretically ideal PM-IM converting filter for application in wavelength converters. The novel filter allows an optimized use of the energy available in XPM-based wavelength converters to maximize the power of the output signal (Chapter 5);
- Study of the dispersion management in 10 Gb/s transmission systems employing SSB modulation format and electrical dispersion compensation without inline optical dispersion compensation through numerical simulation. It is shown that such systems are strongly impaired by intra-channel fiber nonlinearities, presenting a behavior similar to the one observed for signals at high bit-rates operating in a pseudo-linear transmission regime (Chapter 6);
- Study of the nonlinear interactions between ASK and DPSK channels in WDM transmission systems using mixed modulation formats through numerical simulation. This study results in an analytical model to estimate the BER of DPSK signals degraded by XPM due to nonlinear interaction with ASK signals (Chapter 6);
- Study on the intra-channel fiber nonlinearities on signals with finite extinction ratio. It is shown that these nonlinearities yield two new forms of interaction between impulses and the non-zero space level, generating a novel form of ghost impulse and additional timing and amplitude jitter (Chapter 6);
- Further studies of intra-channel nonlinearities in signal with finite extinction ratio show that the small-perturbations approach is unsuitable to devise the optimum dispersion compensation map. It is analytically shown that this type of systems requires asymmetric dispersion compensation maps with reinforced dispersion precompensation (Chapter 6);

The publications that have resulted from this work are outlined in Appendix L.

Chapter 2. Basic Concepts of Optical Monitoring

2.1. Introduction

To understand the role of OMS in optical networks, one may consider that optical signals are fundamentally degraded by amplified spontaneous emission (ASE) noise due to optical amplification, crosstalk, and signal distortion as a result of transmission through optical components and optical fibers [Kilper, 2004]. With the rapid increase of the transmitted bit-rates and the channel density in WDM systems, the impact of signal distortion or crosstalk on the quality of the optical signals may equal or even surpass the currently dominant impact of ASE noise [Kilper, 2004]. As such, there is an urgent need for the development of OMS which effectively distinguish and quantify the impact of these forms of degradation. This chapter intends to briefly describe the main techniques currently available to perform optical monitoring as well as focus on those that hold the most significant potential for application in future networks. Section 2.2 proposes a simple classification for OMS to address the multiple forms of OMS available in the literature, which is used throughout this chapter. Section 2.3 presents a description of some of the most relevant optical monitoring methods proposed in the literature. In section 2.4, particular emphasis is given to optical monitoring methods based on the analysis of asynchronous histograms. Final conclusions are drawn in section 2.5.

2.2. Classification of Optical Monitoring Techniques

Generally, the development of OMS is performed subsequently to prior advancements in transmission technologies or components. Furthermore, the cost of advanced OMS often impose the development of the latter on a requirement basis, i. e. OMS are usually developed as support sub-systems for specific applications, when necessary. For this reason, OMS are usually one step behind the development of the mainstream optical transmission systems. It is not uncommon that a given optical monitoring technology only reaches maturity after the transmission technology that it was initially developed for is dropped, in favor of alternative advancements. As an example, one may consider the recent development of OMS for DPSK systems [Li, 2006] occurring at a time when such systems are being replaced with more advanced differential quadrature phase shift keying (DQPSK) systems. Although this is not a rule, one may consider that the deployment of commercial optical transmission systems, which requires an established maturity of all sub-systems, has been performed with limited or simply inexistent optical monitoring technology. With the reduction of the operability window of optical transmission systems, one may expect that this cycle is broken in the near future as OMS become an enabler of optical transmission systems. Nevertheless, the developments of OMS since the implemntation of WDM systems as brought a large number of solutions, which is steadily increasing [Kilper, 2004]. As such, this study begins by proposing a classification to distinguish OMS according to their specific purpose. In all cases, it will be assumed that the considered OMS operate without interrupting the signal under analysis. Other types of OMS will be referred as measurement instruments and are outside the scope of this work. This analysis is limited to digital optical transmission systems, leaving their analog counterparts to further studies.

Fig. 2.1 presents a schematic of the proposed classification. OMS designed with the purpose of evaluating the performance of the signal under analysis through BER or equivalent quantities such as Q-factor, will be classified as optical performance monitors (OPM). This category of OMS may also be divided in OPM supported by digital information carried on the signal under analysis, and OPM that recur to analysis of the signal waveform to estimate its BER. The prior will be referred here as digital OPM, due to the digital processing required to estimate BER. Analogously, the latter will be referred

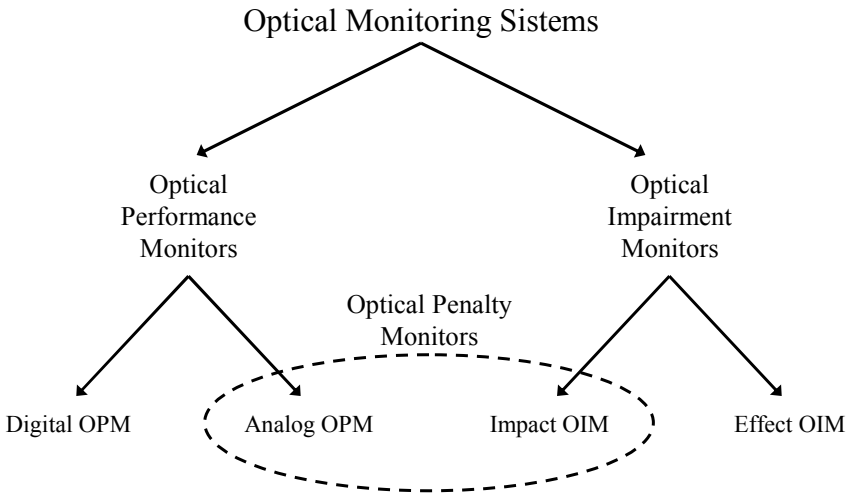

Fig. 2.1. Classification of optical monitoring systems.

here as analog OPM, given the inherent analog nature of the signal processing that is performed.

A common example of digital OPM may be found in the performance counters used in synchronous digital hierarchy (SDH) systems, defined in [ITU G.707, 2003]. In such systems, the performance is estimated by error counting, using a technique referred as bit-interleaved-parity. This technique involves a parity check of interleaved blocks of the signal for the detection of single errors. This provides a rough estimation of the BER, which usually suffices the quality requirements of SDH systems in operation [Park, 2002: 1]. A more evolved approach was taken for the implementation of optical transport networks, defined in [ITU G.709, 2003]. In this case, the BER may be estimated as a sub-product of forward error correction (FEC) techniques [Mizuochi, 2006]. The accuracy of such methods as also allowed their use for the control of GVD- and polarization mode dispersion (PMD) -compensation sub-systems, as demonstrated in [Sugihara, 2002] and [Ishida, 2002], respectively. Digital OPM require a full electrical receiver to detect the signal, followed by complex electronic processing. Therefore, this form of OMS is generally co-located with the electrical receiver of the signal, at the terminal points of the optical path or in intermediate electrical regeneration points. This places significant restrictions on the application of digital OPM in transparent optical networks. An alternative is the use of analog OPM. In this case, the OPM use indicators of the signal's waveform or spectrum to estimate the performance. Perhaps the most notorious have been based on acquiring histograms of the signal under analysis, and from them extrapolate the

BER. Examples of analog OPM may be found in [Wiesmann, 2000], assuming synchronous sampling of the signal under analysis, and [Shake, 1998] or [Hanik, 1999], assuming asynchronous sampling. The latter techniques are further discussed in section 2.4 and Chapter 3. Generally, analog OPM require a simplified electrical receiver and with low speed processing. This may allow a substantial reduction of the cost when compared with digital OPM, with the tradeoff of a reduced accuracy of the BER estimates. As such, analog OPM may become viable for application in arbitrary points of the network.

OMS designed with the purpose of evaluating a given transmission impairment, such as GVD or ASE noise, will be classified as optical impairment monitors (OIM). These may be distinguished between OIM designed to quantify a given transmission impairment, referred here as effect OIM; and those designed to quantify the impact of transmission impairments on the performance of the signal under analysis, referred here as impact OIM. As an example, one may consider that an optical spectrum analyzer (OSA) integrated within an optical transmission system for the estimation of OSNR is included in sub-category of effect OIM. The OSNR estimate is a direct quantification of the noise and signal powers, which is unrelated with other optical impairments[1]. However it has a limited correlation with the system performance. Hence, this type of monitoring alone cannot be used to optimize the system performance. For other examples of effect OIM, one may highlight the works by Yu et al. in [Yu, 2002] to monitor GVD and Luo et al. in [Luo, 2004] to monitor PMD. In the prior case, the authors quantify the phase difference between the upper and lower sidebands of the signal under analysis, whereas the second case uses the power of RF tones, which vary with the amount of accumulated differential group delay (DGD) on the signal. In both cases, the result of the measurement is negligibly affected by transmission impairments other than the intended one. Once again, these monitors quantify given optical impairments but do not relate the attained measurements with the system performance. Another example of effect OIM has been recently presented by Lizé et al in [Lizé, 2007]. The proposed system is based on using a specialized filtering scheme to isolate specific components of the signal and noise that are then analyzed in the optical and electrical domain. This allows an independent quantification of OSNR, GVD and PMD using the same monitor. Furthermore, the authors have demonstrated its

[1] This is assumption considers that optical impairments do not affect significantly the OSNR, which is in first order true for linear transmission effects but may become false when considering strong fiber nonlinearities.

application with non-return-to-zero (NRZ) -ASK, DPSK and duobinary modulation formats, illustrating its flexibility.

Note that the examples presented above for effect OIM deliver measurements in a form which is theoretically independent of the signal under analysis. Alternatively, OMS may use alterations of the signal properties induced by optical impairments to address the impact of the latter. This is the principle of the second proposed sub-category of OIM, the impact OIM, which evaluate the impact of a given impairment on the quality of signal under analysis rather than evaluating the impairment itself. An example of such type of monitors is presented by Weinert et al in [Weinert, 2001]. In this case, the authors propose to use histograms of the signal under analysis to evaluate the jitter present in a return-to-zero (RZ) signal. The impairments that lead to jitter are irrelevant at this point and the monitoring system focuses mainly on addressing the impact of this form of degradation. Note that impact OIM may provide a performance penalty of some sort, which is intimately related with the reachable BER[2]. For this reason, one may consider that the distinction between an impact OIM and the previously referred analog OPM becomes blurred. Hence these two sub-categories of OMS may be included in a sub-category, referred here as optical penalty monitors, as illustrated in Fig. 2.1. These monitors have the advantage of relating the degradation of the signal induced by transmission along the optical path with the actual performance.

2.3. Optical Monitoring Methods

This section presents a set of monitoring methods to estimate three fundamental quantities in optical transmission systems: power, noise and dispersion. The examples of monitors presented in this section fit in the sub-category of effect OIM and are commonly used for the direct control of corresponding compensation systems. Although these are a mere sample of the vast number of alternatives presented in the literature, they represent the dominant principles behind the technologies available for effect OIM.

[2] "reachable BER" assumes that the OMS is placed in intermediate points of the network and in this condition, it is only possible to conjecture arround the BER which is reachable in the signal receiver.

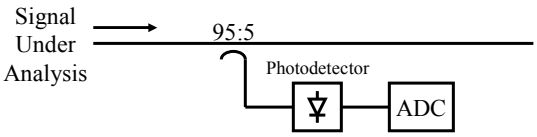

Fig. 2.2. Example of an optical power monitor.

2.3.1. Optical Power Monitoring

Fig. 2.2 presents an example of an optical power monitor. A sample of the signal under analysis is extracted using a tap coupler and fed in to a photodiode with a low cut-off frequency. If the cut-off frequency of the photodiode and corresponding circuitry is low enough, the electrical current generated from the photo-detection process corresponds to the integral of the optical intensity, approximating the average power of the signal under analysis. As such, an analog-to-digital converter (ADC) may be used to estimate the value of the analog electrical photo-current, which is then displayed for the user. Fully analog versions of the optical power monitor using galvanometers to display the value of the electrical photo-current are possible, yet less common. The simplified version of optical power monitors used within optical transmission systems is often referred as monitor diode (MD). Despite its simplicity, the MD is by far the most widespread OMS. Its application ranges from detecting the optical power of the signal under analysis, for alarm generation, to rigorous control of multi-stage optical amplifiers.

Fig. 2.3 presents an example of the integration of MD in a typical commercial WDM transmission system. In the transmitter direction, MD are used to adjust per-channel variable optical attenuator (VOA) to set the required power for each individual channel generated by the transponders, at the multiplexer input. After multiplexing, the WDM signal is fed to an EDFA acting as a booster, which is controlled by monitoring the total power at its input and output ports. In the receiver direction, a monitor diode controls the input power of the incoming WDM signal to adjust the power of a Raman pump and an EDFA acting as pre-amplifier. After the demultiplexer, monitor diodes are used to control VOA that adjust the power at the input of the transponders to acceptable levels. Note that these power levels may also be adjusted by controlling the pre-amplifier output power or the VOA at the transmitter direction of the opposite network element in the far end of the link.

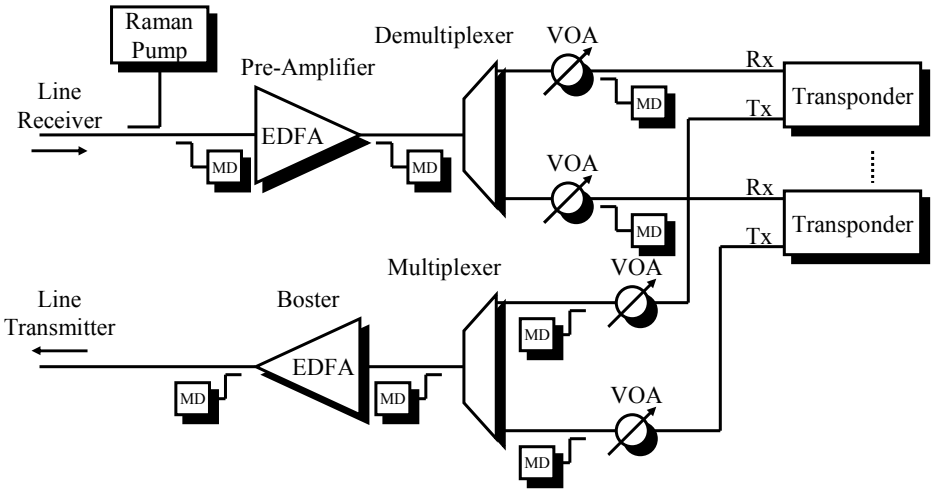

Fig. 2.3. Application optical power monitors in a WDM system.

Typically, an optical power monitor is insensitive to the wavelength of the signal under analysis. However, more elaborate versions of optical power monitors using wavelength dependent responsivity, or preceded by detuned optical filters are commonly used for wavelength dependent monitoring applications [Yang, 2004]. Fig. 2.4-a) presents an example of such a sub-system, where the electrical current at the output of the MD is used to adjust the laser current, simultaneously controlling the wavelength and power of the output signal.

Linear arrays of MD combined with diffraction gratings may also be used for spectral analysis. As shown in Fig. 2.4-b), the spectrum of the WDM signal under analysis is spatially spread by the diffraction grating, with each channel incident over a specific MD or multiple set of MD [Yoshihiro, 2002]. This application is currently used in WDM transmission systems to balance the power spectrum of the WDM signal in long links.

2.3.2. ASE Noise Monitoring

Optical noise results from the process of optical amplification in EDFA or SOA under the form of ASE noise. Although this is merely an approximation, the ASE noise is commonly modeled as complex white Gaussian noise, with a power spectral density (PSD) given by [Desurvire, 1994] (see page 77):

$$N_{sp} = h\upsilon \cdot n_{sp}\left(g-1\right) \tag{2.1}$$

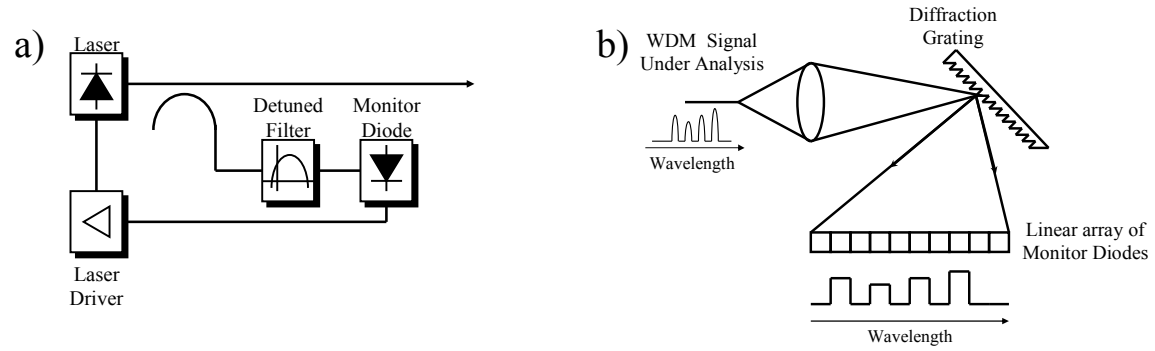

Fig. 2.4. Applications of MD. a) Wavelength dependent power monitor for laser tuning [Yang, 2004]; b)Array of MD combined with a diffraction grating for low resolution spectral monitoring [Yoshihiro, 2002].

where h, υ, n_{sp} and g are the Planck constant, the optical frequency, the spontaneous emission noise factor and the amplifier gain, respectively. The ASE noise is commonly quantified using the OSNR, defined as:

$$osnr = \frac{P_s}{N_{sp} \cdot B_{ref}} \tag{2.2}$$

where P_s is the power of the transmitted signal at the amplifier output and B_{ref} is a reference bandwidth used to measure the OSNR. In the literature, B_{ref} usually takes the value of 12.5 GHz, corresponding to a resolution bandwidth of 0.1 nm for signals operating in the 1550 nm window. Disregarding all other optical impairments and assuming an IM-DD signal with an NRZ modulation format, the performance of the signal may be related with the OSNR through the bit-error ratio, P_e, by [Kilper, 2003]:

$$P_e \approx \frac{1}{2}\mathrm{erfc}\left(\sqrt{osnr \cdot \frac{B_r}{2B_{ref}}}\right) \tag{2.3}$$

where B_r is the electrical bandwidth of the receiver used to detect the signal. The term erfc(x) is the complementary error function, given by $\mathrm{erfc}(u) = 2/\sqrt{\pi} \cdot \int_u^{\infty} e^{-\lambda^2} d\lambda$. Expression (2.3) only takes into account the electrical noise component resulting from the beating of the signal component and the ASE noise, neglecting all other components. Note that if assuming a direct-detection (DD) -DPSK system, the statistical characteristics of the

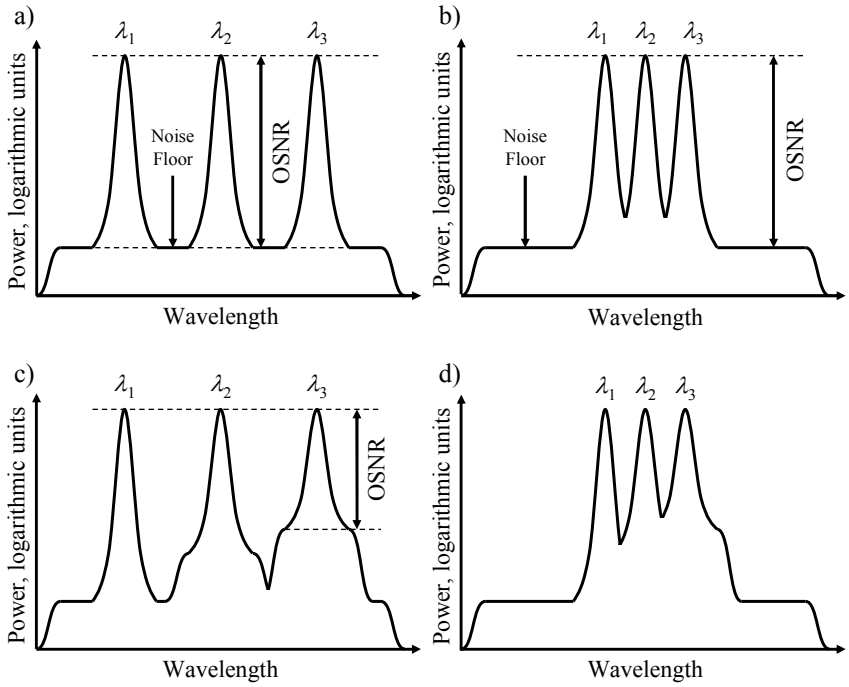

Fig. 2.5. Illustration of the limitations of the OSNR monitoring technique, using spectrum analysis.
a) WDM signal; b) dense WDM signal;
c) WDM signal from meshed network; d) dense WDM signal from meshed network.

ASE noise after detection are significantly different. Hence expression (2.3) would be written as [Chinn, 1996]:

$$P_e \approx 1/2 \cdot \exp\left\{-osnr \cdot \frac{B_o}{B_{ref}}\right\} \tag{2.4}$$

where B_o is the bandwidth of the optical receiver filter. Note that both (2.3) and (2.4) assume wideband optical filtering and reduced distortion induced by the electrical receiving filter. These approximations fail when considering dense WDM systems, where the optical bandwidth of the multiplexer and demultiplexer filters and additional filtering along the optical path is of the order of, or even smaller than, the bandwidth of the signal. Such cases require substantially more complex modeling, such as [Rebola, 2001] for IM-DD systems and [Chinn, 1996] for DD-DPSK systems. Expressions (2.3) and (2.4) show that an evaluation of the OSNR can only provide a qualitative estimate of the BER. An accurate estimate requires accounting for multiple aspects such as modulation format and inter-symbol interference (ISI). Nevertheless, most currently available WDM transmission

systems are limited by ASE noise. In this case and up to a given degree, one may neglect all the other optical impairments and design the system for a required OSNR. This renders OSNR monitoring as an essential function of current optical transmission systems.

The most widespread method to infer the OSNR of optical signals is based on analyzing the corresponding optical spectrum [Kilper, 2003], [Yang, 2002]. Fig. 2.5-a) illustrates the OSNR monitoring technique using spectral analysis. After acquiring the power spectrum of the signal under analysis, the ASE noise component may be recognized by the characteristic flat noise floor whereas the WDM channel components present peaks at the wavelengths λ_1, λ_2 and λ_3. The OSNR is proportional to the ratio (or difference in logarithmic units) between the power of the peaks and the noise floor. However, the deployment of dense WDM systems with reduced channel spacing and high bit-rates renders this approach unfeasible as the noise floor in the optical spectrum is undistinguishable from the signal. In these cases, the edges of the spectra of the WDM channels superimpose, as illustrated in Fig. 2.5-b). This restricts the measurement of OSNR unless one may find a region of the spectrum where there are no channels, to identify the level of the noise floor. A significantly more complex case arises from the deployment of meshed optical network architectures using optical cross-connectors. This allows for each channel within the WDM signal to present its particular OSNR, leading to optical spectra similar to the ones presented in Fig. 2.5-c) and -d), for WDM and dense WDM systems, respectively. In these cases, each channel has a given in-band noise level which is not clearly distinguishable from the channel component. As such, the measurement of the noise floor using a region of the spectrum without WDM channels is useless to determine the OSNR of each channel. For these reasons, meshed optical networks using dense WDM systems favor the application of in-band OSNR monitoring methods, where the OSNR monitoring is carried out for each channel individually [Kilper, 2003].

An example of an in-band OSNR monitoring technique has been proposed by Rasztovits et al. in [Rasztovits-Wiech, 1998] and further developed by Lee et al. in [Lee, 2001]. In this case, the authors assume that the signal component will have a well-defined polarization, whereas optical noise will be unpolarized. Therefore, the polarization extinction ratio is a measure of the OSNR. Fig. 2.6 illustrates the scheme proposed by Rasztovits et al. This scheme is composed by a polarization controller followed by a

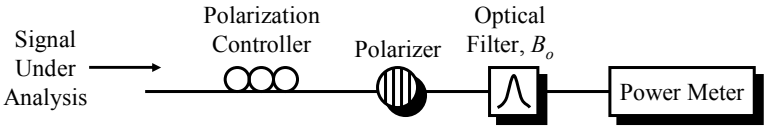

Fig. 2.6. In-band OSNR monitoring system by [Rasztovits-Wiech, 1998].

polarizer in front of a power meter. An optical filter may be placed along the optical path of the signal under analysis, to limit the noise bandwidth. The components of the signal that cross the polarizer are determined by adjusting the polarization controller. As such, setting the polarization controller to have the maximum power at the power meter input yields a measurement of the signal and co-polarized noise components, $P_s+N_{sp}\cdot B_o/2$. Setting the polarization controller to have the minimum power at the power meter input yields only the power of the noise which is orthogonally polarized with the signal, $N_{sp}\cdot B_o/2$. As such, the relation between the maximum and minimum measured powers becomes $1+2\cdot osnr\cdot B_{ref}/B_o$, from which one may extrapolate the OSNR. The main limitation of the approach by Rasztovits et al. results from random variations of the signal polarization due to PMD and nonlinear polarization rotation in the transmission fiber [Kilper, 2003].

In-band OSNR monitoring is also possible by analyzing the electrical spectrum of the received signal. Several approaches have been proposed, such as [Stuart, 2003]. The latter is illustrated in Fig. 2.7 and takes advantage of the fact that the electrical spectrum of the signal retains an approximate conjugate symmetry about specific frequencies, particularly the half-clock frequency. As such, isolating such frequency components, in the absence of noise, results in an in-phase signal component. On the other hand, in the presence of ASE-noise, which is assumed isotropic in the phase space, one should register a quadrature component [Stuart, 2003]. Hence, the monitor takes the relation between the in-phase and quadrature components of the signal at the half-clock frequency as a measure

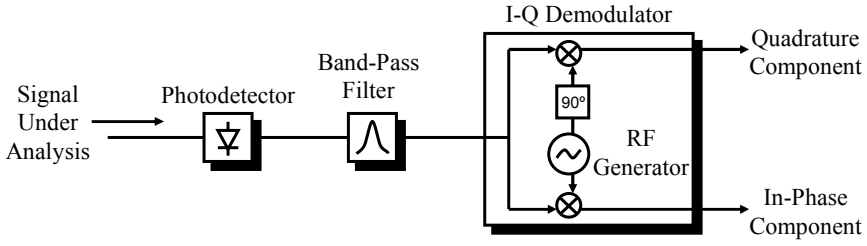

Fig. 2.7. In-band OSNR monitoring system by [Stuart, 2003]. It is assumed that the band-pass filter and the radio frequency (RF) generator are tuned to the half-clock frequency of the signal under analysis.

of the electrical signal-to-noise ratio, which is strongly related with the OSNR. As shown in Fig. 2.7, this is carried out by electrically band-pass filtering the detected signal under analysis at the half-clock signal and using a conventional I-Q demodulator to isolate the in-phase and quadrature components. Despite its simplicity, this approach has the disadvantage of pattern-dependent fluctuations of the measured signal.

The main limitation of the previously mentioned techniques to monitor in-band OSNR results from the fact that both explore the notion that the noise component of the signal under analysis is random whereas the information component is not. In fact, the signal component presents some aspects which may be considered deterministic yet remains inherently random. Recently, a new technique to monitor OSNR using nonlinear amplification has attracted interest [Ng, 2005], [Adams, 2006]. This technique is not based on exploring the random or deterministic distinctions between information and noise components. Instead, it focuses on exploring the statistical behavior of the degraded signal as a whole. To illustrate this technique, consider the examples of probability density functions (PDF) of the instantaneous power of an NRZ signal degraded by ASE noise, $p_{SIG}(p_s)$ presented in Fig. 2.8, where p_s is the instantaneous power. $p_{SIG}(p_s)$ is characterized by two highly probable peaks corresponding to the mark and space symbols. The impact of ASE is manifested mainly by power fluctuations that increase in magnitude with the instantaneous power of the signal. This is shown in the PDF as a broadening of the peaks, particularly the peak corresponding to the mark symbol. For illustrative purposes, consider two cases with high and low OSNR presented in Fig. 2.8. Assume that this signal is amplified by a nonlinear amplifier with a gain characteristic $g(p_s)$ with a positive slope, as

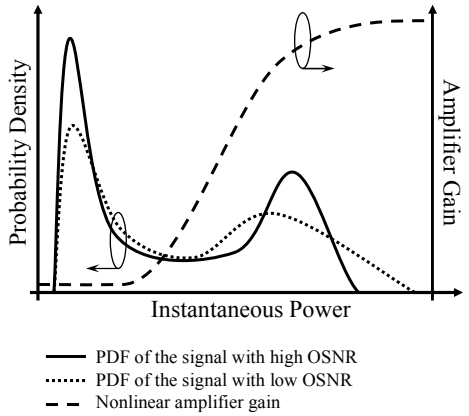

Fig. 2.8. Principle of the in-band OSNR monitoring technique based on nonlinear amplification in [Ng, 2005] and [Adams, 2006].

illustrated in Fig. 2.8. In these conditions, and assuming that the amplifier response is instantaneous, the average power at the amplifier output is approximated by [Ng, 2005]:

$$\bar{P}_{out} = \int_{-\infty}^{+\infty} p_s \cdot g(p_s) \cdot p_{SIG}(p_s) \cdot dp_s \tag{2.5}$$

From (2.5) one may denote that the average output power of the amplifier varies with the statistical distribution of the input signal, which in turn varies with the OSNR, as shown in Fig. 2.8. The works in [Ng, 2005] and [Adams, 2006] explore this variation to monitor OSNR. The case of [Ng, 2005] uses a nonlinear parametric amplifier achieved with FWM in an optical fiber to monitor the OSNR of an RZ signal. In the case of [Adams, 2006], the parametric amplifier is replaced by a NOLM, demonstrating the application of the technique with NRZ, carrier suppressed return-to-zero (CSRZ) and RZ signals.

2.3.3. GVD Monitoring

GVD in single-mode fibers results mainly from the frequency-dependent nature of the refraction index. This dependency leads to a non-uniform delay of the frequency components of a signal traveling through the fiber, which can create significant signal distortion. The GVD is usually characterized by the second term of the Taylor series expansion of the fiber propagation constant around the operation frequency, β_2, commonly referred as group velocity dispersion parameter [Agrawal, 1997] (see page 40). Alternatively, one may also use the dispersion parameter $D=-\beta_2/(2\pi c)$, with c as the speed of light in vacuum, to characterize the GVD. The impact of GVD on the transmission of optical signals may be characterized by a broadening of the impulses, leading to ISI, and the reshaping of the PSD of the signal. GVD may be compensated using electrical or optical dispersion compensation techniques. In the latter case, lumped or distributed dispersion compensation fiber with a dispersion parameter opposite to the dispersion parameter of the transmission fiber may be used. Alternatively, specially designed optical filters have a similar effect [Ooi, 2002]. Electrical dispersion compensation systems are essentially digital or analog filters that rebuild the original shape of the GVD-degraded signal [Killey, 2005]. Dispersion compensation schemes may be dynamic or fixed. In the latter case, the system designer relies in large tolerance margins to ensure signal quality.

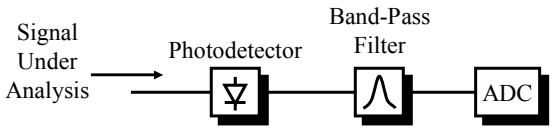

Fig. 2.9. Possible implementation of the GVD monitoring scheme in [Pan, 2001].

The prior case is particularly important as the transmission bit-rate is increased and with the introduction of dynamic optical networks. In this context, GVD monitoring systems become indispensable to accurately control dynamic dispersion compensation systems and ensure signal quality after transmission.

Several GVD monitoring techniques are available in the literature. An example is presented by Pan et al. in [Pan, 2001], which takes advantage of the fact that GVD-induced signal distortion leads to predictable variations of the power of specific frequency components of the RF spectrum of the signal. Pan's GVD monitor is illustrated in Fig. 2.9. The signal under analysis is detected by a high-speed photodetector followed by a band-pass filter centered in the frequency component that is to be analyzed. The power of the filtered electrical signal is digitized by an ADC and processed. In this example, the authors have used the clock frequency component of an NRZ signal, which is inexistent in the absence of GVD but increases with the amount of accumulated dispersion.

Fig. 2.10 illustrates the dependence of the RF spectrum of a NRZ signal at 40 Gb/s and corresponding eye diagrams on the accumulated dispersion. Note that the power of the clock tone increases significantly from null accumulated dispersion to 15 ps/nm but does not change significantly when increasing the accumulated dispersion from 30 ps/nm to 60

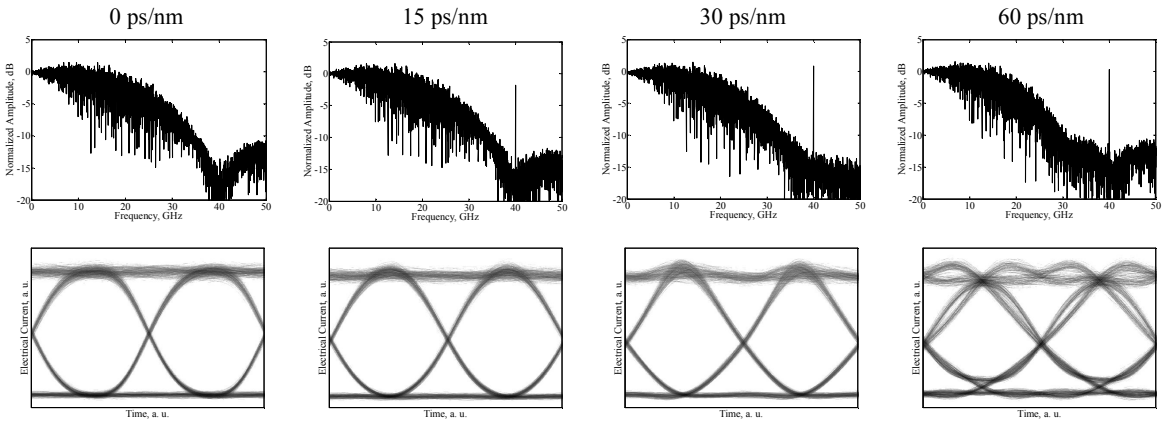

Fig. 2.10. Impact of GVD on the RF spectrum (top row) and eye diagram (bottom row) of a 40 Gb/s NRZ signal.

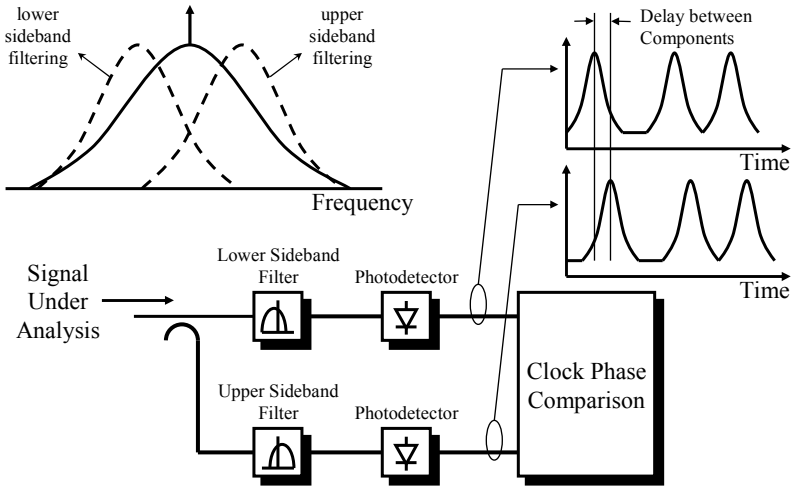

Fig. 2.11. Principle of the GVD monitor using vestigial sideband filtering in [Yu, 2002].

ps/nm. This results from the periodic variation of the RF components of the GVD-impaired signal [Pan, 2001]. Furthermore, the amplitude of the RF components varies substantially with the OSNR and is affected by patterning effects. To handle these limitations, Park et al. have proposed to force a specific IM tone in the transmitter, measuring its amplitude at the GVD monitor instead of using the signal components [Park, 2002: 2]. The frequency of the tone is set to have the required GVD monitoring range and a reasonable sensitivity of the measurement to variations of GVD. However, this approach has two main drawbacks. Modulating the intensity of the transmitted signal leads to some penalty, which may be controlled by limiting the amplitude of the modulation; and the IM tone is substantially affected by fiber nonlinearities, such as SPM [Park, 2003]. The alternative proposed by Park et al. is to use a phase modulation (PM) tone instead and monitor the intensity tone resulting from PM-IM conversion by GVD in the transmission system [Park, 2002: 3]. This approach is substantially less sensitive to fiber nonlinearities [Park, 2002: 4] and allows GVD monitoring independently of PMD.

Another approach to GVD monitoring has been proposed by Yu in [Yu, 2002] to estimate the amount of accumulated dispersion in a signal. This approach takes into account the GVD-induced relative delay between different frequency components of the optical signal. As such, Yu proposes to optically filter the upper and lower sidebands of the optical signal under analysis and recover the clock of each of the resulting vestigial sideband components, as illustrated in Fig. 2.11. It has been shown in [Yu, 2002] that the phase difference between the clock recovered from the upper and lower sidebands of the

signal is directly proportional to the accumulated dispersion. Note that this approach may be applied to arbitrary modulation formats, as long as some form of clock recovery is possible. Furthermore, Yu et al. have shown that their approach is effective even without recovering the clock but simply by comparing the relative phases of the detected upper and lower vestigial sideband components of the signal under analysis.

2.4. Optical Performance Monitoring Using Asynchronous Histograms

OMS based on the analysis of asynchronous histograms have attracted significant attention due to their simplicity and remarkable flexibility. Asynchronous histograms may be acquired by sampling the optical signal at an arbitrary rate in the electrical domain [Hanik, 1999], or optical domain [Shake, 1998], as illustrated in Fig. 2.12-a) and -b), respectively. This avoids the need for clock recovery systems, increasing the flexibility by allowing the potential application of the same monitor to signals with arbitrary bit-rates. Furthermore, low sampling frequencies can be used, potentially reducing the cost of the monitoring system. In the case of electrical sampling, the signal under analysis is detected using a fast photodetector and electrically sampled at an arbitrary bit-rate. The samples then follow to a histogram counter, which is responsible for computing the asynchronous histogram. See Annex I and Annex II for proposals on the sampling system and histogram counter. The fast photodetector is required to detect the signal with minimal distortion. In the case of optical sampling, the samples are produced by an optical sampling gate and follow to a slow photodetector followed by the sample counter. As such, the bandwidth requirements of the photodetector are simply to exceed the sampling frequency, avoiding distortion of the acquired samples. In both cases, the main bandwidth requirements are with the sampling gate (optical or electrical), which should be as high as possible, to avoid averaging effects. See Appendix A for a study on the sampling noise introduced by the sampling process.

To illustrate the process of acquisition of a synchronous or asynchronous histogram, consider the simulation of the scheme presented in Fig. 2.12-a). The simulated signal under analysis is intensity modulated with a 40 Gb/s NRZ deBruijn sequence of 2^{12} symbols degraded by ASE noise to reach an OSNR of 20 dB at a resolution bandwidth of 0.1 nm. It has also been considered that the electrical receiver is noiseless with an electrical bandwidth of 30 GHz and is preceded by an optical filter with a bandwidth of 75 GHz.

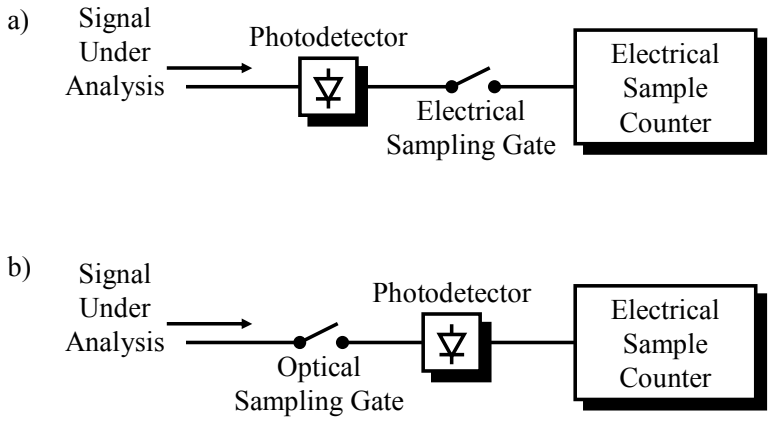

Fig. 2.12. Histogram acquisition systems. a) based on electrical sampling and b) based on optical sampling.

Bandwidth limitations of the sampling gate are disregarded at this point. Fig. 2.13-a) and -b) show a comparison between the simulated synchronous and asynchronous eye diagrams of the signal, and the corresponding histograms. In the case of the histogram acquired synchronously, the considered samples are located within an interval of 10% of the bit-period around the center of the eye diagram. As shown in Fig. 2.13-a), the synchronous histogram of the signal presents two main peaks, corresponding to the samples acquired during the mark and space symbols. The statistical distribution of the samples around the peaks reflects the noise distributions associated with the corresponding symbols. A common approximation of the Q-factor may be obtained from a synchronous histogram by taking the electrical current levels corresponding to the mark and space symbols, μ_1 and μ_0, respectively, and computing the standard deviations of the electrical current associated with the same symbols, σ_1 and σ_0, respectively. Note that this involves setting a decision threshold. In these conditions, the Q-factor may be approximated by:

$$q = \frac{\mu_1 - \mu_0}{\sigma_1 + \sigma_0} \tag{2.6}$$

In the case of the asynchronous histogram, presented in Fig. 2.13-b), one may also distinguish two main peaks corresponding to the mark and space symbols, similarly to the case of the synchronous histogram. However, it is not possible to dissociate the samples corresponding to the mark and space symbols. This results from the large number of samples located between the two peaks, which have been acquired during the transitions

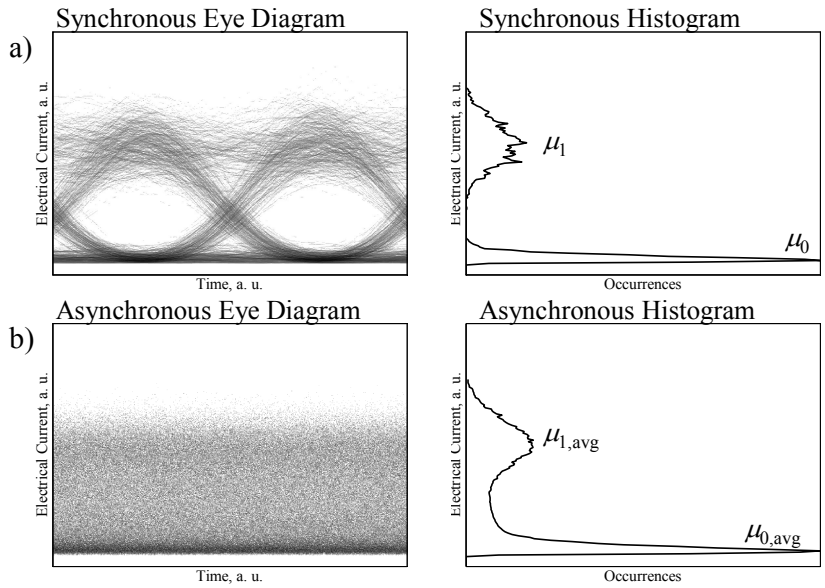

Fig. 2.13. Synchronous (a) and asynchronous (b) eye diagrams and corresponding histograms of an NRZ signal with an OSNR of 20 dB.

between symbols, also referred as cross-point data. This data impairs the asynchronous histogram and may prevent the recognition of the peaks corresponding to the mark and space symbols.

A study of the changes in the shape of asynchronous histograms as a result of optical impairments was first presented by Hanik et al. in [Hanik, 1999]. To illustrate this impact, consider Fig. 2.14-a) and -b), which present examples of asynchronous histograms of the NRZ signal considered in Fig. 2.13, degraded by different levels of ASE noise and accumulated dispersion, respectively. In the first case, it is shown that decreasing the OSNR broadens and reduces the magnitude of the peaks corresponding to the mark and space symbols. This is particularly evident for the mark symbol, where the beating between signal and ASE noise is stronger. Note that the magnitude of the cross-point data is not significantly affected when varying the OSNR. In the case of Fig. 2.14-b), the OSNR is maintained at 30 dB and the accumulated dispersion is increased from 30 ps/nm to 120 ps/nm. The main characteristic of the impact of dispersion on asynchronous histograms is the increase of the amplitude of the cross-point data. This results from the GVD-induced increase of the symbol transition time. It is also shown that the GVD-induced distortion of the signal takes the form of multiple rails arising near the nominal level of the space symbol. Note also that the mark symbol is broadened, similarly to what occurs when the OSNR is decreased.

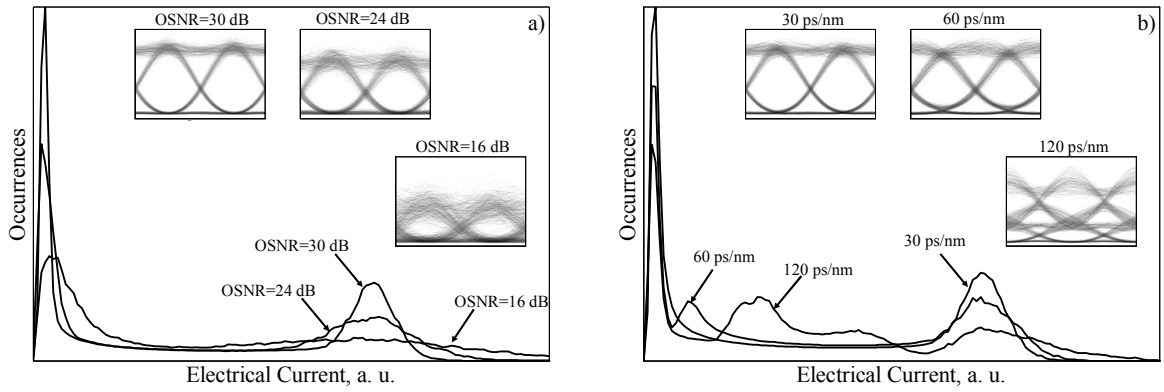

Fig. 2.14. Examples of the asynchronous histograms acquired when varying the a) OSNR without dispersion-induced signal distortion; and b) accumulated dispersion, for an OSNR of 30 dB. Insets present the simulated eye diagrams of the signal under analysis.

The work by Hanik et al. has shown that the analysis of asynchronous histograms allows an identification and evaluation of the impact of optical impairments on asynchronous histograms. Although the quantification of such impacts was left open, Hanik showed that this type of OMS fall within the category of optical penalty monitors, defined in section 2.2. This means that the analysis of asynchronous histograms may be used to extract performance information as an analog OPM and also to identify and quantify the impact of different optical impairments on the signal performance, as an impact OIM.

Shake et al. have contributed significantly to the analysis of asynchronous histograms by developing methods to estimate the Q-factor and corresponding BER, based on processing the asynchronous histograms to remove the cross-point data [Shake, 1998], [Shake, 2000], [Shake, 2001], [Shake, 2002: 2], and [Shake, 2002: 3]. Fig. 2.15 illustrates the basis the Shake's method. It begins by taking the values of electrical current corresponding to the maximums of the peaks associated with the mark and space symbols, $\mu_{1,avg}$ and $\mu_{0,avg}$, respectively. Afterwards, defines two thresholds to eliminate the cross-point data, located at a distance $\alpha_{th} \cdot \Delta\mu$ below and above μ_1 and μ_0, respectively. The terms α_{th} and $\Delta\mu = \mu_{1,avg} - \mu_{0,avg}$ are an adjustment constant and the difference between the electrical current levels associated with the mark and space symbols, respectively. After eliminating the cross-point data it becomes possible to estimate the standard deviations of the electrical current associated with the mark and space symbols as $\sigma_{1,avg}$ and $\sigma_{0,avg}$, respectively. This allows the definition of an average Q-factor as:

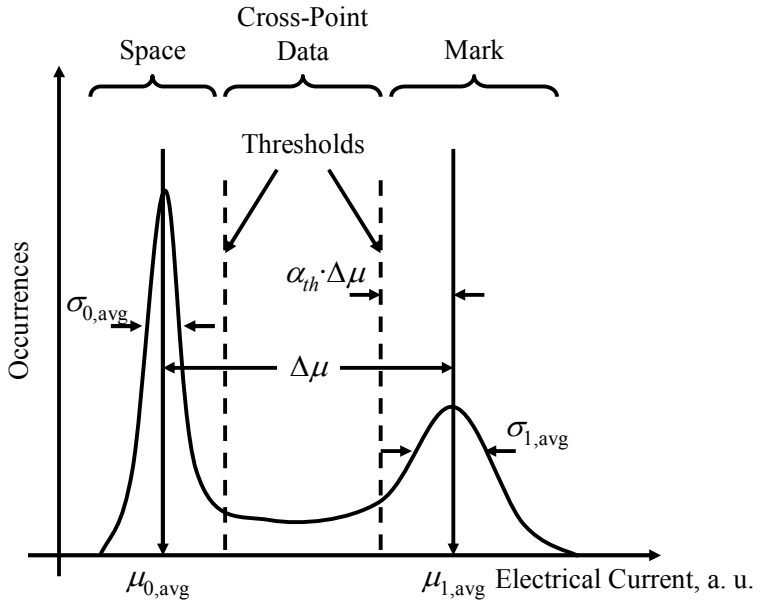

Fig. 2.15. Schematic of the average Q-factor analysis of an asynchronous histogram by [Shake, 1998].

$$q_{\text{avg}} = \frac{\mu_{1,\text{avg}} - \mu_{0,\text{avg}}}{\sigma_{1,\text{avg}} + \sigma_{0,\text{avg}}} \tag{2.7}$$

It has been shown in [Shake, 1998] that the q_{avg} is proportional to q. Furthermore, the proportionality constant that relates these quantities is maintained even if the signal under analysis is degraded by GVD [Shake, 2001]. Note that this application of the analysis of asynchronous histograms to infer the signal performance falls within the previously defined analog OPM sub-category of OMS. However, a simple variation of this technique was developed to simultaneously monitor the impact of GVD on the Q-factor, altering the role of this OMS to be used as an impact OIM. The GVD monitoring technique takes into account the fact that the GVD-induced distortion alters the difference between the average power levels associated with the mark and space symbols and the standard deviation of the mark symbol [Shake, 2002: 4], [Shake, 2003: 2]. In these references, the GVD-induced distortion is quantified through the waveform distortion parameter $X_{\sigma 1}+X_{\mu}$, where $X_{\sigma 1}$ and X_{μ} correspond to the variation of $\sigma_{1,\text{avg}}$ and $\Delta\mu$ between two different measurements, respectively. A variation of the average Q-factor accompanied by a strong variation of the waveform distortion parameter indicates that the degradation (or restoration) of the signal is a result of a change of the accumulated dispersion [Shake, 2003: 2]. Otherwise, the

monitor assumes that the quality variation results from fluctuations of the ASE noise power on the signal bandwidth.

Alternatively, Rasztovits et al. proposed to eliminate the cross-point data by mirroring the outer areas of the asynchronous histogram around the power levels corresponding to the mark and space symbols [Rasztovits-Wiech, 1999]. This approach was also used in [Weinert, 2001] to analyze Q-factor of RZ signals, where the distinction of the mark symbols in asynchronous histograms is less evident. As illustrated in Fig. 2.16, the method by Rasztovits consists in eliminating the region of the histogram between $\mu_{1,\mathrm{avg}}$ and $\mu_{0,\mathrm{avg}}$ and then flip the outer regions of the histogram about the axis defined by the mark and space levels. In principle, this would be enough to produce an estimate of the Q-factor, similarly to the method proposed by Shake et al. However, Rasztovits also proposed to reconstruct the asynchronous histogram with a non-gaussian noise distribution consisting of the sum of strategically centered Gaussian distributions weighted by the probability density function of the signal in the absence of noise, as illustrated in Fig. 2.17 [Rasztovits-Wiech, 1999]. This results in a set of N_b values $\sigma_{SIG}(a_i)$ of the standard deviation of the Gaussian process associated with the electrical current level a_i, which may be used to compute the bit-error ratio as:

$$P_e \approx \frac{1}{2}\left[\sum_{\substack{i \\ a_i < D}} h_{SIG,i} \cdot \mathrm{erfc}\left(\frac{D - a_i}{\sqrt{2}\sigma_{SIG}(a_i)}\right) + \sum_{\substack{i \\ a_i \geq D}} h_{SIG,i} \cdot \mathrm{erfc}\left(\frac{a_i - D}{\sqrt{2}\sigma_{SIG}(a_i)}\right)\right] \tag{2.8}$$

where $h_{SIG,i}$ is the signal histogram and D is a decision threshold. This method is applicable to asynchronous histograms acquired from binary signals with arbitrary forms of distortion. It is more effective than the previously described Shake's method in the sense that the latter assumes that the mark and space symbols are well defined, which is untrue for signals with ISI. As a disadvantage, Rasztovits's method requires a considerable amount of computation, in order to estimate the values of $\sigma_{SIG}(a_i)$ using nonlinear minization algorithms.

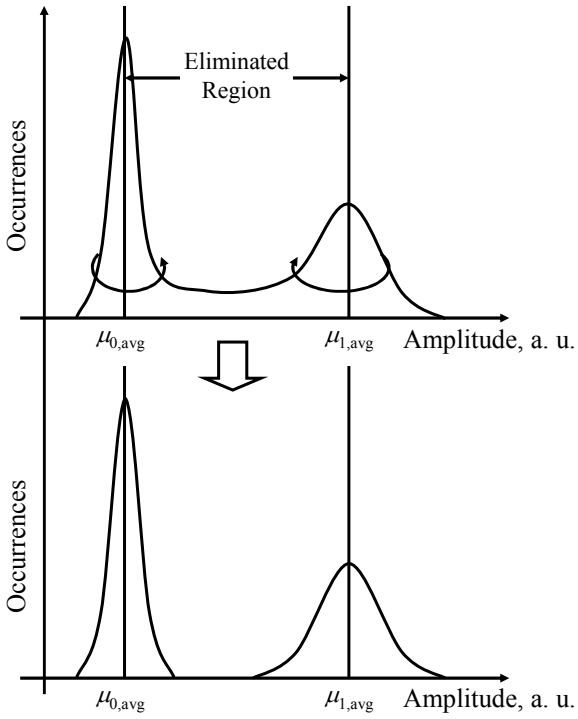

Fig. 2.16. Schematic of the histogram cross-point elimination method by [Rasztovits-Wiech, 1999].

Rasztovits's approach was further developed in [André, 2002: 2], [André, 2002: 3], [Teixeira, 2002], [Ye, 2007], [Ding, 2004], and [Luís, 2004: 6], which present simplified techniques to reduce the computation required to numerically fit the estimated histograms to the histograms acquired from the signal under analysis. The cases of [André, 2002: 2] and [Luís, 2004: 6] will be further detailed in Chapter 3.

The approaches proposed by Rasztovits and Shake required altering the shape of the asynchronous histogram to allow a distinction between the mark and space symbols and from that, extract the signal performance. Alternatively, other authors have proposed techniques to extract information on the optical impairments degrading the signal under analysis without changing the shape of the asynchronous histogram. As an example, Chen et al. have proposed to use the cross-point data of asynchronous histograms to determine the transition time of the signal impulses, which was shown previously to relate directly with amount of accumulated dispersion [Chen, 2003], [Chen, 2004]. The latter reference also extended this study to include the impact of PMD. Another example is the estimation of in-band crosstalk with synchronous histograms proposed by Weinert et al. in [Weinert, 2000: 1] and [Weinert, 2000: 2] and further developed in [Benlachtar, 2003]. This technique uses a de-convolution method to remove the impact of ASE noise from the

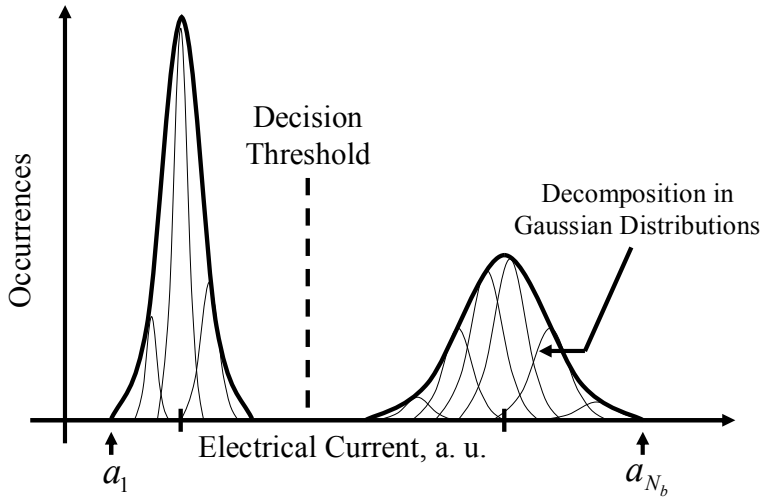

Fig. 2.17. Illustration of the BER estimation method using a multi-Gaussian fitting of the asynchronous histogram, after process to eliminate cross-point data, from [Rasztovits-Wiech, 1999].

synchronous histograms, leaving only the impact of in-band crosstalk, which may be easily analyzed. Further developments of this technique have allowed an evaluation of inter-symbol interference and jitter [Weinert, 2004]. However, its application to asynchronous histograms is not straightforward due to the non-uniform conditional distribution of the Gaussian and arc-sin probability density functions of ASE noise and in-band crosstalk, respectively, which limit the application of de-convolution methods [Luís, 2004: 2]. This limitation may be handled by converting the asynchronously acquired samples in synchronous samples using their intrinsic correlation, as proposed in [Noirie, 2002], [Shake, 2003: 1], and [Mobilon, 2005]. However, these methods require extremely demanding sampling circuits with very low timing jitter. Furthermore, they explore the self-correlation of the acquired samples, which may be limited for signals in the field.

Overall, the analysis of asynchronous histograms to extract monitoring information remains an open field. Even with the advent of advanced modulation formats, such as DPSK, this type of optical monitors remains applicable when other techniques, such as some of the ones mentioned in section 2.3 fail [Li, 2006]. The study of the analysis of asynchronous histograms as a monitoring method will be extended in Chapter 3.

2.5. Conclusions

This chapter has presented a summarized analysis of OMS. A form of classification of OMS has been proposed. This classification categorizes the OMS according to their

purpose and form of analysis of the optical signal. A set of OMS currently available in the literature has been presented. Particular focus has been given to OMS for the evaluation of power, noise and dispersion as these are often considered as fundamental quantities in optical transmission systems. This chapter has also presented the main techniques of analysis of asynchronous histograms as a form of optical monitoring. It has been shown that this particular type of systems presents a significant flexibility, allowing its use to quantify the degradation of optical signals due to multiple impairments simultaneously.

Chapter 3. Optical Monitoring Through the Analysis of Asynchronous Amplitude Histograms

3.1. Introduction

One of the main limitations of OMS based on asynchronous sampling of the signal under analysis is their finite temporal resolution, or aperture time [Sauerwald, 1994], [Kahrs, 2003], resulting from the limited bandwidth of the sampling system. Sampling error may occur due to signal variations during the aperture time of each sample. Other limitations, such as sampling jitter, signal feed-through, signal droop, and aperture uncertainty can be neglected in the case of asynchronous sampling systems, as indicated in Appendix A. The impact of finite aperture time in asynchronous Q-factor monitoring systems can be reduced by setting the response time of the receiver circuits slower than the response of the sampling circuit. This is the case of [Shake, 2002: 2] where the adopted electrical receiver bandwidth is the same as one would typically use in the electrical receiver of an optical communications system, 70% of the monitored signal bit-rate. This design for the OMS presents the additional advantage of directly relating the measured Q-factor with the real Q-factor of the received signal. However, if a fixed OMS is used to monitor signals with different bit-rates, it may be expected that the bandwidth of the electrical receiver would be independent of the bit-rate, as adopted in [Mueller, 1998] and

[Hanik, 1999]. In these references, the bandwidths chosen for the electrical receiver and sampling system are large enough to cover the range of monitored bit-rates and also to avoid integration of the sampled signal, usually referred as averaging effect. These effects could mask the patterns created in the acquired asynchronous histograms by different transmission impairments.

This chapter will begin by addressing the influence of non-ideal sampling in Q-factor monitoring of signals impaired by optical noise, adopting large bandwidths for the optical and electrical receiver filters in section 3.2. Similarly to [Mueller, 1998], a correction factor for the Q-factor is proposed for cases where noise averaging due to the non-ideal sampling is dominant. The proposed correction factor is evaluated through numerical simulation using the Q-factor monitoring technique proposed by André in [André, 2002: 1] and summarized in sub-section 3.2.2. Section 3.3 will present an evolution of this technique to allow the evaluation of the Q-factor of signals affected by ISI. This technique is based on the comparison of the histogram of the signal under analysis, referred in this work as measured asynchronous histogram (MAH) [1] with an estimated histogram. The latter is numerically computed using theoretical assumptions on the waveform of the signal under analysis and the impairments that affect it, such as the accumulated dispersion or even the distortion introduced by the non-ideal sampling system. Numerical simulation results show that the proposed technique can be used to account for averaging effects resulting from non-ideal sampling and Q-factor degradation due to chromatic dispersion-induced signal distortion, under a given limit, or by filtering elements in the electrical receiver. Section 3.4 presents a development of the technique presented in section 3.3 by computing the estimated histogram using a reference asynchronous histogram (RAH). The RAH may be experimentally acquired from a reference signal at a calibration stage, inherently accounting for the impact of non-ideal sampling as well as other effects that distort the waveform of the signal under analysis. An advantage of this approach is that the noise generated within the OMS will have similar impact on the RAH and the MAH. This property will be used to experimentally demonstrate the application of an optical pre-amplifier to improve the sensitivity of the OMS, at the cost of reducing the maximum measurable OSNR. For this purpose, we will

[1] Note that, for simplicity, the acronym MAH will be used in this work to refer to histograms which have been experimentally measured or obtained through numerical simulation.

use an EDFA and, for the first time in OMS based on analysis of asynchronous histograms, a SOA as optical pre-amplifiers. In addition, the proposed technique relies only on evaluating the impact of ASE noise on the shape of the asynchronous histograms, independently of the signal waveform. As such, it becomes possible to use simplified optical processing techniques to enhance the impact of ASE noise on the shape of the asynchronous histograms and, as a consequence, the accuracy of the OSNR estimation. This will be illustrated by effectively evaluating the OSNR of a signal with a RZ modulation format by first converting it to a NRZ modulation format using an optical filter with reduced bandwidth within the OMS. Finally, the proposed method will be applied to a NRZ signal degraded by GVD. It will be shown that the OSNR estimates are reasonably accurate, as long as the reference signal presents similar accumulated dispersion as the signal under analysis. Furthermore, it will be shown that, when using a reference signal which is not degraded by GVD to obtain the RAH and use it to estimate the OSNR of a signal degraded by GVD yields an OSNR penalty which quantifies a GVD-induced OSNR penalty of the signal under analysis.

The work presented in this chapter has been partially published in [André, 2004], [Luís, 2004: 5], [Luís, 2004: 6], [Luís, 2005: 2], [Luís, 2005: 3], and [Luís, 2006: 2]. It also originated the Siemens invention disclosures [Luís, 2004: 1], [Luís, 2004: 3], and [Luís, 2004: 4], which are described in Annex I, Annex II, and Annex III, respectively.

3.2. Impact of Non-Ideal Sampling Systems on Optical Performance Monitoring Systems

3.2.1. Q-Factor Correction due to Non-Ideal Sampling

To evaluate the limitations imposed by finite aperture time, consider the block diagram of a simplified sampling system presented in Fig. 3.1-a). The signal under analysis, $x(t)$, is multiplied by a train of sampling impulses centered in the sampling instants $k \cdot T_a$, where T_a is the sampling period. The sampling impulse, $\psi(t)$, is null outside the sampling period and has a unitary integral. The product is integrated in a way that each sample, x_k , is given by:

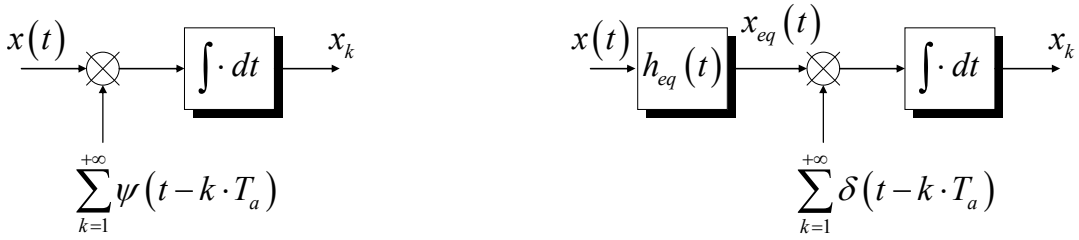

a) b)

Fig. 3.1. Simplified block diagram of the considered sampling system model.
a) Non-ideal system; b) Equivalent non-ideal system.

$$x_k = \int_{(k-1/2)\cdot T_a}^{(k+1/2)\cdot T_a} x(t)\cdot\psi(t-k\cdot T_a)\cdot dt \tag{3.1}$$

In an ideal case, the sampling impulses are infinitesimally short, and would be represented by a Dirac impulse, $\delta(t)$. In this situation, the k-th sample would be given by $x_k = x(k\cdot T_a)$. Consider now, the equivalent sampling system presented in Fig. 3.1-b). The non-ideal sampling system is replaced by an ideal sampling system preceded by an equivalent sampling filter with an impulse response $h_{eq}(t)$. In this system, the k-th sample is given by:

$$x_k = x_{eq}(k\cdot T_a) = \int_{-\infty}^{+\infty} x(t)\cdot h_{eq}(k\cdot T_a - t)\cdot dt \tag{3.2}$$

By comparing (3.1) with (3.2), the two systems become equivalent by having $h_{eq}(t) = \psi(-t)$. Fig. 3.1-b) shows that performance quality measurements performed with the acquired samples evaluate $x_{eq}(t)$ instead of $x(t)$. Therefore, the equivalent filtering effect will be referred as an averaging effect, to distinguish it from the cases where a filter is positioned prior to the sampling system. This results from the fact that each sample approximates the average value of the signal during the aperture time.

To assess the impact of the sampling process in the Q-factor evaluation, consider the signal under analysis given by $x(t) = s(t) + n(t)$, where $s(t)$ and $n(t)$ are signal and noise components, respectively. The ratio between the variance of the noise after the equivalent sampling filter, $\sigma_{n,eq}^2$, and the variance of the monitored noise, σ_n^2, is given by:

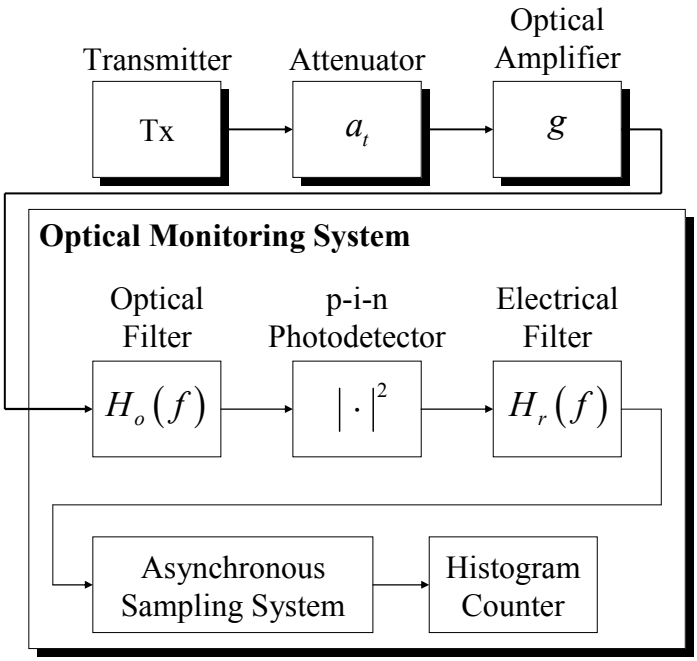

Fig. 3.2. Block diagram of the considered optical transmission system.

$$\frac{\sigma_{n,eq}^2}{\sigma_n^2} = \frac{\int_{-\infty}^{+\infty} S_n(f) \cdot \left| H_{eq}(f) \right|^2 \cdot df}{\int_{-\infty}^{+\infty} S_n(f) \cdot df} \tag{3.3}$$

where $S_n(f)$ is the PSD of the monitored noise and $H_{eq}(f)=\mathcal{F}[h_{eq}(t)]$ is the transfer function of the equivalent sampling filter, with $\mathcal{F}[\cdot]$ as the Fourier transform operator. Applying the Schwarz's inequality to (3.3) it becomes easy to demonstrate that $\sigma_{n,eq}^2 \le \sigma_n^2$. Therefore, if the distortion of the signal component is considered negligible, the sampling process may influence the Q-factor measurement by reducing the evaluated noise power.

To apply the results to an optical transmission system, consider the block diagram presented in Fig. 3.2 for the OMS. The monitored optical signal is initially filtered through an optical filter with a low-pass equivalent transfer function $H_o(f)$. After that, the signal is detected by a p-i-n photodetector with unitary responsivity. An electrical filter, with transfer function given by $H_r(f)$ models the frequency limitations of the receiver electronics. Finally, the filtered electrical current is sampled for histogram counting. The sampling system is assumed to have a structure equivalent to the system presented in Fig. 3.1-b). The optical and electrical filter bandwidths are assumed to be large enough to

neglect signal distortion due to filtering. In these conditions, the Q-factor, in linear units, can be approximated by:

$$q = \frac{\mu_1 - \mu_0}{\sigma_1 + \sigma_0} \tag{3.4}$$

where μ_m and σ_m are the values of the mean and standard deviation of the electrical current for the symbol "m", with m=0 and 1 for the space and mark symbols, respectively. If the signal-spontaneous emission beat noise is considered dominant, the standard deviation of the electrical current for the symbol "m" can be approximated by [Rebola, 2002]:

$$\sigma_m^2 = k_{sp}(P_m) \int_{-\infty}^{+\infty} \left|H_r(f)\right|^2 \cdot \left|H_o(f)\right|^2 \cdot df \tag{3.5}$$

where $k_{sp}(P_m)$ is a term that depends on the noise characteristics and the optical power at the receiver input for the symbol "m", P_m . Due to the non ideal sampling process, the variance of the noise that is actually measured is given by:

$$\sigma_{m,eq}^2 = k_{sp}(P_m) \int_{-\infty}^{+\infty} \left|H_{eq}(f)\right|^2 \cdot \left|H_r(f)\right|^2 \cdot \left|H_o(f)\right|^2 \cdot df \tag{3.6}$$

Therefore, the measured Q-factor becomes:

$$q_{eq} = (\mu_1 - \mu_0) / (\sigma_{1,eq} + \sigma_{0,eq}) = q/\kappa \tag{3.7}$$

where the correction factor, κ, is given by:

$$\kappa^2 = \frac{\int_{-\infty}^{+\infty} \left|H_{eq}(f)\right|^2 \cdot \left|H_r(f)\right|^2 \cdot \left|H_o(f)\right|^2 \cdot df}{\int_{-\infty}^{+\infty} \left|H_r(f)\right|^2 \cdot \left|H_o(f)\right|^2 \cdot df} \tag{3.8}$$

The correction factor allows a simple and direct adjustment of the measured Q-factor in conditions where noise averaging due to the non-ideal sampling process is dominant. This

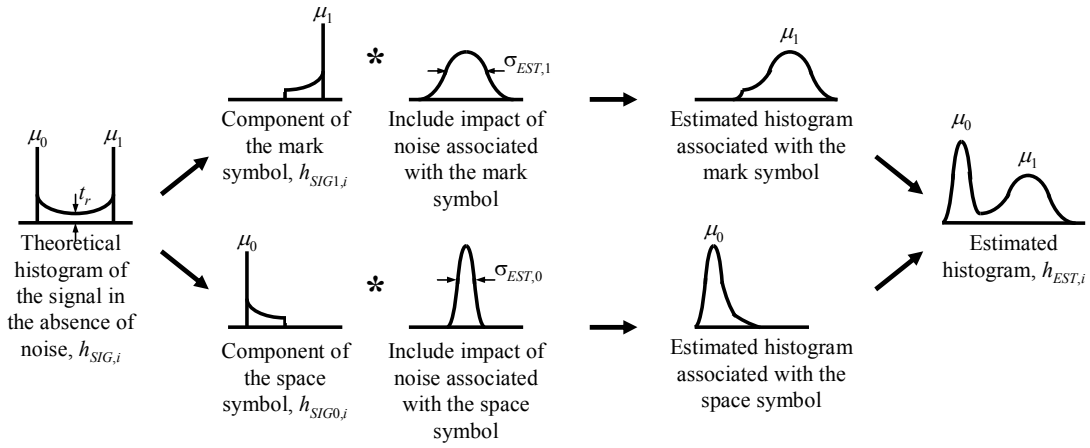

Fig. 3.3. Diagram of the method to estimate the asynchronous histogram of a signal impaired with ASE-noise proposed in [André, 2002: 1].

factor is only dependent on the physical characteristics of the measurement system and can be obtained by calibration of the device.

An alternative approach to assess the impact of finite aperture time on OMS is presented in Appendix A. This approach handles the impact of finite aperture time as an additional noise component, defining the signal-to-sampling noise ratio as a measurement quality parameter. The shape of the sampling impulses is also taken into account, showing that the even shapes, such as rectangular, present a significantly reduced measurement penalty.

3.2.2. Validation of the Q-Factor Correction Method

3.2.2.1. Q-Factor Estimation Method

This section contains a validation of the Q-factor correction method presented in section 3.2.1 using the Q-factor estimation technique based on the analysis of asynchronous histograms proposed by André in [André, 2002: 1]. Simulation results will be used to illustrate the application of the Q-factor correction factor, as well as the corresponding validity limits.

The Q-factor estimation technique presented in [André, 2002: 1] consists in computing an asynchronous histogram based on fundamental parameters of the signal under analysis, referred in this work as the estimated histogram. Restricting this analysis to the case of NRZ signals, the parameters that condition the shape of the estimated histogram will be the nominal levels and corresponding noise variances associated with the mark and

space symbols. In addition, the shape and average duration of the symbol transition will be used. These parameters may be adjusted to numerically match the estimated histogram to the MAH. The values of the signal parameters that result from the numerical adjustment may then be used to extrapolate the quality of the signal under analysis.

Fig. 3.3 presents a schematic of the method proposed in [André, 2002: 1] to compute the estimated histogram. This method consists in calculating the theoretical histogram of the signal under analysis, in the absence of noise, $h_{SIG,i}$, and numerically include the impact of optical and electrical noise. We begin by calculating $h_{SIG,i}$ by considering that the received signal, in the absence of noise and neglecting the influence of the sampling system, is a linear superposition of NRZ binary pulses with equal probability for the mark and space symbols. The transitions from space to mark and from mark to space have amplitude shapes given by $s_{01}(t)$ and $s_{10}(t)$, respectively. The transitions from mark to mark and from space to space have constant levels μ_1 and μ_0, respectively. We also consider that the histograms have N_b bins. The i-th bin is centered in the electrical current amplitude level a_i and presents width Δ. Under these conditions, the value of the i-th bin of the theoretical histogram of the signal, in the absence of noise is given by [André, 2002: 1]:

$$h_{SIG,i} = \begin{cases} 0, \text{ for } a_i > \mu_1 + \Delta/2 \text{ or } a_i < \mu_0 - \Delta/2 \\ \dfrac{2T + s_{01}^{-1}\left(a_i + \Delta/2\right) - s_{10}^{-1}\left(a_i + \Delta/2\right)}{4T}, \text{ for } \mu_0 - \Delta/2 \le a_i \le \mu_0 + \Delta/2 \\ \dfrac{s_{01}^{-1}\left(a_i + \Delta/2\right) - s_{01}^{-1}\left(a_i - \Delta/2\right) + s_{10}^{-1}\left(a_i - \Delta/2\right) - s_{10}^{-1}\left(a_i + \Delta/2\right)}{4T}, \\ \qquad\qquad \text{for } \mu_0 + \Delta/2 < a_i < \mu_1 - \Delta/2 \\ \dfrac{2T - s_{01}^{-1}\left(a_i - \Delta/2\right) + s_{10}^{-1}\left(a_i - \Delta/2\right)}{4T}, \text{ for } \mu_1 - \Delta/2 \le a_i \le \mu_1 + \Delta/2 \end{cases} \quad (3.9)$$

where T, $s_{01}^{-1}(a)$ and $s_{10}^{-1}(a)$ are the bit period of the signal and the inverse functions of $s_{01}(t)$ and $s_{10}(t)$, respectively. To include the influence of electrical noise in the histogram it is simply necessary to convolve $h_{SIG,i}$ with the histogram of the electrical noise, which in most cases may assumed Gaussian, to obtain an estimate of the histogram of the received

signal. In the case of optical and electrical noise the method becomes more complex due to the nonlinear characteristics of the photodetector. In these cases, the histogram of the signal can be separated in two components:

$$h_{SIG0,i} = \begin{cases} h_{SIG,i} \text{ for } a_i < \overline{I}_s \\ 0 \text{ otherwise} \end{cases} \quad h_{SIG1,i} = \begin{cases} h_{SIG,i} \text{ for } a_i \geq \overline{I}_s \\ 0 \text{ otherwise} \end{cases} \tag{3.10}$$

where $\overline{I}_s$ is the average current level. $h_{SIG0,i}$ and $h_{SIG1,i}$ correspond to the areas of the histogram related to the space and mark symbols, respectively, as represented in Fig. 3.3. After the separation, each histogram component is convolved with gaussian noise with the corresponding standard deviation, $\sigma_{EST,0}$ and $\sigma_{EST,1}$. The final histogram is obtained by adding the histogram components.

To illustrate the application of the estimated histogram technique, consider the system presented in Fig. 3.2. The transmitter simulates a periodic NRZ optical signal with 2^{12} symbols at a bit-rate B = 40 Gb/s. The transmitted power impulses have a full raised cosine space to mark transition shape given by:

$$s_{01}(t) = (\mu_1 + \mu_0)/2 - (\mu_1 - \mu_0)/2 \cdot \cos(\pi t/t_r), \quad 0 < t < t_r \tag{3.11}$$

where t_r is the transition time, which takes the value of 6.25 ps (25% of the bit period). The mark to space transition is given by $s_{10}(t) = \mu_1+\mu_0-s_{01}(t)$. An optical attenuator with attenuation a_t, and an optical amplifier with gain g, compose the transmission path. The spontaneous emission noise generated in the optical amplifier presents a power spectral density given by $N_{sp} = h\upsilon \cdot n_{sp} \cdot (g\text{-}1)$, where $n_{sp} = 2$ is the spontaneous emission noise factor; h is the Plank constant and υ is the optical frequency. After the optical amplifier, the signal follows to the OMS. The influence of the sampling system is neglected at this point by assuming its equivalent bandwidth is 128 times larger than the signal bit-rate. However, this limitation will be considered in sub-section 3.2.2.2. To stabilize the numerical simulation results, each histogram is computed from the acquisition of 2^{20} samples.

Fig. 3.4 presents a comparison between the numerically simulated histogram and the corresponding estimated histogram in a logarithmic scale. The transmitted power and

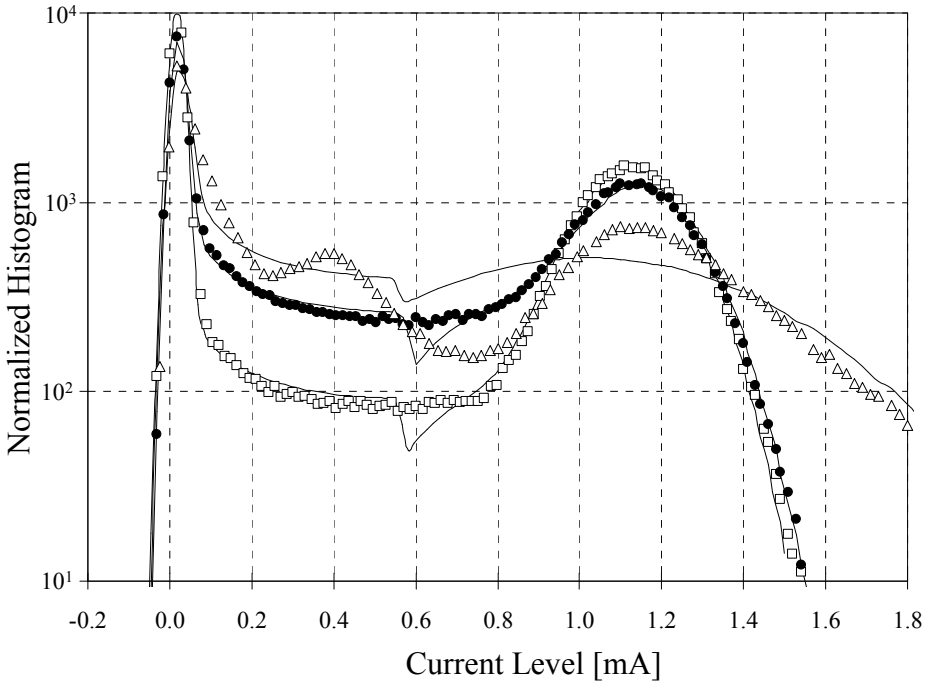

Fig. 3.4. MAH of a 40 Gb/s signal obtained with an ideal sampling system from simulated signals with: □ – raised cosine pulse shape; ● – rectangular pulse shape filtered by a Bessel filter with a bandwidth of 70% of the signal's bit-rate; Δ - raised cosine pulse shape degraded by an accumulated chromatic dispersion of 34 ps/nm. Continuous lines – estimated histograms using the raised cosine approximation.

the amplifier gain were set to 0 dBm and 20 dB, respectively. The attenuation was set to 22.5 dB to allow a Q-factor of the simulated signal of 8, in linear units. To obtain the actual Q-factor of the simulated signal, the semi-analytical exhaustive Gaussian approach presented in [Rebola, 2001] was used, which takes into consideration the influence of the optical and electrical filter shapes.

The parameters of the estimated histogram (μ_0, μ_1, σ_0, σ_1 and t_r) were adjusted to match the numerically simulated histogram using the Nelder-simplex non-linear minimization algorithm. From Fig. 3.4 a reasonable match between the theoretical and simulated histograms can be observed. The most evident discrepancy occurs in the central area and corresponds to the point of separation between the two components of the estimated histogram. However, it does not contribute significantly to the error of the match. The resulting set of parameters for the estimated histogram, can be used to evaluate the Q-factor using (3.4). As a result, an estimated Q-factor of 8.2 was obtained and additionally, the value of t_r was estimated as 8 ps, close to the actual value of 6.25 ps.

The main limitation of the presented technique is that prior knowledge of the received pulse shape is required to obtain the theoretical histogram. Nevertheless, approximations, like the raised cosine transition presented previously, can be used to model signals with different shapes, as long as some similarity between the actual shape of the pulse and the theoretical model is maintained. To illustrate this, Fig. 3.4 presents a comparison between the simulated histogram of a rectangular signal filtered by a Bessel filter with a bandwidth of 70% of the bit-rate and the corresponding estimated histogram, obtained with the raised cosine approximation. The simulation conditions were identical to the ones used before in this sub-section, except for the attenuation value, set to grant a Q-factor of 8. As can be noticed the matching is quite good and an estimated Q-factor of 8.2 was obtained. Additionally, the estimated value of t_r was 23 ps, which reflects the effect of the filter on the pulse transition time. Fig. 3.4 also presents a comparison between the simulated histogram of a raised cosine signal, under the same conditions as above, however with dispersion-induced degradation. For this purpose, a dispersive element with 34 ps/nm was placed before the attenuator in Fig. 3.2, which reduced the Q-factor of the signal under analysis to 4.4. Even though the signal and noise powers at the receiver are the same as in the previous case, chromatic dispersion induced enough distortion to prevent the fitting algorithm from finding an appropriate set of parameters. Hence, an incorrect Q-factor estimate of 2.3 was achieved in these conditions.

3.2.2.2. Impact of the Sampling Aperture on the Q-Factor estimation

To illustrate the application of the correction factor proposed in section 3.2.1, the system presented in Fig. 3.2 has been simulated using a 40 Gb/s NRZ raised cosine signal with a transition time of 6.25 ps. Finite sampling aperture time was considered by simulating rectangular sampling impulses. Attenuation values of 22.5 dB and 20.8 dB were chosen to provide simulated signals with Q-factors of 8 and 10, respectively. The remaining parameters of the system are identical to the ones used to obtain Fig. 3.4. The technique presented in section 3.2.2.1 was used to estimate values of q_{eq}, without correction due to non-ideal sampling. Following, we obtain the corrected values of the Q-factor, q_{cor}, by multiplying q_{eq} with the correction factor as: $q_{cor} = \kappa \cdot q_{eq}$. The dependence of q_{eq}/q and q_{cor}/q on the aperture time is presented in Fig. 3.5 , where each value was obtained by averaging the results from 16 simulations.

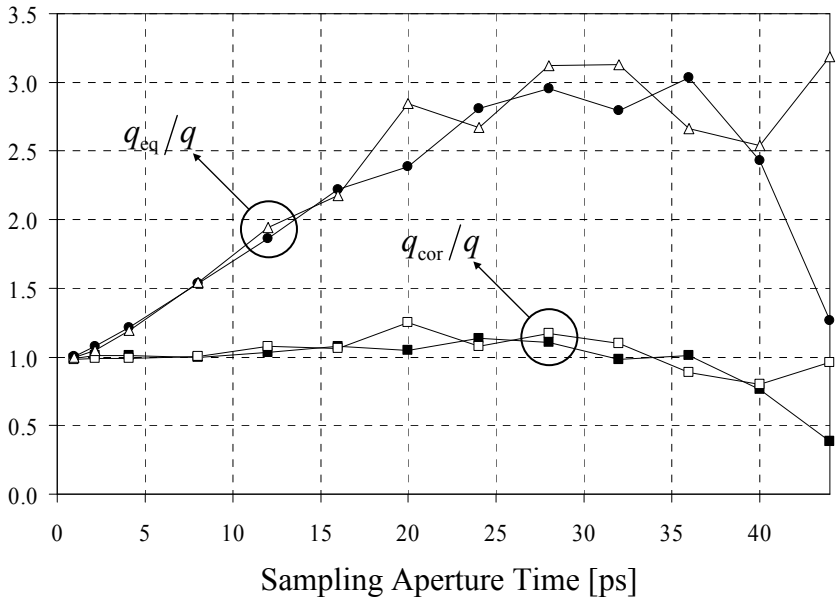

Fig. 3.5. q_{eq}/q and q_{cor}/q as a function of the aperture time for a 40 Gb/s signal. ● - q_{eq}/q for q=8; ○ - q_{eq}/q for q=10; ■ - q_{cor}/q for q=8; □ - q_{cor}/q for q=10.

In order to have a better understanding of Fig. 3.5, it may be divided in three different regions. For sampling apertures below 20 ps, the averaging effect of non-ideal sampling influences mainly the noise component. Therefore, q_{eq} increases steadily with the aperture time due to the noise averaging. In this area, the correction factor can be applied, providing accurate values of the Q-factor. From sampling apertures of 20 ps to 35 ps, near the symbol period, the signal component also becomes significantly affected by the non-ideal sampling, and the model used to obtain the estimated histogram becomes inaccurate. The distortion induced by the non-ideal sampling in the signal component leads to new relative maximums in the simulated histogram, which are interpreted as noise by the fitting algorithm. To illustrate this effect, Fig. 3.6 presents the simulated and theoretical histograms, obtained with an aperture time of 28 ps for a Q-factor of 8. The new relative maximums lead to an overestimation of the values of σ_0 and σ_1, reducing the growth of the estimated value of q_{eq}. As the correction factor continues to increase steadily with the aperture time, the values of q_{cor} start to decrease. However, a margin of 25 % of error is maintained. For aperture times above 35 ps the averaging of the signal and noise components due to non-ideal sampling as degraded the shape of the histogram to a point where the nonlinear minimization algorithm is unable to match the estimated histogram to the MAH. To illustrate this effect, Fig. 3.6 also presents the simulated and theoretical

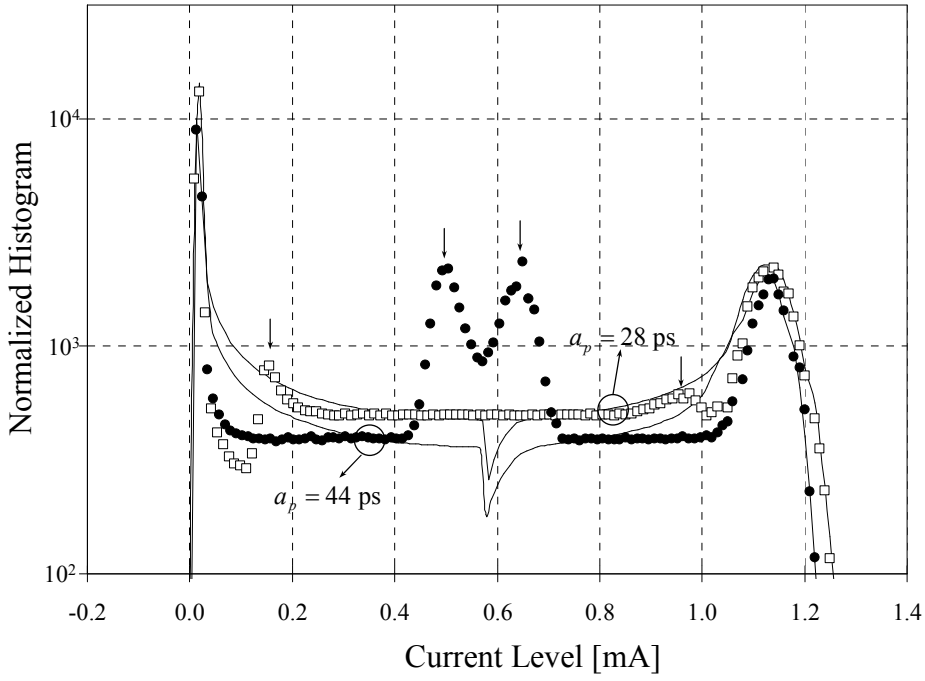

Fig. 3.6. MAH of a 40 Gb/s signal obtained with a non-ideal sampling system from simulated signals with: □ – aperture time of 28 ps; ● – aperture time of 44 ps. Continuous lines – estimated histogram. Arrows indicate new relative maximums that result from the averaging effect induced by non-ideal sampling.

histograms, obtained with an aperture time of 44 ps for a Q-factor of 8. In these conditions, the Q-factor estimates performed over the simulated histograms lose physical meaning.

3.3. Asynchronous Q Measurements in the Presence of ISI

3.3.1. Theory

The asynchronous Q-factor estimation technique, presented in section 3.2.2, is based on the analysis of a theoretical histogram, obtained from a signal with null or negligible ISI (see Fig. 3.3). This allowed the decomposition of the theoretical histogram in two distinct components, corresponding to the mark and space symbols. However, as shown in section 3.2.2, this technique delivers poor results if applied to signals with significant distortion or when using non-ideal sampling systems. Therefore, we will adopt the approach proposed in [Rasztovits-Wiech, 1999]. Unlike the model presented in section 3.2.2, which considers that the histogram is approximated by the sum of two Gaussian distributions, the Rasztovits approach assumes that the histogram is composed by a sum of multiple Gaussian distributions centered in a given set of current levels and weighted by

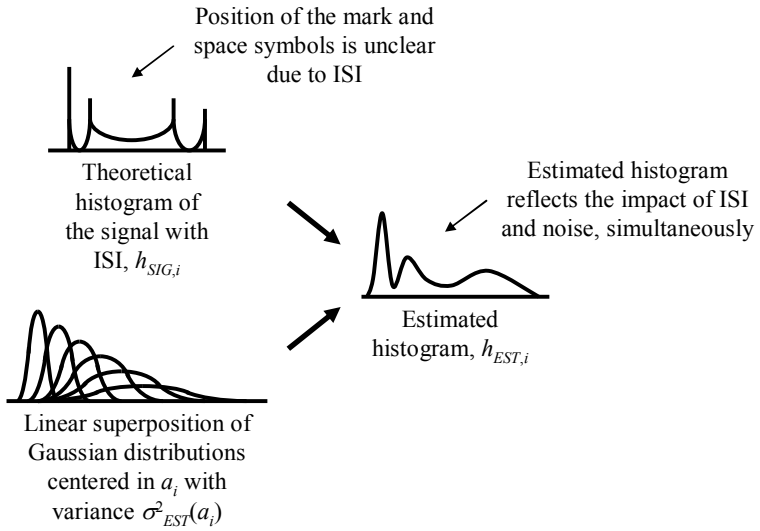

Fig. 3.7. Diagram of the proposed method to estimate the asynchronous histogram of a signal impaired with ISI and ASE-noise.

the probability of occurrence of the corresponding current level, as schematically represented in Fig. 3.7. This approach allows handling histograms of signals impaired by ISI, where the distinction between the mark and space levels is unclear.

Using the Rasztovits approach, it is possible to describe the estimated histogram as [Rasztovits-Wiech, 1999]:

$$h_{EST,n} = \sum_{i=1}^{N_b} \frac{h_{SIG,i}}{\sqrt{2\pi \cdot \sigma^2_{EST}(a_i)}} \cdot \exp\left[-\frac{(a_n - a_i)^2}{2\sigma^2_{EST}(a_i)} \right] \tag{3.12}$$

where $\sigma^2_{EST}(a_i)$ is the estimated variance of the gaussian process associated with the current level a_i, given by [Rasztovits-Wiech, 1999]:

$$\sigma^2_{EST}(a_i) = b_{sp} \frac{a_i}{osnr_{EST}} + \sigma^2_{\min} \tag{3.13}$$

The first term on the right side of (3.13) accounts for the signal dependent noise component, where $osnr_{EST}$ is the estimated OSNR of the ASE-noise included in the estimated histogram and b_{sp} is a proportionality constant dependent on the characteristics

of the receiver. The term $\sigma^2_{\min}$ accounts for the noise components that are independent of the signal. The latter will be neglected in this work. Using expression (3.12) to obtain the theoretical histogram, replaces the noise related fitting parameters σ_0 and σ_1, used in section 3.2.2, by the parameter $osnr_{EST}$.

The next step in the proposed technique is to obtain an approximation of $h_{SIG,i}$ that includes the distortion suffered by the signal under analysis. Depending on the types of distortion considered, this can become an extremely complex operation. Rasztovits et al. have proposed to use a nonlinear minimization algorithm where the unknown variables correspond to the values of $h_{SIG,i}$. However, the study performed in Appendix B shows that the required number of bins of the histogram may rapidly exceed one hundred to allow a wide range of Q-factor estimates. As such, the Rasztovits approach may lead to prohibitive computation times. Simplified approaches were proposed by [Ding, 2004] and [Ye, 2007] by considering a reduced number of strategically positioned Gaussian distributions. This work proposes to perform a short numerical simulation of the considered system in the absence of noise to obtain an estimate of $h_{SIG,i}$. Afterwards, the noise can be included recurring to (3.12). The system parameters considered for the short simulation will correspond to the parameters that condition the distortion of the signal under analysis, in this case, the accumulated dispersion. Also included is the impact of the non-ideal sampling, modeled using the corresponding equivalent filter, as defined in section 3.2.1.

The value of the accumulated GVD, as well as the remaining signal parameters (μ_1, μ_0, t_r and $osnr_{EST}$) are adjusted in each iteration of the fitting process by the non-linear minimization algorithm. The histogram estimation process can be very time consuming since a short simulation of the system is required for each iteration of the fitting process in order to obtain estimates of $h_{SIG,i}$. However, this estimate may be relatively inaccurate because the fitting process only requires the theoretical and simulated histograms to be similar. This allows a significant reduction of time interval simulated to obtain $h_{SIG,i}$. In this work, sequences with 32 symbols and 64 samples per symbol will be simulated to estimate $h_{SIG,i}$. Processing times of tens of seconds were achieved.

To illustrate the application of the proposed technique, Fig. 3.8 presents a comparison between the theoretical and simulated histograms of a signal in the same conditions as used for Fig. 3.6 with the sampling system presenting an aperture time of 44 ps. Fig. 3.8 shows that the theoretical histogram is now a reasonable estimate of the

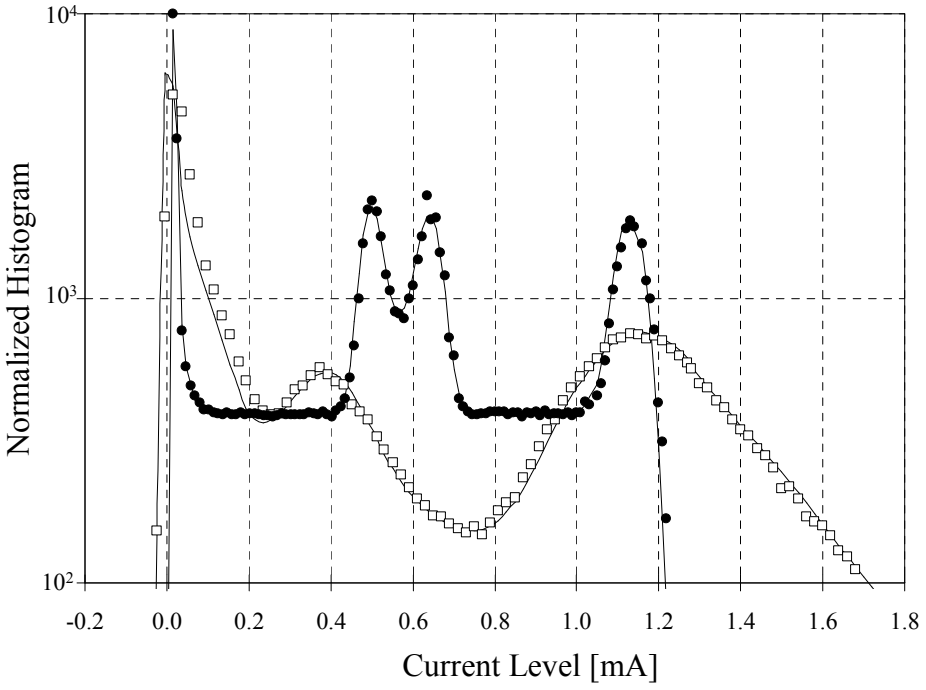

Fig. 3.8. Estimated and simulated asynchronous histograms of a 40 Gb/s signal. ● – Raised cosine signal, acquired with a sampling system with an aperture time of 44 ps; - □ raised cosine signal degraded by an accumulated chromatic dispersion of 34 ps/nm; continuous lines – estimated histograms.

simulated histogram. This was achieved because the effect of the sampling system was included in the short simulations used to estimate $h_{SIG,i}$. Fig. 3.8 also presents a comparison between the estimated and simulated histograms of a signal distorted by chromatic dispersion, similar to the one used in Fig. 3.4. By including the influence of chromatic dispersion in the short simulations used to estimate $h_{SIG,i}$, we obtained a reasonable match between the theoretical and simulated histograms.

In the presence of ISI, the Q-factor can no longer be calculated using (3.4). In this case, a more general definition of the Q-factor is required [Matera, 2000]:

$$P_e = 1/2 \cdot \mathrm{erfc}\left(q/\sqrt{2}\right) \tag{3.14}$$

where P_e is the bit-error probability. To estimate the bit-error probability of a binary sequence of N symbols, an exhaustive gaussian approach can be used [Correia, 1996]:

$$P_e = \frac{1}{2N} \cdot \left[\sum_{\substack{k=1 \\ (m_k=0)}}^{N} \operatorname{erfc}\left(\frac{x_{th} - \mu_{0,k}}{\sqrt{2} \cdot \sigma_{0,k}} \right) + \sum_{\substack{k=1 \\ (m_k=1)}}^{N} \operatorname{erfc}\left(\frac{\mu_{1,k} - x_{th}}{\sqrt{2} \cdot \sigma_{1,k}} \right) \right] \tag{3.15}$$

where m_k is the value of the k-th symbol, either 0 or 1, and x_{th} is the decision threshold. $\mu_{m,k}$ and $\sigma_{m,k}$ are the mean and standard deviation of the electrical current conditioned to the symbol "m", in the sampling instant of the k-th bit. Expression (3.15) cannot be used directly with data from an asynchronous histogram. However, using the technique proposed in this section results in an estimate of $h_{SIG,i}$ and also of the simulated signal, $s(t)$. The latter can be used to determine the values of $\mu_{m,k}$. The values of $\sigma_{m,k}$ can be obtained directly from (3.13) by taking: $\sigma_{m,k}^2 = \sigma^2\left(\mu_{m,k}\right) \big/ \kappa^2$. The correction factor is required, due to the averaging effect caused by non-ideal sampling. The sampling instant and decision threshold are chosen in order to minimize the bit-error probability. Finally, the corrected Q-factor, q_{cor}, is obtained by inverting (3.14).

The presented technique combines the simplicity of the asynchronous histogram method with the accuracy of an exhaustive Gaussian approach. This allows an evaluation of signals affected by ISI. The following section presents some numerical results that illustrate the applicability of the proposed method.

3.3.2. Numerical Simulation Results

To evaluate the histogram estimation and Q-factor measurement techniques presented in section 3.3.1, Fig. 3.9 presents the dependence of q_{cor}/q on the aperture time of the sampling circuit. The simulation conditions are identical to the ones used to obtain Fig. 3.5. However, unlike the results presented in Fig. 3.5, the accuracy of the Q-factor estimates is approximately independent on the aperture time. This results from including the averaging effect due to non-ideal sampling in the signal component of the theoretical histogram. However, as the shape of the histogram becomes more complex due to the averaging effect, the fitting algorithm used presents a greater difficulty in obtaining appropriate values for the parameters of the theoretical histogram, requiring a greater number of iterations. To limit the processing time, the maximum number of iterations of the fitting process was set to 400, which allowed a maximum estimation error of 14%.

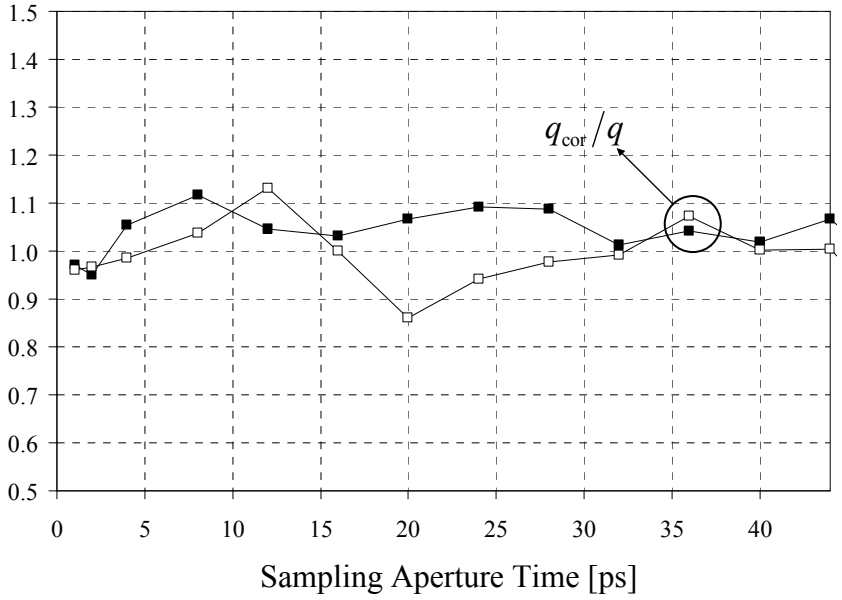

Fig. 3.9. Ratio between estimated and actual Q-factor values as a function of the aperture time for a 40 Gb/s signal. The theoretical histogram and Q-factor estimation techniques used are presented in section III. ■ - q_{cor}/q for q=8; □ - q_{cor}/q for q=10.

With the presented technique to obtain the theoretical histograms, the accuracy of the results depends strongly on the ability of the non-linear minimization algorithm to match the estimated histograms to the MAH. This becomes increasingly difficult as the shape of the histogram becomes complex. To evaluate the limitations of the theoretical histogram estimation method we considered a case where the received signal is degraded by dispersion. Fig. 3.10 presents the evolution of the estimated Q-factor and the actual Q-factor of the simulated signal, as a function of the accumulated chromatic dispersion. The presented results show that the estimated Q-factor values follow, with reasonable accuracy, the actual Q-factor values of the simulated signal for accumulated dispersion values below 68 ps/nm. For values of accumulated dispersion above this limit, the dispersion-induced degradation of the signal is interpreted by the fitting process as additional noise, which causes the estimated Q-factor values to drop significantly (see Fig. 3.10).

Another example of the application of the proposed technique is the inclusion of the distortion due to electrical filtering in the receiver. This effect has become quite relevant as many proposals for monitoring systems using asynchronous histograms have considered significant electrical filtering in the receiver of the OMS (see works by Shake et al.). Therefore, the effects of this type of distortion on Q-factor monitoring with

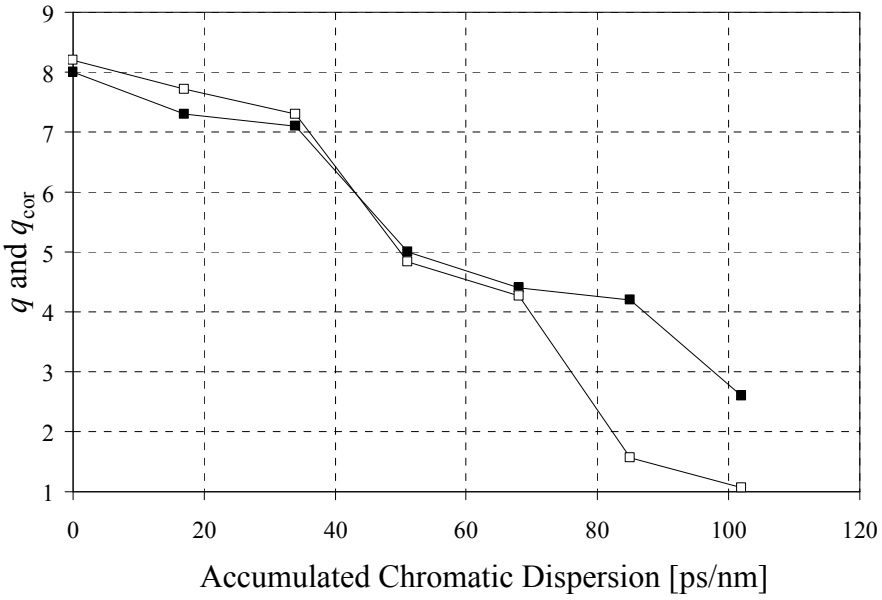

Fig. 3.10. Estimated and actual Q-factors of a raised cosine signal as a function of the accumulated dispersion. The signal at the amplifier input presets an average power of –22.5 dBm.
□ – estimated Q-factor values; ■ – actual Q-factor values.

asynchronous histograms must be addressed. The following presents a short study of the Q-factor dependence on the electrical filter bandwidth.

Fig. 3.11 presents the values of the asynchronously estimated Q-factor and the reference Q-factor, as a function of the electrical filter's –3 dB cut-off frequency, B_e, normalized to the signal bit-rate. The electrical receiving filter used was a 5th order Bessel filter, to avoid significant delay distortion. The numerical simulations were performed on a 40 Gb/s signal, using a sampling aperture time of 3 ps. This value was chosen to ensure that the sampling distortion did not interfere with the measurement. The attenuator was set to a value of 22.5 dB, which corresponds to a reference Q-factor value of 8, if the electrical filter –3 dB cut-off frequency is set to 160 GHz.

The results presented in Fig. 3.11 show that the estimated Q-factor corresponds approximately to the reference Q-factor. A maximum error of 5% was registered for a normalized bandwidth of 0.4. Both graphics clearly illustrate that increasing the electrical receiver filter bandwidth increases the system performance by reducing the distortion induced by this filter. However, after the optimum point is reached, the increase of the receiver filter bandwidth does not lead to significant benefits in terms of signal distortion. Instead, the noise component, which also depends on the receiver filter bandwidth, becomes dominant and degrades the system performance. The best performance obtained

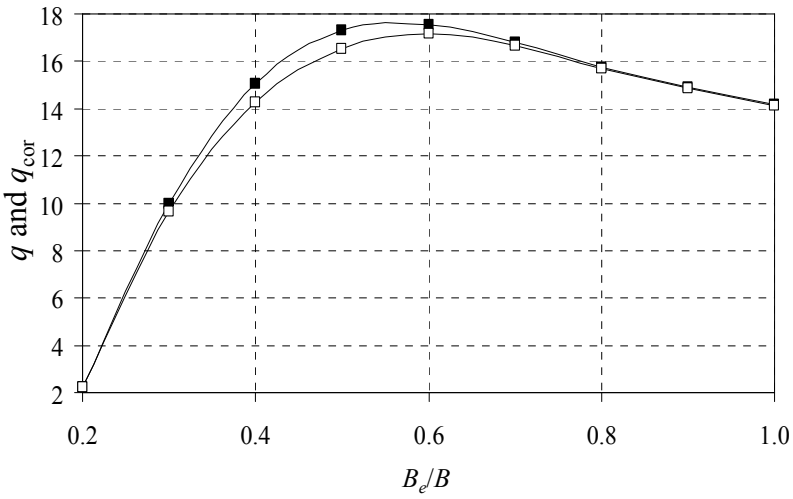

Fig. 3.11. Estimated and actual Q-factors as a function of the electrical receiver filter bandwidth normalized to the bit-rate. The signal at the amplifier input presets an average power of –22.5 dBm. □ – estimated Q-factor values; ■ – actual Q-factor values.

by both measurements corresponds to a normalized –3 dB cut-off frequency of 0.6. The Q-factor estimation technique was able to obtain a good accuracy for all values of the filter bandwidth.

3.4. Optical Signal-to-Noise Ratio Estimation Using Reference Asynchronous Histograms

3.4.1. OSNR Estimation Method

3.4.1.1. Estimation Method Using Reference Histograms Without the Impact of ASE-Noise

The main limitation of the Q-factor technique presented in section 3.3 is that prior knowledge of the received pulse shape is required to obtain $h_{SIG,i}$. Nevertheless, several approximations of this shape can be used, as long as some similarity between the actual shape of the impulse and the theoretical model is maintained, as illustrated in section 3.2.2.1. An alternative approach has been proposed in [Luís, 2006: 2] and it is schematically represented in Fig. 3.12. This approach is based on approximating $h_{SIG,i}$ in (3.12) with a RAH, $h_{REF,i}$, which is experimentally acquired from a reference signal. The RAH may be acquired in a calibration stage and memorized for later use in normal operation. Note that by using this approximation the model automatically includes the impact of non-ideal sampling, optical and electrical filtering at the OMS and other factors

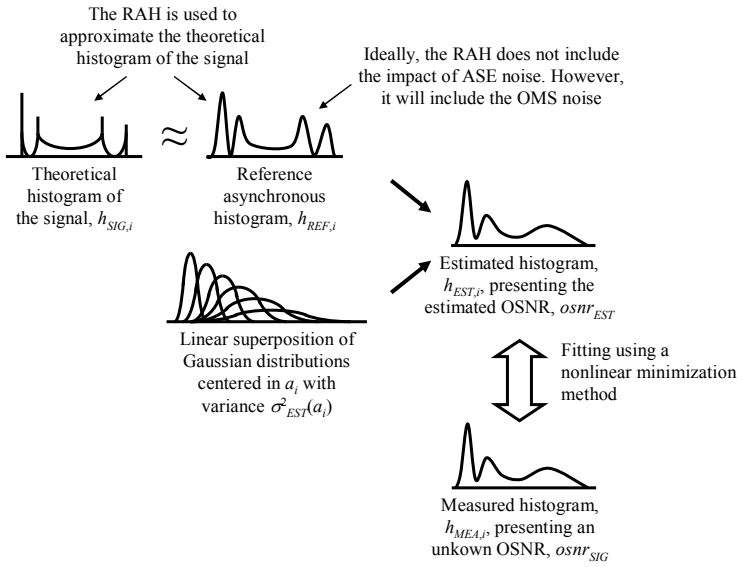

Fig. 3.12. Diagram of the proposed method to estimate the asynchronous histogram of a signal impaired with ASE-noise using a reference histogram.

that affect the monitoring process, such as quantization noise. In addition, assuming that the RAH results from a reference signal with a similar amount of accumulated dispersion to the signal under analysis, it may be considered that dispersion-induced distortion will not affect the measurement. However, unlike the previous method, the OMS has no specific information regarding the signal waveform, namely the levels for the mark and space symbols. As such, this approach is unsuited for the estimation of quality parameters such as the Q-factor. However, it will be shown that this approach allows the estimation of other signal parameters, such as the OSNR.

Ideally, the reference signal is unimpaired by noise and the RAH is identical to $h_{SIG,i}$. A more realistic approach assumes that the reference signal is affected by the noise generated in the OMS. Hence the RAH may be expressed as [Teixeira, 2002]:

$$h_{REF,i} = h_{SIG,i} * h_{OMS,i} \tag{3.16}$$

where $h_{OMS,i}$ is the histogram of the noise generated by the OMS. Assuming that the impact of the OMS noise on the signal is small, when compared with the impact of ASE noise, we may directly replace $h_{SIG,i}$ by $h_{REF,i}$ in (3.12), yielding:

$$h_{EST,n} = \sum_{i=1}^{N_b} \frac{h_{REF,i}}{\sqrt{2\pi \cdot \sigma_{EST}^2(a_i)}} \cdot \exp\left[-\frac{(a_n - a_i)^2}{2\sigma_{EST}^2(a_i)} \right] \tag{3.17}$$

Note that using (3.17) to estimate the MAH does not require knowledge of the parameters of $h_{SIG,i}$. Instead, the fitting is performed only on the value of $osnr_{EST}$. When a match between the estimated histogram and the MAH is found, we may assume that $osnr_{EST}$ is an estimate of the OSNR of the signal under analysis, $osnr_{SIG}$. This results in a substantial reduction of the computation effort required for the implementation of the proposed method, in comparison with the approaches presented in section 3.2, [Ye, 2007], [Ding, 2004], and [Rasztovits-Wiech, 1999], where the number of fitting variables may grow rapidly with the complexity of the histogram. However, the proposed method does not allow evaluating quality parameters that depend on the signal waveform, such as Q-factor.

As previously mentioned, the approximation proposed by (3.17) is valid for the cases where the contribution of the ASE noise to the MAH is substantially larger than the contribution of the OMS noise, i. e. $\sigma_{SIG}^2(a_i) > \sigma_{OMS}^2$, where $\sigma_{SIG}^2(a_i) = b_{sp} \cdot a_i / osnr_{SIG}$ is the variance of the signal-ASE noise beat of the signal under analysis. This condition may also be expressed as:

$$a_i > \sigma_{OMS}^2 \cdot osnr_{SIG} / b_{sp} \tag{3.18}$$

which implies that the proposed approximation is only valid above a given power level or below a maximum measurable $osnr_{SIG}$. These limits are conditioned by the variance of the electrical noise generated by the OMS, in agreement with the general conditions for OSNR measurements predicted in [Yang, 2002]. To illustrate the implications of condition (3.18), Fig. 3.13 presents a comparison between an experimental asynchronous histogram of a NRZ signal with $OSNR_{SIG}$ = 10·log$_{10}$($osnr_{SIG}$) of 16 dB, in logarithmic units, measured with a resolution bandwidth of 0.1 nm, and the corresponding estimated histogram. The RAH was obtained by acquiring a histogram of the same signal with an OSNR of 28 dB, in logarithmic units, considered here as a noiseless signal. The value of $osnr_{EST}$ was adjusted to find the best match between the estimated histogram and the MAH using the Nelder-simplex non-linear minimization algorithm. As shown in Fig. 3.13, the region of the

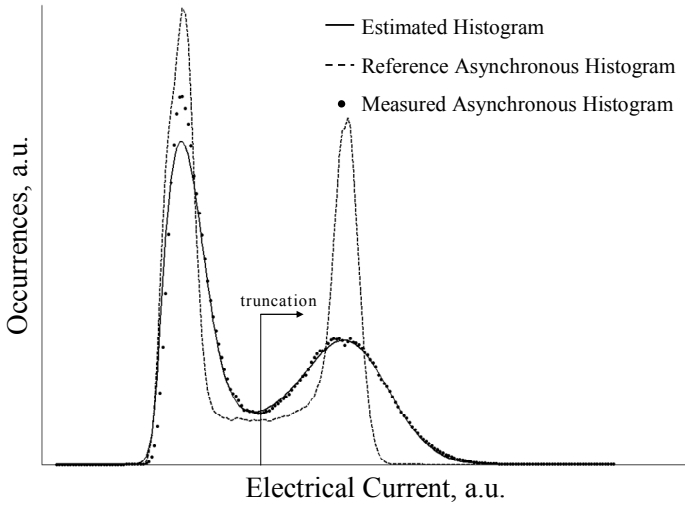

Fig. 3.13. Comparison between the measured histogram of a signal with an OSNR of 16 dB and the corresponding estimated histogram. A reference histogram with an OSNR of 28 dB was used to obtain the estimated histogram.

estimated amplitude histogram corresponding to low current levels near the space symbol presents significant error since condition (3.18) is not observed. The region corresponding to the mark symbol verifies condition (3.18) and is well approximated. As such, to avoid the error for low current levels, the histograms used in this analysis will be truncated bellow the level corresponding to the average signal power, as shown in Fig. 3.13.

An experimental validation of this method has been reported in [Luís, 2006: 2] with the estimation of the OSNR of 10 Gb/s signals and is described in Appendix C. In addition, a variation of this technique to estimate the impact of single-source in-band crosstalk has been experimentally validated and reported in [Luís, 2004: 2]. The latter is described in detail in Appendix D.

3.4.1.2. Estimation Method Using Reference Histograms Impaired by ASE-Noise

The main drawback of the method presented in sub-section 3.4.1.1 is the requirement of a noiseless reference signal. The corresponding RAH may be easily acquired in laboratory conditions but would be difficult to obtain in a field installation. Therefore, this sub-section propose an adaptation by using a RAH with finite OSNR. The reference signal then becomes characterized by an OSNR given by $osnr_{REF}$, in linear units, or $OSNR_{REF} = 10 \cdot \log_{10}(osnr_{REF})$, in logarithmic units, which corresponds to a signal-ASE noise beat variance given by $\sigma^2_{REF}(a_i) = b_{sp} \cdot a_i / osnr_{REF}$. The initial value of $OSNR_{REF}$ may be measured at a calibration stage, using external equipments when installing the OMS in

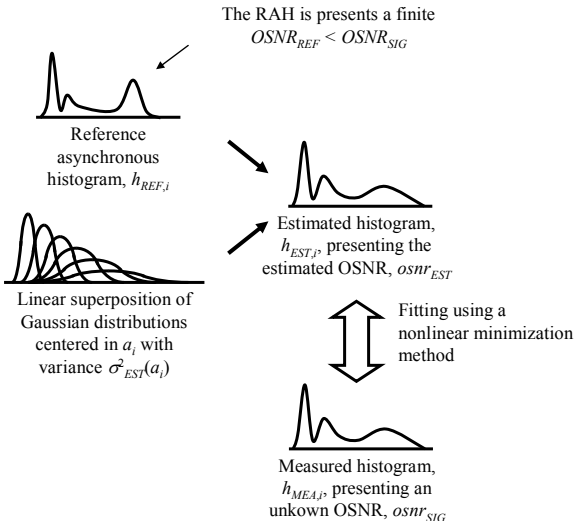

Fig. 3.14. Diagram of histogram estimation *Method A*.

the field. Alternatively, the output of the network planning may be used to estimate this value. Subsequent histogram acquisitions will reflect the changes of OSNR of the signal under analysis with respect to $OSNR_{REF}$. Further updates of the RAH and corresponding $OSNR_{REF}$ may be required when the traffic on the network is rearranged. However, these updates may be performed without the support of external equipment simply acquiring a RAH of the new signal and using the previous RAH and corresponding $OSNR_{REF}$ to estimate the new value of $OSNR_{REF}$.

Consider the case where $osnr_{SIG} < osnr_{REF}$, i. e. the signal under analysis presents a higher degradation than the reference signal. As such, the method described in section 3.4.1.1 may be used to include the impact of additional noise on the RAH to approximate the MAH, as represented in Fig. 3.14. In this case, the match between the MAH and the estimated histogram will be found when the estimated variance of the signal-ASE beat noise, initially defined by (3.13), reflects the difference between the corresponding noise variances of the signal under analysis and the reference signal, i. e.:

$$\sigma^2_{EST}(a_i) \approx \sigma^2_{SIG}(a_i) - \sigma^2_{REF}(a_i) = b_{sp} \cdot a_i \cdot \left[osnr^{-1}_{SIG} - osnr^{-1}_{REF} \right] \tag{3.19}$$

Finally, assuming that when a match between the MAH and the estimated histogram is found we have $osnr_{SIG} \approx osnr_{EST}$, yields:

$$\sigma^2_{EST}\left(a_i\right) = b_{sp} \cdot a_i \cdot \left[osnr^{-1}_{EST} - osnr^{-1}_{REF} \right] \tag{3.20}$$

which replaces expression (3.13) for the implementation of the novel method. Note that, if $osnr_{REF}$ is known from the calibration stage, the only unknown variable is $osnr_{EST}$. On the other hand, one could consider $osnr_{REF}$ and $osnr_{EST}$ as unknown variables and find the best combination of both which would match the estimated histogram to the MAH. However, this is outside the scope of this work and will be addressed elsewhere.

Expressions (3.17) and (3.20) correspond to an adaptation of the method described in section 3.4.1.1 to handle ASE noise-degraded RAH when the signal under analysis presents a higher degradation than the reference signal and will be referred in this work as *method A*. Similarly to the case presented in section 3.4.1.1, the validity of the approximation used in (3.20) requires that the variance of the signal-ASE noise beat affecting the signal under analysis is higher than the variance of the noise affecting the reference signal added to the variance of the OMS noise, assuming that the latter may be approximately described by a Gaussian distribution. This is represented by the condition:

$$\sigma^2_{SIG}\left(a_i\right) > \sigma^2_{REF}\left(a_i\right) + \sigma^2_{OMS} \tag{3.21}$$

Note that, for very high $osnr_{REF}$, the contribution of the ASE noise affecting the reference signal at the OMS input may be neglected in comparison with the contribution of the OMS noise. As such, the validity condition (3.21) may be written as $osnr_{SIG} < b_{sp} \cdot a_i \big/ \sigma^2_{OMS}$. This implies that the range of *method A* depends directly on the power at the OMS input. However, when reducing $osnr_{REF}$ the impact of the OMS noise becomes negligible and the validity condition may be written simply as $osnr_{SIG} < osnr_{REF}$. Note that the latter is independent of the power at the OMS input, suggesting that reducing $osnr_{REF}$ allows an increase of the sensitivity of the OMS at the cost of reducing the maximum measurable OSNR.

Consider now the case when the signal under analysis is less degraded than the reference signal, i. e. $osnr_{SIG} < osnr_{REF}$. When using *method A*, the nonlinear minimization algorithm will diverge to an arbitrarily high value of $osnr_{EST}$, corresponding to the lowest possible value of $\sigma^2_E\left(a_i\right) = \sigma^2_R\left(a_i\right)$ [see expression (3.20)]. As such, the condition of

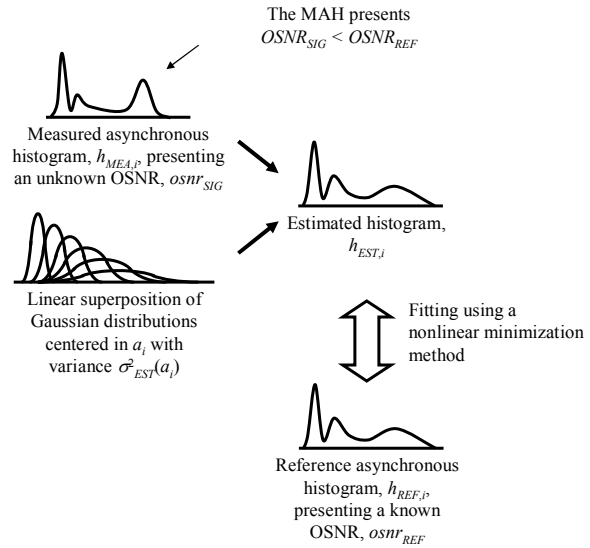

Fig. 3.15. Diagram of histogram estimation *Method B*.

failure of *method A* may be identified when the distance between the estimated and reference histograms, defined in this work as $d_{RE}^2 = \sum_{n=1}^{N_b} \left| h_{REF,n} - h_{EST,n} \right|^2$, converges to zero. Although it is not possible to calculate an estimate of the MAH by including the impact of ASE noise in the RAH, as proposed for *method A*, it is possible to do just the opposite. If the signal under analysis is less degraded by ASE noise than the reference signal, we may calculate an estimate of the RAH by including the impact of ASE noise in the MAH, as represented in Fig. 3.15. The amount of ASE noise that has to be included to find a match will allow an estimation of the $osnr_{SIG}$. This method will be referred here as *method B*. In this case, (3.17) becomes:

$$h_{EST,n} = \sum_{i=1}^{N_b} \frac{h_{MEA,i}}{\sqrt{2\pi \cdot \sigma_{EST}^2(a_i)}} \cdot \exp\left[-\frac{(a_n - a_i)^2}{2\sigma_{EST}^2(a_i)} \right] \tag{3.22}$$

where $h_{MEA,i}$ represents the MAH. In addition, considering that the roles of the reference signal and the signal under analysis are swapped, expression (3.20) will become:

$$\sigma_{EST}^2(a_i) = b_{sp} \cdot a_i \cdot \left[osnr_{REF}^{-1} - osnr_{EST}^{-1} \right] \tag{3.23}$$

Expressions (3.22) and (3.23) allow estimating the OSNR of the signal under analysis when it is lower than the OSNR of the reference signal. Similarly to (3.21), the validity of the approximation used to estimate the RAH is given by:

$$\sigma_{REF}^2 > \sigma_{SIG}^2 + \sigma_{OMS}^2 \tag{3.24}$$

Note that for high $osnr_{SIG}$, the impact of the ASE noise degrading the signal under analysis is negligible in (3.24), and the validity condition becomes $osnr_{REF} < b_{sp} \cdot a_i \big/ \sigma_{OMS}^2$. This implies that the maximum $osnr_{REF}$ is conditioned by the power at the OMS input. Furthermore, it indicates that the reachable OSNR range may be increased by reducing $osnr_{REF}$, similarly to *Method A*. For low $osnr_{REF}$ the OMS noise is negligible and the validity condition simply becomes $osnr_{SIG} > osnr_{REF}$.

The remaining problem with the proposed methods is the binary decision between using *method A* or *B*. Since $osnr_{SIG}$ is usually unknown, it may not be compared with $osnr_{REF}$ in order to select the appropriate method. As such, we propose to initially use *method A* and test its condition of failure, defined by previously. If the value of d_{RE} converges to zero, one may assume that $osnr_{SIG} < osnr_{REF}$. As such, a new calculation will be required, using *method B*.

3.4.2. Experimental Validation

3.4.2.1. Experimental Setup

Consider the experimental setup presented in Fig. 3.16. A pseudo-random binary sequence of 2^{14}-1 symbols at 40 Gb/s is used to modulate the intensity of a continuous waveform signal, generating a NRZ signal. An additional pulse carver driven by a 20 GHz clock signal may be used to convert the NRZ mark symbols in RZ impulses with a full-width at half maximum of 12.5 ps. The optical signal is combined in a 50:50 coupler with ASE noise generated by a set of two EDFA connected in series with a 0.8 nm optical filter. A VOA is used to set the noise power and control the OSNR at the output of the coupler. A sample of the degraded signal is sent to an optical spectrum analyzer to accurately determine the OSNR with a resolution bandwidth of 0.1 nm. The remaining signal power is fed to a VOA used to control the power at the input of the OMS. Alternatively, a lump of

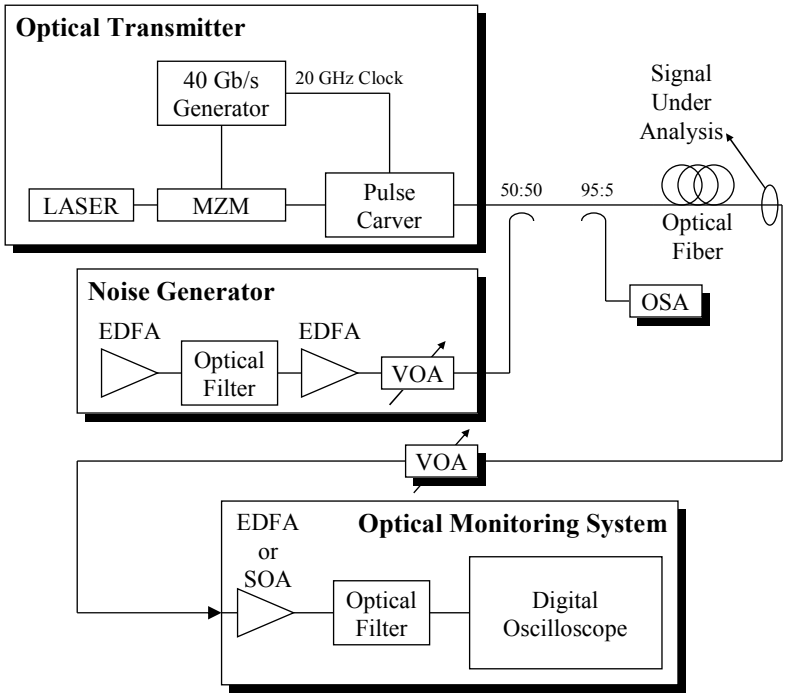

Fig. 3.16. Experimental setup for the validation of the OSNR estimation technique based on the analysis of reference asynchronous histograms.

standard single-mode fiber (SSMF) may be placed prior to the VOA to introduce GVD on the signal under analysis. The monitoring system will consist of an unsynchronized digital oscilloscope equipped with an optical front-end with a bandwidth of 65 GHz to obtain the asynchronous amplitude histograms. In addition, the signal at the OMS input may be amplified, using an EDFA, with a noise figure of approximately 6 dB, or a SOA with a noise figure of 9 dB. Two optical filters with bandwidths of 0.6 nm or 0.35 nm may be used prior to the digital oscilloscope to limit the optical noise generated by the optical pre-amplifier. In addition, the latter filter will be used to perform RZ-to-NRZ conversion. Each histogram will be computed by acquiring 10^6 asynchronous samples of the signal.

To estimate the OSNR, the OMS must first be calibrated for a known reference OSNR. This will be carried out by setting the signal under analysis with the required reference OSNR and acquiring the RAH. Normal operation of the proposed system will be carried out by setting the desired OSNR on the signal under analysis and acquiring the MAH. The latter will be compared with the RAH to estimate the corresponding OSNR.

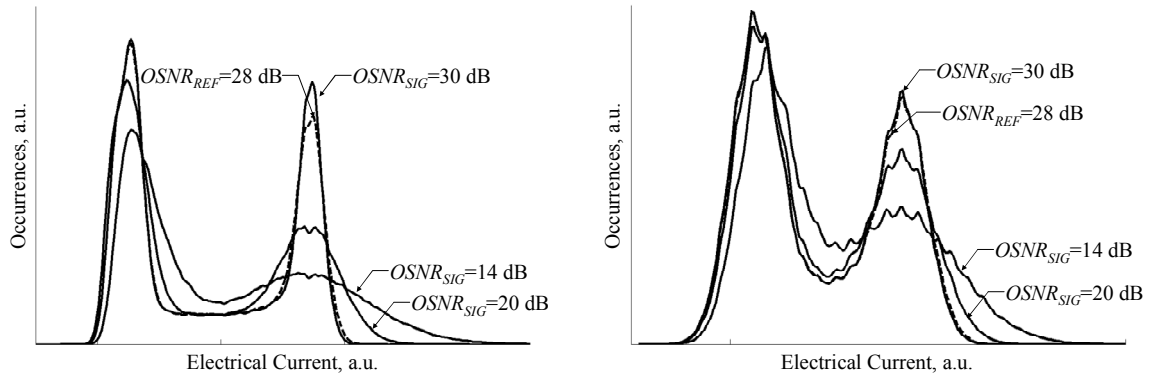

Fig. 3.17. Asynchronous histograms of the reference signal considering an OSNR of 28 dB (dashed line) and the signal under analysis with OSNR values of 14 dB, 20 dB and 30 dB (continuous lines) for a) power at the OMS input of 0 dBm and b) power at the OMS input of -5 dBm. Optical amplification or filtering in the OMS is not considered in this case.

3.4.2.2. OSNR Monitoring of NRZ Signals Without Optical Pre-Amplification

We begin by validating the OSNR estimation method using NRZ signals. The reference signal will be obtained in nearly noiseless conditions, with an OSNR of 28 dB. GVD-induced distortion and pre-amplification or filtering within the OMS will not be considered at this point. Note that the bandwidth of the ASE noise at the OMS input has been previously limited at the noise generator at 0.8 nm. Fig. 3.17-a) and -b) present examples of the measured histograms for $OSNR_{SIG}$=14 dB, 20 dB and 30 dB as well as the reference histogram with $OSNR_{REF}$=28 dB. Average powers at the input of the OMS of 0 dBm and -5 dBm have been considered. In the first case, the impact of ASE noise is clearly distinguishable on the shape of all presented histograms, particularly in the region of the histograms corresponding to the mark level. When the power at the OMS input is reduced to -5 dBm [see Fig. 3.17-b)], the impact of the electrical noise, generated at the oscilloscope receiver, and the quantization noise, resulting from the limited resolution of the ADC of the oscilloscope, becomes evident from the broadening of the peaks of the mark and space symbols, and the spikes of the histograms, respectively. In these conditions, the histogram obtained for $OSNR_{SIG}$=30 dB is indistinguishable from the reference histogram with $OSNR_{REF}$=28 dB. Fig. 3.18-a) and -b) present the dependence of $OSNR_{EST}$ on $OSNR_{SIG}$, considering average powers of 0 dBm and -5 dBm at the input of the OMS, respectively, for $OSNR_{REF}$ = 16 dB, 22 dB and 28 dB. For a qualitative analysis, the insets of Fig. 3.18-a) and -b) present eye diagrams of the signal at the oscilloscope input.

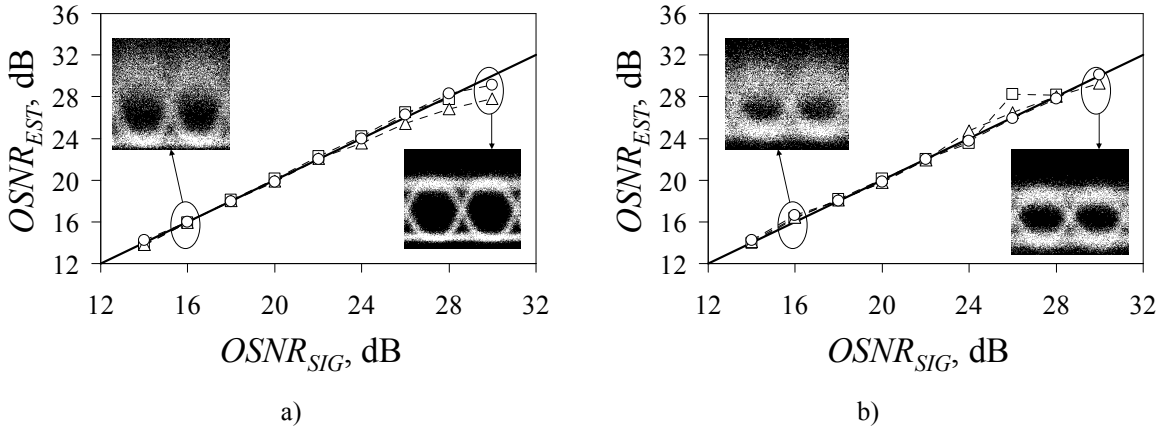

Fig. 3.18. Dependence of the estimated OSNR on $OSNR_{SIG}$ for $OSNR_{REF}$=28 dB (□), $OSNR_{REF}$=22 dB (Δ) and $OSNR_{REF}$=16 dB (○).Optical amplification or filtering in the OMS is not considered in this case. The insets present the eye diagram of the signal under analysis for OSNR values of 16 dB and 30 dB. a) power at the OMS input of 0 dBm and b) power at the OMS input of -5 dBm.

The results presented for $OSNR_{REF}$=28 dB were estimated using only *method A*, thus are limited to $OSNR_{SIG} < OSNR_{REF}$. For $OSNR_R$ = 16 dB and 22 dB, the estimates were obtained using *method A* for $OSNR_{SIG} < OSNR_{REF}$ and *method B* for $OSNR_{SIG} > OSNR_{REF}$. The selection between *method A* and *B* was performed automatically using the technique described in section 3.4.1.2.

Analyzing only the results obtained for $OSNR_{REF}$=28 dB it is shown, in Fig. 3.18-a), that $OSNR_{EST}$ follows $OSNR_{SIG}$ accurately in all the considered range with estimation errors below 1 dB. In the case of Fig. 3.18-b) with $OSNR_{REF}$=28 dB, $OSNR_{EST}$ becomes independent of $OSNR_{SIG}$ for values higher than 24 dB due to the impact of the OMS noise, as previously shown in Fig. 3.17-b). For values of $OSNR_{SIG}$ above this limit, the impact of ASE noise will not be reflected in the MAH due to the OMS noise. This shows that the minimum power at the input of the OMS is conditioned by the power of the oscilloscope noise, as indicated by (3.21). However, the sensitivity of the OMS may be improved by reducing the OSNR of the reference signal and using also *method B*, as indicated in sub-section 3.4.1.2. To demonstrate this, consider the dependence of $OSNR_{EST}$ on $OSNR_{SIG}$ shown in Fig. 3.18-a) and -b) for $OSNR_{REF}$ = 16 dB and 22 dB. Fig. 3.18-b) shows that, with $OSNR_{REF}$ = 16 dB or 22 dB, the estimated OSNR follows the real OSNR values with errors bellow 1 dB on the considered range. The advantage of reducing the reference OSNR is not verified in Fig. 3.18-a) with a power at the OMS input of 0 dBm. In this case, the maximum measurable OSNR with $OSNR_{REF}$ = 22 dB becomes limited to 27 dB with

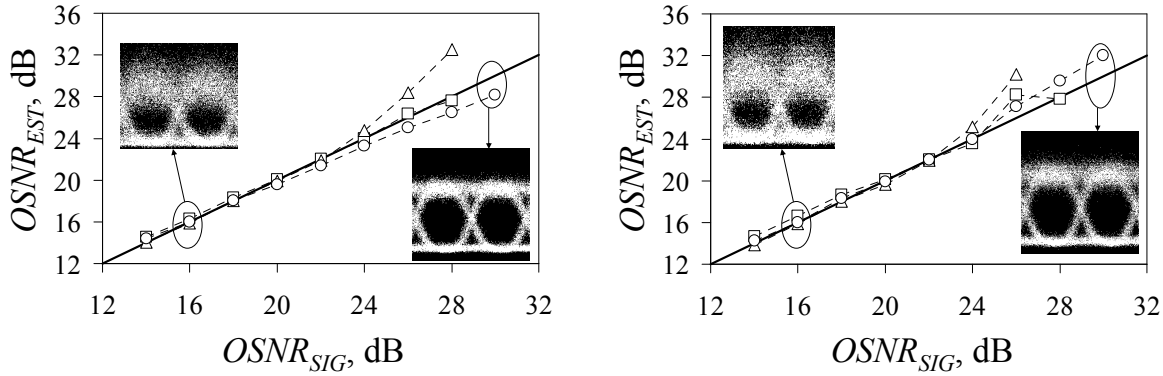

Fig. 3.19. Dependence of the estimated OSNR on $OSNR_{SIG}$ for $OSNR_{REF}$=28 dB (□), $OSNR_{REF}$=22 dB (Δ) and $OSNR_{REF}$=16 dB (○). An EDFA is used within the OMS for pre-amplification. The insets present the eye diagram of the signal under analysis for OSNR values of 16 dB and 30 dB.
a) power at the OMS input of -20 dBm and b) power at the OMS input of -25 dBm.

errors bellow 1 dB. With $OSNR_{REF}$ = 16 dB, this limit is extended above 30 dB with no significant improvement in comparison with the case of $OSNR_{REF}$ = 28 dB. Experimental validation of the proposed method for average power at the OMS input below -5 dBm was not possible due to the impact of the OMS noise.

3.4.2.3. OSNR Monitoring of NRZ Signals With Optical Pre-Amplification

In this sub-section, we propose to include an optical pre-amplifier within the OMS to increase its sensitivity. Note that the proposed method is only sensitive to the OSNR penalty between the RAH and the MAH. As such, the ASE noise generated by the pre-amplifier will not invalidate the measurement as long as a similar amount of noise is present in the RAH.

Consider the use of an EDFA within the OMS depicted in Fig. 3.16, as an optical pre-amplifier operating in a constant output power mode. We also include the 0.6 nm filter in the OMS to limit the pre-amplifier noise. This allowed the acquisition of valid asynchronous histograms with an average power at the OMS input as low as -25 dBm. Fig. 3.19-a) and -b) present the dependence of $OSNR_{EST}$ on the $OSNR_{SIG}$, assuming $OSNR_{REF}$=16 dB, 22 dB and 28 dB, and considering average powers of -20 dBm and -25 dBm at the input of the OMS, respectively. In the case of $OSNR_{REF}$=28 dB, the OSNR estimates follow a behavior similar to the one observed for higher powers in Fig. 3.18-a) and -b). Note that, in the case of an average power at the OMS input of -25 dBm, $OSNR_{EST}$ is independent of $OSNR_{SIG}$, for values above 24 dB. This limitation is due to the noise

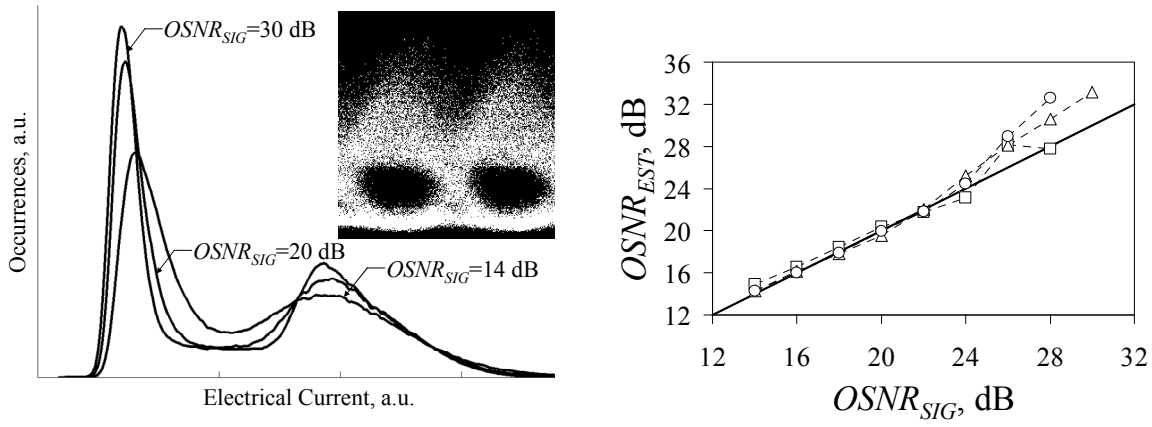

a) b)

Fig. 3.20. Impact of a SOA pre-amplifier on the asynchronous histograms (a) and dependence of the estimated OSNR on $OSNR_{SIG}$ (b) for various $OSNR_{REF}$ and $OSNR_{SIG}$ values and an input power at the OMS input of -15 dBm. □: $OSNR_R$=28 dB; Δ: 22 dB; and ○: 16 dB.
The inset presents the eye diagram of the signal at the oscilloscope input for $OSNR_{SIG}$=30 dB.

generated by the digital oscilloscope and also due to the noise generated by the pre-amplifier, which masks the impact of ASE-noise on the signal under analysis. However, it occurs for an average power at the OMS input 20 dB below the corresponding case without an optical pre-amplifier, demonstrating the advantage of the pre-amplified approach. When $OSNR_{REF}$ is reduced to 22 dB and 16 dB, we verify that the maximum measurable OSNR is limited to 24 dB and 26 dB, respectively, for errors below 1 dB and for both considered values of power at the OMS input.

Consider now the use of a SOA as an optical pre-amplifier within the OMS. The smaller dimensions and simple integration of SOAs may be an advantage in comparison with the application of an EDFA in an OMS. Nevertheless, the reduced gain and nonlinear characteristics may become a detriment to the effectiveness of the OMS. In the case of this experiment, the considered SOA was initially designed for nonlinear application with 2.5 Gb/s signals, which is clearly insufficient for amplification of the 40 Gb/s signal under analysis without significant distortion. Fig. 3.20-a) presents the typical asynchronous histograms for $OSNR_{SIG}$=14 dB, 20 dB and 30 dB, obtained when using the SOA pre-amplifier. As shown, the peak corresponding to the mark symbol is significantly broadened in comparison with Fig. 3.18-a) and –b). This results from the overshoot generated by the SOA, which is also observable from the eye diagram inset Fig. 3.20-a). Fig. 3.20-b) presents the dependence of the $OSNR_{EST}$ as a function of the $OSNR_{SIG}$ for $OSNR_{REF}$=16 dB, 22 dB and 28 dB, considering an average power of -15 dBm at the input of the OMS.

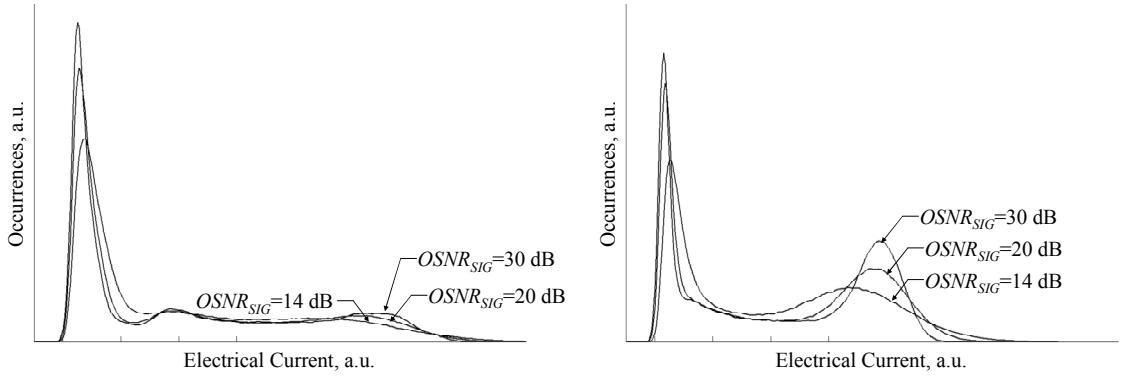

Fig. 3.21. Examples to asynchronous histograms of a) an RZ signal and b) the NRZ signal resulting from the RZ-to-NRZ conversion, for OSNR values of 14 dB, 20 dB and 30 dB.

Lower power levels at the OMS input were not achievable due to the limited gain of the SOA, which in such conditions is unable to yield an average power at the input of the oscilloscope above the minimum limit of -5 dBm, presented in section 3.4.2.2.

As shown in all considered cases, the maximum measurable OSNR is limited to 24 dB for an estimation error below 1 dB. Similarly to the case of the EDFA pre-amplifier, this limitation results from the additional ASE noise introduced by the SOA. However, it may be noted that the signal distortion induced by the SOA does not impact significantly on the maximum measurable OSNR. Otherwise, Fig. 3.20 would present OSNR measurement errors even for low values of $OSNR_{SIG}$.

3.4.2.4. OSNR Estimates of RZ Signals

Fig. 3.21-a) presents the asynchronous histograms acquired from an RZ signal with OSNR values of 14 dB, 20 dB and 30 dB. An EDFA pre-amplifier was used to increase the OMS sensitivity. Unlike the asynchronous histograms of a NRZ signal, the asynchronous histograms of the RZ signal do not allow a clear distinction between the mark and space symbols. This results from the limited duty-cycle of the RZ signal, which yields a low probability for a sample to be acquired during a mark symbol. Since the latter are the most affected by ASE noise, it also becomes difficult to distinguish between histograms acquired from signals with different OSNR, as shown in Fig. 3.21-a).

Several techniques have been proposed to handle this limitation. Shake et al. have proposed to eliminate the samples in the central area of the histogram, thus exposing the mark symbol [Shake, 1998], [Shake, 2000], and [Shake, 2002: 3]. Alternatively, Rasztovits

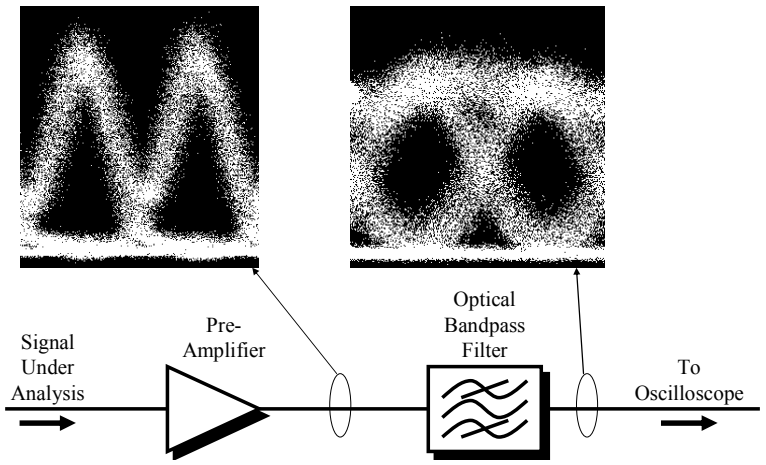

Fig. 3.22. RZ to NRZ conversion scheme using a narrow optical filter for analysis of the asynchronous histogram of the signal. The insets present the eye diagrams of the RZ signal before the filter and the NRZ signal after the optical filter.

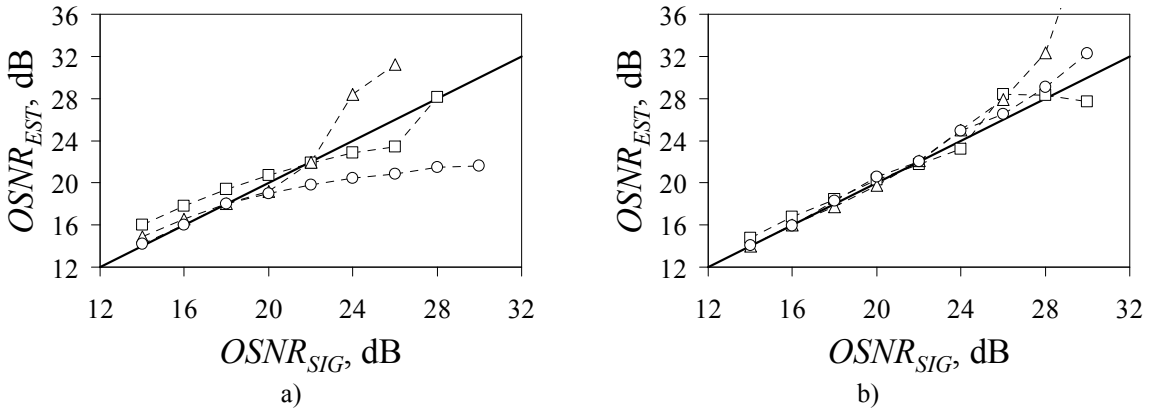

Fig. 3.23. Dependence of the estimated OSNR on $OSNR_{SIG}$ for an unfiltered (a) and filtered (b) RZ signal with $OSNR_{REF}$=28 dB (□),$OSNR_{REF}$=22 dB (Δ) and $OSNR_{REF}$=16 dB (○).
An EDFA is used as optical amplifier to achieve a power at the OMS input of -20 dBm.

et al. and Weinert et al. have proposed to mirror the histogram area above the maximum of the mark symbol to create a bell-shaped histogram, similar to what could be obtained from a synchronous sampling system [Rasztovits-Wiech, 1999] and [Weinert, 2001]. In both cases, the handling of the histograms is directed at isolating the mark symbols rather than enhancing the impact of ASE noise to facilitate its measurement. As such, these techniques may be inappropriate for the estimation of OSNR.

Fig. 3.22 illustrates the approach proposed in this work by converting the RZ signal to an NRZ signal. This is carried out by filtering the RZ signal within the OMS with an optical filter with a bandwidth of 0.35 nm. As show in the eye diagrams inset Fig. 3.22, the outcome of the optical filter is a low quality NRZ signal, which may be used for the OSNR

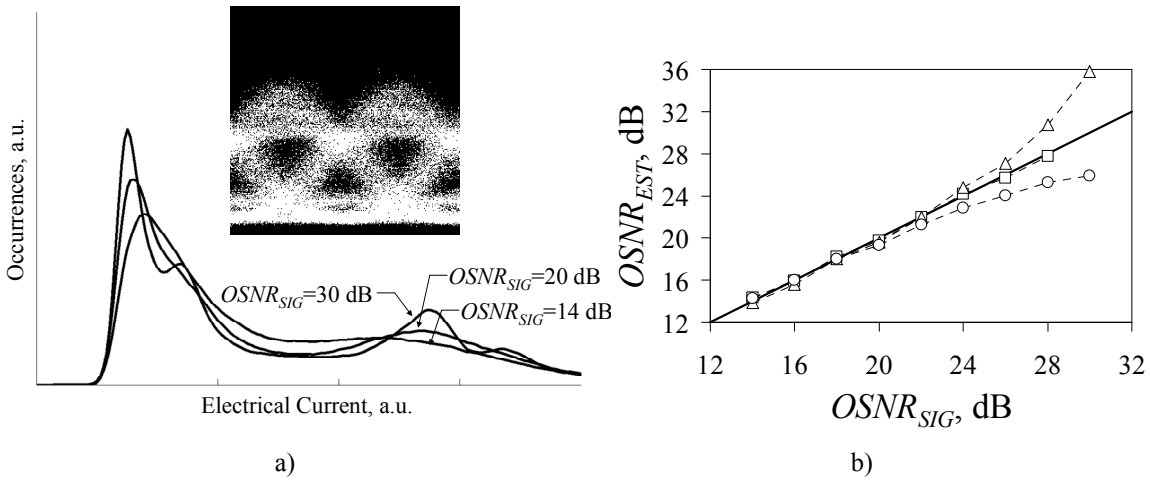

a) b)

Fig. 3.24. Impact of GVD on the asynchronous histograms (a) and dependence of the estimated OSNR on $OSNR_{SIG}$ (b) for various $OSNR_{REF}$ and $OSNR_{SIG}$ values and an input power at the OMS input of -15 dBm. □: $OSNR_{REF}$=28 dB; Δ: $OSNR_{REF}$=22 dB; and ○: $OSNR_{REF}$=16 dB.
The inset presents the eye diagrams of the signal at the oscilloscope input for $OSNR_{SIG}$ = 30 dB.

estimates. Note that the presented setup requires a pre-amplifier to compensate the losses of the optical filter, which eliminates a significant part of the spectrum of the signal under analysis. As such, we will use of the EDFA in the OMS. Fig. 3.21-b) presents the asynchronous histograms of the RZ-to-NRZ converted signal for the same OSNR values used for Fig. 3.21-a). As shown, the histograms present clearly distinguishable space and mark symbols. Furthermore the mark symbol clearly reflects the impact of the ASE noise, as originally intended.

Fig. 3.23-a) and -b) present a comparison of $OSNR_{EST}$ without and with RZ-to-NRZ conversion, respectively, assuming an OMS input power of -20 dBm and $OSNR_{REF}$=16 dB, 22 dB and 28 dB. In the case of Fig. 3.23-a), the nonlinear minimization algorithm is unable to accurately estimate $OSNR_{SIG}$ due to the weak dependence between the OSNR of the signal under analysis and the histogram shape. After RZ-to-NRZ conversion, the analysis becomes similar to that of a NRZ signal, as reported in sections 3.4.2.2 and 3.4.2.3. In this case, the OSNR estimates are within a 1 dB error margin up to $OSNR_{SIG}$=24 dB for $OSNR_{REF}$=22 dB and 28 dB, and up to $OSNR_{SIG}$=27 dB for $OSNR_{REF}$=16 dB.

3.4.2.5. OSNR Estimates of GVD-Degraded NRZ Signals

Consider the application of the proposed method to GVD-degraded signals. This results from the fact that the OMS may be placed in arbitrary points of the network. Hence, there is the possibility that the signal under analysis presents nonzero accumulated

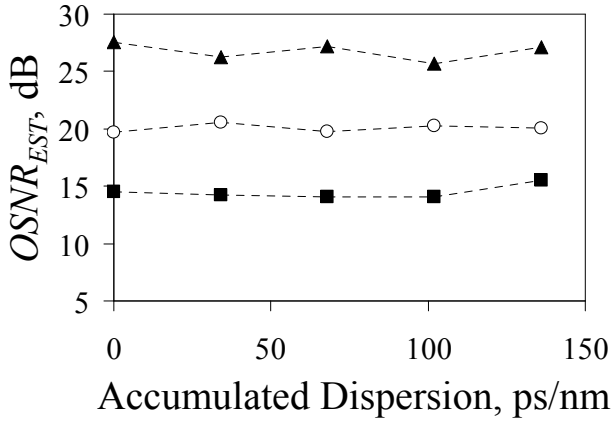

Fig. 3.25. Dependence of the estimated OSNR on the accumulated dispersion of the measured and reference signals. ▲: $OSNR_{SIG}$=26 dB and $OSNR_{REF}$=22 dB; ○: $OSNR_{SIG}$=20 dB and $OSNR_{REF}$=16 dB; ■: $OSNR_{SIG}$=28 dB and $OSNR_{REF}$=14 dB.

dispersion. As such, the asynchronous histogram of such signals will reflect the distortion of the nonzero accumulated dispersion. To illustrate these changes, Fig. 3.24-a) presents the asynchronous histogram of the 40 Gb/s NRZ signal affected by 102 ps/nm of accumulated dispersion, corresponding to transmission through 6 km of SSMF. The eye diagram inset Fig. 3.24-a) illustrates the GVD-induced degradation of the 40 Gb/s NRZ signal. As shown, the impact of GVD on the asynchronous histograms is particularly evident for $OSNR_{SIG}$=30 dB. In this case, one may notice the distortion of the mark and space symbols presented as additional peaks. As such, the changes of the asynchronous histogram can be used to estimate the impact of accumulated dispersion, as proposed by [Hanik, 1999], [Shake, 2002: 4], [Shake, 2003: 2], [Ye, 2007], and [Weinert, 2004]. However, for lower OSNR values, the impact of GVD becomes less evident due to the dominant ASE-induced degradation present in the signal. In these cases, the GVD-impact will be masked by the ASE noise and becomes indistinguishable.

Fig. 3.24-b) presents the dependence of $OSNR_{EST}$ on $OSNR_{SIG}$, for $OSNR_{REF}$=16 dB, 22 dB and 28 dB, considering an average power of -20 dBm at the input of the OMS and introducing an accumulated dispersion of 102 ps/nm on the signal. An EDFA was used as pre-amplifier to allow a reduced power at the OMS input and it is assumed that the accumulated dispersion of the MAH is identical to that of the RAH. As shown, the OSNR estimates have the similar behavior as shown previously in Fig. 3.19 for signals unaffected by GVD. This indicates that the accumulated dispersion has negligible impact on the OSNR estimation method as long as this impact is identical in the RAH and the MAH. To

verify this property, Fig. 3.25 presents the dependence of $OSNR_{EST}$ on the accumulated dispersion for several values of $OSNR_{SIG}$ and $OSNR_{REF}$. As shown in all considered cases, the estimated OSNR varies negligibly with the accumulated dispersion, validating the application of the proposed method for GVD-degraded signals.

The case presented in Fig. 3.25 assumes that the optical path of the signals propagated through the optical network remains unchanged from the moment that the RAH is acquired to the moment that a MAH is acquired, which is acceptable for circuit switched static networks. However, recent deployment of commercial systems using optical cross-connects allows operators to rapidly alter the paths of the optical signals and consequently, of their accumulated dispersion. As such, a realistic approach requires assuming that the accumulated dispersion of the RAH and MAH will differ along time. For this purpose, we may note that the impact of GVD on the histogram shape will be interpreted by the nonlinear minimization algorithm as additional ASE, which allows associating it with an OSNR penalty. Under these conditions, the application of the proposed method to MAH with different GVD-degradation than the corresponding RAH will result in an underestimation or overestimation of the OSNR, which reflects the GVD-induced OSNR penalty. This is illustrated in Fig. 3.26, where a RAH with $OSNR_{REF}$=22 dB without GVD induced degradation is used to estimate the OSNR of the same signal with an accumulated dispersion of 102 ps/nm. As shown for $OSNR_{SIG}$=22 dB, the OSNR estimate shows a GVD-induced OSNR penalty of approximately 7.4 dB. This penalty increases linearly with $OSNR_{SIG}$ due to the decrease of the ASE noise-impact on the asynchronous histograms.

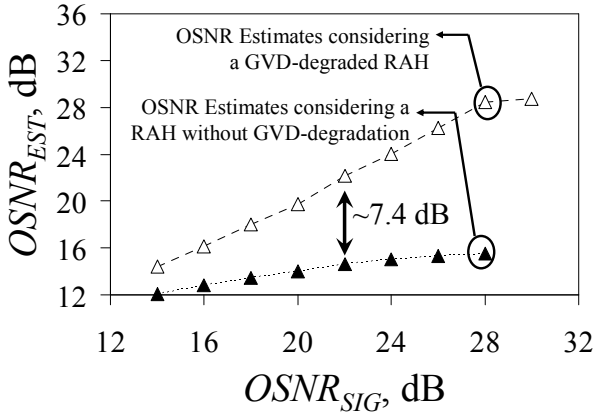

Fig. 3.26. OSNR estimates of an NRZ signal using a RAH with $OSNR_{REF}$=22 dB and a power at the OMS input of -5 dBm. Δ: Estimates using RAH with null accumulated dispersion; ▲: Estimates using RAH with an accumulated dispersion of 102 ps/nm.

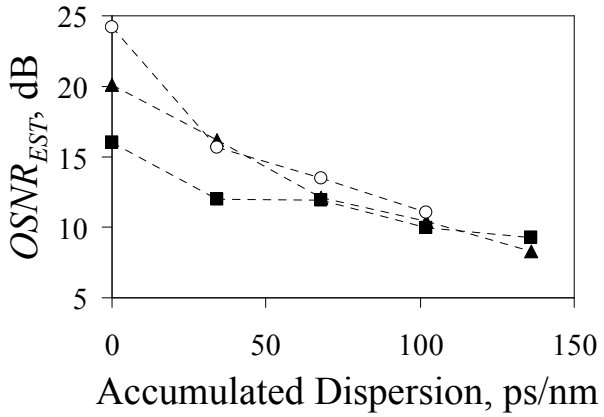

Fig. 3.27. Dependence of the OSNR estimates of an NRZ signal on the accumulated dispersion of the signal under analysis, using reference signals with null accumulated dispersion. ○: $OSNR_{SIG}$=$OSNR_{REF}$=24 dB; ▲: $OSNR_{SIG}$=$OSNR_{REF}$=20 dB; ■: $OSNR_{SIG}$=$OSNR_{REF}$=16 dB.

To further illustrate the principle of the GVD-induced OSNR penalty, Fig. 3.27 presents the dependence of $OSNR_{EST}$ on the accumulated dispersion of the signal under analysis, assuming $OSNR_{SIG}$=$OSNR_{REF}$, which take the values of 14 dB, 20 dB and 26 dB. As shown in Fig. 3.27, the values of $OSNR_{EST}$ decrease with the accumulated dispersion for all cases, reflecting the penalty due to the GVD-induced distortion of the asynchronous histograms. Furthermore, as the value of accumulated dispersion exceeds 68 ps/nm, corresponding to 4 km of SSMF, the impact of GVD on the shape of the asynchronous histograms becomes dominant over the impact of ASE noise. As a consequence, the values of $OSNR_{EST}$ converge, regardless of the value of $OSNR_{SIG}$, reflecting the penalty of the dominant impairment, which in this case is GVD.

Note that the GVD-induced OSNR penalty may only be directly related with the actual BER of the signal if the receiver used to detect it presents the same optical and electrical characteristics as the OMS.

3.5. Conclusions

This chapter has presented a study on the application of asynchronous amplitude histograms of optical signals for monitoring of Q-factor and OSNR. This study addressed, in the first place, the limitations imposed by non-ideal sampling. It has been shown that the impact of finite sampling aperture time may be modeled with an equivalent filter, which reproduces the averaging effect of the sampling system. It has been analytically shown that when the sampling aperture time is increased, while maintaining values bellow the bit

period, the bandwidth of the equivalent filter is decreased, limiting the equivalent optical noise bandwidth of the signal under analysis. As a consequence, a quality measurement performed using such sampling system yields an overestimated Q-factor. To tackle this limitation, a Q-factor correction factor has been proposed. Numerical simulations have shown that the application of the correction factor allowed an increase of the sampling aperture time to values near the symbol period. These simulations have assumed the monitoring of 40 Gb/s NRZ signals and a Q-factor monitoring technique based on the analysis of asynchronous histograms proposed by other authors.

It has also been shown, through numerical simulations, that increasing the sampling aperture time to values exceeding the bit period leads to distortion of the signal. This distortion is interpreted by the histogram analysis algorithm as additional noise, leading to an underestimated Q-factor. Hence a novel technique for Q-factor estimation using asynchronous amplitude histograms has been proposed to handle this limitation, as well as accounting for the presence of ISI on the signal under analysis. This technique is based on the comparison of the histogram of the signal under analysis with an estimated histogram, obtained through numerical computation. The estimated histogram includes the impact of non-ideal sampling as well as the influence of the optical effects degrading the signal. A match between both histograms is achieved by adjusting the parameters that condition these optical effects with a non-linear minimization algorithm. In the presented case with NRZ signals, these parameters are the current levels for the mark and space symbols, the average transition time, the OSNR and the amount of accumulated dispersion. The application of the proposed technique has been successful in accurately evaluating the Q-factor of a simulated signal for sampling aperture times exceeding the bit period. In addition, the application of the novel technique has been illustrated by evaluating signals degraded by chromatic dispersion or affected by electrical filtering in the receiver. It has been verified that the main limitation of the proposed technique lies in the capacity of the non-linear minimization algorithm to estimate the signal parameters required to obtain the Q-factor, which decreases with the high number of unknown variables.

To reduce the complexity of the computation required to obtain the estimated histogram an alternative technique has been proposed by taking a reference histogram acquired from the signal under analysis in a calibration stage and numerically including the impact of ASE noise in order to produce an estimated histogram. Through the comparison

of the estimated histogram and the histogram of the signal under analysis, it has been possible to estimate the OSNR of the latter, regardless of the OSNR that affected the reference asynchronous histogram at the calibration stage, as long as the waveform of the signal is maintained. This technique requires the adjustment of a single variable, the OSNR, to find a match between the estimated and measured histograms. Experimental validation of this technique has shown that the maximum measurable OSNR decreases with the power of the signal at the input of the OMS due to the influence of the noise generated in the OMS. However, this limitation may be overcome by lowering the value of the reference OSNR. Furthermore, the proposed technique allowed the use of optical pre-amplification to increase the sensitivity of the OMS by as much as 10 dB and 20 dB, when using a SOA or an EDFA pre-amplifier, respectively. This was achieved at the cost of limiting the maximum measurable OSNR to values as low as 24 dB.

The technique based on reference histograms may be applied, in principle, to arbitrary modulation formats. This work has experimentally demonstrated its application to 40 Gb/s NRZ signals with and without GVD-induced degradation, and also 40 Gb/s RZ signals. In the latter case, the RZ signal was converted to a NRZ signal within the OMS by narrow-band optical filtering, to enhance the impact of ASE noise on the shape of the acquired histograms. All considered cases presented negligible changes of sensitivity or maximum measurable OSNR. Finally, the impact of GVD-induced changes on the shape of the measured histograms with respect to the reference histograms was analyzed. It was shown that the proposed method interprets these variations as additional noise, thus underestimating the OSNR. Nevertheless, the reduction of the OSNR estimates may be interpreted as a GVD-induced OSNR penalty, thus reflecting an actual penalty between the signal under analysis and the reference signal.

Chapter 4. Basic Concepts of All-Optical Fiber Wavelength Conversion

4.1. Introduction

This chapter focuses on the fundamental concepts behind fiber-based AOWC. Given the large variety of proposals for such systems in the literature, this work will concentrate on the principles that govern XPM-based and FWM-based wavelength converters. Particular focus will be given to the first, which are also the basis of the work presented in Chapter 5. AOWC based on nonlinear birefringence in optical fibers are outside the scope of this work and will not be considered. This chapter is structured as follows. Section 4.2 presents the basic concepts behind fiber nonlinearity, presenting their application to XPM-based AOWC in sub-section 4.2.1. Sub-section 4.2.2 focuses on the operation of FWM-based AOWC. A summary and conclusions are outlined in section 4.3.

4.2. AOWC Based on Fiber Nonlinearity

The response of any dielectric material to light becomes nonlinear for intense electromagnetic fields, and optical fibers are not an exception [Agrawal, 1997] (see page 60). The fiber nonlinearity results from the third order susceptibility to intense optical fields, which is responsible of phenomena such as FWM and nonlinear refraction

[Agrawal, 1995] (see page 15). It is normally expressed as a dependence of the fiber refraction index on the optical power, $n_{ref}(z,t)$. This dependence may be approximated by [Agrawal, 1997] (see page 62):

$$n_{ref}(z,t) = n_0 + n_2 \cdot \frac{P(z,t)}{A_{eff}} \tag{4.1}$$

where n_0 is the fiber refraction index in linear transmission regime, A_{eff} is the fiber effective area, n_2 is the nonlinear index coefficient, and $P(z,t)$ is the instantaneous optical power in the fiber at the z coordinate and the t instant. The consequence of the nonlinear refraction is a variation of the fiber propagation constant, β' as a function of the instantaneous power [Agrawal, 1997] (see page 67):

$$\beta'(z,t) = \beta(z,t) - \gamma P(z,t) \tag{4.2}$$

where $\beta(z,t)$ if the fiber propagation constant assuming a linear propagation regime, and γ is the fiber nonlinearity coefficient, given by [Agrawal, 1997] (see page 67):

$$\gamma = \frac{n_2 \cdot \omega_o}{c \cdot A_{eff}} \tag{4.3}$$

ω_o is the optical angular frequency and c is the speed of light in vacuum. The nonlinear response of optical fibers may be considered instantaneous for pulse-widths greater than 1 ps [Agrawal, 1995] (see page 38). This enables its use for ultra-fast applications in optical processing systems, in particular AOWC. The following sub-sections present some of the most significant techniques for wavelength conversion using XPM and FWM.

4.2.1. AOWC Based on Fiber XPM

Expression (4.2) implies that a signal transmitted in an optical fiber is delayed according to its instantaneous power. As such, assuming that the transmitted optical signal is composed by a single channel, the nonlinear phase shift is given by [Kazousky, 1996] (see page 587):

$$\phi_{SPM} = -\gamma L_{eff} \cdot P_p \tag{4.4}$$

where P_p is the channel power and L_{eff} is the fiber effective length, given by:

$$L_{eff} = \frac{1 - e^{-\alpha L}}{\alpha} \tag{4.5}$$

with α and L as the fiber attenuation coefficient and length, respectively. Under these conditions, the nonlinear phase shift phenomenon is referred as SPM. For a multi-channel system with N_{ch} channels, the nonlinear phase shift of the i-th channel is given by the sum of the SPM with the nonlinear phase shift induced by the other channels, usually referred as XPM:

$$\phi_{NL,i} = \phi_{SPM,i} + \phi_{XPM,i} \tag{4.6}$$

where $\phi_{SPM,i}$ is the previously mentioned SPM of the i-th channel and $\phi_{XPM,i}$ is the XPM-induced phase shift, given by:

$$\phi_{XPM,i} = -2\gamma L_{eff} \sum_{\substack{m=1 \\ m \neq i}}^{N_{ch}} P_{p,m} \tag{4.7}$$

where $P_{p,m}$ represents the power of the m-th interfering channel. Expression (4.7) assumes that all channels are co-polarized. Otherwise, the term 2 on the right hand side of (4.7) would be reduced to a minimum of 2/3 for orthogonally polarized channels. Expression (4.7) shows that XPM may be used to transfer information encoded on the intensity of each channel to the phase of the other channels. In the particular case of a two channels system, one may use XPM to transfer the intensity encoded data of a channel (pump) to the phase of the other channel (probe). This is the fundamental principle of fiber-XPM based AOWC and is common to wavelength converters using other types of nonlinear devices, such as SOA. However, (4.7) neglects the propagation delay of the interfering channels, limiting

its validity. To include this aspect, we must rewrite (4.7) taking into account the fact that the interfering channels are intensity modulated and may travel at different group velocities within the fiber. This leads to a time domain dependence of the XPM-induced phase shift as [Chiang, 1996]:

$$\phi_{XPM,i}(t) = -2\gamma \sum_{\substack{m=1 \\ m\neq i}}^{N_{ch}} \int_0^L P_{p,m}\left(t - \frac{L}{v_{g,m}} + d_{i,m}\cdot z\right)\cdot e^{-\alpha z}\cdot dz \tag{4.8}$$

where L is the fiber length and $v_{g,m}$ is the group velocity of the m-th interfering channel. The exponential term regards the fiber attenuation, with α as the attenuation parameter. The term $d_{i,m}$ is referred as the walkoff parameter, and may approximated by [Chiang, 1996]:

$$d_{i,m} = \left(v_{g,i}\right)^{-1} - \left(v_{g,m}\right)^{-1} = \int_{\lambda_i}^{\lambda_m} D(\lambda)\cdot d\lambda \tag{4.9}$$

where λ_i and λ_m are the carrier wavelengths of the i-th and m-th channels, respectively, and $D(\lambda)=S\cdot(\lambda-\lambda_0)$ is the dispersion parameter as a function of the operation wavelength, λ, with S as the dispersion slope and λ_0 as the zero dispersion wavelength. Expression (4.9) may be approximated by:

$$d_{i,m} \approx D_i\cdot\Delta\lambda_{i,m} - S\cdot\Delta\lambda_{i,m}^2/2 \tag{4.10}$$

where $D_i=D(\lambda_i)$ is the dispersion parameter for the carrier wavelength of the i-th channel, and $\Delta\lambda_{i,m}=\lambda_i-\lambda_m$ is the wavelength spacing between the i-th and m-th channels. Expression (4.8) shows that the walkoff between channels propagating in the fiber leads to a temporal broadening of the corresponding XPM-induced phase shift. As such, an effective transfer of the information encoded on the intensity of a given channel to the phase of another channel requires a low walkoff parameter, to avoid distortion of the XPM-induced phase shift.

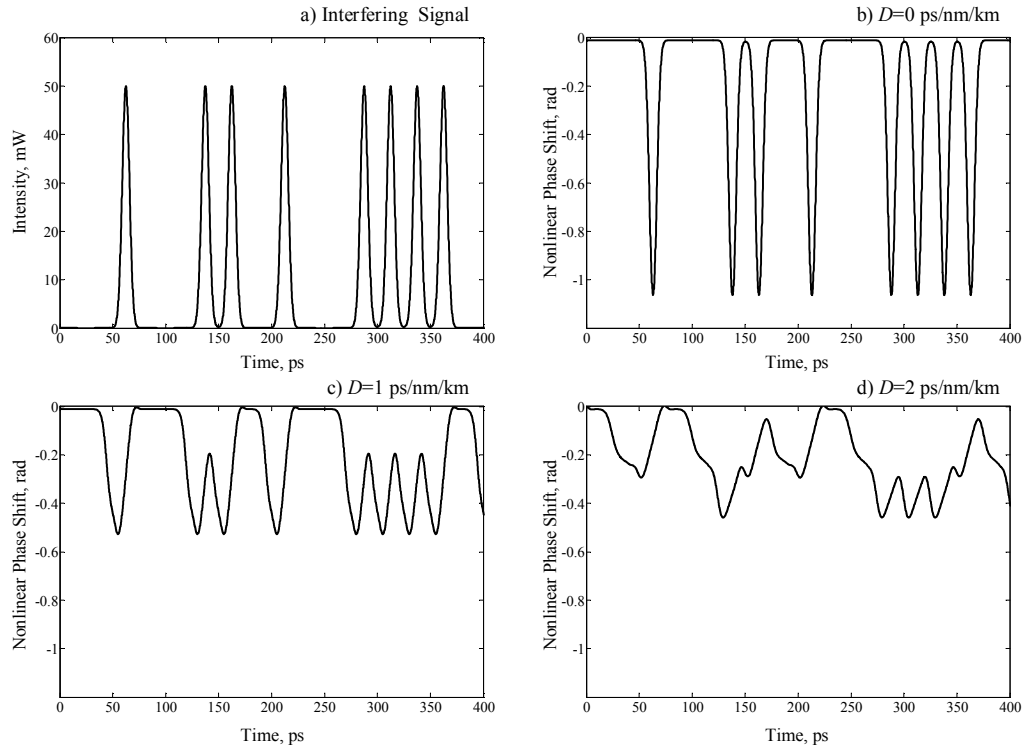

Fig. 4.1. Example of the impact of walkoff on the XPM. a) Instantaneous power of the interfering signal; b) XPM-induced phase shift, considering a fiber with a dispersion parameter of a) 0 ps/nm/km; b) 1 ps/nm/km; and c) 2 ps/nm/km.

The impact of walkoff on the XPM-induced phase shift is illustrated in Fig. 4.1-a) to -d), which present the nonlinear phase shift induced by a single interfering channel, transmitting a sequence of gaussian impulses with peak power of 50 mW, pulse-width of 8 ps at a rate of 40 Gb/s. The wavelength spacing between channels is 2 nm. The considered fiber presents a length of 10 km, nonlinearity coefficient of 1.37 $W^{-1}\cdot km^{-1}$ and dispersion parameters of 0 ps/nm/km, 1 ps/nm/km, and 2 ps/nm/km for Fig. 4.1-b), c), and d), respectively. Simulation of the propagation on the fiber was carried out using the split-step Fourier method (SSFM) [Agrawal, 1995] (see page 50). As shown in Fig. 4.1-b) for a dispersion parameter of 0 ps/nm/km, the XPM-induced phase shift corresponds directly to the intensity of the interfering channel. However, an increase of the dispersion parameter to 1 ps/nm/km is enough to significantly broaden the phase impulses. A further increase of the dispersion parameter to 2 ps/nm/km yields a strong distortion of the XPM-induced phase shift, leading to the loss of information. Note that (4.8) also neglects the impact of GVD and SPM on the XPM-induced phase shift. Analysis of this impact requires a significantly more complex analysis, which will be approached in Chapter 5.

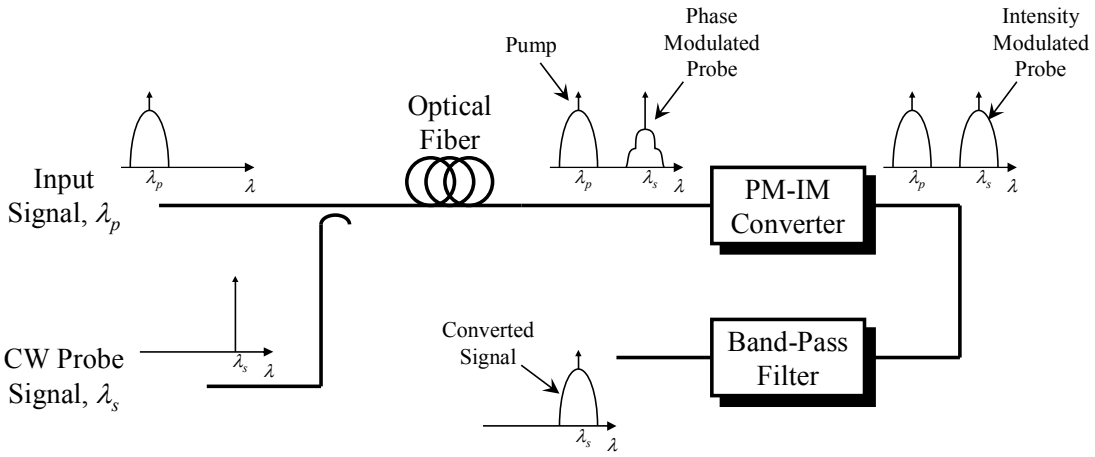

Fig. 4.2. General structure of a fiber XPM-based AOWC.

Fig. 4.2 presents the basic structure of an XPM-based AOWC. The original signal (pump), carries information by intensity modulation of an optical carrier at a wavelength λ_p. The pump is combined with a CW signal (probe) at a wavelength λ_s, and injected in an optical fiber. At the output of the optical fiber, the probe signal will be affected by SPM and XPM due to the pump signal. One may neglect the SPM-impact since this translates into a constant phase shift in the case of a CW probe. According to the approximation presented in (4.8) and assuming low walkoff and a short optical fiber, the XPM-induced phase shift of the probe will be proportional to the IM of the pump channel. As such, the XPM-based AOWC requires a PM-IM converting device, to translate the XPM-induced phase shift of the probe in IM. This can be performed using interferometric devices, such as NOLM [Yu, 2000: 1] or detuned optical filters [Öhlén, 2000]. In either case, the result for the PM-IM conversion is an IM probe, presumably with a replica of the information originally carried by the pump. To complete the AOWC, it may also be necessary to eliminate the pump using optical filtering. Note that, when using interferometric processes to perform PM-IM conversion, the actual structure of the AOWC will differ from the presented in Fig. 4.2, although it may generally be modeled in that form, as illustrated in [Jinno, 1992].

The effectiveness of fiber XPM-based AOWC depends mainly on two aspects: i) the characteristics of the fiber, and ii) the type of PM-IM converter. In the case of the fiber characteristics, it was shown above that a fiber XPM-based AOWC requires low walkoff parameter. This condition has been expressed by Bononi et al in [Bononi, 1998] through the cut-off frequency of the XPM-induced phase shift, B_{XPM}. This corresponds to the

highest frequency component of the pump signal IM which is effectively converted in PM of the probe channel. B_{XPM} is given by [Bononi, 1998]:

$$B_{XPM} = \frac{1}{2\pi \cdot \left| d_{sp} \right| L} \tag{4.11}$$

where d_{sp} is the walkoff between the probe and pump channels. This takes the same form as presented in (4.10) appropriately replacing the subscripts. From expression (4.11) it becomes clear that the most appropriate fibers for application in AOWC are dispersion shifted fibers (DSF). These fibers typically have a nearly null dispersion parameter at the wavelengths of interest in multi-wavelength transmission systems (~1550 nm), fulfilling the low walkoff condition. In fact, the use of DSF in wavelength converters has long been proposed in the literature. We may highlight the works by Blow et al. in [Blow, 1990] and Ohlén et al. in [Öhlén, 2000], in which the authors propose fiber XPM-based AOWC using DSF. In the first case, the authors use an interferometric loop whereas in the second case the authors propose the use of detuned filtering to perform PM-IM conversion.

The development of highly nonlinear-dispersion shifted fibers (HN-DSF) with flattened dispersion has allowed a significant improvement of the characteristics of fiber XPM-based AOWC. These fibers typically have a nonlinearity coefficient increased by a factor ranging from 5 to 10 in comparison to conventional DSF [Onishi, 1997]. According to (4.7), this allows a reduction of the pump power or fiber length by the same proportion to achieve similar nonlinear induced phase shift. Normally, the reduction of the fiber length is more beneficial, given the proportional increase of the XPM cut-off frequency, with the detriment of reducing the magnitude of the XPM-induced nonlinear phase shift. The use of distributed Raman amplification been proposed Wang et al. in [Wang, 2005], to maintain high pump and probe powers along the nonlinear fiber and reinforce the XPM-induced nonlinear phase shift. This technique has allowed a significant decrease of the required pump power with relatively short lengths of HN-DSF. Recently, new types of optical fibers have been proposed, with remarkably high nonlinearity coefficients. A noteworthy example is the development of Bismuth oxide-based fiber (BOF) [Sugimoto, 2004]. These fibers have nonlinearity coefficients nearly 500 times larger than conventional DSF. This allows a reduction of the required fiber length to values of the

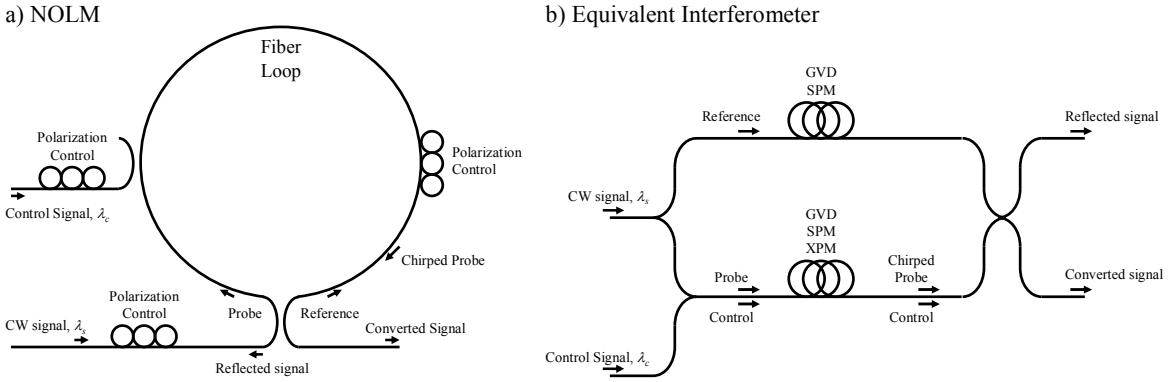

Fig. 4.3. General structure of a fiber NOLM wavelength converter. a) Implementation; b) equivalent interferometric structure [Jinno, 1992].

order of 1 m [Sugimoto, 2004], providing the possibility of integration in scales that are competitive with nonlinear semiconductor devices. As an example, a fiber XPM-based AOWC operating at 160 Gb/s and using a BOF with a length of 1 m has been successfully demonstrated by Lee et al. in [Lee, 2005: 1] and [Lee, 2005: 3]. Note that although the decrease of the fiber length seems beneficial, these fibers have a very short interaction length between the pump and probe channels hence require very high power levels to operate effectively [Lee, 2005: 1].

Regarding the type of PM-IM converter, one may find two main alternatives in the literature: NOLM or detuned filters. The NOLM was first proposed by Doran, et al. in [Doran, 1988], and in a two wavelength operation mode [Blow, 1990]. Fig. 4.3-a) presents the typical structure of a NOLM used for wavelength conversion. In this system, a CW signal at a wavelength λ_s is injected in both directions of a fiber loop, using a polarization maintaining coupler. We will designate the component propagating in the counter-clockwise and clockwise directions simply as probe and reference signals, respectively with the complex envelopes $u_s(t)$ and $u_{ref}(t)$. The input signal carrying information encoded in its intensity, $P_p(t)$, is also injected in the fiber loop in the counter-clockwise propagation direction through a polarization maintaining coupler. This signal corresponds to the pump signal in Fig. 4.2. However, will be referred here as control signal, following the nomenclature in [Blow, 1990]. Polarization controllers may be used at the control signal and CW signal input ports, and within the fiber loop, to adjust the relative polarizations of the signals. The principle of the NOLM lies in the nonlinear interference of the control signal with the co-propagating probe signal, assuming that the nonlinear interference of the

control signal with the counter-propagating reference signal is negligible. To model the NOLM, consider the analogy proposed by Jinno, in [Jinno, 1992]. This analogy considers the NOLM as an equivalent interferometer as illustrated in Fig. 4.3-b). Each arm of the equivalent interferometer contains a fiber segment with a length corresponding to the loop length. The CW signal is injected in both arms of the interferometer, originating the probe and reference signals. The control signal is injected only in the arm of the interferometer which is carrying the probe signal. As such, the model by Jinno neglects the nonlinear interaction of the control signal with the reference signal, which has been shown to provide a reasonable approximation of the nonlinear phenomena in NOLM [Jinno, 1992]. Note that a direct implementation of the interferometer scheme would be difficult to achieve due to the long length of the interferometer arms. This length would exceed the coherence length of the laser used to generate the CW signal leading to a random phase noise difference between the probe and reference signal, which along with random fluctuations of the probe and reference polarization due to PMD in the fibers would degrade the output signal. However, the use of SOA in an interferometric structure for the purpose of wavelength conversion has been extensively studied in recent years [Leuthold, 1999]. As such, the interferometer analogy will be considered here to model the operation of the corresponding NOLM, assuming that the propagation conditions in the fibers of the upper and lower arms are identical.

In the aforementioned conditions, we may approximate the complex envelopes of the probe and reference signals at the output of the fibers in the lower and upper arms of the interferometer as $u_s(t\text{-}L/v_{gs})\cdot\exp[j\phi_{SPM}+j\phi_{XPM}(t)]$ and $j\cdot u_{ref}(t\text{-}L/v_{gs})\cdot\exp[j\phi_{SPM}]$, respectively, where ϕ_{SPM} is the SPM-induced phase shift, assumed constant and L is the loop length. The term $\phi_{XPM}(t)$ is the time varying XPM-induced phase shift, resulting from the nonlinear interference of the probe signal with the control signal in the lower arm of the interferometer, given by (4.8) and the $\pi/2$ phase shift in the reference signal waveform results from the characteristic of the coupler. These waveforms neglect the impact of GVD in the fiber loop, assuming that the wavelength of the CW signal is near the zero dispersion wavelength. Including the GVD impact requires a significantly more complex analysis, which is presented in Chapter 5. Given the complex envelopes of the probe and reference signals the complex envelope of the reflected signal at the upper output arm of the interferometer is given by:

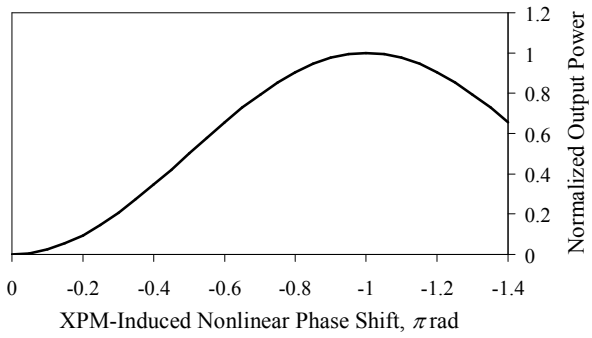

Fig. 4.4. Relation between the power at the output of a NOLM, normalized to the power of the CW signal, and the XPM-induced phase shift, normalized to π. The x-axis has been reversed to facilitate interpretation.

$$u_{refl}(t) = j\sqrt{P_{CW}}\,\frac{e^{j\phi_{SPM}}}{2}\cdot\left[e^{\phi_{XPM}(t)}+1\right] \tag{4.12}$$

where P_{CW} is the average power of the CW signal. Similarly to (4.12), one may write the complex envelope of the converted signal at the lower output arm of the interferometer as:

$$u_{out}(t) = \sqrt{P_{CW}}\,\frac{e^{j\phi_{SPM}}}{2}\cdot\left[e^{\phi_{XPM}(t)}-1\right] \tag{4.13}$$

Taking the square module of $u_{out}(t)$ from (4.13), the instantaneous power of the converted signal may be written as [Kolleck, 1997]:

$$P_{out}(t) = P_{CW}\cdot\sin^2\left[\phi_{XPM}(t)\right] \tag{4.14}$$

Expression (4.14) shows that the instantaneous power at the NOLM output is directly related with the XPM-induced phase shift, and consequently, with the instantaneous power of the control signal. However, this relation is nonlinear, as illustrated in Fig. 4.4. As such, one may conclude that the waveforms and spectrums of the signals at the input and output of the NOLM are distinct. To illustrate this effect, Fig. 4.5-a) and -b) presents simulated examples of the spectrums of the probe and control signals at the input of the fiber in the lower arm of the interferometer and the spectrum of the converted signal at the output of the NOLM, respectively. For this purpose, the control signal is a sequence of RZ Gaussian

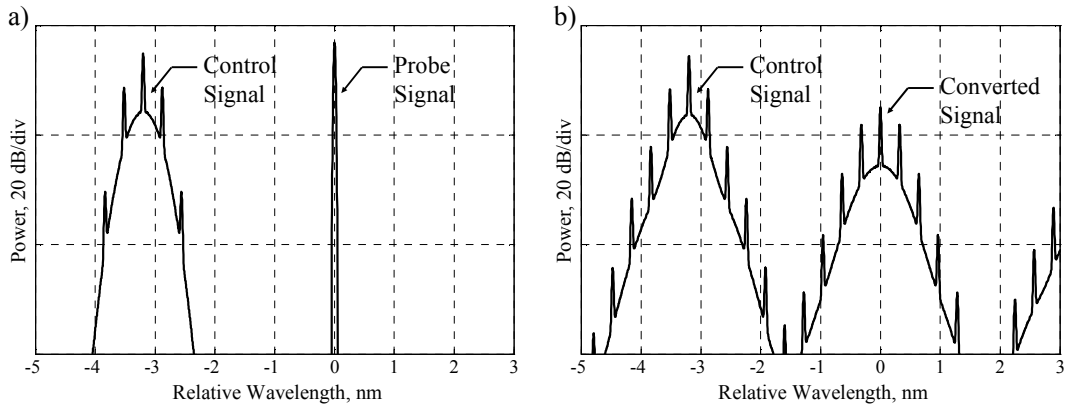

Fig. 4.5. Power spectrums of the optical signal at the input of the fiber in the lower arm of an interferometric structure equivalent to a NOLM (a) and the output of a NOLM (b).

impulses with a pulse-width of 8 ps, defined here at half maximum, and peak power of 62.8 mW, at a bit-rate of 40 Gb/s. The simulated fiber is a 10 km DSF with nonlinearity coefficient of 2.5 $W^{-1}\cdot km^{-1}$ and attenuation parameter of 0.25 dB/km. The CW signal wavelength is coincident with the zero dispersion wavelength of the fiber and the control signal is positioned 3.2 nm (~400 GHz) below. As shown, the spectrum of the converted signal is broader than the spectrum of the control signal at the fiber input. This results from SPM in the fiber but also from the nonlinear PM-IM conversion. The impact of the latter may be observed in the eye diagrams of the control and converted signals presented in Fig. 4.6. It is shown that, the nonlinear PM-IM conversion characteristic of a NOLM may be used to compress the XPM-induced phase impulses, to achieve a full-width at half maximum (FWHM) lower than the input impulses. This aspect is explored in Chapter 5 to derive rules for the design of NOLM based wavelength converters.

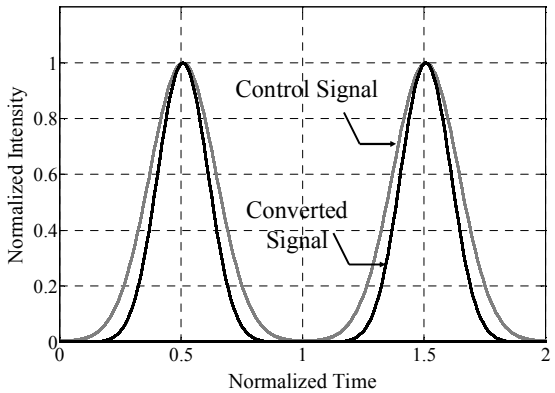

Fig. 4.6. Comparison between the eye patterns of the control signal at the input of a NOLM (gray) and the corresponding converted signal (black).

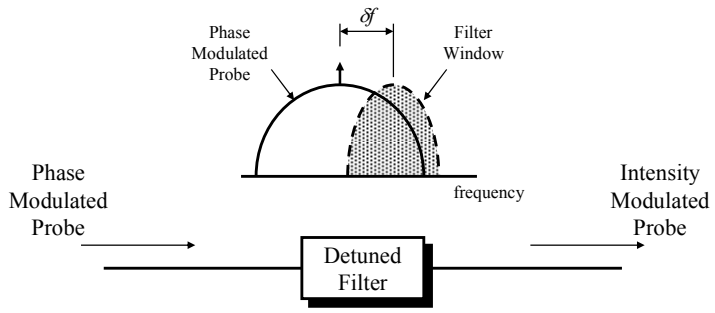

Fig. 4.7. Principle of the PM-IM converter based on a detuned filter.

The alternative to NOLM wavelength converters is the use of PM-IM conversion with detuned filters as first proposed by Öhlén and Olsson in two works [Öhlén, 2000], and [Olsson, 2000]. This type of converter takes advantage of the dynamic XPM-induced frequency shift of the probe channel, $\Delta f_{XPM}(t)$, given by:

$$\Delta f_{XPM}(t) = -\frac{1}{2\pi}\frac{d\phi_s(t)}{dt} \tag{4.15}$$

This is performed setting a band-pass filter with bandwidth B_{oc}, centered at an offset frequency, δf, from the average central frequency of the probe channel, as illustrated in Fig. 4.7. Considering $H_o(f)$ as the low-pass equivalent transfer function of the detuned filter, defined with respect to the central frequency of the probe channel, and $h_o(t)$ as the corresponding impulse response, the power at the detuned filter output is given by:

$$P_{out}(t) = \left|\sqrt{P_{CW}} \cdot \exp\left[j\phi_s(t)\right] * h_o(t)\right|^2 \tag{4.16}$$

where * represents the convolution operation, and $\sqrt{P_{CW}} \cdot \exp\left[j\phi_s(t)\right]$ is an approximation of the phase modulated probe signal with P_{CW} as the average probe power. Note that (4.16) generally does not have a closed form and allows little insight on the characteristics of the signal at the detuned filter output. An alternative, yet simple interpretation of the PM-IM conversion phenomena may be performed with the quasi-static approximation used in RF communications to characterize wideband frequency modulation (FM) signals [Carlson, 1986] (see page 247). This approximation assumes that the XPM-induced dynamic

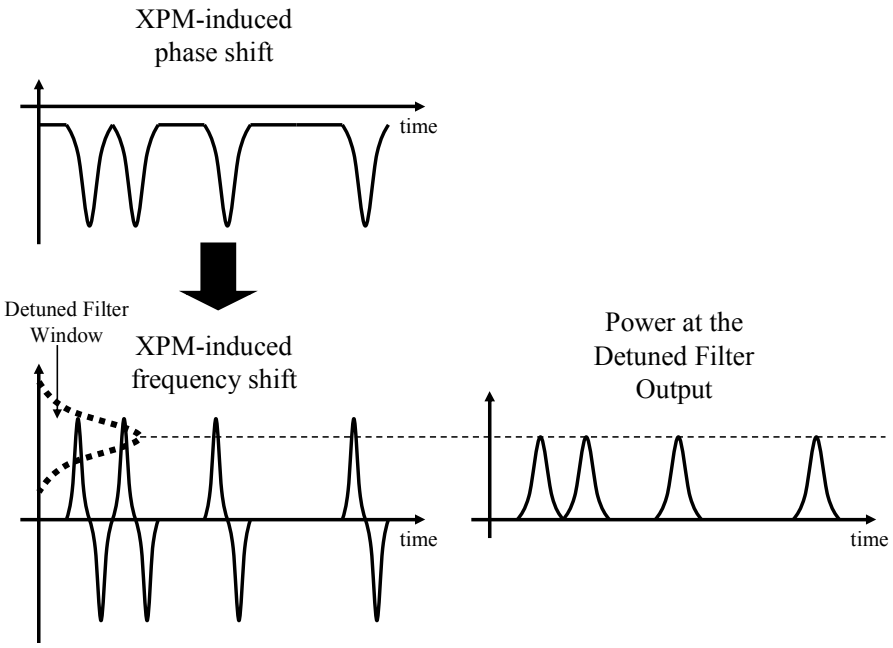

Fig. 4.8. Principle of the simplified model for the characterization of AOWC using detuned filters for PM-IM conversion.

frequency shift varies slowly when compared with the fluctuations of the probe channel. If so, one may assume that the probe light only travels through the detuned filter when the dynamic XPM-induced frequency shift places the probe signal within the filter window, as illustrated in Fig. 4.8. Within the limits of this model, the power at the detuned filter output is approximated by:

$$P_{out}(t) \approx P_{CW} \cdot \left| H_o\left[\Delta f_{XPM}(t)\right] \right|^2 \tag{4.17}$$

Expression (4.17) and Fig. 4.8 show that the variations of the instantaneous frequency of the probe generate power impulses which are related with the impulses of the original signal at the AOWC input. However, it is required that the input signal presents a nonzero derivative at each symbol, which is the case of RZ signals. In the case of NRZ signals at the input of the AOWC, the output signal only presents power impulses when the input signal switches symbols. The wideband FM approximation in (4.17) has a limited validity since the bandwidth of the probe channel in an XPM-based wavelength converter is always comparable to the bandwidth of the dynamic XPM-induced frequency shift. To evaluate this approximation, consider an example of the detuned filtering of a single Gaussian phase

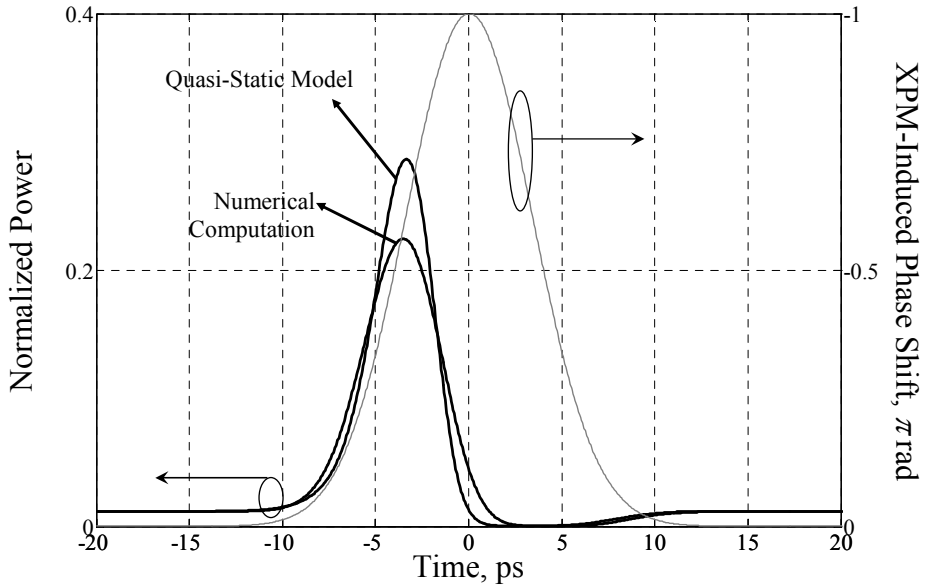

Fig. 4.9. Comparison of the XPM-induced phase impulse with the intensity impulse at the output of the detuned filter. The latter is computed using numerical computation and the proposed quasi-static model.

impulse with a FWHM of 8 ps and amplitude of π rad. The detuned filter is also Gaussian, with B_{oc}=150 GHz and δf=200 GHz. Fig. 4.9 presents traces of the phase impulse and resulting power impulse at the detuned filter output, computed using (4.16) and (4.17). It is shown that (4.17) overestimates significantly the peak power of the output impulses. To the author's knowledge, an expedite way to compute the peak power of the output impulses has not yet been presented in the literature and the optimization of the detuned filter characteristics has been carried out through extensive simulation or experiment [Perlin, 2002]. However, the approximation in (4.17) provides a simple estimate of the power of the space symbols, given by $P_{CW} \cdot H_o(0)$, and allows some insight on the required settings of the detuned filter for an effective PM-IM conversion.

4.2.2. AOWC Based on Fiber FWM

Similarly to SPM and XPM, FWM arises in optical fibers as a consequence of the third order susceptibility of optical fibers to the presence of intense optical fields. In FWM interactions, three signals at arbitrary optical frequencies, υ_m, υ_n, and υ_p, generate a fourth signal at a distinct optical frequency $\upsilon_{mnp}=\upsilon_m+\upsilon_n-\upsilon_p$. The new signal is often referred as the anti-stokes wave or idler [Agrawal, 1995] (see page 407). This process has shown great potential for wavelength conversion at ultra-high bit-rates using arbitrary modulation formats [Inoue, 1992: 1].

To address the FWM phenomena in optical fibers, consider the propagation of three signals injected in an optical fiber with average powers $\overline{P}_m$, $\overline{P}_n$ and $\overline{P}_p$. The power of the FWM-generated light at the fiber output may be approximated by [Inoue, 1992: 1]:

$$\overline{P}_{FWM} = \frac{1024\pi^6}{n_0^4 \lambda^2 c^2} d_F^2 \cdot \overline{P}_m \cdot \overline{P}_n \cdot \overline{P}_p \cdot e^{-\alpha L} \cdot L_{eff}^2 \cdot \eta_{mnp} \tag{4.18}$$

where λ is the operation wavelength and d_F is the degeneracy factor, which takes the values d_F=3, in a partially degenerate case when m=p; and d_F=6 in the non-degenerate case, when $m \neq p$ [Inoue, 1995]. The term η_{mnp} is the FWM efficiency, given by:

$$\eta_{mnp} = \frac{\alpha^2}{\alpha^2 + \Delta\beta_{mnp}^2} \left\{ 1 + \frac{4e^{-\alpha L} \sin^2\left(\Delta\beta L/2\right)}{\left[1 - \exp\left(-\alpha L\right)\right]^2} \right\} \tag{4.19}$$

assuming that the original signals are co-polarized. The term $\Delta\beta_{mnp}$ is the phase mismatch between the propagation constants of the original signals, β_m, β_n, and β_p, and the FWM-generated signal, β_{mnp}, given by:

$$\Delta\beta_{mnp} = \beta_m - \beta_n + \beta_p - \beta_{mnp} \tag{4.20}$$

Expression (4.18) shows that the power of the FWM-generated signal is maximized when $\Delta\beta$ is null, leading to unitary η_{mnp}. As such, expanding the propagation constants in (4.20) around the zero dispersion frequency, $\upsilon_o = c/\lambda_o$, allows rewriting it as [Inoue, 1992: 2]:

$$\Delta\beta_{mnp} = -\frac{\pi\lambda^4}{c^2} \cdot S\left[\left(\upsilon_m - \upsilon_o\right) + \left(\upsilon_p - \upsilon_o\right)\right] \cdot \left(\upsilon_m - \upsilon_n\right) \cdot \left(\upsilon_p - \upsilon_n\right) \tag{4.21}$$

Equation (4.21) shows that the phase matching condition ($\Delta\beta$=0) may be reached when the zero dispersion frequency is set between the frequencies υ_m and υ_p, i. e. $\upsilon_m - \upsilon_o = \upsilon_o - \upsilon_p$ [Inoue, 1992: 2]. In these conditions, the FWM-generated signal will be

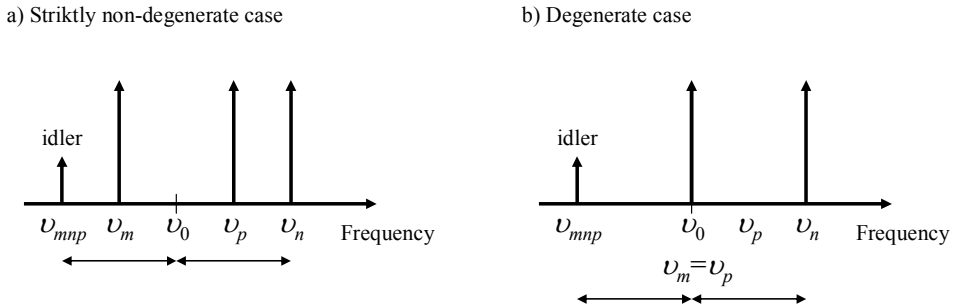

Fig. 4.10. Schematic representation of the waves generated by FWM in optical fibers. a) Non-degenerate case; b) partially degenerate case.

positioned at a frequency $\upsilon_{mnp}=\upsilon_m-\upsilon_n+\upsilon_p=2\upsilon_o-\upsilon_k$, i. e. symmetric to υ_k with respect to υ_o, as illustrated in Fig. 4.10-a). A more interesting case of FWM for wavelength conversion arises in the partially degenerate case, when $m=p$. In these conditions, $\Delta\beta_{mnp}$ may be rewritten as [Inoue, 1992: 1]:

$$\Delta\beta_{mnp} = -\frac{\lambda^4\pi}{c^2}\cdot 2S\left(\upsilon_m-\upsilon_n\right)^2\left(\upsilon_m-\upsilon_0\right) \tag{4.22}$$

Expression (4.22) shows that the phase matching condition may be reached by setting $\upsilon_m=\upsilon_o$, as illustrated in Fig. 4.10-b).

The application of FWM for wavelength conversion is carried out by injecting a CW pump and a modulated signal at the optical frequencies υ_{pump} and υ_{signal}, as illustrated in Fig. 4.11. This will lead to the generation two primary idler waves at the optical frequencies $\upsilon_{conv}=2\cdot\upsilon_{pump}-\upsilon_{signal}$ and $\upsilon_{reg}=2\cdot\upsilon_{signal}-\upsilon_{pump}$. In this case, it becomes useful to approximate the complex envelopes of the FWM-generated signals as [Inoue, 1995]:

$$u_{conv} = j\frac{(2\pi)^2}{n_0\lambda}d_F\cdot u_{pump}^2\cdot u_{signal}^*\cdot\exp\left[\left(-\frac{\alpha}{2}+j\beta_{conv}\right)L\right]\cdot \frac{1-\exp\left[\left(-\alpha+j\Delta\beta_{pump,signal}\right)L\right]}{\alpha-j\Delta\beta_{pump,signal}} \tag{4.23}$$

and

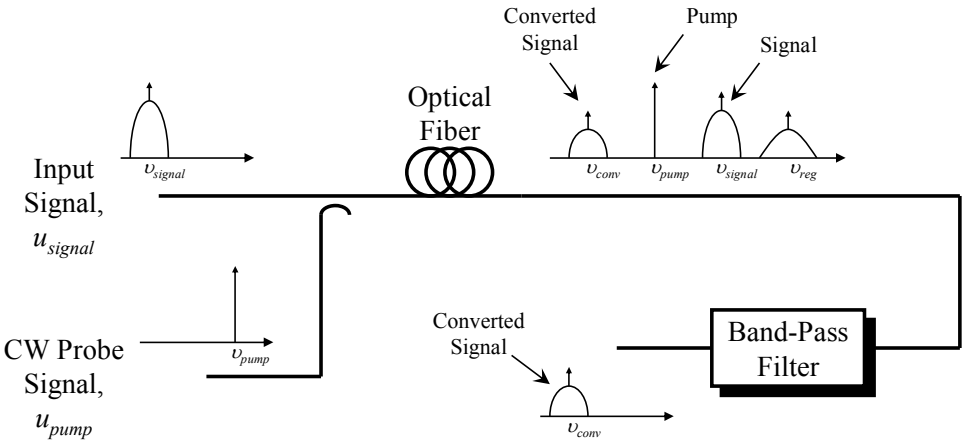

Fig. 4.11. General structure of a fiber FWM-based AOWC.

$$u_{reg} = j\frac{(2\pi)^2}{n_0\lambda} d_F \cdot u_{signal}^2 \cdot u_{pump}^* \cdot \exp\left[\left(-\frac{\alpha}{2} + j\beta_{reg}\right)L\right] \cdot \frac{1-\exp\left[\left(-\alpha + j\Delta\beta_{signal,pump}\right)L\right]}{\alpha - j\Delta\beta_{signal,pump}} \tag{4.24}$$

The terms u_{pump}, u_{signal}, u_{conv}, and u_{reg} are the complex envelopes of the waves corresponding to the pump, signal, and the two FWM-generated idlers at the frequencies υ_{conv} and υ_{reg}, respectively. β_{conv} and β_{reg} are the propagation constants for the corresponding idler waves and $\Delta\beta_{pump,signal}$ and $\Delta\beta_{signal,pump}$ are the phase mismatch, obtained by appropriately replacing the subscripts in (4.22). Note that expressions (4.23) and (4.24) neglect the impact of fiber nonlinearities other than FWM and do not account for GVD. Expression (4.24) shows that u_{reg} is proportional to the square of the complex envelope of the signal. As such, if the original signal is phase modulated, the information carried by the signal may no longer be recoverable. Alternatively, if the original signal is intensity modulated, the square operation may leave the information unaffected. In fact, the nonlinear characteristic of the FWM transfer may be used to regenerate an intensity modulated signal, as proposed by Ciaramella et al. in [Ciaramella, 2000]. On the other hand, (4.23) shows that u_{conv} is proportional to the conjugate of the complex envelope of the signal. As such, u_{conv} may be considered a converted signal, as long as the conjugation operation does not affect the information carried by the converted signal. As such, the typical fiber-FWM based AOWC uses an optical filter centered at υ_{conv} to select the

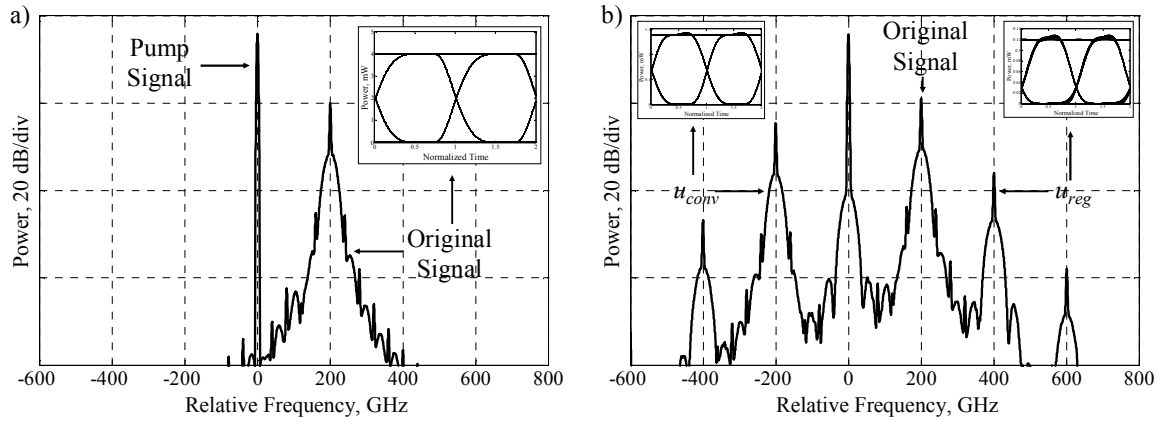

Fig. 4.12. Power spectrums of the optical field at the input (a) and output (b) of the fiber, in a FWM-based AOWC. The insets present eye diagrams of the original signal, u_{conv} and u_{reg}.

converted signal only. This is the principle of the wavelength conversion technique using fiber FWM proposed by Inoue et al. in [Inoue, 1992: 1]. In this reference, the authors demonstrated experimentally the conversion of a 622 Mb/s frequency shift keying (FSK) signal over a range of 7.6 nm, using a DSF with 10 km.

To illustrate the process of signal generation using FWM, consider the simulated transmission of a pump and probe signals spaced of 200 GHz, with average powers of 50 mW and 2 mW, respectively, in a 10 km DSF with nonlinearity coefficient of 2.5 $W^{-1}\cdot km^{-1}$. Fig. 4.12-a) presents the power spectrum of the signal at the fiber input. The inset of Fig. 4.12-a) presents an eye diagram of the original signal, generated as a 40 Gb/s NRZ deBruijn sequence of 2^{11} symbols. The pump is centered at the zero dispersion frequency of the fiber. Simulation of the fiber transmission was carried out using the SSFM. Fig. 4.12-b) presents the power spectrum at the DSF output. It is shown that the fiber gives rise to u_{conv} and u_{reg}, located 200 GHz below the pump and above the original signal, respectively. The insets of Fig. 4.12-b) present eye diagrams of u_{conv} and u_{reg}, which have been isolated using a 3rd order gaussian filter with a bandwidth of 120 GHz centered in the corresponding frequencies of these signals. Note that the eye diagram of u_{conv} is nearly identical to the eye diagram of the original signal, with a small degradation due to the optical filtering. Furthermore, the spectrum of u_{conv} corresponds to the spectrum of the original signal attenuated due to the limited FWM efficiency, and symmetric. In contrast, u_{reg} presents an eye diagram which is moderately distorted in comparison with the eye diagram of the original signal due to the squared characteristic of FWM. Additional FWM components also arise at the frequencies located 200 GHz below and above u_{reg} and u_{conv},

respectively, although the latter is not visible in the figure. This results from subsequent FWM of u_{conv} and u_{reg} with the signal and pump components.

Note that unlike XPM-based wavelength converters, FWM-based wavelength converters do not require a multi-stage approach, as the output of the nonlinear device already includes the converted signal. However, FWM-based AOWC do not allow an arbitrary choice of the wavelength of the converted signal. Instead, the wavelength of the converted signal depends on the relation between the pump and signal wavelengths. Furthermore, maximizing the FWM efficiency requires setting the pump wavelength at the zero dispersion wavelength of the fiber, which limits further the wavelength range of the AOWC. Despite these limitations, a large number of proposals for fiber FWM-based AOWC have been presented in the literature, from which we may highlight [Lee, 2003] and [Zhang, 2005]. In the first case, the authors proposed the use of highly nonlinear photonic crystal fibers with reduced lengths (15 m), to achieve wavelength conversion of intensity modulated 10 Gb/s signals over a range of 10 nm. In [Zhang, 2005], this range was significantly extended to 100 nm, covering the entire operating range of practical optical telecommunications systems. Wavelength conversion of signals at bit-rates of 40 Gb/s and 160 Gb/s has also been achieved in works by Lee et al. [Lee, 2005: 2] and [Lee, 2005: 3], respectively, using very short BOF. Other proposed applications involve multi-wavelength conversion, e. g. [Watanabe, 1998] for intensity modulated signals and [Devgan, 2006] for phase modulated signals. In these references, the authors propose the use of multiple signals and a single pump. This generates multiple idlers, corresponding to replicas of the original signals. Additional techniques for fiber FWM-based AOWC have been proposed using non-degenerate FWM. In this case, the wavelength converter may use two pumps, which allows, as an example, arbitrary choice of the signal and converted signal wavelengths [Tanemura, 2004].

4.3. Conclusions

This chapter has presented the basic concepts behind the operation of fiber-based AOWC. Particular focus has been given to fiber XPM-based AOWC where operation of NOLM has been described using a simplified model and neglecting the XPM frequency limitations. The operation of XPM-based AOWC using detuned filters for PM-IM conversion has also been approached, where a heuristic model to evaluate the relation

between the XPM-induced frequency shift and the characteristics of the detuned filter has been proposed. Finally, the basic principles of FWM-based AOWC have been described, addressing the main parameters that condition the efficiency of this type of wavelength converters.

Chapter 5. Effectiveness of Cross-Phase Modulation-Based Fiber Wavelength Converters

5.1. Introduction

AOWC have been considered as key elements in future wavelength or time division multiplexing optical networks [Yoo, 1996], [Chan, 1998]. Among the most promising wavelength converter configurations are fiber wavelength converters using XPM due to the fentosecond response of this phenomena [Agrawal, 1997]. As a consequence, a substantial research effort has been taken for the development of such systems. This chapter will be devoted to the study of the effectiveness of very high bit-rate wavelength converters using XPM. We begin by evaluating the frequency limitations of XPM in fibers commonly used for the purpose of wavelength conversion in section 5.2. This will be carried out by deriving a closed-form analytical model that relates the instantaneous power at the fiber input with the XPM-induced PM. The analytical model will be validated using numerical simulation for modulation frequencies in the terahertz range. Section 5.3 presents an application of the analytical model derived in section 5.2 for the design of wavelength converters based on NOLM. It will be shown that, XPM frequency limitations impact the required power at the wavelength converter input and impose limits on the maximum loop length. Closed-form approximate expressions for these quantities will be derived. Section

5.4 presents a study on the design of optical filters for the purpose of converting the XPM-induced PM at the fiber output in IM. It will be shown that an optimum hypothetical filter would allow a remarkable increase of the power at the wavelength converter output, without the need to amplify the probe signal. Since such filter is difficult to realize, a simplified version, referred in this work as a carrier phase-shifting filter (CPSF) is proposed and analyzed. The performances of fiber-wavelength converters using the CPSF and detuned filters is compared, showing the significant advantage of the prior with respect to output power and dispersion tolerance. Disadvantages of the CPSF regarding pattern dependent distortion are also analyzed. The work presented in this chapter has been partially published in [Luís, 2005: 4], [Luís, 2006: 1], [Luís, 2006: 3], and [Luís, 2007: 1].

5.2. XPM Cut-Off Frequency in Fiber Wavelength Converters

5.2.1. Principle

In fiber XPM-based AOWC, the output/input power efficiency can, in principle, be controlled by adjusting the probe signal power. Hence, the bandwidth of the wavelength converter becomes a dominant design parameter, strongly depending on the characteristics of the optical fiber used. To the author's knowledge, accurate analytical models to evaluate the bandwidth of the wavelength converter, for ultra-high bit-rate signals, have not been presented so far. In most cases, design rules for the dimensioning of XPM based AOWC are based on the impact of walkoff between channels, e. g. [Öhlén, 2000], [Perlin, 2002], and [Man, 1998], among others. Recently, [Herrera, 2005] proposed a more elaborate analytical model to obtain the small-signal XPM-characteristics in a HN-DSF, which is accurate for modulation frequencies up to 80 GHz. However, with the eminent deployment of 160 Gbit/s signals and very short pulses (less than 3 ps of FWHM) the level of accuracy must be significantly extended. This section presents a small-signal equivalent linear model to obtain the XPM-induced PM, improving previous models by including the impact of GVD and SPM. The proposed model is validated with numerical simulation and used to compare the XPM characteristics of a conventional DSF, a HN-DSF and also the recently developed ultra-highly nonlinear BOF [Sugimoto, 2004]. The XPM cut-off frequency is introduced as a design parameter and its relation with the maximum XPM-induced phase modulation is assessed.

5.2.2. Analytical Model for the XPM Cut-Off Frequency

A typical fiber XPM–based AOWC consists of an optical fiber, combined with a PM-IM converter. To obtain an equivalent linear model for the XPM in a fiber with length L, assume the co-polarized propagation of a continuous wave probe and an intensity modulated pump channels, at the group velocities v_{gs} and v_{gp}, respectively. The Fourier transform of the XPM-induced infinitesimal PM at a distance z from the fiber input is given by [Cartaxo, 1999:1]:

$$d\tilde{\phi}_{XPM}(z,\omega) = -2\gamma \cdot \tilde{P}_p(z,\omega) \cdot dz \tag{5.1}$$

where ω is the angular modulation frequency and γ is the fiber nonlinearity coefficient. The term $\tilde{P}_p(z,\omega)$ is the Fourier transform of the pump IM at a distance z from the fiber input, obtained using a small-signal approximation [Cartaxo, 1999:1]:

$$\tilde{P}_p(z,\omega) = \tilde{P}_p(0,\omega) \cdot \cos(qz) \cdot \exp\left(-\alpha z - j\omega z / v_{gp}\right) \tag{5.2}$$

The three terms on the right hand side of (5.2) correspond to the Fourier transform of the pump IM at the fiber input, the IM-IM conversion factor due to the impact of GVD on the pump channel, and the effect of attenuation and group delay of the pump channel due to the propagation along the fiber. $q = \omega^2 \cdot \lambda_p^2 \cdot D_p / (4\pi c)$, where D_p, c and α are the dispersion parameter at the pump wavelength, λ_p, the speed of light and the attenuation coefficient, respectively. The impact of SPM on the pump channel will be neglected in this work. The infinitesimal XPM-induced PM is converted by GVD and SPM in infinitesimal PM at the fiber, output given by [Cartaxo, 1999:1], [Luís, 2005: 1]:

$$\begin{aligned} d\tilde{\phi}_s(z,\omega) = d\tilde{\phi}_{XPM}(z,\omega) \cdot \left[C_{PM-PM,GVD}(z,\omega) + C_{PM-PM,SPM}(z,\omega) \right] \cdot \\ \exp\left[-j\omega (L-z) / v_{gs} \right] \end{aligned} \tag{5.3}$$

where the term $\exp[-j\omega(L-z)/v_{gs}]$ describes the propagation delay of the probe channel. The terms $C_{PM\text{-}PM,GVD}(z,\omega)$ and $C_{PM\text{-}PM,SPM}(z,\omega)$ are the PM-PM conversion factors from the z

coordinate to the end of the fiber, due to the impact of GVD and SPM, respectively given by [Cartaxo, 1999: 2]:

$$C_{PM-PM,GVD}(z,\omega)=\cos\left[b(L-z)\right] \tag{5.4}$$

$$\begin{aligned} C_{PM-PM,SPM}(z,\omega)&=\frac{2\cdot b\cdot\gamma\cdot\bar{P}_s(z)}{\alpha^2+b^2}\cdot \\ &\cdot\left\{\cos\left[2\theta-b(L-z)\right]-\sqrt{\alpha^2+b^2}\cdot\cos(\theta)\cdot(L-z)\cdot e^{-\alpha(L-z)}-\cos(2\theta)\cdot e^{-\alpha(L-z)}\right\}\end{aligned} \tag{5.5}$$

where $P_s(z) = \bar{P}_s(0)\cdot e^{-\alpha z}$ is the average power of the probe channel at the z coordinate of the fiber, respectively; $b=\omega^2\cdot\lambda_s^2\cdot D_s/(4\pi c)$ and θ = atan(b/α), where λ_s and D_s are the wavelength and dispersion parameter of the probe channel, respectively. The XPM-induced PM at the fiber output, represented here in the frequency domain, $\tilde{\phi}_s(\omega)$, results from integrating all the XPM-contributions along the fiber [Cartaxo, 1999:1], [Luís, 2005: 1]:

$$\tilde{\phi}_s(\omega)=\int_0^L d\tilde{\phi}_s(z,\omega)=H_{\phi,XPM}(\omega)\cdot P_p(0,\omega) \tag{5.6}$$

where $H_{\phi,XPM}(\omega) = H_{\phi,GVD}(\omega) + H_{\phi,SPM}(\omega)$ is the equivalent transfer function of the XPM-induced PM. Note that (5.6) allows an equivalent linear relation between the instantaneous power of the pump channel and the XPM-induced PM in the probe channel. The contributions $H_{\phi,GVD}(\omega)$ and $H_{\phi,SPM}(\omega)$ are the equivalent transfer functions for the XPM-induced PM, considering the impact of GVD and SPM on the PM-PM conversion, respectively. Solving the integral in (5.6) yields $H_{\phi,GVD}(\omega)$ and $H_{\phi,SPM}(\omega)$ as:

$$\begin{aligned} H_{\phi,GVD}(\omega)=&-\frac{\gamma}{a_{sp}^2+(b+q)^2}\left[a_{sp}\cdot\cos(bL)+(b+q)\cdot\sin(bL)-e^{-a_{sp}L}\left(a_{sp}\cdot\right.\right. \\ &\left.\left.\cos(qL)-(b+q)\cdot\sin(qL)\right)\right]-\frac{\gamma}{a_{sp}^2+(b-q)^2}\cdot\left[a_{sp}\cdot\cos(bL)+(b-q)\cdot\right. \\ &\left.\sin(bL)-e^{-a_{sp}L}\left(a_{sp}\cdot\cos(qL)+(b-q)\cdot\sin(qL)\right)\right]\end{aligned} \tag{5.7}$$

$$H_{\phi,SPM}(\omega) = -\frac{4b\cdot\gamma^2\cdot\overline{P}_s(0)}{\alpha^2+b^2}\cdot\left\{\frac{1}{\kappa_{sp}^2+b^2}\cdot\left[\kappa_{sp}\cdot\cos(bL-2\theta)+b\cdot\sin(bL-2\theta)-\right.\right.$$
$$\left.e^{-\kappa_{sp}L}\cdot\left(\kappa_{sp}\cdot\cos(2\theta)-b\cdot\sin(2\theta)\right)\right]-e^{-\alpha L}\cdot\left[\cos(2\theta)\cdot\frac{1-e^{-a_{sp}L}}{a_{sp}}-\right. \quad (5.8)$$
$$\left.\left.\sqrt{\alpha^2+b^2}\cdot\cos(\theta)\cdot\frac{1-e^{-a_{sp}L}-a_{sp}L}{a_{sp}^2}\right]\right\}$$

where $a_{sp} = \alpha\text{-}j\omega d_{sp}$ and $\kappa_{sp} = 2\alpha\text{-}j\omega d_{sp}$. The term $d_{sp} = v_{gs}^{-1} - v_{gp}^{-1}$ is the walkoff parameter, which may be approximated by $d_{sp} \approx D_s\cdot(\lambda_s\text{-}\lambda_p)\text{-}(\lambda_s\text{-}\lambda_p)^2\cdot S/2$. The term S is the dispersion slope parameter.

To investigate numerically the validity of (5.6), consider that the pump channel is intensity modulated by a sinusoidal signal, superimposed on a constant power level. By changing the pump modulation frequency, it is possible to determine the frequency response of the probe channel's XPM-induced PM. We define the normalized PM index as the ratio between the amplitudes of the XPM-induced PM and the pump IM at the fiber input, $PM(\omega) = |H_{\phi,GVD}(\omega)+H_{\phi,SPM}(\omega)|$ [Luís, 2005: 1].

Fig. 5.1-a), -b) and -c) present the PM index calculated for a conventional DSF, a HN-DSF and a BOF. The fiber lengths indicated in Fig. 5.1 where chosen to provide maximum PM-index values of 1, 2 and 4 rad/W with all fiber types. Table 5.1 provides the relevant fiber parameters. The probe and pump channels are transmitted with average powers of 10 mW, at the wavelengths λ_s = 1545 nm and λ_p = 1555 nm. Note that, for the DSF and HN-DSF, both channels are located symmetrically with respect to the zero dispersion wavelength of 1550 nm, minimizing the walkoff. The analytical results are compared with numerical simulation results, obtained by solving the coupled nonlinear Schrödinger equations with the SSFM. For comparison purposes, Fig. 5.1 also presents the analytical results obtained when neglecting the impact of GVD and SPM, which correspond to the approach followed in previous works. These were calculated setting b = 0, q = 0 and $H_{\phi,SPM}(\omega) = 0$.

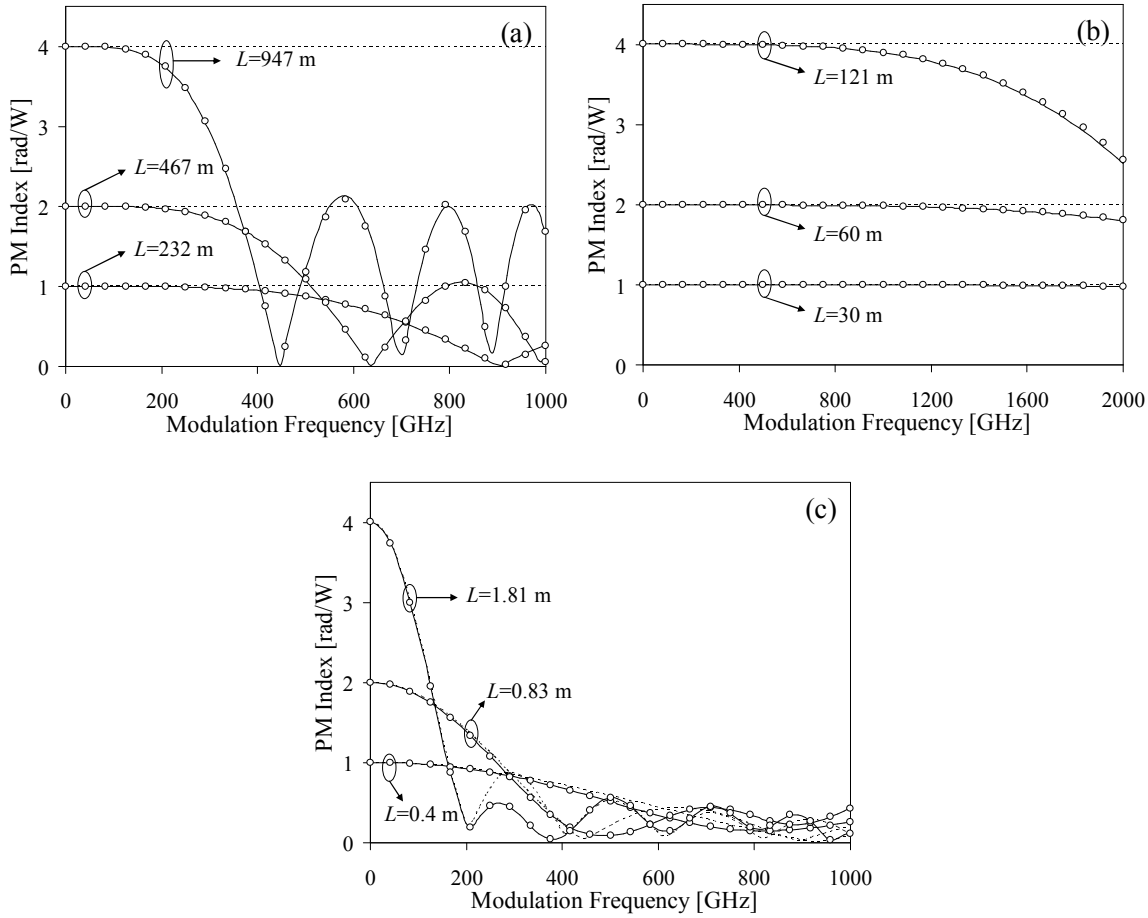

Fig. 5.1. Dependence of the PM index on the modulation frequency when using a) DSF, b) HN-DSF, and c) BOF. Circles – simulation results; continuous lines – analytical results using the proposed model; dashed lines – analytical results neglecting the impact of GVD and SPM.

Fig. 5.1 shows that, in all considered cases, the analytical results provide accurate estimates of the simulation results for low modulation frequencies. However, as the modulation frequency is increased, the analytical results neglecting the impact of GVD and SPM fail to accurately estimate the PM-index. This is most noticeable in the DSF and HN-DSF, where the walkoff-impact has been minimized. In the case of the BOF, the high walkoff leads to a less relevant GVD- and SPM-impact, particularly at low modulation frequencies. In all considered cases, the analytical results obtained with the proposed model follow the simulation results accurately, validating its application for small signals.

Parameter	BOF	DSF	HN-DSF
Nonlinearity Coefficient, $W^{-1}\cdot km^{-1}$	1300	2.17	16.7
Dispersion Parameter, ps/nm/km	-270	0	0
Dispersion Slope, $fs/km/nm^2$	-20	85	18
Null Dispersion Wavelength, nm	1550	1550	-
Attenuation Coefficient, dB/km	800	0.25	0.72

Table 5.1. Fiber parameters at a wavelength of 1550 nm.

The results presented in Fig. 5.1 show that the behavior of the PM index resembles a low pass filter, as initially observed by Bononi et al. in [Bononi, 1998]. As such, we introduce the XPM cut-off frequency, B_{XPM}, such that $PM(2\pi \cdot B_{XPM}) = PM(0)/2$. This parameter is the highest frequency component of the input IM signal that is effectively converted in PM at the fiber output due to XPM. Note that B_{XPM} does not necessarily correspond to the AOWC-bandwidth (defined here as the maximum frequency component of the input IM signal that is effectively converted in IM at the AOWC output), due to the nonlinear characteristic of the PM-IM converter. Nevertheless, for small-signals, this characteristic can be linearized, in which case the XPM cut-off frequency coincides with the AOWC-bandwidth [Herrera, 2005]. Otherwise, the nonlinearity of the PM-IM converter will significantly affect the shape of the output signal and the XPM cut-off frequency can only be used as a reference limit for the input signal bandwidth. Note that, the most commonly proposed PM-IM converters are interferometers (e. g. nonlinear optical loop mirrors [Kolleck, 1997]) and detuned filters [Olsson, 2000], which have the ability to compress the XPM-induced phase impulses, producing output intensity impulses with shorter pulse-widths than the input impulses. In such cases, the XPM cut-off frequency can be considered as a worst-case limit for the AOWC-bandwidth and used in the design of such devices.

Fig. 5.2 shows the trade-off between maximum PM-index, given by $PM(0) = \left[1 - \exp(-\alpha L)\right] \cdot 2\gamma/\alpha$, and the XPM cut-off frequency when using the DSF, the HN-DSF and the BOF for the same conditions as in Fig. 5.1. As can be seen, the characteristic of XPM cut-off frequency versus maximum PM-index remains approximately linear, in the logarithmic scale. The BOF presents the most limiting

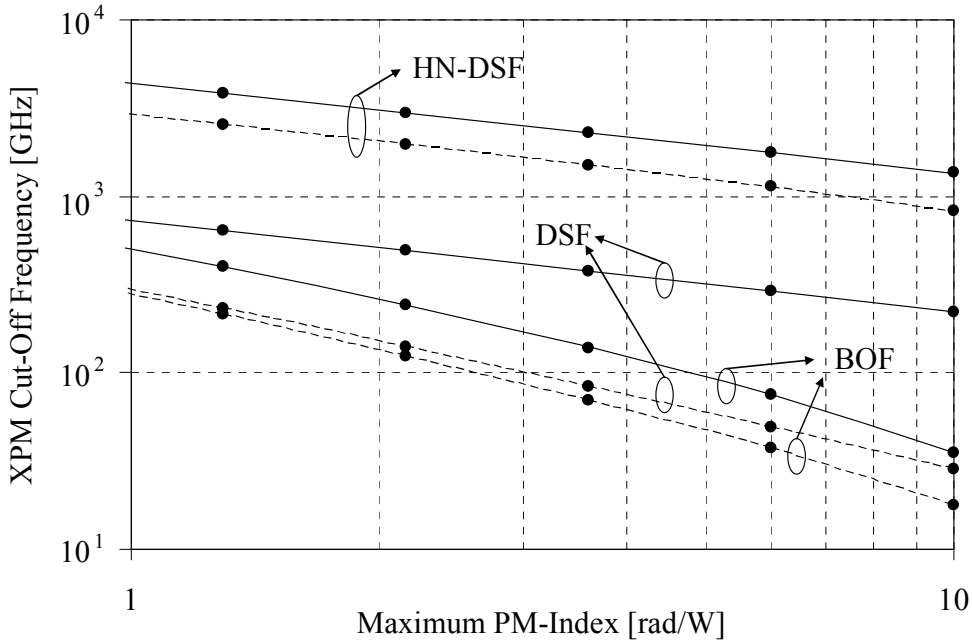

Fig. 5.2. Dependence of the XPM cut-off frequency on the maximum PM-index for various fiber types. Continuous lines – analytical results, considering λ_s=1545 nm and λ_p=1555 nm; dashed lines – analytical results, considering λ_s=1545 nm and λ_p=1565 nm; dots – simulation results.

characteristic, with an XPM cut-off frequency bellow 100 GHz for a maximum PM-index of 5 rad/W. The low dispersion parameters of the DSF and HN-DSF allow significantly higher XPM cut-off frequencies, remaining above the 100 GHz and 1 THz ranges, respectively.

Fig. 5.2 also presents the characteristic of XPM cut-off frequency versus maximum PM-index when shifting the pump wavelength by 10 nm. The result is a reduction of the XPM cut-off frequency in all considered cases. The strongest impact occurs in the DSF with XPM bandwidths bellow 100 GHz for a maximum PM-index above 3 rad/W. The low dispersion slope of the HN-DSF and BOF allows a less significant reduction of the XPM-bandwidth. In the presented example, numerical simulation results are used to validate the analytical results.

To complete the study presented in this section, consider the dependence of the XPM cut-off frequency on the probe wavelength for different values of the pump wavelength presented for the DSF, HN-DSF, and BOF in Fig. 5.3-a), b) and c), respectively. The presented results have been analytically computed and compared with numerical simulation results. From all cases presented in Fig. 5.3 it becomes evident that as the probe wavelength is located near the pump wavelength or positioned symmetrically

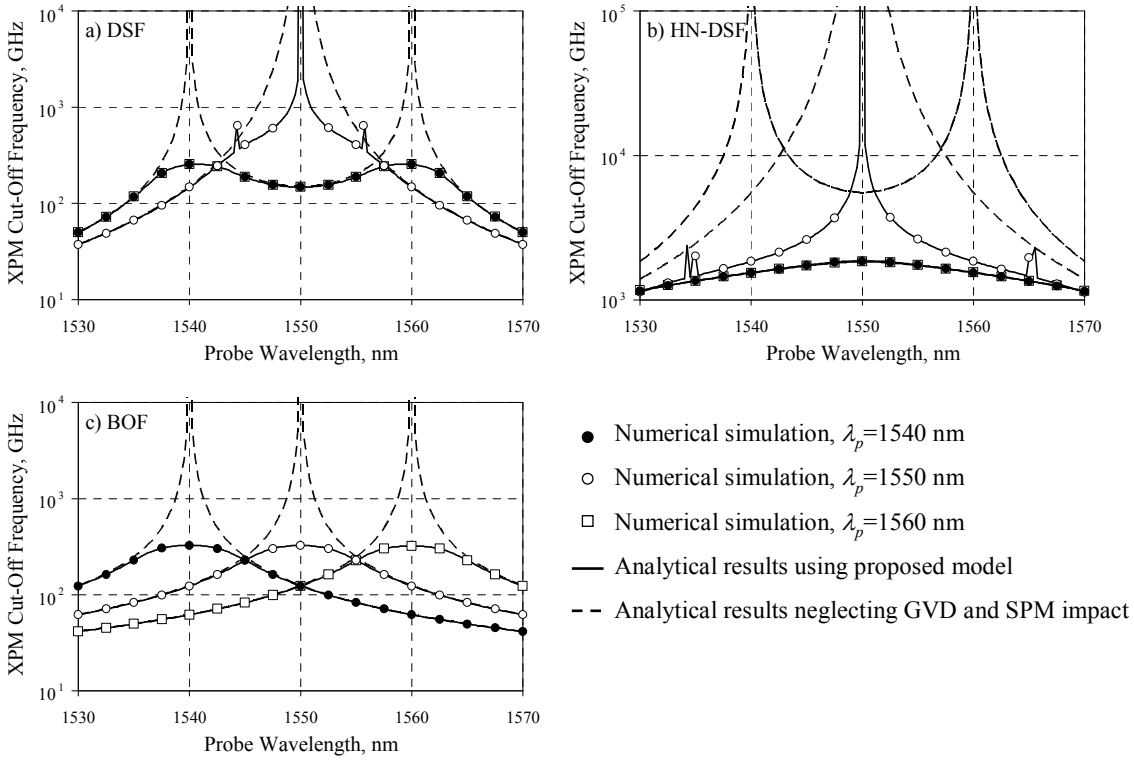

Fig. 5.3. Dependence of the XPM cut-off frequency on the probe wavelength for various values of the pump wavelength and fiber types.
a) DSF with a length of 947 m; b) HN-DSF with a length of 121 m; and c) BOF with a length of 1.81 m

around the zero dispersion wavelength, the walkoff between channels is reduced and consequently, the XPM bandwidth is increased. The latter case is particularly noticeable for the DSF and HN-DSF in Fig. 5.3-a) and b), respectively.

Note that the practical implementation of wavelength converters with the probe wavelength located near the pump wavelength may become difficult due to the need to separate the pump and probe signals. Nevertheless, some noteworthy configurations have been recently proposed to handle this limitation, from which we highlight [Tsuji, 2006]. The three presented examples show that, when neglecting the impact of GVD and SPM, the expected XPM cut-off frequency increases indefinitely as the walkoff is canceled. The actual XPM cut-off frequency, obtained using numerical simulation is well predicted using the proposed model and is generally finite, even when setting the probe wavelength in positions of null walkoff. A notable exception occurs when placing the pump and probe wavelengths precisely in the zero dispersion wavelength, as shown in Fig. 5.3-a) and b). This particular case shows limitless XPM cut-off frequency, both analytically and through numerical simulation, which corresponds to the limits of the proposed model and the

SSFM. A rigorous analysis would require considering alternative simulation methods [Agrawal, 1995]. Nevertheless, is of little interest for wavelength conversion and will not be addressed in this work. The spikes of the XPM cut-off frequency observed in Fig. 5.3-a) and b) for λ_p=1550 nm correspond to XPM resonances and are consistent with [Evangelides, 1999] and [Nelson, 1999].

Additionally, the results presented in Fig. 5.3-a) and b) show that the dependence of the XPM cut-off frequency on the probe wavelength, for pump wavelengths symmetrically positioned around the zero dispersion wavelength, are superimposed. This seems to indicate that the operation of the wavelength converter on the normal and anomalous dispersion regimes is similar in terms of the XPM cut-off frequency. However, one may note that this study is conducted for small signals with sinusoidal modulation. Hence this distinction does not apply. When using large signals, one may expect that the pump or probe signals enter a solitonic propagation regime, when positioned in an anomalous dispersion wavelength. As such, the pulse broadening induced by GVD is substantially reduced. This behavior has been reported in [Jinno, 1992], among many other works on wavelength conversion. Nevertheless, it is not predicted by the small-signals models used in this work.

5.3. Impact of XPM Frequency Limitations in Fiber NOLM-Based Wavelength Converters

5.3.1. Principle

Consider the simplified structure for a NOLM wavelength converter presented in Fig. 5.4, as first proposed by Doran, et al. in [Doran, 1988], and in a two wavelength operation mode [Blow, 1990]. A CW probe is injected through a polarization insensitive coupler in both directions of a fiber loop. A polarization controller is used to adjust the state of polarization of the signals in the loop. Without disturbances, the result of the interference between the probe components traveling in opposite directions of the loop will lead to cancellation of the power at the output port, with all the probe power reflected at the input port. A high power control signal is also injected in the fiber loop, propagating in only one of the directions. As such, the control signal will induce XPM on the probe component traveling in the same direction. Hence the interference of the probe components

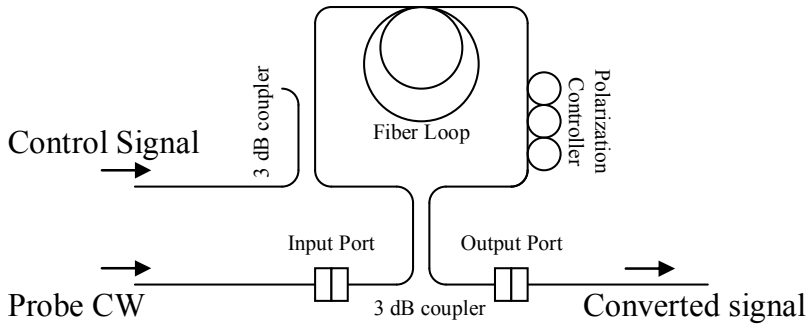

Fig. 5.4. Schematic diagram of the considered nonlinear optical loop mirror.

traveling in opposite directions of the loop will lead to the appearance of light impulses at the output port.

The XPM process is efficient, as long as the control channel and the co-propagating probe component travel together in the optical fiber. This is not always possible due to walkoff between channels [Jinno, 1992], [Man, 1998], and [Yu, 2001]. As such, the design of NOLM wavelength converters using fiber XPM has been based on minimizing the walkoff between the interfering channels, neglecting the impact of other effects such as GVD and SPM. This approximation is usually valid when using fibers with very low GVD. However, when signals with pulse-widths of tens of picoseconds or less are used, even the lowest amount of dispersion may already have significant impact on the output signal pulse-width and peak power [Yu, 2001]. This section presents a study of the impact of the XPM-frequency limitations on the design of NOLM wavelength converters. Approximate closed-form expressions will be derived to obtain the required XPM-bandwidth in order to achieve signal pulse-width maintenance, and validated using numerical simulation.

5.3.2. Design of Fiber NOLM Wavelength Converters Considering XPM-Frequency Limitations

Assuming ideal couplers, negligible counter-propagating XPM, and optimized polarization controller adjustment, the instantaneous power of the converted signal can be approximated by [Kolleck, 1997]:

$$P_{out}(t) = P_{CW} \cdot \sin^2\left[\phi_s(t)\right] \tag{5.9}$$

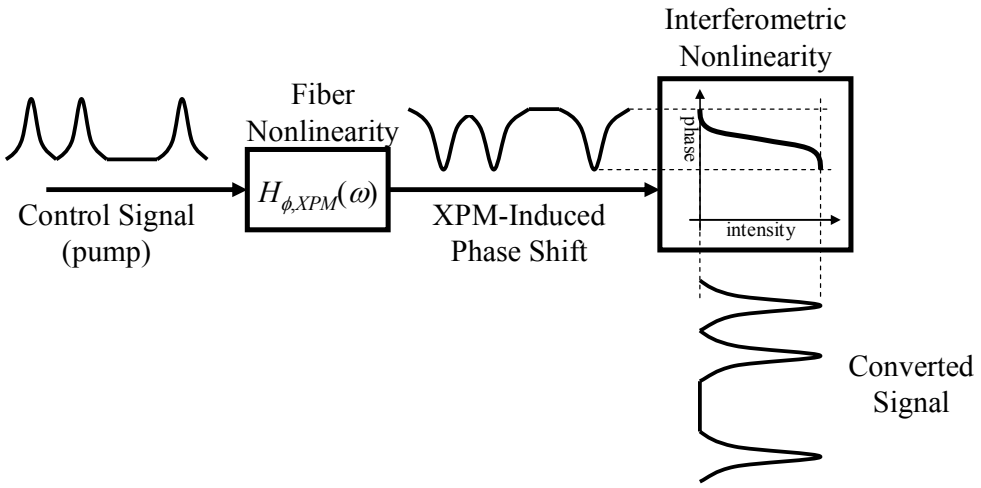

Fig. 5.5. Schematic representation of the model used to describe the operation of a NOLM wavelength converter.

where P_{CW} is the average power of the CW signal at the NOLM input and $\phi_s(t)$ is the XPM-induced PM. The latter is given by (5.6) in the frequency domain but will be used here in the time domain.

The operation of the NOLM wavelength converter will be modeled as schematically represented in Fig. 5.5. Given the waveform of the signal at the input of the NOLM control port, the XPM-induced phase shift will be computed using the model presented in sub-section 5.2.2. Afterwards, the waveform of the output signal will be obtained using (5.9). The considered design parameters of the NOLM are the fiber characteristics, in particular its length, which will determine the XPM cut-off frequency; and the power of the control signal, which will condition the maximum XPM-induced phase shift. The pulse-widths of the output and input impulses will be compared to define an optimization criteria. It will be assumed that the maximum tolerable pulse-width of the output impulses is identical to the pulse-width of the input impulses.

To the author's knowledge, a general closed-form analytical expression for the shape of the output impulses as a function of the shape of the input impulses it yet to be derived, given the inherent nonlinearity of (5.9) and the equivalent linear model for the XPM-induced phase shift. However, an approximate closed form analytical model of the NOLM may be achieved by assuming the input signal composed of Gaussian impulses, and approximating the transfer function of the equivalent linear model for the XPM-

induced PM also with a Gaussian response. As such, assume a Gaussian impulse injected on the control port with an instantaneous power given by:

$$P_p(t) = P_{peak} \cdot \exp\left[-4\ln(2) \cdot \frac{t^2}{\tau_{in}^2}\right] \tag{5.10}$$

where $P_p(t)$ is the control signal, in the time domain. The terms P_{peak} and τ_{in} are the peak power and pulse-width of the impulse, respectively. The -3 dB bandwidth of the power spectral density of the input signal is given by:

$$B_{in} = \frac{2 \cdot \ln(2)}{\pi \cdot \tau_{in}} \tag{5.11}$$

For the purpose of obtaining design rules for the NOLM, consider the transfer function of the XPM-induced PM, $H_{\phi,XPM}(f)$, approximated with a Gaussian filter with a XPM cut-off frequency, B_{XPM}, as:

$$H_{\phi,XPM}(f) \approx -PM(0) \cdot \exp\left[-\ln(2) \cdot \frac{f^2}{B_{XPM}^2}\right] \tag{5.12}$$

Note that the approximation of (5.12) neglects the asymmetric XPM-induced chirp, which would otherwise yield non-gaussian XPM-induced phase impulses [Jinno, 1992]. As such, its validity is limited to cases of low walkoff, generally consistent with ultra-fast wavelength converters. Using (5.10), and (5.12) yields a XPM-induced phase shift of the co-propagating probe signal as:

$$\phi_s(t) = -\pi \cdot \eta \cdot \exp\left[-4\ln(2) \cdot \frac{t^2}{\tau_{XPM}^2}\right] \tag{5.13}$$

where τ_{XPM} is the pulse-width of the XPM-induced phase impulse, given by:

$$\tau_{XPM}^2 = \tau_{in}^2 + \frac{4\ln(2)}{\pi^2 \cdot B_{XPM}^2} \tag{5.14}$$

and η is the switching efficiency, defined here as:

$$\eta = P_{peak} \cdot PM(0) \cdot \frac{B_{XPM} \cdot \tau_{in}}{\sqrt{\left(\pi^2 B_{XPM} \cdot \tau_{in}\right)^2 + 4\ln(2)}} = \frac{P_{peak} \cdot PM(0) \cdot \tau_{in}}{\pi \cdot \tau_{XPM}} \tag{5.15}$$

Setting $\eta = 1$ yields a full switch of the output signal, i. e. the peak power of the output impulse corresponds to P_{CW}. Note that the definition of switching efficiency used in this work differs from the commonly used definition proposed in [Man, 1998]. The latter relates the power at the output of the NOLM with and without power at the control port. Instead, (5.15) relates to the swing of the nonlinear characteristic of the interferometric process of the loop mirror. The advantage of the proposed approach is that it allows a clear distinction between the cases where, for a RZ input impulse, the output signal is a clear RZ impulse, i. e. $\eta \leq 1$, and the cases where the converted impulses split, becoming distorted, i. e. $\eta > 1$. Expression (5.14) shows that the pulse-width of the XPM-induced phase impulses will always be higher than the pulse-width of the input impulses due to the XPM frequency limitations. Replacing (5.13) in (5.9) provides the instantaneous power at the NOLM output as:

$$P_{out}(t) = P_{CW} \cdot \sin^2\left\{-\frac{\pi \cdot \eta}{2} \cdot \exp\left[-4\ln(2) \cdot \frac{t^2}{\tau_{XPM}^2}\right]\right\} \tag{5.16}$$

Note that when neglecting the XPM frequency limitations, i. e. $B_{XPM} \rightarrow \infty$, expression (5.16) is consistent with the models presented in [Yu, 2000: 1], [Jinno, 1992], and [Jinno, 1994]. Using (5.16), we obtain the pulse-width of the output impulse, τ_{out}, as:

$$\tau_{out}^2 = -\frac{\tau_{XPM}^2}{\ln(2)} \cdot \ln\left\{\frac{2}{\pi \cdot \eta} \cdot \arcsin\left[\frac{1}{\sqrt{2}} \cdot \sin\left(\frac{\pi \cdot \eta}{2}\right)\right]\right\} \tag{5.17}$$

Expression (5.17) shows that, for unitary efficiency ($\eta = 1$), the pulse-width of the output impulses is identical to the pulse-width of the XPM-induced phase impulses, $\tau_{out} = \tau_{XPM}$, which has been shown by (5.14) to exceed the pulse-width of the input impulses. These results show that the impact of the XPM frequency limitations prevent the fulfillment of the optimization criteria imposed initially. However, it is possible to dimension the NOLM to produce output impulses with similar pulse-width as the input impulses, as long as the switching efficiency is reduced. To estimate the required XPM cut-off frequency, $B_{XPM,req}$, and the required switching efficiency, η_{req}, in these conditions we replace (5.14) in (5.17) and set $\tau_{out} = \tau_{in}$, yielding:

$$\frac{B_{XPM,req}}{B_{in}} = \frac{1}{\sqrt{\ln(2)}} \cdot \sqrt{-\frac{\ln\left\{\frac{2}{\pi \cdot \eta_{req}} \cdot \arcsin\left[\frac{1}{\sqrt{2}} \cdot \sin\left(\frac{\pi \cdot \eta_{req}}{2}\right)\right]\right\}}{\ln\left\{\frac{4}{\pi \cdot \eta_{req}} \cdot \arcsin\left[\frac{1}{\sqrt{2}} \cdot \sin\left(\frac{\pi \cdot \eta_{req}}{2}\right)\right]\right\}}} \tag{5.18}$$

Note that, for simplicity, (5.18) may be empirically approximated by:

$$\frac{B_{XPM,req}}{B_{in}} \approx \frac{1}{\sqrt{\ln(2)}} \cdot \sqrt{\frac{1+\eta_{req}^{2.5}}{1-\eta_{req}^{2.5}}} \tag{5.19}$$

Fig. 5.6 presents the dependence of the required XPM cut-off frequency, normalized by the -3 dB bandwidth of the input signal, on the required switching efficiency. As shown the required XPM cut-off frequency always exceeds the cut-off frequency of the input signal, regardless of the switching efficiency. Dimensioning the NOLM with lower values of the XPM cut-off frequency or higher switching efficiency will lead to output impulses broader than the input impulses. In addition, setting a switching efficiency higher than 1 will generate output impulses that no longer retain the shape of RZ impulses, presenting significant distortion. Illustrative traces of the input and output impulses under the aforementioned conditions are presented inset Fig. 5.6.

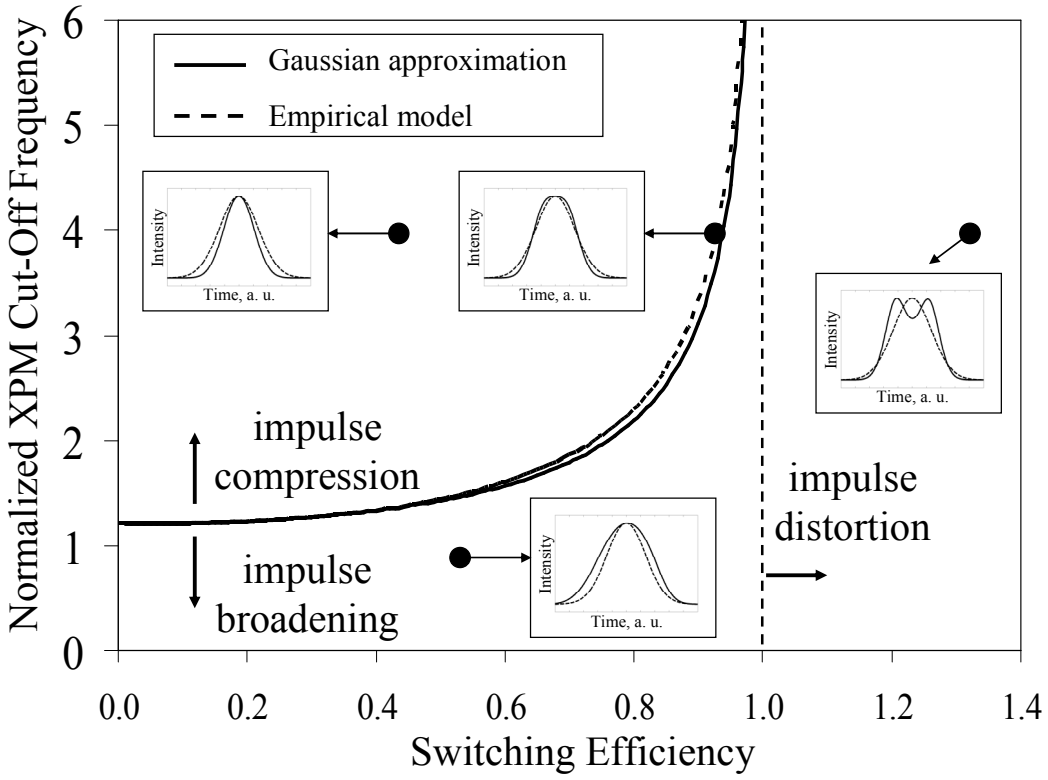

Fig. 5.6. Theoretical dependence of the required XPM cut-off frequency, normalized to the input signal 3 dB bandwidth, on the required switching efficiency to achieve an input pulse-width similar to the output pulse-width. Insets preset traces of the input impulse (dashed line) and output impulse (continuous line) in different operation points.

Fig. 5.6 also illustrates the previous observation that, with unitary switching efficiency the XPM frequency limitations prevent the maintenance of the pulse-width as the required XPM cut-off frequency increases indefinitely. This is consistent with the results presented by Man et al. in [Man, 1998]. However, it is introduced here in a formal and easily quantifiable form.

The empirical approximation presented in (5.19) is also shown in Fig. 5.6, allowing a reasonable estimate of the required normalized XPM cut-off frequency. Note that these results assume Gaussian impulses and a Gaussian XPM equivalent transfer function. As such, other impulse shapes and a more realistic modeling of the XPM will result in a distinct outcome. Nevertheless, they may be used to gain insight on the impact of the XPM-frequency limitations on the effectiveness of fiber NOLM-based wavelength converters.

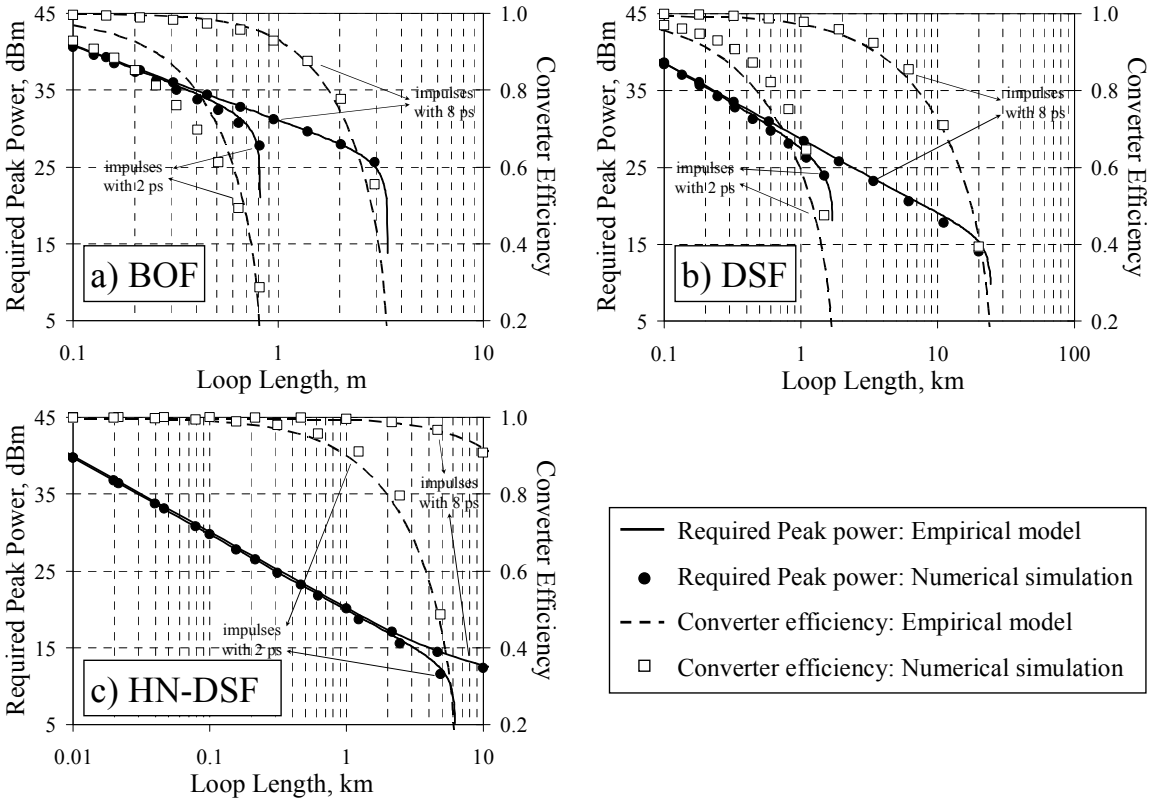

Fig. 5.7. Required input peak power at the input of a NOLM and corresponding switching efficiency, as a function of the fiber length to maintain the pulse-width of the converted impulses with different fiber types and assuming λ_s = 1545 nm and λ_p = 1555 nm. Input impulses with pulse-widths of 2 ps and 8 ps have been assumed. Considered fiber types a) BOF; b) DSF; c) HN-DSF.

To illustrate the application of (5.18) it will be assumed that the point of operation of the wavelength converter may be set by adjusting the peak power of the input impulses and the length of the NOLM, with the remaining system parameters fixed. To compute the required peak power of the input impulses as a function of the fiber length it is first necessary to calculate the corresponding XPM cut-off frequency using the model presented in section 5.2. Afterwards, expression (5.18) may be numerically inverted to obtain the required switching efficiency as a function of the previously determined XPM cut-off frequency. Finally, the required peak power of the input impulses may obtained from (5.15). A more direct approach can be achieved using the empirical approximation presented in (5.19). In this case, inverting (5.19) to obtain the required switching efficiency and replacing it in (5.15) yields:

Pulse-width	Maximum Loop Length			Loop Length for $\eta = 0.9$		
	BOF	DSF	HN-DSF	BOF	DSF	HN-DSF
8 ps	3.3 m	23 km	90 km	1.2 m	3.4 km	11.2 km
2 ps	0.8 m	1.6 km	6 km	0.2 m	0.2 km	1 km

Table 5.2. Maximum loop length and loop length corresponding to a switching efficiency of 0.9, for the implementation of a NOLM using different fiber types. These results were obtained analytically.

$$P_{peak,req} = \frac{2\sqrt{\ln(2)}}{PM(0)\cdot B_{XPM}\cdot \tau_{in}} \left(\frac{\pi^2 \tau_{in}^2 B_{XPM}^2}{4\ln(2)} - 1 \right)^{0.4} \cdot \left(\frac{\pi^2 \tau_{in}^2 B_{XPM}^2}{4\ln(2)} + 1 \right)^{0.1} \qquad (5.20)$$

Expression (5.20) provides a simple form to estimate the impact of the XPM frequency limitations on the design of fiber NOLM wavelength converters, by directly relating the required input peak power with the pulse-width of the input impulses and the XPM cut-off frequency. Fig. 5.7 presents the dependence of $P_{peak,req}$ on the loop length for the three fiber types considered in section 5.2, calculated using (5.20). The value of B_{XPM} has been computed using the analytical model presented in section 5.2.2. The analytically estimated results are compared with numerical simulation results. The latter where obtained by simulating the complete wavelength converter and increasing the power at the NOLM input until a match between the pulse-widths of the input and output impulses is achieved. All considered cases assume λ_s = 1545 nm and λ_p = 1555 nm, and input impulses with pulse-widths of 8 ps and 2 ps. These pulse-widths correspond to the typical values used for the transmission of 40 Gb/s and 160 Gb/s signals, respectively.

As shown in for all cases in Fig. 5.7, a good agreement was achieved between the estimated and simulated values of the required peak power, validating the applicability of the presented model. The discrepancies observed for the switching efficiency result from the non-Gaussian shape of the numerically simulated XPM-induced phase impulses. Fig. 5.7 shows that increasing the fiber length decreases the peak power requirement of the wavelength converter due to the increase of the maximum PM index. Furthermore, the decrease of the XPM cut-off frequency with the longer loop lengths leads to the broadening of the XPM-induced phase impulses which has to be compensated by decreasing even further the peak power of the impulses at the wavelength converter input. This translates into a reduced peak power of the impulses at the wavelength converter

output, which may be compensated up to some point by increasing the power of the CW probe. Ultimately, the XPM frequency limitation broadens the phase impulses to a point for which the interferometric process is unable to compensate, thus setting a limit for the loop length. The values of maximum loop length observed in Fig. 5.7 are expressed in Table 5.2. Also indicated in are the loop lengths for a switching efficiency of 0.9, which corresponds to an output peak power of $0.97 \cdot P_{CW}$.

Note that the results presented here fail to consider the impact of XPM of the probe propagating in the counter-clockwise direction. This impact translates in a reduction of the efficiency of the NOLM and degradation of the output signal, which may impair the effective conversion of high bit-rate signals.

As an example of the application of the results presented in this section, consider the work by Yu, et al., presented in [Yu, 2000: 1] and [Yu, 2000: 2]. In these references, the authors demonstrate the wavelength conversion of 40 Gb/s signals with 8 ps impulses using a NOLM with 3 km of DSF. From observation of Fig. 5.7-b) it is shown that in this particular case, the required peak power for pulse-width maintenance is approximately 23.9 dBm (~243 mW) and leads to a switching efficiency of less than 0.9, which is consistent with [Yu, 2000: 1] and [Yu, 2000: 2]. Lower peak powers would reduce the switching efficiency, leading to pulse compression, as also observed in [Yu, 2000: 1] and [Yu, 2000: 2].

Alternatively, NOLMs using HN-DSF have also been proposed for the wavelength conversion of 40 Gb/s RZ impulses with ~8 ps pulse-width, e. g. [Yu, 2000: 3]. As illustrated in Fig. 5.7, this fiber type allows a significant increase of the loop length without substantial reduction of the switching efficiency, which allows the use o relatively low power levels at the AOWC input. In addition, it is observable that the required input peak power and switching efficiency of a NOLM using HN-DSF is similar for input impulses of 8 ps or 2 ps, for loop lengths below 200 m. This results from the very high XPM cut-off frequency. In fact, the application of NOLMs using HN-DSF with loop lengths as large as 1 km has been reported for 160 Gb/s signals with pulse-widths as low as 2 ps, e. g. [Bogoni, 2004]. Other experiments using impulses with 500 fs pulse-width have also been reported, e. g. [Sakamoto, 2001]. In this case, the loop length was reduced to 50 m to allow the required XPM cut-off frequency (above 2 THz), at the cost of increasing the peak power of the input impulses to values exceeding 4 W.

Finally, the application of BOF in NOLMs has not been reported so far, to the author's knowledge. However, we may expect that such wavelength converters operating at 40 Gb/s would require loop lengths below 2 m for conversion efficiencies above 0.8 and required input peak powers above 25 dBm. For operation at 160 Gb/s, the loop lengths would have to be reduced to less than 30 cm with input peak powers exceeding 35 dBm, in order to reach the same conversion efficiency. Alternatively, experimental application of such fibers in wavelength converters using cross-polarization modulation has been presented using signals with 40 Gb/s [Meloni, 2005], using a BOF with 2 m, and 160 Gb/s [Lee, 2005: 1], [Lee, 2005: 3], and [Lee, 2005: 4], using a BOF with 1 m. The longer lengths of fiber allowed a substantial reduction of the required input peak power. This shows that despite the limitations of the BOF for application in AOWC using XPM, it may be used with other less-limited methods of wavelength conversion.

5.4. Carrier Phase Shifting Filter

5.4.1. Principle

In XPM-based wavelength converters using interferometers or detuned filters for PM-IM conversion, the power of the converted signal depends on the switching efficiency, as shown in section 5.3. In such wavelength converters, the maximum peak power of the converted impulses corresponds to the average power of the CW probe[1]. As such, the average power of the converted signal is only a fraction of the average power of the probe channel. The unused energy is dissipated or reflected by the PM-IM converter. This presents a limitation to the application of wavelength converters in all-optical transmission systems due to the recurring need to amplify the converted signals. Besides the evident increase of the overall cost of the system, there is also the impact of OSNR degradation which, despite the regenerative properties of all-optical wavelength converters, will eventually degrade the signal performance.

Several works have considered the improved design of optical filters for PM-IM conversion of the XPM-induced phase shift in wavelength converters (e. g. [Leuthold,

[1] This assumption disregards the insertion losses of the wavelength converter, which include fiber losses and the insertion losses of the PM-IM converter.

2003], [Leuthold, 2004], and [Perlin, 2002]). In the latter case, the amplitude and phase response of a detuned fiber Bragg grating (FBG) filter is chosen to achieve converted impulses identical to the input impulses. The amplitude and phase response of the filter are specified for a given detuning frequency that allows a sufficiently high suppression of the CW carrier frequency while maintaining optimized conditions of XPM-induced nonlinear phase shift. The works by Leuthold et al. have followed an alternative approach by designing a non-detuned filter which forces the interference of the blue shifted and red shifted frequency components of the probe signal after XPM and XGM with the pump signal in a SOA. The constructive or destructive interference of the spectral components yields output impulses with peak powers clearly exceeding the average probe power[2]. This indicates a more efficient use of the probe energy for the production of the converted signal. As a limit, the average power of the converted signal would be identical to the average power of the probe signal, indicating that the PM-IM converter is lossless. This provides benchmark values for the maximum reachable peak power of the output impulses as $P_{peak,out} \approx 1.87\ T/\tau \cdot P_{CW}$, in the case of Gaussian impulses with a pulse-width τ, or $P_{peak,out} \approx 2\ T/\tau \cdot P_{CW}$, in the case of raised cosine impulses with the same pulse-width. To approximate this limit one must use PM-IM conversion methods that allow a full use of the available probe power. This section presents a study on the design of an optimized filter for PM-IM conversion in fiber XPM-based wavelength converters. It will be shown that the ideal filter induces a phase shift on the frequency of the carrier component of the CW probe. For this reason, this filter will be referred here as CPSF. The proposed concept is similar to that which was proposed in [Leuthold, 2003] and [Leuthold, 2004], yet it is applied for probe signals affected by fiber XPM instead of XPM and cross-gain modulation (XGM) in a SOA. As such, it is fundamentally distinct. A description of the proposed fiber wavelength converter and the design of the CPSF are presented in section 5.4.2. The application of the proposed technique and a comparison with previous techniques is performed by numerical simulation in section 5.4.3, along with some considerations on the practical implementation of the proposed filter. To complete this study, section 5.4.3 also presents a study on the impact of accumulated dispersion on the power penalty of the converted signals.

[2] This comparison is performed after removing the gain of the SOA.

5.4.2. CPSF Design

The complex envelope of the probe signal at the fiber output may be approximated by:

$$u_s(t) = \sqrt{P_{CW}} \cdot \exp\left[\phi_s(t)\right] \tag{5.21}$$

where $\phi_s(t)$ is the probe phase shift, approximated by (5.6). Expression (5.21) assumes that the amplitude of the probe signal is unaffected by propagation along the fiber. Assuming an ideal wavelength converter, we have the instantaneous power of the converted signal proportional to the instantaneous power of the signal at the wavelength converter input, $P_p(t)$. As such, the complex envelope of the required signal at the output of the PM-IM converter may be described as:

$$u_{out}(t) = \sqrt{g \cdot P_{CW} \cdot \frac{P_p(t)}{P_{peak}}}, \tag{5.22}$$

where g is an ideal conversion gain, depending on the shape of the output impulses. Note that (5.22) neglects the delays resulting from fiber propagation and the PM-IM converter and assumes that the output signal is unchirped. The low-pass equivalent transfer function of an ideal PM-IM converting filter is described by [Leuthold, 2004], [Madsen, 1999]:

$$H_{PM-IM}(f) = \frac{\tilde{u}_{out}(f)}{\tilde{u}_s(f)} \tag{5.23}$$

where $\tilde{u}_{out}(f)$ and $\tilde{u}_s(f)$ are the Fourier transforms of $u_{out}(t)$ and $u_s(t)$, respectively. Generally, a closed form expressions for $\tilde{u}_s(f)$ is not possible to obtain. As such, (5.23) will be computed numerically. Fig. 5.8-a) and -b) present examples of the amplitude and phase characteristics of $H_{PM\text{-}IM}(f)$, assuming 40 Gb/s signals at the input of the wavelength converter composed by Gaussian and raised cosine impulses with various values of peak power and a pulse-width of 8 ps. Note that the phase of $H_{PM\text{-}IM}(f)$ does not consider the delay introduced by the filter, hence some delay has to be added, in order to maintain

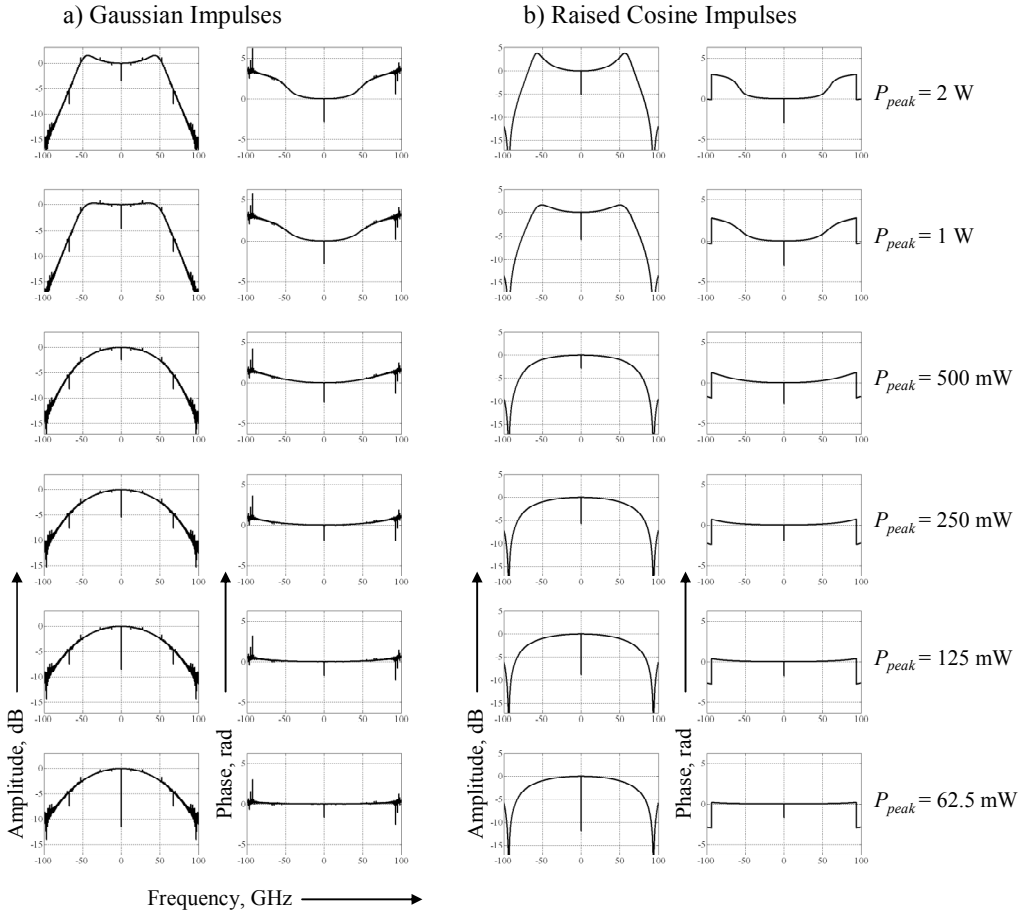

Fig. 5.8. Examples of the amplitude and phase characteristics of the numerically computed PM-IM converting filter for various values of peak power of the input impulses, assuming a) Gaussian impulses; b) Raised cosine impulses.

causality. Nevertheless, this delay will disregarded here. The simulated fiber is a HN-DSF, whose parameters are described in Table 5.1. The XPM in the fiber was modeled using the analytical model presented in section 5.2.

Fig. 5.8-a) and b) show that in all considered cases, the transfer function of the PM-IM converting filter is similar to a band-pass filter, centered in the carrier frequency of the probe channel. To facilitate their comparison, the amplitude spectra presented in Fig. 5.8-a) and -b) have been normalized to the maximum level of the central frequency components. The overall shape of the amplitude and phase characteristics of the PM-IM converting filter results from the need to reshape the output impulses to match the input impulses. The main particularity of the PM-IM converting filter is an amplitude deep and phase shift,

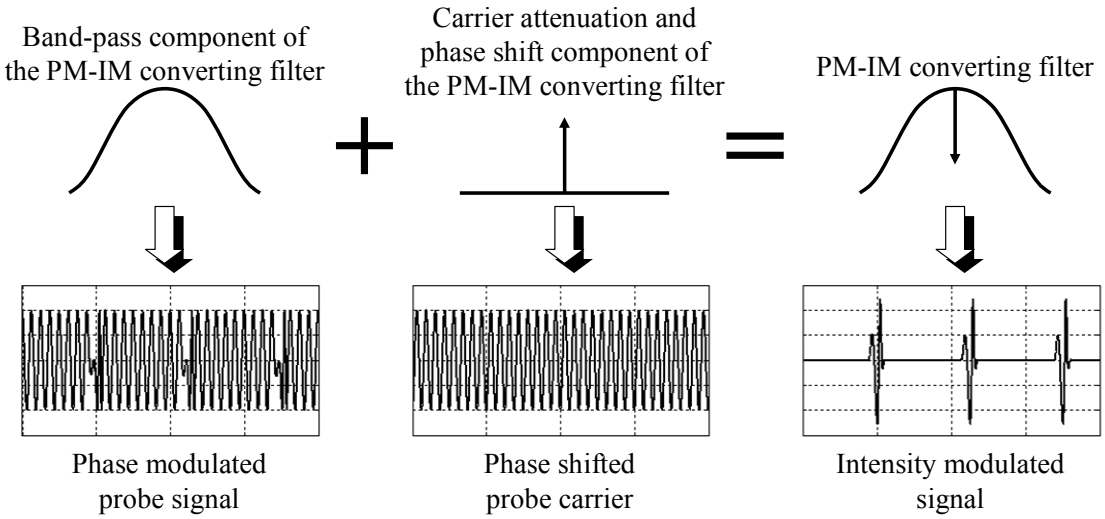

Fig. 5.9. Principle of the PM-IM converting filter.

located precisely at the carrier frequency. These parameters will be referred in this work as carrier attenuation , a_c, and carrier phase shift, ϕ_c.

The physical principle behind the presented PM-IM converting filter is illustrated in Fig. 5.9. One may decompose the filter in two distinct components. One component is a band-pass filter, which is used to reshape the signal, whereas the other component is a infinitesimally selective filter, which cancels all the spectral components of the phase modulated probe signal, leaving only the carrier component, which is appropriately delayed. The result of the filtering process is the sum of both components, which will generate the intensity modulated output signal.

To model the PM-IM converting filter in a realistic way, consider a hypothetical filter which induces the carrier phase shift and attenuation in a narrow bandwidth around the carrier wavelength, as shown in Fig. 5.10. This bandwidth will be referred here as

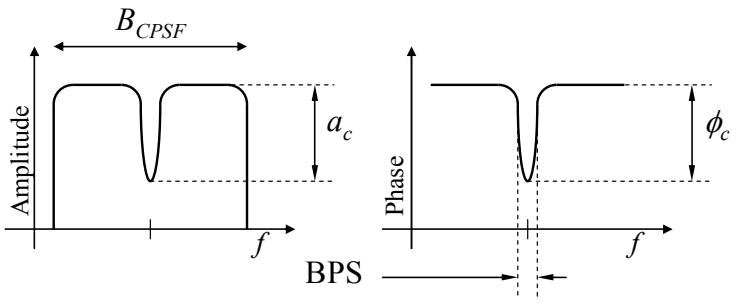

Fig. 5.10. Principle of the carrier phase shifting filter.

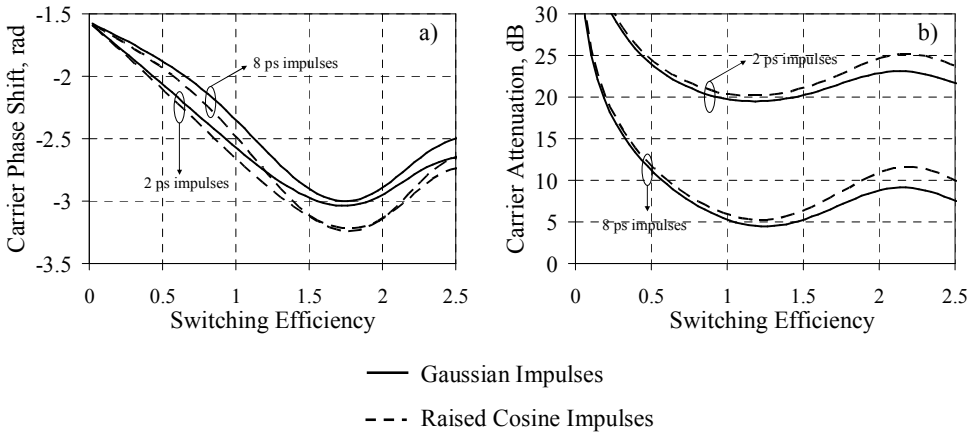

Fig. 5.11. Numerically computed values of the carrier phase shift (a) and attenuation (b) for the design of a CPSF.

bandwidth of phase shift (BPS). The hypothetical filter presented in Fig. 5.10 will referred here as CPSF, to distinguish it from the previously presented PM-IM converting filter. The frequency limitations of the CPSF will be modeled by a band-pass filter with a bandwidth, B_{CPSF}. In principle, practical implementation of the CPSF can be achieved using micro-mirrors technology, similarly to [Leuthold, 2004], or properly designed fiber gratings [Luís, 2006: 1]. The latter case is discussed in Appendix E. The CPSF may be described by the expression:

$$H_{CPSF}(f) = \left[1 + \left(\frac{e^{j\phi_c}}{\sqrt{a_c}} - 1\right) \cdot H_D(f)\right] \cdot H_B(f) \tag{5.24}$$

where $H_B(f)$ imposes the bandwidth limitation of the CPSF and $H_D(f)$ sets the bandwidth of the phase shift. To dimension the CPSF, one may use the values of ϕ_c and a_c obtained from the numerical computation of (5.23) by having:

$$\phi_c = \arg\left[H_{PM-IM}(0)\right], \tag{5.25}$$

where arg[·] is the argument of a complex term, and

$$a_c = \left|H_{PM-IM}(0)/N\right|^{-2}, \tag{5.26}$$

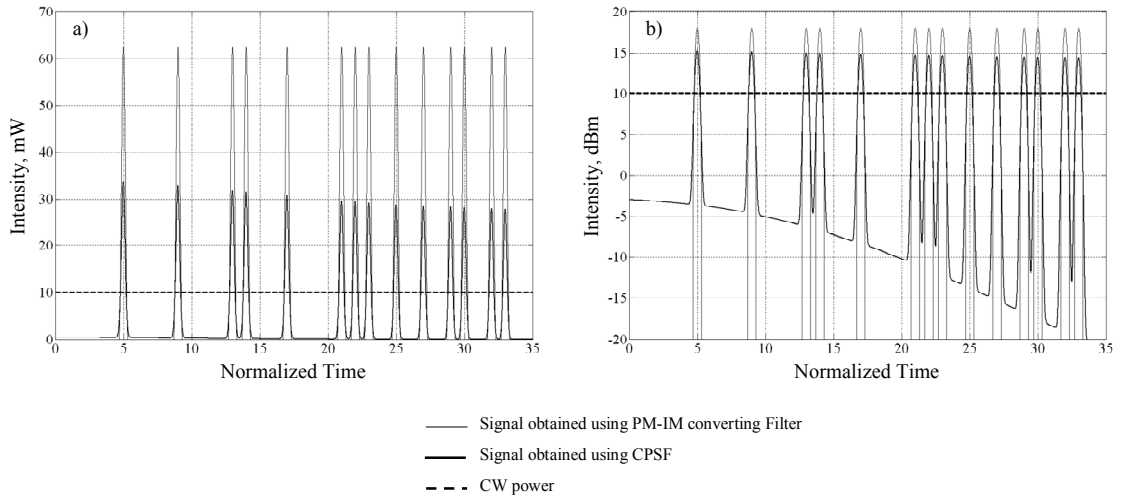

Fig. 5.12. Comparison of the traces of the instantaneous power at the output of a PM-IM converting filter, a CPSF and the probe average power. a) linear scale and b) logarithmic scale.

where N is a normalization constant required to avoid gain. Fig. 5.11-a) and -b) show the values of ϕ_c and a_c, respectively obtained from (5.25) and (5.26) as a function of the switching efficiency. Gaussian and raised cosine impulses have been considered, with input pulsewidths of 2 ps and 8 ps. As shown, the minimum carrier attenuation requirement is reached for a switching efficiency of approximately 1.2, varying negligibly with the impulse shape and pulse-width for the considered impulse shapes. However, for such switching efficiency the required carrier attenuation varies significantly with the pulse-width from approximately 5 dB with 8 ps impulses to 20 dB for 2 ps impulses. The required carrier phase shift for a switching efficiency of 1.2 varies from -2.6 rad, for 8 ps Gaussian impulses, to -2.9 rad, for 2 ps raised cosine impulses, as shown in Fig. 5.11-a). These results show that for an hypothetical implementation of the CPSF, one would be able to define a fixed carrier phase shift around -2.7 rad and vary only the carrier attenuation to adapt the filter to the input signal.

Fig. 5.12-a) and -b) present the example of a comparison between traces of the output power at the CPSF output and the PM-IM converting filter in a linear and logarithmic scale, respectively, assuming Gaussian impulses at the wavelength converter input with pulse-width of 8 ps and a peak power of 500 mW. The remaining parameters of the example are identical to the ones used for the referred power in Fig. 5.8. For the CPSF, we have assumed that $H_B(f)$ and $H_D(f)$ are first order Gaussian filters with bandwidths of

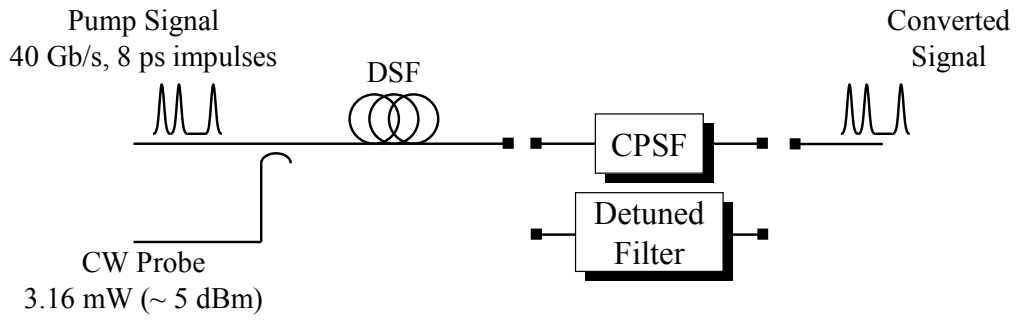

Fig. 5.13. Simulated wavelength converter using a CPSF or a detuned filter for PM-IM conversion.

125 GHz and 1 GHz, respectively. The values of ϕ_c and a_c were obtained from the numerical computation of (5.23) with the values of -2.6 rad and 5.6 dB, respectively.

Fig. 5.12-a) and -b) show that the impulses at the output of the CPSF have an average peak power approximately 3 dB below the peak power of the impulses at the output of the ideal PM-IM converting filter. This results from assuming that the maximum transmission of the CPSF is unitary, whereas the PM-IM converting filter may present gain for nonzero frequencies, as illustrated in Fig. 5.8. Nevertheless, the average peak power of the impulses at the output of the CPSF is still 5 dB above the average power level of the CW probe, illustrating the efficiency of this filter as a PM-IM converter. Further studies have shown that ϕ_c regulates the relative eye opening of the converted signal whereas the value of a_c sets the extinction ratio of the output signal. Following studies will involve an optimization of ϕ_c and a_c by extensive computation of the system under analysis using the analytical model derived in section 5.2.2.

Fig. 5.12 -a) and -b) also shown a noticeable fluctuation of the peak power of the impulses and the extinction ratio. This effect results from the finite BPS of 1 GHz, which affects the frequency components of the signal around the carrier frequency. As a result, the signal at the output of the CPSF presents low frequency fluctuations that have a strong dependency on the signal pattern. This effect is investigated with further detail in section 5.4.3 and Appendix E.

5.4.3. Simulation Results

This section presents a study of the performance of a wavelength converter using a CPSF. For comparison purposes, the simulation scheme used in this sub-section will be similar to the one used by Olson et al. in [Olsson, 2000] and [Öhlén, 2000]. As such,

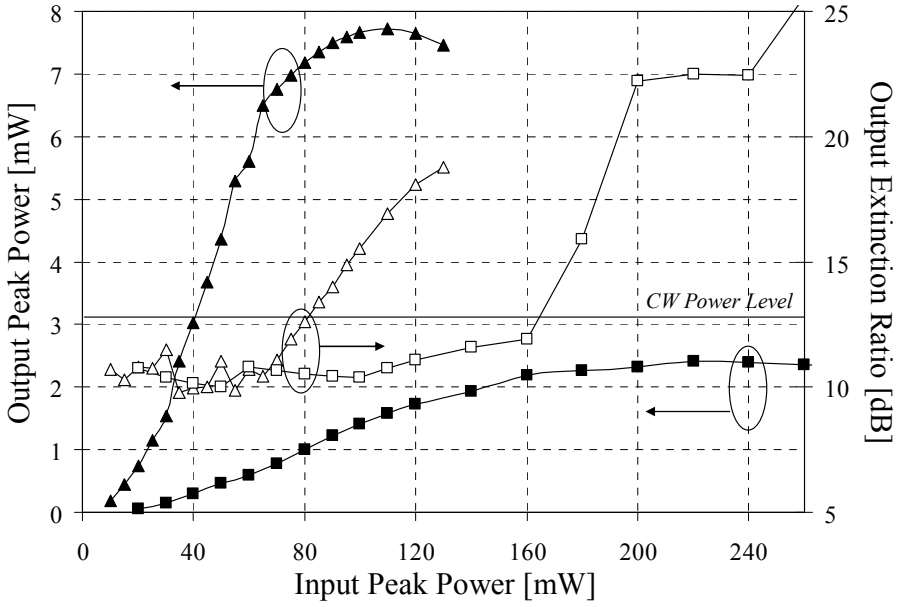

Fig. 5.14. Transmission characteristics of wavelength converters using the CPSF (triangles); and detuned filter (squares).

consider the fiber wavelength converter scheme presented in Fig. 5.13. The simulated pump signal is a 40 Gbit/s deBruijn sequence of 2^7 Gaussian pulses with full-width at half maximum of 10 ps. The probe is a CW signal with an average power at the fiber input of 3.16 mW (~5 dBm). The pump and probe signals are transmitted at the wavelengths λ_s = 1545 nm and λ_p = 1555 nm, respectively, and injected in a 10 km DSF segment with zero dispersion wavelength at 1550 nm, loss of 0.25 dB/km, dispersion slope of 0.086 ps/km/nm^2, nonlinear refractive index of 2.8×10^{20} m^2/W and effective area of 60 μm^2. Transmission in the DSF will be simulated by solving the coupled nonlinear Schrödinger equations using the SSFM [Agrawal, 1995]. The PM-IM converting filter is a CPSF, as described in section 5.4.2, with a BPS of 1 GHz. For comparison with the CPSF, PM-IM conversion will also be performed using a detuned filter, [Olsson, 2000], modeled as a 6-th order Gaussian filter with bandwidth B_{oc}, centered at a frequency spacing δf from the average probe frequency. Note that, to avoid the need for a notch filter, as performed in [Olsson, 2000], we will consider $B_{oc}<1.6\cdot\delta f$, for which the super gaussian filter provides a minimum isolation of 43 dB.

Fig. 5.14 presents the transmission characteristic of the wavelength converter when using the CPSF and the detuned filter. For each input peak power value, the parameters of the optical filters (a_c and ϕ_s for the CPSF; B_{oc} and δf for the detuned filter) have been

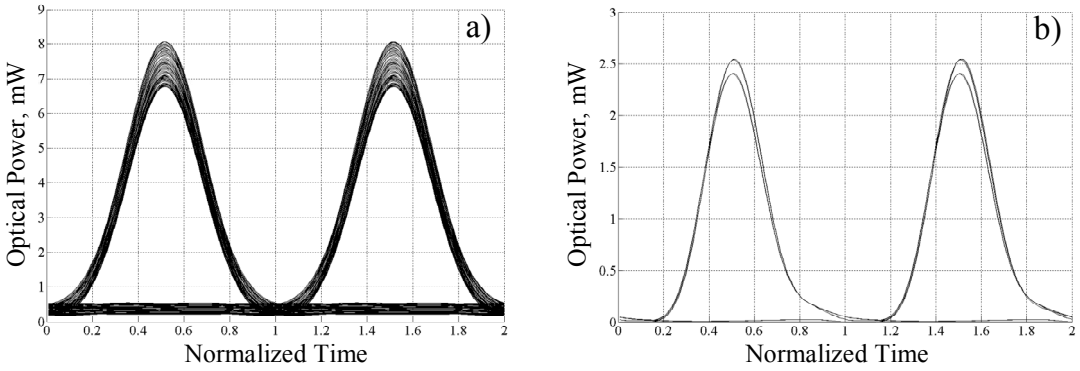

Fig. 5.15. Eye patterns at the output of the wavelength converter using a) the CPSF, considering an input peak power of 70 mW; and b) detuned filter, considering an input peak power of 220 mW.

optimized to obtain the highest output peak power and extinction ratio values above 10 dB. As can be seen, the maximum output peak powers are 2.4 mW with the sideband filter and 7.6 mW with the proposed filter, using input peak powers of 240 mW and 95 mW, respectively. This shows that the wavelength converter using the CPSF requires half the input switching power for the triple of the maximum output peak power. For input peak powers above 60 mW the converter is fully switched and the value of a_c may be set to 0 dB. In these conditions, the converted signal presents the same average power as the probe signal at the DSF output. Increasing the converter input power even further improves output extinction ratio but reduces the peak power as the converter leaves the maximum switching point. Note that the results obtained using the detuned filter are consistent with [Olsson, 2000]. The drawback of the CPSF is a reduction of the maximum extinction ratio from 22.5 dB to 17.5 dB, shown in Fig. 5.14. Nevertheless, in practical systems this has negligible impact since these values are already high. Furthermore, the limited extinction ratio may be compensated by increasing the value of a_c, at the cost of reducing the output peak power.

Fig. 5.15 presents the eye patterns of the converted signals. In both cases, pulse-widths bellow 10 ps have been observed, due to the pulse compression characteristic of fiber wavelength converter [Olsson, 2000]. Low frequency power fluctuations in the output signal of the proposed system can be observed in Fig. 5.15-a). As illustrated in section 5.4.2, these result from the finite BPS of the CPSF. Nevertheless, the results presented in Fig. 5.14 assume the worst case of peak power and extinction ratio. To analyze the patterning effect, Fig. 5.16 presents the dependence of the normalized patterning on the sequence length for different values of BPS and considering several polynoms to generate

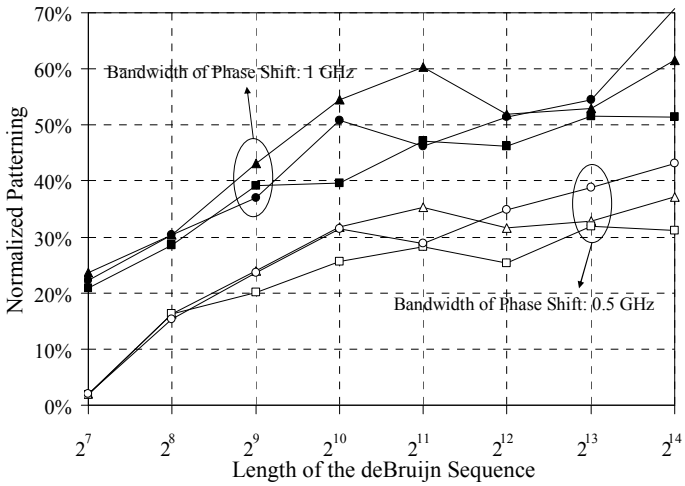

Fig. 5.16. Dependence of the normalized patterning of the converted signal on the deBruijn sequence length.

the pump deBruijn sequences. The normalized patterning is defined as the difference between the minimum and maximum eye opening at the sampling instant, normalized by the average eye opening.

Fig. 5.16 shows that, in most cases, the normalized patterning increases steadily with the sequence length, showing small variations when changing the polynom used. Further analysis revealed that the long sequences of zeros and ones in each deBruijn sequence are responsible for the highest degradation. As such, increasing the length of the deBruijn sequence used will generally increase the normalized patterning apart from small variations depending on the polynoms used. Reducing BPS will reduce the impact of the CPSF on the central frequency components of the chirped CW, thus reduce the patterning effect. This is shown in Fig. 5.16, when setting the BPS to 0.5 GHz. Nevertheless, it will also limit the detuning range.

Fig. 5.17 shows the dependence of the output peak power and the extinction ratio of the signal on the detuning of the CPSF or the CW source, considering an input peak power of 70 mW and BPS of 1 GHz. It is shown that the variation of the output peak power and the extinction ratio is negligible within a frequency range of ±0.4 GHz, or ±3.2 pm, which is enough to withstand currently available CW sources [Funabashi, 2004]. It can be shown that the tolerable frequency range is directly proportional to BPS. Therefore, a tradeoff must be found for the BPS, according to the application of the filter. Note that the impact of the patterning effect can also be reduced by using scrambled signals. As a reference, we can consider the signals defined for SDH [ITU G.707, 2003], where the maximum length

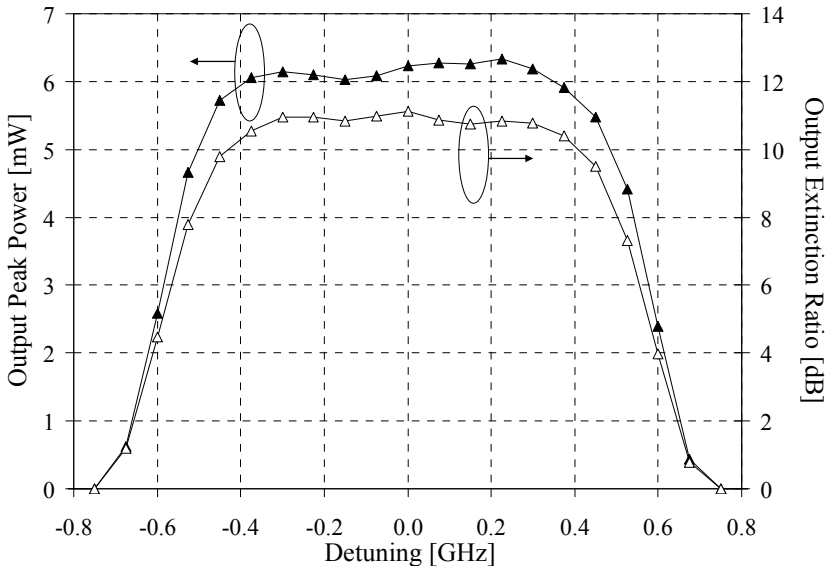

Fig. 5.17. Dependence of the output peak power and extinction ratio on the detuning of the proposed filter.

of a sequence of zeros or ones is limited to 7 symbols. This corresponds to the results presented in Fig. 5.14 and Fig. 5.15. On the other hand, the more recent recommendation for optical transport networks predicts scrambled signals with a maximum sequence of zeros or ones of 16 symbols [ITU G.709, 2003]. In these cases the patterning effect may significantly degrade the converted signal, unless the payload signals are already scrambled. Also, the impact of detuning can be mitigated by adding control mechanisms that tune the proposed filter.

To determine the power penalty, consider the optically preamplified receiver presented in Fig. 5.18. The incoming signal is amplified by an EDFA with gain and noise figure of 30 dB and 6 dB, respectively. The signal is filtered by a rectangular optical filter with bandwidth of 320 GHz, to avoid signal distortion, and follows to a p-i-n photodiode with unitary responsivity. The electrical part of the receiver is modeled by a 3rd order Bessel filter with a cut-off frequency of 65% of the signal bit-rate. We also evaluate the

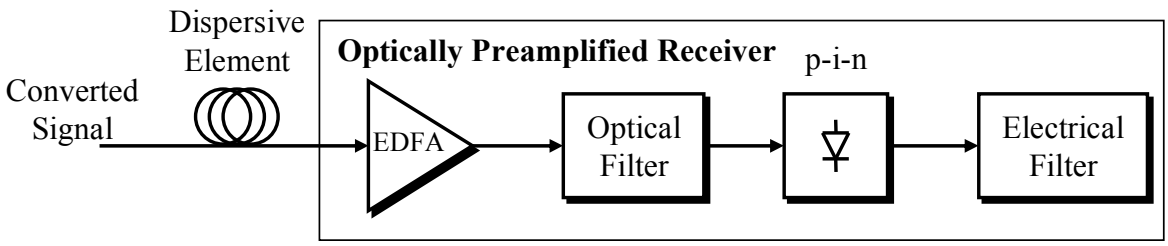

Fig. 5.18. Model of the considered pre-amplified optical receiver.

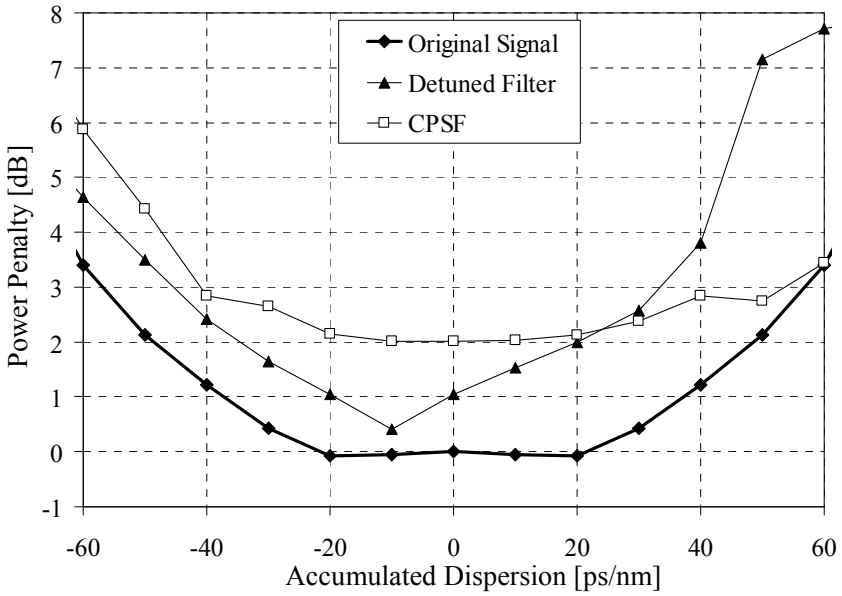

Fig. 5.19. Dependence of the power penalty on the accumulated dispersion.

dispersion tolerance of the converted signals by placing a linear dispersive element prior to the pre-amplified receiver. The sensitivity power penalty due to wavelength conversion was calculated using the semi-analytical model for the BER presented in [Rebola, 2002], assuming that the original unconverted signal corresponds to a null power penalty. This signal allows a receiver sensitivity of -31.2 dBm, obtained for a BER of 10^{-12}.

Fig. 5.19 presents the dependence of the power penalty on the accumulated dispersion for the original and converted signals. It can be seen that, using the CPSF leads to a power penalty of 2 dB. This degradation is mainly due to the patterning effect. Using the detuned filter leads to a power penalty of 1 dB, mostly due to a low extinction ratio.

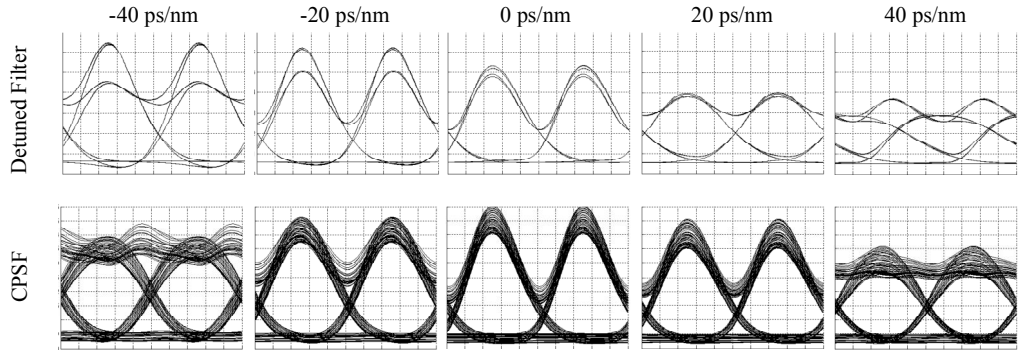

Fig. 5.20. Eye patterns for the converted signals at the electrical filter output, for different accumulated dispersion values.

These effects are shown in the eye patterns presented in Fig. 5.20 for 0 ps/nm.

With accumulated dispersion within the range ±20 ps/nm it is shown that the power penalty of the signals converted with the CPSF remains almost unchanged. This can also be seen on Fig. 5.20 as the eye patterns for 20 ps/nm and -20 ps/nm are similar. This behavior indicates that the residual chirp of the converted signal has only a moderate impact on the power penalty. This impact only becomes significant outside the range ±30 ps/nm. Assuming a criteria of maximum power penalty degradation of 1 dB, the proposed filter allows an accumulated dispersion range between -40 ps/nm and 57 ps/nm, whereas the original signal is limited to the range ±38 ps/nm. The signal obtained with the detuned filter presents a highly symmetrical behavior, showing that the residual chirp has a strong impact on the power penalty. Therefore, this system is restricted to the range from -26 ps/nm to 20 ps/nm. Nevertheless, it presents the lowest power penalty value of 0.2 dB for an accumulated dispersion of -10 ps/nm.

5.5. Conclusions

A novel analytical model for the characterization of XPM in ultra-fast all optical wavelength converters has been presented and validated using numerical simulation. The model achieves remarkable accuracy at modulation frequencies exceeding the terahertz range by accounting for GVD on the propagation of the pump and probe channels along the fiber and for GVD and SPM on the propagation of the probe channel. The XPM cut-off frequency has been introduced as a design parameter for wavelength converters, presenting a logarithmic dependence on the maximum XPM-induced phase modulation. Application of the model allowed comparing the frequency limitations and characteristic of XPM cut-off frequency versus maximum phase modulation index in typical DSF, HN-DSF and also the recently developed BOF. It has been shown that the HN-DSF remains the most appropriate fiber for wavelength conversion of ultra-high bit-rate signals, as a consequence of its very high XPM cut-off frequency, above 1 THz. This results from the low fiber dispersion and dispersion slope parameters. The BOF has significant frequency limitations due to the high dispersion parameter. Hence is more appropriate for cases of low sensitivity or low bandwidth requirements.

The novel analytical model for the XPM-induced PM has been applied to the design of NOLM wavelength converters. This allowed the derivation of approximate close-

form expressions for the dimensioning of the loop length and the required input peak power, accounting for the XPM cut-off frequency. It has been shown that the required XPM cut-off frequency always exceeds the cut-off frequency of the signal to be converted. Furthermore, analytical and numerical simulation results demonstrated that the XPM frequency limitations ultimately impose a maximum loop length.

This chapter has also presented a novel filter for PM-IM conversion, to increase the efficiency of fiber wavelength converters. The improved filter allowed a reduction of the required input peak power and increase of the maximum output peak power by factors of 2 and 3, respectively, in comparison to wavelength converters using detuned filters. In terms of the required switch power, the obtained results make the proposed system comparable with recently developed amplified wavelength converters using alternative methods of amplification, such as [Galili, 2005] and [Wang, 2005]. This was achieved by a more efficient use of the probe signal power. The main drawback of the proposed filter results from pattern dependent power fluctuations of the output signal. As such, signal scrambling may be required to avoid long sequences of mark or space symbols. The proposed filter tolerates fluctuations of the input wavelength of ±3.2 pm, making it appropriate for currently available high bit-rate commercial systems. The power penalty of the converted signals was found to be 2 dB in back-to-back configurations, against 1 dB, obtained when using detuned filters. Nevertheless, the converted signal using the proposed filter as low residual chirp. Therefore, the dispersion tolerance is nearly duplicated.

Chapter 6. Nonlinear Transmission Impairments in Systems with Advanced Modulation Techniques

6.1. Introduction

The capacity demand in optical communications has increased continuously over the recent years, with little evidence of saturation. In contrast, this increase was accompanied with the imperative requirement for the reduction of investment costs and operational expenditures of optical networking systems. The response to these demands began with the improvement of all-optical processing systems, with the purpose of realizing transparent optical networks. The main developments in optical transmission systems in recent years have regarded optical transmission techniques. In particularly, a significant effort was devoted to the development of advanced modulation techniques to handle fiber dispersion and nonlinearity. A number of advanced optical modulation formats have attracted increased attention. Some of these formats carry information through on-off keying, but also modulate the optical phase in order to enhance the signals' robustness to fiber dispersion and/or nonlinearities. This group includes formats such as duobinary, alternate mark inverse, chirped RZ, and alternating-phase ASK formats, such as CSRZ [Gnauck, 2005].

Transmission techniques, such as electronic pre-distortion have also been proposed [Killey, 2005]. The latter is based on the digital or analog reshaping of the signal to be transmitted in order to pre-compensate the distortion introduced by the fiber transmission system [Winzer, 2005]. Electronic pre-distortion may be applied to arbitrary modulation formats [Essiambre, 2005: 1], achieving remarkable transmission distances without the use of optical dispersion compensation [Chadrasekhar, 2006]. In addition, electronic pre-distortion allows the compensation of single-channel fiber nonlinearities [Klekamp, 2006]. However, this method involves quite complex high-speed electronics to reach maximum performance, which may detriment its application. Alternatively, SSB versions of the aforementioned modulation formats have also been proposed [Fonseca, 2006: 1], [Fonseca, 2006: 2], [Fonseca, 2007: 3], and [Fonseca, 2007: 2]. These allow a reduction of the optical bandwidth of the signal, significantly improving its tolerance to fiber dispersion [Sieben, 1999]. Furthermore, SSB modulation formats have the particular property of avoiding spectrum back-folding upon direct detection, preserving the phase distortion of the signal [Sieben, 1999]. This allows the use of simple analog electrical circuitry at the receiver or SSB transmitter, to respectively post- or pre-compensate fiber dispersion [Sieben, 1999], [Fonseca, 2006: 2]. This allowed a remarkable increase of the maximum transmission distance without optical dispersion compensation. However, the absence of inline dispersion compensation leads to strong nonlinear inter and intra-channel interactions, as shown by Essiambre et al. in [Essiambre, 2006]. This limits considerably the application of these transmission techniques in long-haul systems [Chadrasekhar, 2006]. Nevertheless, alternative dispersion compensation schemes based solely on concentrated dispersion management have been proposed [Fonseca, 2007: 2], and [Luís, 2007: 2].

Optical phase modulation formats such as DPSK have also resurfaced in the recent years with the improvements on optical transmitter linewidths and the use of direct detection techniques combined with the improvements on the technology to fabricate stable delay interferometers and balanced photodetectors [Gnauck, 2005], [Bosco, 2005]. DPSK modulation formats encode the binary information to be transmitted in a binary differential signal, which is transmitted in the phase of the optical signal. Recovery at the receiver is performed by correlating the phase of a received symbol with the phase of the previous symbol, avoiding the need to use an absolute phase reference. This allows the use of direct detection, instead of the significantly more complex coherent detection employed

in non-differential phase modulation formats. Since optical phase modulation formats do not carry information on the intensity of the optical field, their transmission in optical fibers yields less nonlinearities. Furthermore, the use of differential direct-detection affects the noise distribution in a way that a theoretical margin improvement of 3 dB may be achieved. Although in practice this margin is rather hard to reach [Bosco, 2005], the most recent transmission distance records have been achieved using DPSK modulation formats e. g. [Charlet, 2003], among others. The main degradation in phase modulation formats results from the impact of ASE generated in optical amplifiers, which combined with fiber nonlinearities yields prohibitive phase fluctuations on the optical signal. However, this limitation may be handled using FEC techniques. Currently, DPSK systems have reached sufficient maturity for deployment in commercial long and ultra-long haul optical communications networks at bit rates exceeding 40 Gb/s. One of the main obstacles to the deployment of such systems in currently installed infrastructure is the nonlinear interaction with legacy ASK signals [Rohde, 2000], [Spinnler, 2004], [Lenihan, 2005], and [Griesser, 2005]. The development of design tools for the planning of systems using mixed modulation formats presents an urgent challenge for the ongoing transition from ASK to DPSK systems. Studies on this topic have been previously presented, which show dominant impact of XPM [Rohde, 2000], [Spinnler, 2004], and [Lenihan, 2005]. However, these studies have been limited to the assessment of the nonlinear crosstalk degradation though experiment or simulation, without a deeper description of the influence of fundamental system parameters, such as residual dispersion, on the XPM degradation of the DPSK signals. Griesser et al. has proposed a simple model for the XPM-degradation of a DQPSK signal by an interfering ASK signal in [Griesser, 2005]. This model is based on an adaptation of the approximate model presented by Ho in [Ho, 2004] for nonlinear phase noise originating from XPM, which is replaced by the interfering ASK signal. The model by Ho assumes that the dominant XPM-degradation in DPSK signals results from the XPM-induced PM originating from ASE noise-induced IM on the interfering signal. However, Ho's model assumes that the XPM-induced PM depends only on the walkoff between channels, disregarding the impact of GVD and SPM. As such the influence of residual dispersion on the XPM-degradation of DPSK signals by ASK signals remains unaccounted for. In particular, the generation of XPM-induced IM resulting from the conversion of XPM by GVD and SPM has not been investigated so far.

Finally, when considering advanced transmission techniques, one must account for the advancements in the transmission of signals at incredibly high bit-rates of over 1 Tb/s [Weber, 2005], [Weber, 2006], among others. As such, the study of the characteristics of optical transmission of signals at such high bit-rates as drove researchers in recent years. Perhaps the most challenging aspect of the transmission in optical fibers of signals at ultra-high bit-rates is the behavior of Kerr fiber nonlinearities. For such systems, Essiambre et al. have demonstrated the dominance of degradation induced by nonlinear interactions between different symbols of the same signal [Essiambre, 2002]. These interactions are usually referred has intra-channel nonlinearities. More specifically, IXPM and IFWM due to the similarities with the commonly known inter-channel nonlinearities XPM and FWM. The optimization of the performance of such systems by Mecozzi et al. in [Mecozzi, 2001] and Killey et al in [Killey, 2000: 2] as led to the development of specialized dispersion maps under which the system can reach a particular transmission regime, usually referred as pseudo-linear transmission regime [Essiambre, 2002]. The latter is characterized by having an optimum dispersion compensation scheme similar to what would be used for a linear system, yet supporting strong fiber nonlinearities. Further advancements on the study of the propagation of signals at ultra-high bit-rates have led Fonseca et al. to devise a generalization of the pseudo-linear regime, referred as pseudo-solitonic regime, for signals with finite extinction ratio [Fonseca, 2007: 1]. Although Fonseca et al. restricted their study to numerical simulation, they have shown that the previously developed rules for pseudo-linear systems only apply in the case of signals with infinite extinction ratio. Although the currently available signal generators allow remarkably high extinction ratios, one may assume that an infinite extinction ratio is merely theoretical. In practice, a minimum power level is always present in optical signals. Furthermore, signal generators for commercial applications typically use pulse carving techniques, which are often limited to extinction ratios of 15 dB. Finite extinction ratio is also a strong limitation for all-optical processing systems based on fiber or semiconductor devices, as shown for the first case in Chapter 5.

Following this analysis, this chapter presents three studies on the performance degradation of optical transmission systems using advanced modulation formats due to fiber nonlinearities. Section 6.2 presents a study on the dispersion management in SSB systems using electrical dispersion pre-compensation and optical dispersion post-

compensation. It is shown that the electrical dispersion compensation is equivalent to optical dispersion compensation, from the point of view of fiber nonlinearities and that, sharing the total residual dispersion at the transmitter and receiver allows an increase of required OSNR by a factor of 3 dB. The nonlinear characteristics of the SSB transmitter are also considered. Section 6.3 will be devoted to the study of the impact of XPM-degradation of DPSK signals due to nonlinear interference with ASK signals. This study will involve a pump-probe analysis of the impact of XPM-induced IM and PM on the electrical current fluctuations at the DPSK receiver. Afterwards, a simplified model for the estimation of the XPM-induced BER degradation will be presented and validated using numerical simulation. Finally, section 6.4 presents an analytical study on the impact of intra-channel fiber nonlinearities on signals with finite extinction ratio. Analytical expressions are derived to identify novel nonlinear perturbation components resulting from the interactions between components of a signal. In particular, the interactions between impulses and the nonzero space level. Final conclusions of this chapter are presented in section 6.5.

The work presented in this chapter has been partially published in [Luís, 2007: 1], [Luís, 2007: 2], [Luís, 2007: 3], and [Luís, 2007: 4].

6.2. Dispersion Management in Optical Transmission Systems Without Inline Dispersion Compensation

6.2.1. Principle

The emergent deployment of low-cost multi-section transmission links at 10 Gb/s in metropolitan or regional networks as led to the development of dispersion tolerant optical modulation formats, such as optical SSB with electrical dispersion pre-compensation [Fonseca, 2006: 2] or the use of electronically pre-distorted signals [Killey, 2005], [Essiambre, 2006], to avoid the costly use of dispersion compensating fiber. Electrical dispersion pre-compensation may be achieved using passive electrical dispersive lines without compensating fiber nonlinearities [Fonseca, 2006: 2]. On the other hand, electronic pre-distortion requires complex high-speed electronics yet allows the compensation of SPM [Essiambre, 2006]. In both cases, the high accumulated dispersion and concentrated dispersion compensation leads to strong pulse broadening and, as a

consequence of fiber nonlinearity, to IFWM and IXPM [Essiambre, 2002], as experimentally reported in [Mecozzi, 2001].

It is shown in sub-section 6.2.2 that intra-channel nonlinearities strongly degrade electrically pre-compensated 10 Gb/s RZ-SSB systems without inline dispersion compensation. To improve system performance, partial optical dispersion pos-compensation combined with electrical dispersion pre-compensation is proposed. This allows a significant increase of the maximum launched power compared to a full electrically pre-compensated system. It is shown that electrical dispersion pre-compensation effectively replaces optical dispersion pre-compensation with negligible changes of the system response to fiber nonlinearities. In addition, the limitations of the SSB transmitter in producing the electrically pre-compensated signal are addressed, regarding the impact of the limited modulation depth on the system performance. It is shown that low modulation depth signals yield an asymmetric optimum dispersion compensation map.

6.2.2. Dispersion Management in Single-Channel RZ-SSB Transmission Systems Without Inline Dispersion Compensation

6.2.2.1. Simulated Transmission System

Fig. 6.1 depicts the simulated transmission system. Similarly to [Fonseca, 2006: 2], the SSB signal is produced by driving a dual Mach-Zehnder modulator (MZM) with a 10 Gb/s on-off keyed RZ signal with a duty cycle of 50 % and its Hilbert transform . The non-ideal Hilbert transformer (HT) is modeled using the experimental characterization of a hybrid coupler [Fonseca, 2006: 2]. The detailed implementation of the SSB transmitter is outside the scope of this work and may be found in Appendix G. Electrical dispersion pre-compensation is done by a dispersive line with transfer function [Fonseca, 2006: 2]:

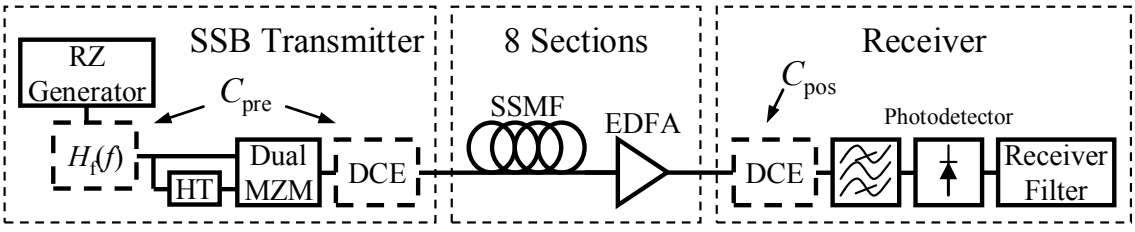

Fig. 6.1. Simulated transmission system for analysis of single-channel transmission using SSB signals.

$$H_{EDC}(f)=\begin{cases}H_T^*(f), & f\geq 0\\ H_T(f), & f<0\end{cases} \tag{6.1}$$

where $H_T(t)$ is approximated by linear response of an equivalent dispersion pre-compensating fiber [Agrawal, 1997]:

$$H_T(f)=\exp\left(j\frac{\pi C_{pre}\lambda^2 f^2}{c}\right) \tag{6.2}$$

where λ, c and C_{pre} are the operation wavelength, speed of light in vacuum and the amount of pre-compensation, respectively. Alternatively, optical dispersion compensation elements (DCE) may be used for pre- and post-compensation. In this work, the DCE are assumed lossless. The amount of post-compensation is given by C_{pos}. The signal is a *deBruijn* sequence of 2^{11} symbols. The long sequence accounts for patterning effects due to high accumulated dispersion. The SSB modulator is initially set for a modulation depth of 0.4, defined between 0 and 1, yielding an extinction ratio of 6 dB. Low modulation depths reduce the impact of the nonlinear characteristic of the dual MZM and the non-ideal HT, improving the sideband suppression and the effectiveness of the electrical pre-compensation [Fonseca, 2006: 2]. The transmission link is composed of 8×80 km sections of SSMF, with inline optical amplifiers to compensate the section losses. The SSMF has attenuation and nonlinearity coefficients of 0.22 dB/km and 1.37 $W^{-1}\cdot km^{-1}$, respectively. The dispersion parameter is D=17 ps/nm/km, yielding a total accumulated dispersion of 10.88 ns/nm. Transmission along the fiber will be simulated by solving the nonlinear Schrödinger equation using the SSFM. The receiver is composed by a 3rd order super-Gaussian optical filter with a 320 GHz bandwidth, followed by a squared law photodetector. The electrical receiver is modeled by a 3rd order Bessel filter with a –3 dB cut-off frequency of 10 GHz. C_{pre} and C_{pos} are optimized using the eye opening penalty (EOP), defined here as [Elbers, 2000]:

$$\mathrm{EOP} = 10 \cdot \log_{10}\left(\frac{2\overline{I}_s}{\mu_1 - \mu_0}\right) \tag{6.3}$$

where μ_1 and μ_0 are the minimum and maximum electrical current at the receiver for the mark and space symbols, respectively. $\overline{I}_s$ is the average electrical current. Performance evaluations rely on the required OSNR ($OSNR_{\mathrm{REQ}}$) at 0.1 nm bandwidth, for a BER of 10^{-12} obtained using the semi-analytical model presented in [Rebola, 2001].

6.2.2.2. Pre- and Pos-Dispersion Compensation

Before optimizing the dispersion compensation, one must consider that the proposed system presents some characteristics which are commonly associated with higher bit-rate systems. In particular, the total amount of accumulated dispersion along the link is sufficient to spread the transmitted RZ impulses over a large number of bit-slots. This indicates that one may expect some resemblance of the optimized dispersion compensation scheme with the dispersion schemes required for high bit-rate pulse overlapped transmission, in particular the pseudo-linear transmission regime defined in [Essiambre, 2002]. The latter is characterized by strong variations of the signal waveform due to accumulated dispersion averaging the intra-channel fiber nonlinearities. Previous works have shown that the transmission properties rely strongly on the dispersion map, [Essiambre, 2002]. Optimum dispersion compensation is achieved by using dispersion pre- and pos-compensation to set the point of zero accumulated dispersion, $z_0 = -C_{\mathrm{pre}}/D$, in a position that divides the link in two portions with identical accumulated nonlinear phase [Essiambre, 2002], [Mecozzi, 2001]. For high modulation depth, this position is slightly shifted backwards from the middle of the link [Mecozzi, 2001]. While in the pseudo-linear regime, higher launched powers are allowed before significant nonlinear distortion occurs, which translates to a longer reach [Essiambre, 2002].

Following the results presented in [Essiambre, 2002] for high bit-rate signals, Fig. 6.2 presents the dependence of the EOP on the amount of C_{pre} (electrical and optical) and C_{pos} for an average launched power of 7 dBm. As shown, both cases present similar behavior, illustrating the equivalency between electrical and optical pre-compensation. However, the electrically pre-compensated system is more tolerant to variations of C_{pre} and C_{pos}. This results from the less dominant impact of fiber nonlinearities when comparing

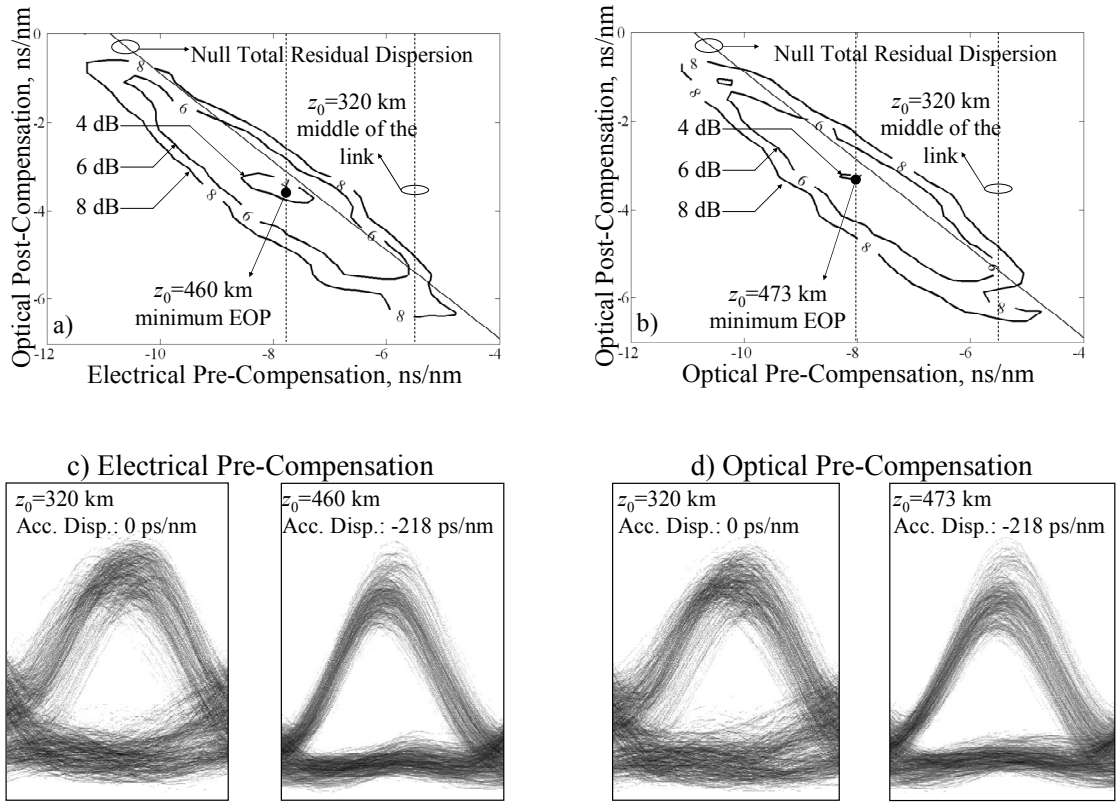

Fig. 6.2. Dependence of the EOP on C_{pre} and C_{pos} for a power of 7 dBm and eye diagrams of the received signal with electrical (a), (c); and optical (b), (d) C_{pre}. The vertical lines are values of z_0.

with the degradation introduced by the non-ideal transmitter. Lowest EOP was obtained for C_{pre} = -7.8 ns/nm and C_{pre} = -8.0 ns/nm with electrical and optical C_{pre}, which correspond to z_0 = 460 km and z_0 = 473 km, respectively. A total accumulated dispersion of -218 ps/nm (corresponding to the simulation resolution) optimizes performance in both cases.

As previously stated, the dependence of the EOP on C_{pre} and C_{pos} resembles the characteristics of the pseudo-linear regime [Essiambre, 2002], which is useful to draw some conclusions regarding the impact of fiber nonlinearities. Nonetheless, the presented case cannot be considered as pseudo-linear transmission in the strictest sense. The impact of fiber nonlinearities is illustrated by the received signal eye diagrams presented in Fig. 6.2-c) and –d) where the non-optimized cases are predominantly degraded by amplitude and temporal jitter. Considering that this is a single channel system, these forms of degradation may be attributed to IFWM and IXPM, respectively. The latter is nearly canceled with optimized C_{pre} and C_{pos} whereas IFWM is significantly reduced, as predicted in [Mecozzi, 2001].

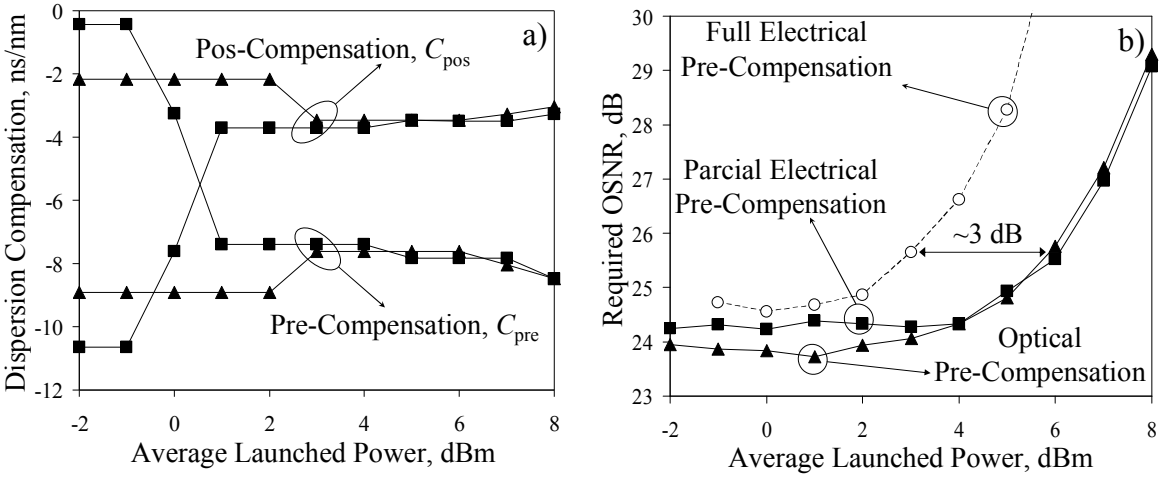

Fig. 6.3. Power dependence of the (a) optimum C_{pre} and C_{pos} and (b) $OSNR_R$. ■ – partial electrical C_{pre}; ▲ - partial optical C_{pre}; ○ – full electrical pre-compensation.

Fig. 6.3-a) presents the optimized C_{pre} and C_{pos} when increasing the average power for both considered cases. For power values below 0 dBm, the system is operating on a linear regime. As such, the performance is unaffected by arbitrary C_{pre} and C_{pos} while maintaining the total accumulated dispersion of the link. Increasing the launched power yields a nonlinear regime and C_{pre} and C_{pos} converge to the optimum values, stabilizing for powers above 2 dBm. Note that the optimum residual dispersion varies negligibly from the linear to the nonlinear regime, consistently with the characteristics of the pseudo-linear regime [Essiambre, 2002].

To assess the system performance, Fig. 6.3-b) presents the dependence of $OSNR_{REQ}$ on the launched power, with C_{pre} and C_{pos} optimized for each power value. In both considered cases for powers above 4 dBm, fiber nonlinearities are the dominant impairment, increasing $OSNR_{REQ}$. In these conditions, there are negligible differences between the performances obtained using electrical or optical C_{pre}. The performance of a similar system using full electrical pre-compensation is also presented. It is shown that the proposed system allows a 3 dB increase of the launched power before reaching similar $OSNR_{REQ}$ as the full electrical-pre-compensated system. This shows the improvement of the proposed scheme to handle fiber nonlinearities in electrically pre-compensated systems. Further studies were performed using electrical C_{pos} either alone or combined with optical or electrical C_{pre}. These results are presented in Appendix H. However, the achieved results have shown dominant EOP degradation due to the beating of the SSB signal components at the receiver, significantly impairing the transmission. Further studies

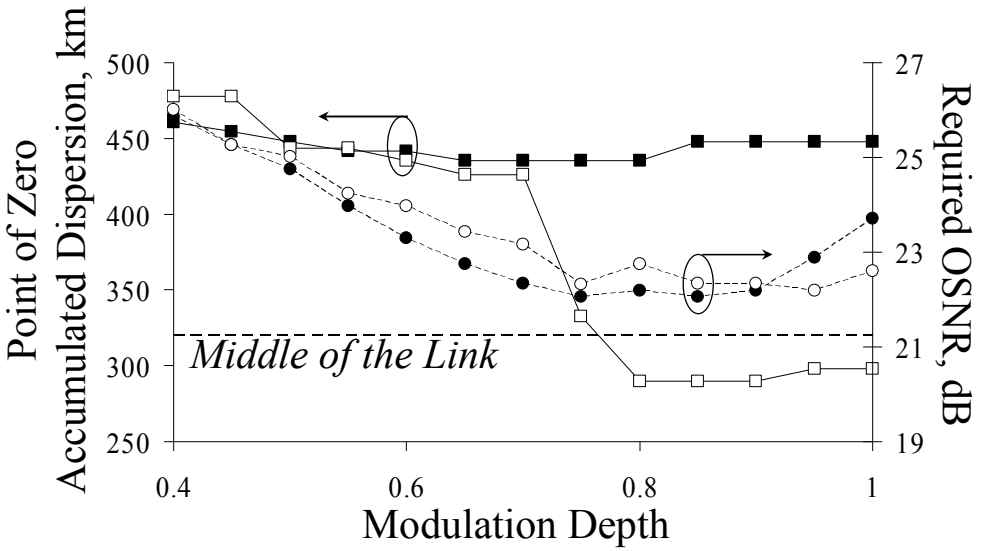

Fig. 6.4. Optimum z_0 for 7 dBm launched power. ■ – electrical C_{pre}; □ - optical C_{pre}. Circles are $OSNR_R$ with: • - electrical C_{pre}; ○ - optical C_{pre}.

on the transmission of NRZ-SSB signals using electrical dispersion pre-compensation are presented in Appendix I. In addition, a short study on the impact of XPM on IM-DD systems without dispersion compensation is presented in Appendix J.

6.2.2.3. Impact of Reduced Modulation Depth on the Optimized Dispersion Map

In sub-section 6.2.2.2, it was shown that the considered system presents minimum EOP when setting z_0 forwards from the middle of the link (320 km) by approximately 20% of the link length, using optical or electrical C_{pre} [see Fig. 6.2-a) and –b)]. To explain this behavior, it can be assumed that the nonzero power of the space symbols leads to interactions between these and the mark symbols, which would otherwise be neglected [Mecozzi, 2001]. This alters the symmetry of the accumulated nonlinear phase generated along the transmission path, thus changing also the optimum dispersion map. An analytical evaluation of this effect is outside the scope of this study but will be considered in further detail in section 6.4. Nevertheless, a relation between modulation depth and the optimum dispersion map may be established. Fig. 6.4 presents the optimum value of z_0 as a function of the modulation depth, considering optical and electrical C_{pre}. Increasing the modulation depth with optical C_{pre} changes z_0 from the value presented in sub-section 6.2.2.2 to a value slightly shifted backwards from the middle of the link. The transition occurs quite abruptly at modulation depths around 0.7. This shows that the optimum dispersion compensation map is significantly affected by the modulation depth. The $OSNR_{REQ}$, also presented in Fig.

6.4, is improved mostly due to the increased eye opening. With electrical C_{pre}, the SSB transmitter is unable to accurately reproduce the pre-compensated signal when the modulation depth is increased. Hence, the optimum dispersion map will not change in the same manner as with optical C_{pre}. In fact, the optimum z_0 remains constant with the modulation depth. The $OSNR_{REQ}$ is minimum for a modulation depth of 0.75. From this point up to a modulation depth of 0.9, the signal distortion of the SSB transmitter cancels the performance improvement achieved by increasing the modulation depth. For higher modulation depths the performance becomes degraded by the SSB transmitter.

6.3. XPM-Degradation of DPSK Signals due to ASK Signals in Mixed Modulation Format-Multi-Wavelength Transmission Systems

6.3.1. Principle

This section is devoted to analyzing the XPM-degradation of DPSK signals by ASK signals. It focuses on the particular case of 40 Gb/s DPSK signals installed in 10 Gb/s ASK infrastructure. Sub-section 6.3.2 presents a pump-probe analysis adapted to the study of DPSK signals. This analysis shows the relevance of the XPM-induced IM when using transmission systems with standard fiber and illustrate the strong dependence of this degradation on the residual dispersion. Sub-section 6.3.3 proposes a simplified model to compute the BER of a DPSK signal due to XPM-degradation induced by an interfering ASK signal. It is shown that the proposed model yields acceptable results when the degradation resulting from the XPM-induced IM is dominant.

Fig. 6.5 illustrates the principle used for the pump-probe analysis of the XPM-degradation of DPSK signals due to ASK signals. Similarly to what is usually considered for intensity modulated-directly detected systems, the propagation of a CW probe and an ASK pump channels along a transmission system is simulated. However, at the receiver side, the probe channel is demodulated by a delay interferometer (DI) and detected using a balanced photodetector followed by a differential amplifier, similarly to what is performed for directly detected DPSK systems [Gnauck, 2005]. The XPM induced on the probe by the pump along the transmission path will be converted by GVD and SPM in XPM-induced PM and IM.

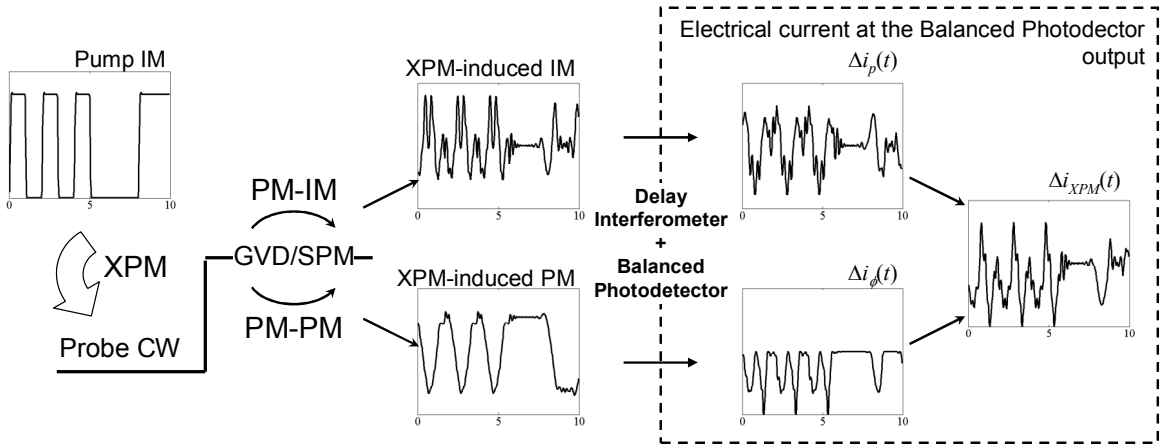

Fig. 6.5. Simplified diagram of the XPM contributions to the electrical current fluctuations at the DPSK receiver output.

As shown in Fig. 6.5, the DI and the balanced photodetector convert the XPM-contributions in electrical current fluctuations which would degrade the performance of the probe channel in case it was modulated. A separate analysis of these contributions allows assessing the effect of the system parameters on their relative magnitude. In particular, this work focuses on the dependence of the XPM degradation on the residual dispersion. Note that previous works have shown that the XPM-induced PM is governed by the walkoff parameter [Ho, 2004], whereas the XPM-induced IM depends also on the PM-to-IM conversion due to GVD and SPM along the link, which is related to the residual dispersion [Cartaxo, 1999:1]. As such, the dominant contribution will determine the relevant parameters to be considered for assessing the XPM-degradation. Numerical simulation shows that, unlike systems using only DPSK signals [Ho, 2004], the XPM-induced IM may become dominant when using SSMF.

6.3.2. Pump-Probe Analysis of XPM-Induced Intensity and Phase Fluctuations

Consider the simulated *N* sections transmission system presented in Fig. 6.6. A CW probe co-polarized with a 10 Gb/s NRZ - ASK pump are multiplexed with a wavelength spacing of 0.4 nm and transmitted. For Monte-Carlo simulations, the probe will be replaced by a 40 Gb/s DPSK signal, produced by phase modulating it with a differentially pre-coded deBruijn sequence. Each transmission section is composed by an 80 km transmission fiber segment, followed by a linear DCE and a noiseless optical amplifier, which fully compensate the dispersion and losses in that section. At the last section, a

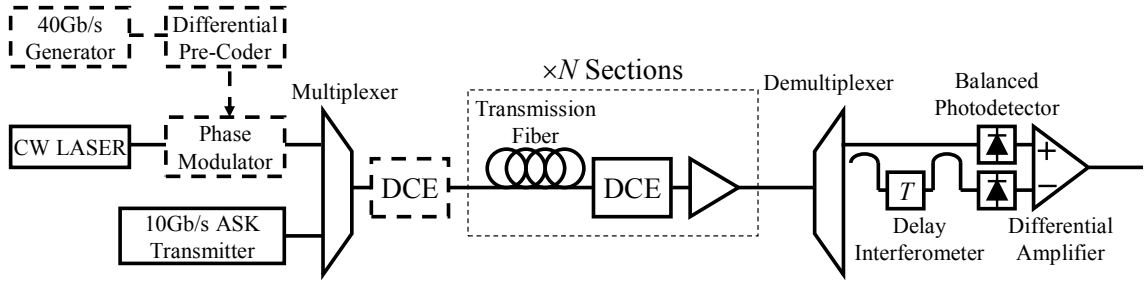

Fig. 6.6. Simulated transmission system for the pump-probe analysis of the XPM-degradation in mixed DPSK and ASK Systems.

given amount of dispersion may be left uncompensated, thus setting the residual dispersion of the link. In addition, a DCE may be placed at the transmitter side for dispersion pre-compensation. Note that the latter will have negligible impact on the XPM since this phenomena will only begin to occur at the first segment of transmission fiber. Transmission along the fiber is governed by the generalized coupled nonlinear Schrödinger equations and the relevant fiber parameters are presented in Table 6.1. The fibers considered in this work are SSMF and Truewave fiber (TW). At the receiver side, the probe is demultiplexed and fed to a DPSK receiver. The latter is composed by a DI with delay T=25 ps, corresponding to the symbol period of a 40 Gb/s DPSK signal, followed by a balanced photodetector and a differential amplifier with unitary overall gain. The impact of optical filtering will not be considered in this work.

To isolate the contributions of the XPM-induced IM and PM to the probe electrical current fluctuations, consider the optical field at the DI input generally approximated by:

$$u_s(t) = \sqrt{P + p_{XPM}(t)} \cdot \exp\left[j\phi_{XPM}(t) \right] \tag{6.4}$$

where P is the average probe power and $p_{XPM}(t)$ and $\phi_{XPM}(t)$ are the XPM-induced IM and

Parameter	SSMF	TW
Nonlinearity Coefficient, $W^{-1} \cdot km^{-1}$	1.37	1.5
Dispersion Parameter, ps/nm/km	17	2.8
Attenuation Coefficient, dB/km	0.22	0.25

Table 6.1. Transmission fiber parameters at a wavelength of 1550 nm.

PM, respectively. From (6.4), the electrical current at the DPSK receiver may be written as:

$$i_d(t) = P\sqrt{1+\Delta p_{XPM}(t)/P + p_{XPM}(t)\,p_{XPM}(t-T)/P^2}\cdot \cos\left[\Delta\phi_{XPM}(t)\right] \tag{6.5}$$

where $\Delta\phi_{XPM}(t)$ is the differential XPM-induced PM given by:

$$\Delta\phi_{XPM}(t) = \phi_{XPM}(t) - \phi_{XPM}(t-T) \tag{6.6}$$

and $\Delta p_{XPM}(t)$ will be referred as the differential XPM-induced IM, for simplicity, although it is not a differential signal:

$$\Delta p_{XPM}(t) = p_{XPM}(t) + p_{XPM}(t-T) \tag{6.7}$$

Equation (6.5) may be simplified assuming small XPM-impact as $p_{XPM}(t)<<P$ and $\Delta\phi_{XPM}(t)<<1$. Under such conditions, $i_d(t)$ becomes:

$$i_d(t) \approx P\left[1+\frac{\Delta p_{XPM}(t)}{2P}\right]\cdot\left[1-\frac{\Delta\phi^2_{XPM}(t)}{2}\right] \tag{6.8}$$

where the square root and cosine terms have been approximated by the first two terms of the corresponding *Taylor* series and the beating of the two XPM-induced IM terms in (6.5) was neglected. The XPM-induced current fluctuations will be approximated by:

$$\begin{aligned}\Delta i_{XPM}(t) &= i_d(t) - P = \Delta i_p(t) + \Delta i_\phi(t) - \frac{\Delta p_{XPM}(t)\,\Delta\phi^2_{XPM}(t)}{4} \\ &\approx \Delta i_p(t) + \Delta i_\phi(t)\end{aligned} \tag{6.9}$$

where $\Delta i_p(t)=\Delta p_{XPM}(t)/2$ and $\Delta i_\phi(t)=-P\cdot\Delta\phi^2_{XPM}(t)/2$ are the contributions to the electrical current fluctuations due to XPM-induced IM and PM, respectively illustrated in Fig. 6.5,

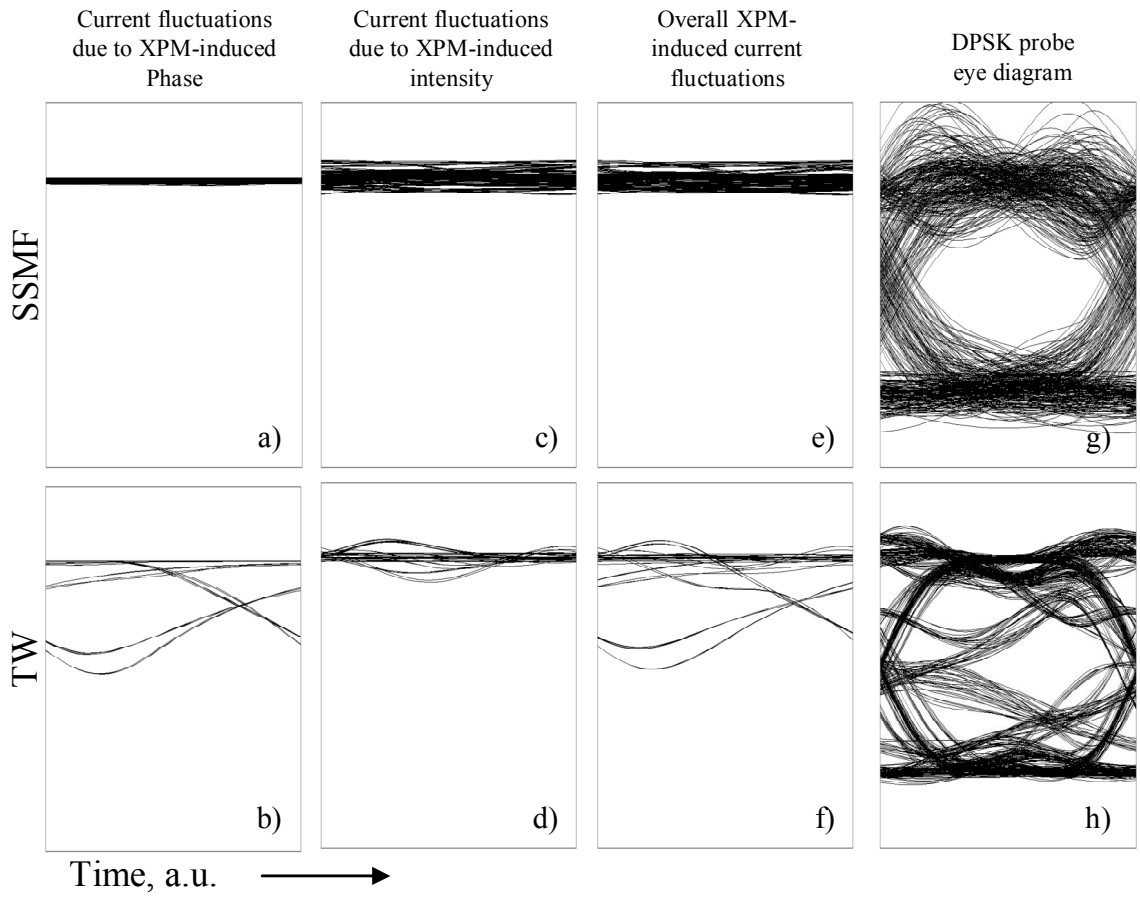

Fig. 6.7. Eye diagrams of the XPM-induced electrical current fluctuations of the probe. a) and b) – due to XPM-induced PM; c) and d) – due to XPM-induced IM; e) and f) total XPM-induced current fluctuations; g) and h) - eye diagrams assuming a 40 Gb/s DPSK probe. The top and bottom rows assume transmission through SSMF and TW with 400 ps/nm and null total residual dispersion, respectively.

and the term corresponding to the beating between the differential XPM-induced PM and IM contributions has been neglected. Equation (6.9) allows the rapid assessment of the contributions of XPM-induced PM and IM to the overall XPM-induced electrical current fluctuations.

To illustrate the application of (6.9), the system depicted in Fig. 6.6 is simulated, assuming a 20 sections system and an average power per channel of 0 dBm. Fig. 6.7-a)-f) present the eye patterns of the received electrical current of the probe. The XPM contributions have been isolated by taking $p_{XPM}(t)$ and $\phi_{XPM}(t)$ of the optical field prior to the DI and calculating $\Delta i_p(t)$ and $\Delta i_\phi(t)$ separately. Fig. 6.7-b), d) and f) show that, in the case of the TW with null total residual dispersion, the contribution of the XPM-induced PM is dominant with respect to the contribution of the XPM-induced IM, due to the low walkoff. With SSMF, the nonlinear coupling is reduced by the high walkoff but the

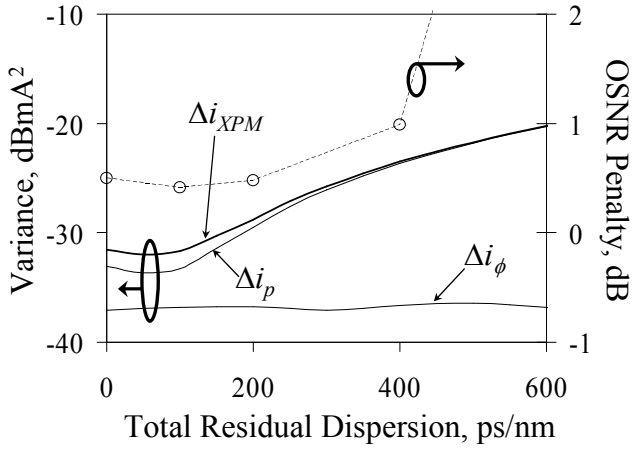

a) SSMF

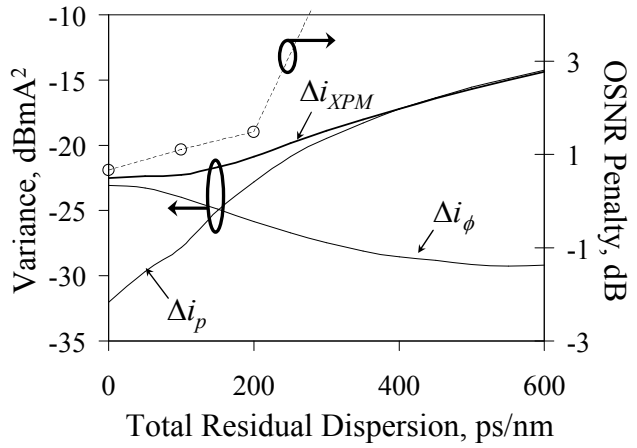

b) TW

Fig. 6.8. Comparison between the variances of the total XPM-induced current fluctuations and the contributions from the XPM-induced PM and IM obtained through pump-probe analysis using a) SSMF, 20 sections; and b) TW, 10 sections. The circles are the OSNR penalty obtained using Monte-Carlo simulation.

residual dispersion of 400 ps/nm increases the PM-IM conversion. As a consequence, the contribution of the XPM-induced IM to the electrical current fluctuations becomes dominant. For comparison with a case of normal transmission, we have replaced the CW probe with a DPSK signal and Fig. 6.7-g) and h) present the corresponding eye diagrams. In the case of nonzero residual dispersion, the DPSK signal is pre-compensated to maintain null accumulated dispersion. Fig. 6.7-g) and h) show that the degradation of the mark and space symbols resemble the CW probe fluctuations, particularly at the instant of maximum eye opening. An additional degradation of the DPSK eye diagram is also present due to SPM, which is not taken into account by the pump-probe analysis.

The dependence of the XPM-degradation on the residual dispersion of the link will be assessed by varying the dispersion compensation in the last section and estimating the

variance of the XPM-contributions to the electrical current fluctuations. Dispersion pre-compensation will not be considered at this point since a CW probe is used. Fig. 6.8-a) and –b) present this dependence considering SSMF and TW. The number of transmission sections using the TW was reduced to 10 due to the excessively high XPM-degradation. In the case of the SSMF, the contribution of the XPM-induced IM is dominant along the considered range, increasing with the total residual dispersion due to the corresponding increase of the PM-IM conversion. The XPM-induced PM is reduced by the high walkoff and varies negligibly with the total residual dispersion. When using TW, the contribution of the XPM-induced PM is dominant due to the low walkoff between channels for low residual dispersion (less than 200 ps/nm). However, for residual dispersion above 300 ps/nm the PM-IM conversion enhances the contribution of the XPM-induced IM, making it dominant. The presented results are merely an example for a fully dispersion compensated dispersion map. Further investigations presented in Appendix K have revealed that in most cases of interest, the XPM-induced IM is dominant with respect to the XPM-induced PM.

To relate the electrical current variances with the performance of a DPSK signal, Fig. 6.8-a) and –b) present the XPM-induced OSNR penalty, defined as the ratio between the required OSNR for a BER of 10^{-4} in single-channel operation and two channels operation. The required OSNR estimates were achieved by loading the signal with ASE noise prior to the DI to reach the required BER, computed using Monte-Carlo method. The final result was the average of the outcomes of 10 simulations using distinct delays between channels. This simulation scheme does not consider the impact of nonlinear phase noise, assuming that the XPM-degradation is dominant. Fig. 6.8 shows that the OSNR penalty follows, in a reasonable manner, the evolution of the variance of the XPM-induced electrical current fluctuations for both considered cases, generally increasing with the residual dispersion. Note that previous models considering only the XPM-induced PM would assume that the XPM-degradation is maintained or decreases with the residual dispersion, given the behavior of the XPM-induced PM. Such analysis would be accurate when using TW with low residual dispersion but would fail when using SSMF or even TW with high residual dispersion. As such, one may assume that performance estimates of a DPSK signal require accounting not only the XPM-induced PM but mainly the XPM-induced IM.

6.3.3. BER Degradation due to XPM

To derive a simplified analytical model for the BER of XPM-degraded DPSK signals, consider the DPSK receiver presented in Fig. 6.6, when assuming the probe modulated with a DPSK signal. In single-channel operation, the incoming signal presents an OSNR given by ρ. Neglecting the impact of the post-detection filter and assuming that the noise components at the output of the constructive and destructive ports of the DI are independent yields the PDF of the electrical current at the balanced photodetector output as [Jacobsen, 1994]:

$$p_I(x) = p_{I,q}(x) * p_{I,m}(-x) \tag{6.10}$$

where * denotes the convolution. $p_q(x)$ and $p_m(x)$ are the PDF of the electrical current at the output of the photodetectors associated with the constructive and destructive ports of the DI, respectively. For a mark symbol, $p_q(x)$ and $p_m(x)$ are given by [Chinn, 1996]:

$$p_{I,q}(x) = \frac{2\rho}{I_s}\exp\left[-\frac{2\rho}{I_s}(x+I_s)\right]\cdot I_0\left(\frac{4\rho}{I_s}\sqrt{x\cdot I_s}\right), \quad x>0 \tag{6.11}$$

$$p_{I,m}(x) = \frac{2\rho}{I_s}\exp\left(-\frac{2\rho\cdot x}{I_s}\right), \quad x>0 \tag{6.12}$$

where I_s is the average signal power at the DI input and $I_0(x)$ is the modified Bessel function of the first kind. For a space symbol the PDF of the electrical currents of the constructive and destructive ports are swapped. As a consequence, the PDF of the electrical decision circuit conditioned to the mark, $p_{I,1}(x)$, and space, $p_{I,0}(x)$, symbols are symmetrical, $p_{I,1}(x)=p_{I,0}(-x)$. The bit-error probability for a given decision threshold, x_{th}, is given by:

$$P_e(x_{th}) = \frac{1}{2}\int_{-\infty}^{x_{th}} p_{I,1}(x)\,dx + \frac{1}{2}\int_{x_{th}}^{+\infty} p_{I,0}(x)\,dx \tag{6.13}$$

which, under the conditions described above, is symmetrical and takes a minimum value at x_{th}=0 for $P_e(0) = 1/2 \cdot e^{-\rho}$ [Jacobsen, 1994].

Consider now that the impact of XPM may be approximated by assessing the electrical current fluctuations associated with the XPM-induced IM, $\Delta i_p(t)$, and XPM-induced PM, $\Delta i_\phi(t)$, as described in section 6.3.2. Due to the strong correlation between $\Delta i_p(t)$ and $\Delta i_\phi(t)$, an accurate description of the PDF of Δi_{XPM} is rather complex. However, in some cases of interest, one may consider that the impact of one of the XPM components is dominant. In such cases, the total XPM-induced current fluctuations may be approximated by the dominant component. As shown in section 6.3.2, the XPM-impact in systems with mixed modulation formats may be reduced almost exclusively to cases where the impact of the XPM-induced IM is dominant. Furthermore, the cases where the XPM-induced PM is dominant have been studied elsewhere, as described in sub-section 6.3.1. In the cases of interest here, we may approximate the XPM-induced current fluctuations by $\Delta i_{XPM}(t) \approx \Delta i_p(t)$. To obtain the PDF of $\Delta i_{XPM}(t)$ one may consider that, for a sufficiently high number of interfering channels or transmission sections, $p_{XPM}(t)$ is approximately Gaussian with null average and variance given by [Jiang, 2003]:

$$\sigma^2_{XPM,P} = \sum_{i=1}^{M} \left[\int_{-\infty}^{+\infty} S_i(f) \cdot \left| H_{XPM,P,i}(f) \right|^2 df \right] \tag{6.14}$$

where M is the number of interfering channels and $S_i(f)$ is the power spectral density of the i-th interfering channel. The term $H_{XPM,P,i}(f)$ corresponds to the transfer function of the equivalent linear model for the XPM-induced IM, computed for the system under study and the i-th interfering channel. Under these assumptions, one may consider that $\Delta i_{XPM}(t)$ is also Gaussian with null average and a variance, $\sigma^2_{\Delta i,XPM}$, obtained by including the impact of the DI on (6.14):

$$\sigma^2_{\Delta i,XPM} = \sum_{i=1}^{M} \left[\int_{-\infty}^{+\infty} S_i(f) \cdot \left| H_{XPM,P,i}(f) \right|^2 \cdot 2 \cdot \cos^2(\pi f T) \cdot df \right] \tag{6.15}$$

Given (6.15), one may approximate the PDF of the XPM-induced current fluctuations by:

$$p_{XPM}(x) = \frac{1}{\sqrt{2\pi\sigma^2_{\Delta i,XPM}}} \exp\left(-\frac{x^2}{2\sigma^2_{\Delta i,XPM}}\right) \tag{6.16}$$

Considering that the XPM-induced current fluctuations are independent of the original signal and noise components, the bit-error probability of the XPM-impaired DPSK signal, $P_{e,XPM}(x_{th})$, may be approximated using the principle proposed by Killey, et al. in [Killey, 2000: 1]:

$$P_{e,XPM}(x_{th}) = \frac{1}{2} p_{XPM}(x_{th}) * \int_{-\infty}^{x_{th}} p_{I,1}(x)\,dx + \frac{1}{2} p_{XPM}(-x_{th}) * \int_{x_{th}}^{+\infty} p_{I,0}(x)\,dx \tag{6.17}$$

Since $p_{XPM}(x)$ is symmetric, (6.17) may be written as:

$$P_{e,XPM}(x_{th}) = P_e(x_{th}) * p_{XPM}(x_{th}) \tag{6.18}$$

Expression (6.18) allows computing the minimum bit-error ratio for the XPM-impaired DPSK signal as:

$$P_{e,XPM}(0) = \int_{-\infty}^{+\infty} p_{XPM}(x) \cdot P_e(x) \cdot dx \tag{6.19}$$

Expression (6.19) provides a simple model to estimate the BER degradation of a DPSK signal due to XPM induced by neighboring ASK signals and may be numerically computed in a fraction of the time required for more complex yet more accurate methods [Gnauck, 2005].

To validate (6.19), consider the transmission system presented in Fig. 6.6 with 10 sections, assuming a DPSK modulated probe. ASE noise will be added to the signal at the receiver end, in order to reach an OSNR of 11 dB. Both channels are transmitted with an average power at the input of each section of 0 dBm. For comparison purposes, single-channel transmission of the DPSK signal will also be considered. The XPM impact was calculated by assessing the BER as a function of the decision threshold for single DPSK

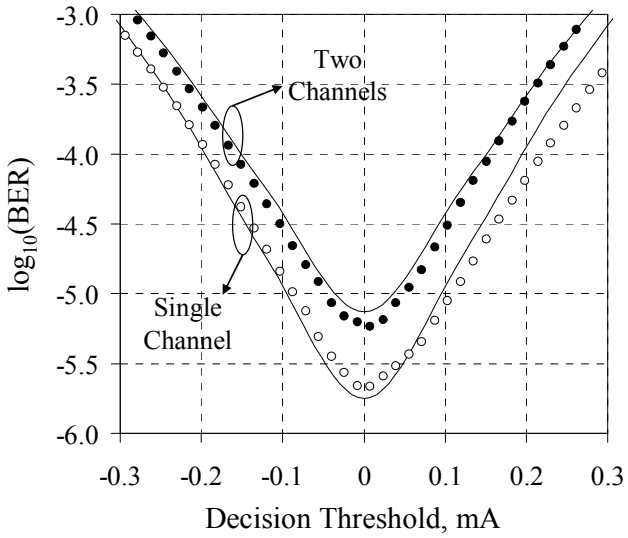

Fig. 6.9. BER as a function of the decision threshold considering a pre-compensation value of 200 ps/nm circles – Monte Carlo result; lines – Analytical results.

channel transmission and two channels transmission, as presented in Fig. 6.9. For this example, a dispersion precompensation value of 200 ps/nm was assumed. The results where obtained using Monte Carlo simulation and the analytical model presented previously in this section, where the variance of the XPM-induced intensity noise was obtained using the model proposed by [Luís, 2005: 1]. As shown, the proposed model follows the Monte Carlo result with reasonable accuracy, reflecting the impact of the XPM-degradation on the BER. Note that the discrepancies observed for the single-channel case result from the impact of SPM, which is neglected by the presented model. Such discrepancies are less significant for two channels transmission as the XPM becomes the dominant impairment.

Fig. 6.10 presents the dependence of the Q-factor on the pre-compensated dispersion for single and two channels operation, calculated using Monte Carlo simulation and the proposed analytical model. Monte Carlo results show a minimum XPM-penalty of less than 0.5 dB for a pre-compensated dispersion of 100 ps/nm. This penalty increases rapidly with the pre-compensated dispersion, surpassing 1 dB for values above 250 ps/nm. Note that the value of dispersion pre-compensation for minimum penalty and the limit for 1 dB of degradation are reasonably well predicted by the analytical model, validating its application for the design of such systems. The discrepancies observed for low values of dispersion pre-compensation (less than 100 ps/nm) between the analytical and simulation results obtained for two channels operation result from the fact that, for such values, the

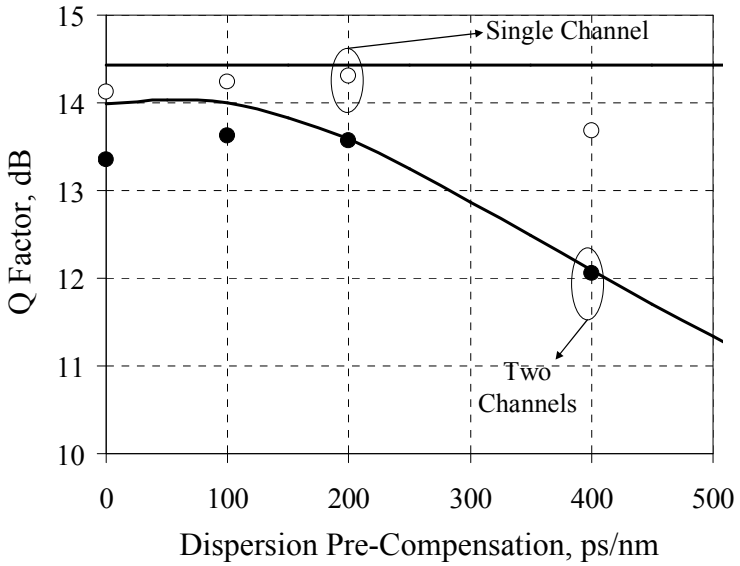

Fig. 6.10. Q-Factor as a function of the amount of dispersion pre-compensation
circles – Monte Carlo results; lines – Analytical results.

XPM-induced intensity noise is no longer dominant, as shown in section 6.3.2. In such cases a more accurate analysis using more rigorous methods is required. Note also that the discrepancies observed on the single channel analytical and simulation results for high pre-compensation values (higher than 350 ps/nm) are due to the impact of SPM.

6.4. Intra-Channel Fiber Nonlinearities in Signals with Finite Extinction Ratio

6.4.1. Principle

To analyze the intra-channel fiber nonlinearities, consider the work of Mamyshev et al. presented in [Mamyshev, 1999]. Mamyshev et al proposed to distinguish the impact of intra-channel fiber nonlinearities in signals composed of RZ impulses according to the relation between the pulse-width of the transmitted RZ impulses, t_0, and the symbol period, T. For the cases with $t_0 < T$, it is considered that the system is operating in a solitonic regime, where the pulse shape is maintained throughout the transmission link. However, for $t_0 > T$, it was shown that the nonlinear interactions were substantially reduced due to the temporal spreading of each impulse over a large interval. This became referred as pulse-overlapped transmission regime [Mamyshev, 1999], also known as pseudo-linear regime.

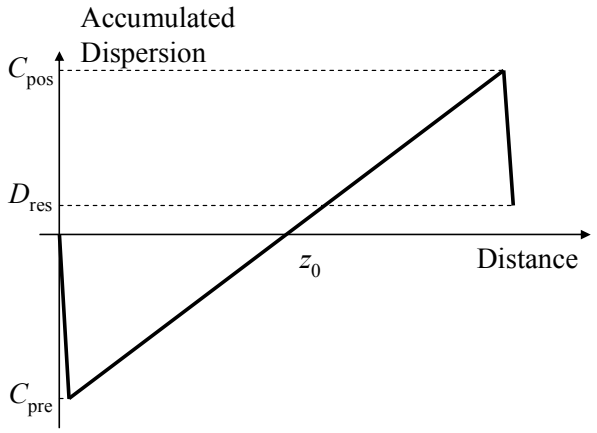

Fig. 6.11. Dispersion compensation map for the analysis of intra-channel fiber nonlinearities.

Essiambre et al. showed in [Essiambre, 1999] that the pseudo-linear regime is characterized by fast changes of the signal waveform due to GVD, accompanied by strong nonlinear phenomena. This corresponds, in a general form, to the transmission of high bit-rate signals in moderately dispersive fibers Under these conditions, the signal is dominantly degraded by intra-channel nonlinear effects such as IFWM, originating amplitude jitter in the mark symbols and ghost pulses is the space symbols, and IXPM, leading to temporal jitter of the impulses [Essiambre, 2002]. Optimized performance may be achieved using a symmetrical dispersion map, as shown in Fig. 6.11 for a link with a single transmission fiber section [Mecozzi, 2000], [Mecozzi, 2001]. Prior to transmission, a linear DCE with a total dispersion C_{pre}, performs dispersion pre-compensation of the signal. Along the transmission fiber, the signal accumulates a given amount of dispersion $L \cdot D$, where L is the fiber length and D is the dispersion parameter. At the end of the link, the total accumulated dispersion of the signal is reduced by another DCF segment with a total dispersion C_{pos}. We will characterize this particular dispersion compensation map using the total accumulated dispersion of the link, given by $D_{res}=C_{pre}+L \cdot D+C_{pos}$ and the coordinate of the transmission fiber with null accumulated dispersion, $z_0=-C_{pre}/D$. Design rules for such systems have been presented in [Killey, 2000: 2], setting the optimum z_0 at a coordinate near the middle of the link (depending on the attenuation coefficient of the transmission fiber) and nearly null D_{res} [Mecozzi, 2001]. The latter characteristic is similar to what is usually observed in un-chirped linear transmission regimes, hence the designation of pseudo-linear regime. It is a well known result that in optimum conditions the impact of IXPM is nearly canceled and the impact of IFWM is substantially reduced

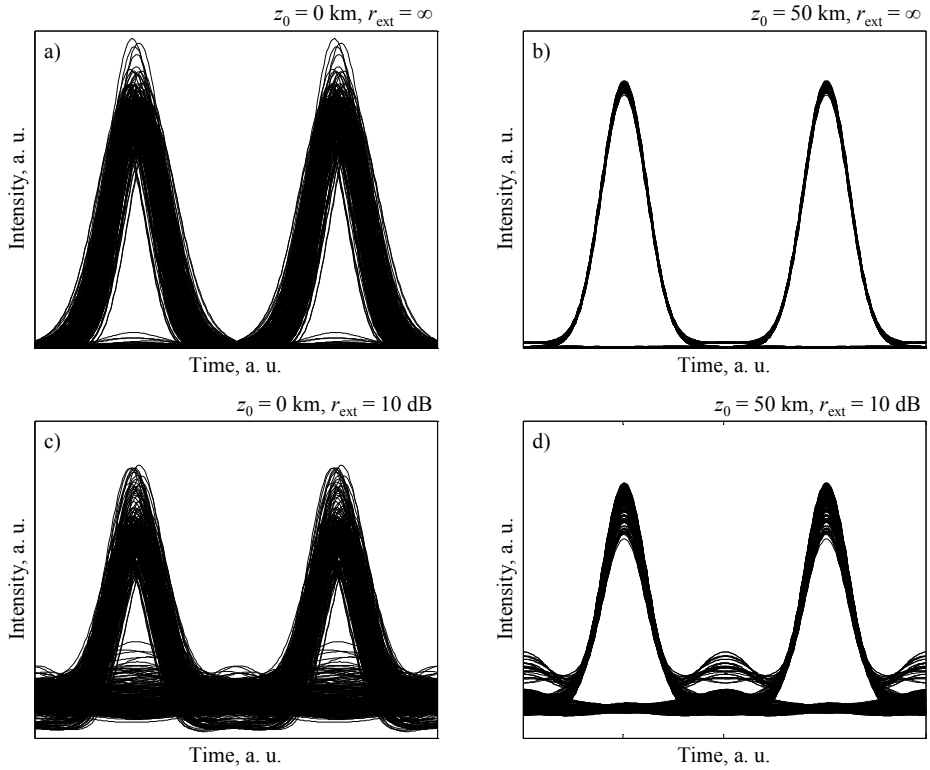

Fig. 6.12. Comparison of the eye diagrams of a 40 Gb/s RZ signal with 10 dB and infinite extinction ratio, assuming an asymmetric dispersion compensation map (z_0=0 km) and a symmetric dispersion compensation map (z_0=50 km). All cases assume null residual dispersion, D_{res}=0 ps/nm.

[Mecozzi, 2001]. This is illustrated in Fig. 6.12-a) and -b), which present the simulated eye diagrams of a 40 Gb/s RZ signal with infinite extinction ratio, a full-width at half maximum of 6.6 ps and a peak power of 25 mW transmitted through the considered system. For illustrative purposes we have assumed a lossless fiber, to enhance the impact of nonlinear phenomena, with a length of 100 km, dispersion parameter of 2.8 ps/nm/km, and nonlinearity coefficient γ=1.5 $W^{-1}\cdot km^{-1}$. Fig. 6.12-a) shows that, for z_0=0 km, the signal is significantly degraded by temporal jitter, due to IXPM, and presents well noticeable ghost pulses in the space symbols and amplitude jitter in the mark symbols, resulting from IFWM. When z_0 is increased to 50 km the temporal jitter is nearly canceled and the amplitude jitter of the mark symbols and ghost pulses are minimized, as predicted in [Mecozzi, 2001].

The approach followed in this work considers more realistic signals with finite extinction ratio and has been first suggested by Fonseca, et al. in [Fonseca, 2007: 1]. This reference shows that nonzero power in the space symbols yields strong power fluctuations at these symbols, dominantly degrading the system performance. This effect is illustrated

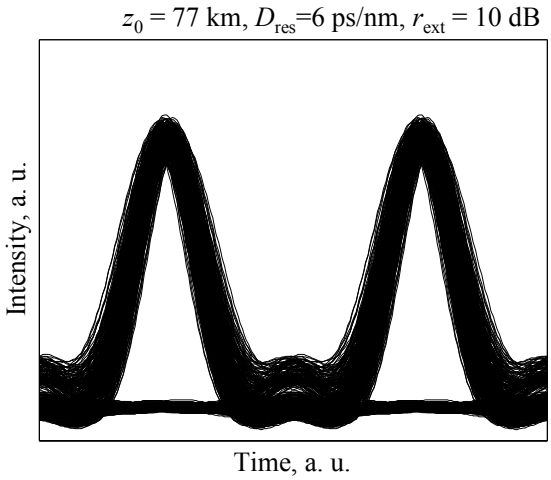

Fig. 6.13. Eye diagrams of a 40 Gb/s RZ signal with 10 dB extinction ratio, assuming an optimized asymmetric dispersion compensation map with z_0=77 km and D_{res}=6 ps/nm.

in Fig. 6.12-c) and d), which present the simulated eye diagrams of a signal under the same conditions as the one used for Fig. 6.12-a) and b), but with an extinction ratio r_{ext} = 10 dB. As shown in Fig. 6.12-c), the impact of fiber nonlinearities yields amplitude and temporal jitter of the mark symbols, similar to what is verified in Fig. 6.12-a) for infinite extinction ratio.

However, the degradation of the space symbols clearly exceeds the previously observed for infinite extinction ratio. Significant power fluctuations arise in the space symbols, as a result of the non-negligible nonlinear interaction with the mark symbols. In addition, new ghost pulses arise in the time interval between consecutive mark impulses. These new symbols are clearly distinguishable in Fig. 6.12-d), where the IXPM and IFWM are canceled and minimized, respectively. In this figure, it is shown that the nonzero power of the space symbols yields interactions with the mark symbols which are not foreseen by the conventional approach to intra-channel nonlinearities. These interactions result in additional amplitude jitter of the mark and space symbols and some non-negligible temporal jitter. In addition we have a new form of ghost pulses, which for distinction, will be referred here as “child pulses”. As a consequence of the additional distortion, Fonseca et al. have shown that the optimum dispersion compensation map is substantially altered by setting z_0 away from the middle of the link and leaving a relatively high residual dispersion. The latter characteristic is typical of solitonic transmission regimes. As such, this particular transmission regime has been named pseudo-solitonic [Fonseca, 2007: 1]. For illustration purposes, Fig. 6.13 presents the eye pattern of the signal used to obtain Fig.

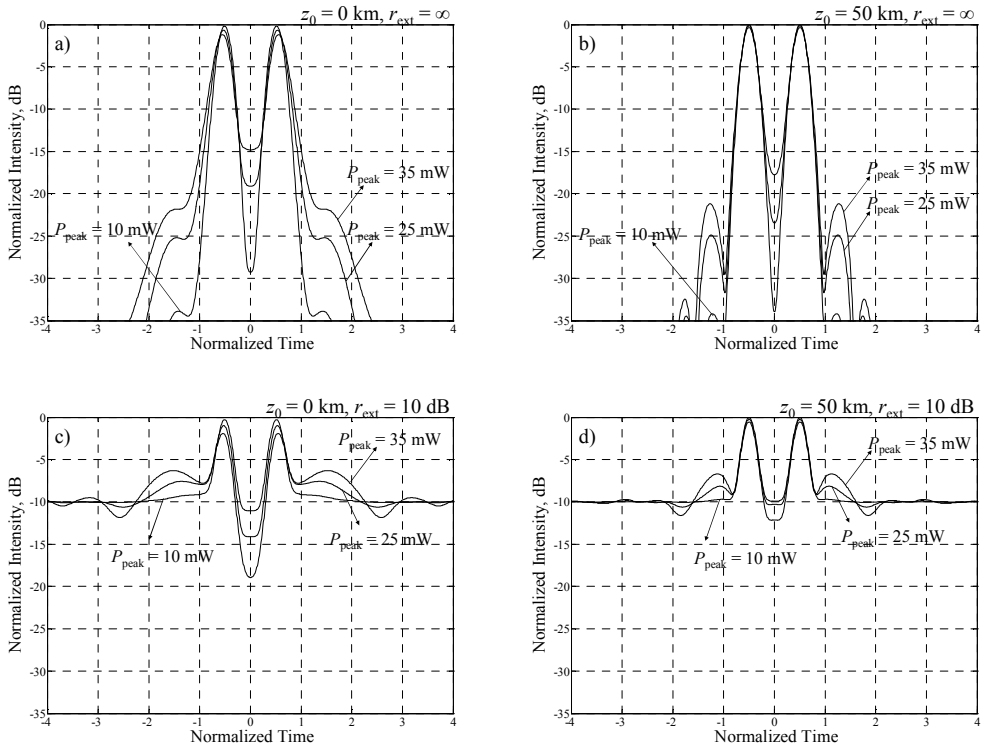

Fig. 6.14. Comparison of the traces of two RZ impulses with a spacing of 25 ps after transmission, with 10 dB and infinite extinction ratios, assuming an asymmetric dispersion compensation map (z_0=0 km) and a symmetric dispersion compensation map (z_0=50 km). All cases assume D_{res}=0 ps/nm and peak powers of 10 mW, 25 mW, and 35 mW. The time axis is normalized to the symbol period and the intensity axis is normalized to the peak power.

6.12-c) and d) with optimized dispersion compensation map (z_0 = 77 km, and D_{res} = 6 ps/nm). This optimization was performed by extensively varying z_0 and D_{res} to find the minimum EOP. It is shown that the optimized case corresponds to a minimization of the amplitude jitter of the mark and space symbols with an increase of the temporal jitter. Note that using other optimization criteria, such as mask opening penalty (see [Elbers, 2000]) would yield a substantially distinct result.

For a more complete illustration of the degradation involved in the pseudo-solitonic transmission regime, Fig. 6.14-a) to –d) present the simulated traces of a signal consisting of two mark impulses surrounded by space symbols after transmission in the considered system, assuming D_{res}=0, z_0=0 km and z_0=50 km, with infinite and 10 dB extinction ratios. Impulse peak powers, P_{peak}, of 10 mW, 25 mW, and 35 mW have been assumed. In the case of Fig. 6.14-a) and -b), the impact of IXPM is clearly noticeable by observing the shift of the center of mass of the transmitted impulses whereas IFWM generates ghost impulses adjacent to the transmitted impulses. The latter will have most significant impact on the

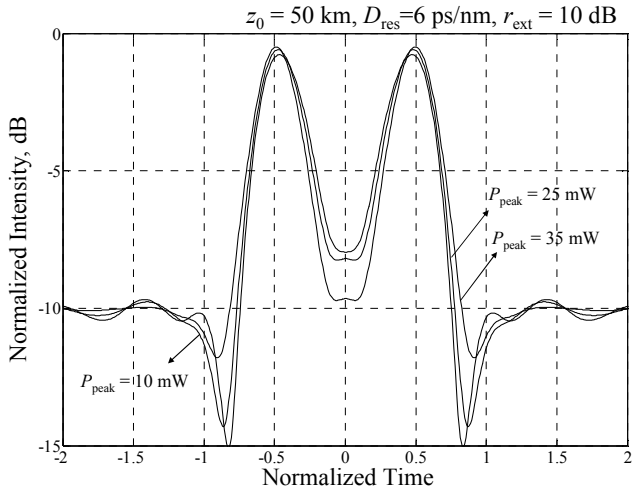

Fig. 6.15. Traces of two RZ impulses with a spacing of 25 ps after transmission, with 10 dB extinction ratio, assuming an optimized dispersion compensation map with z_0=77 km and D_{res}=6 ps/nm, for peak powers of 10 mW, 25 mW, and 35 mW. The time axis is normalized to the symbol period and the intensity axis is normalized to the peak power.

symbols immediately adjacent to the transmitted impulses. Setting z_0=50 km nearly cancels the temporal shift of the impulses and reduces significantly the magnitude of the ghost pulses.

In case of finite extinction ratio, presented in Fig. 6.14-c) and -d), the perturbation of the space symbols has a significantly higher magnitude than the perturbations observed with infinite extinction ratio, and extends for a large number of symbols adjacent to the transmitted impulses. Furthermore, one may notice the increase of the power at the center of the impulses, which eventually results in the formation of the child impulse between the original impulses, similarly to what is observed in collisions between solitons. Note that, unlike soliton transmission, where the signal shape is preserved throughout the transmission path, the transmitted signal undergoes significant waveform changes due to the strong impact of GVD. Increasing z_0 to 50 km tends to compress the perturbation generated by the original impulses to a smaller time interval. However, it has little impact on reducing its magnitude. Fig. 6.15 presents the trace of the two impulses considered in Fig. 6.14-c) and -d), when setting the previously determined optimized values of z_0 and D_{res}. As shown in Fig. 6.15, the optimized dispersion map leads to a substantial reduction of the magnitude of the nonlinear perturbation, resulting in an improved system performance. However, the presented trace shows that the increase of the power at the center of the two impulses is not reduced. Furthermore, the impact of IXPM and IFWM is

strongly increased in comparison with the case of z_0=50 km, which translates in strong temporal jitter. This results in the distortion previously observed in Fig. 6.13.

The following work presented in this section regards a more formal analysis of the intra-channel fiber nonlinearities in signals with finite extinction ratio, following the simulation work performed by Fonseca et al. in [Fonseca, 2007: 1]. Analytical expressions for the nonlinear distortion is derived using a small-perturbations model and their validity is assessed in section 6.4.2. Section 6.4.3 presents a discussion of the achieved results.

6.4.2. Small-Perturbations Analysis

6.4.2.1. General Model

To analyze intra-channel nonlinearities in signals with finite extinction ratio, consider the normalized field envelope of the transmitted signal $u(z,t)$. It is assumed that, at the fiber input, $u(0,t)$ takes the form of a linear superposition of M components, $u_i(z,t)$, as:

$$u(0,t) = \sum_{i=1}^{M} u_i(0,t) \tag{6.20}$$

When considering signals with infinite extinction ratio, it can be assumed that the i-th component represents the i-th symbol, as taken in [Mecozzi, 2000], [Mecozzi, 2001], and [Essiambre, 2002], among others, to describe intra-channel nonlinearities. However, in the case of finite extinction ratio, it will be considered that the M-th component has constant power, corresponding to the zero level. This component will be referred here as zero component whereas the remaining components will be named impulse components. Note that although the zero component has constant power, it is necessary to include phase modulation to match the phase modulations present in the other components as:

$$\arg\left[u_M(0,t)\right] = \sum_{i=1}^{M-1} \arg\left[u_i(0,t)\right] \tag{6.21}$$

where the term arg[x] denotes the argument of x. For simplicity, it will be assumed that all the signal components are in-phase, hence arg[$u_M(0,t)$] becomes constant or null.

Propagation of the signal along the fiber may be described using the nonlinear Schrödinger equation [Kazousky, 1996] (see page 478):

$$\frac{\partial u(z,t)}{\partial z} + j\frac{\lambda^2}{4\pi c}\frac{dD_{ac}(z)}{dz}\frac{\partial^2 u(z,t)}{\partial t^2} - \frac{1}{2g(z)}\frac{dg(z)}{dz}u(z,t) = -j\gamma\left|u(z,t)\right|^2 \cdot u(z,t) \tag{6.22}$$

where γ, λ and c are the nonlinearity coefficient, the central wavelength of the signal and the speed of light in vacuum, respectively. The term $g(z)$ represents the net gain of the link at the z coordinate. For instance, for a single fiber segment with no inline amplification, $g(z)$ becomes $g(z)=\exp(-\alpha z)$, with α as the attenuation coefficient of the fiber. Similarly, $D_{ac}(z)$ represents the accumulated dispersion of the link at the z coordinate. Once again, for a single fiber segment link with no dispersion compensation we have $D_{ac}(z)=D\,z$, with D as the dispersion parameter of the fiber. In the case of a dispersion pre-compensated link, $D_{ac}(z)$ takes the form $D_{ac}(z)=C_{pre} + D\,z$. Note that (6.22) uses the engineers' notation, which differs from the physics' notation used in [Mecozzi, 2000], [Mecozzi, 2001], and [Essiambre, 2002] without changing the significance of the results. Furthermore, the high order terms of dispersion have been neglected for simplicity. To describe the intra-channel nonlinearities, a small perturbations analysis will be performed, similarly to the method presented in [Mecozzi, 2000]. As such, it will be considered that the signal can be written in the form:

$$u(z,t) = u_0(z,t) + \Delta u(z,t) \tag{6.23}$$

where $\Delta u(z,t)$ is the nonlinear perturbation and $u_0(z,t)$ is the information component. It is assumed that each component $u_i(z,t)$ corresponds to its counterpart, $u_{0,i}(z,t)$. Since it is considered that $u_0(z,t)$ propagates linearly through the fiber, it can be described by:

$$\frac{\partial u_0(z,t)}{\partial z} + j\frac{\lambda^2}{4\pi c}\frac{dD_{ac}(z)}{dz}\frac{\partial^2 u_0(z,t)}{\partial t^2} - \frac{1}{2g(z)}\frac{dg(z)}{dz}u_0(z,t) = 0 \tag{6.24}$$

Hence replacing (6.23) and (6.24) in (6.22) yields the equation for the propagation of the nonlinear perturbation as:

$$\frac{\partial \Delta u(z,t)}{\partial z} + j\frac{\lambda^2}{4\pi c}\frac{dD_{\text{ac}}(z)}{dz}\frac{\partial^2 \Delta u(z,t)}{\partial t^2} - \frac{1}{2g(z)}\frac{dg(z)}{dz}\Delta u(z,t) = -j\gamma\left|u(z,t)\right|^2 \cdot u(z,t) \tag{6.25}$$

Equation (6.25) can be significantly simplified if it is assumed that the nonlinear perturbation will not generate further nonlinear contributions. This allows replacing $u(z,t)$ by $u_0(z,t)$ in (6.25), which produces the equation usually used to describe the propagation of the nonlinear perturbation [Essiambre, 2002]:

$$\frac{\partial \Delta u(z,t)}{\partial z} + j\frac{\lambda^2}{4\pi c}\frac{dD_{\text{ac}}(z)}{dz}\frac{\partial^2 \Delta u(z,t)}{\partial t^2} - \frac{1}{2g(z)}\frac{dg(z)}{dz}\Delta u(z,t) = -j\gamma\left|u_0(z,t)\right|^2 \cdot u_0(z,t) \tag{6.26}$$

To distinguish the contributions of each component of $u(z,t)$ we replace (6.20) in (6.26), yielding [Essiambre, 2002]:

$$\frac{\partial \Delta u(z,t)}{\partial z} + j\frac{\lambda^2}{4\pi c}\frac{dD_{\text{ac}}(z)}{dz}\frac{\partial^2 \Delta u(z,t)}{\partial t^2} - \frac{1}{2g(z)}\frac{dg(z)}{dz}\Delta u(z,t) = -j\gamma\sum_{m=1}^{M}\sum_{n=1}^{M}\sum_{p=1}^{M} u_{0,m}(t,z)\cdot u_{0,n}^{*}(t,z)\cdot u_{0,p}(t,z) \tag{6.27}$$

Assuming that the nonlinear perturbation may also be separated in different components as:

$$\Delta u(z,t) = \sum_{m=1}^{M}\sum_{n=1}^{M}\sum_{p=1}^{M}\Delta u_{m,n,p}(z,t) \tag{6.28}$$

equation (6.27) can be written as a set of $m\times n\times p$ coupled nonlinear equations [Essiambre, 2002]:

$$\frac{\partial \Delta u_{m,n,p}(z,t)}{\partial z} + j\frac{\lambda^2}{4\pi c}\frac{dD_{ac}(z)}{dz}\frac{\partial^2 \Delta u_{m,n,p}(z,t)}{\partial t^2} - \frac{1}{2g(z)}\frac{dg(z)}{dz}\Delta u_{m,n,p}(z,t) = \\ -j\gamma \cdot u_{0,m}(t,z)\cdot u_{0,n}^{*}(t,z)\cdot u_{0,p}(t,z) \tag{6.29}$$

Taking the Fourier transform, (6.29) can be written as:

$$\frac{\partial \Delta \tilde{u}_{m,n,p}(z,\omega)}{\partial z} - \left(\frac{1}{2g(z)}\frac{dg(z)}{dz} + j\frac{\lambda^2\omega^2}{4\pi c}\frac{dD_{ac}(z)}{dz}\right)\cdot \Delta \tilde{u}_{m,n,p}(z,\omega) = \\ -j\gamma \cdot \mathcal{F}\left[u_{0,m}(t,z)\cdot u_{0,n}^{*}(t,z)\cdot u_{0,p}(t,z)\right] \tag{6.30}$$

where ω is the angular frequency, $\mathcal{F}(\cdot)$ denotes the Fourier transform, and $\Delta\tilde{u}_{m,n,p}(z,\omega)=\mathcal{F}[\Delta u_{m,n,p}(z,t)]$. To solve (6.30) we start by making a variable transform:

$$\Delta \tilde{u}_{m,n,p}(z,\omega) = \tilde{a}(z,\omega)\cdot \exp\left\{\frac{\ln\left[g(z)\right]}{2} + j\frac{\lambda^2\omega^2}{4\pi c}D_{\text{ac}}(z)\right\} \tag{6.31}$$

Thus replacing (6.31) in (6.30) yields:

$$\frac{\partial \tilde{a}(z,\omega)}{\partial z} = -j\gamma \cdot \mathcal{F}\left[u_{0,m}(t,z)\cdot u_{0,n}^{*}(t,z)\cdot u_{0,p}(t,z)\right]\cdot \\ \exp\left[-\frac{\ln\left[g(z)\right]}{2} - j\frac{\lambda^2\omega^2}{4\pi c}D_{\text{ac}}(z)\right] \tag{6.32}$$

A solution of (6.32) is given by:

$$\tilde{a}(L,z) = \tilde{a}(0,z) - j\gamma \cdot \int_0^L \mathcal{F}\left[u_{0,m}(t,z)\cdot u_{0,n}^{*}(t,z)\cdot u_{0,p}(t,z)\right]\cdot \\ \exp\left[-\frac{\ln\left[g(z)\right]}{2} - j\frac{\lambda^2\omega^2}{4\pi c}D_{\text{ac}}(z)\right]\cdot dz \tag{6.33}$$

where L is the length of the link. By taking back the variable transform, (6.33) becomes:

$$\begin{aligned}\Delta\tilde{u}_{m,n,p}(L,\omega) = \Delta\tilde{u}_{m,n,p}(0,\omega)\cdot\sqrt{\frac{g(L)}{g(0)}}\exp\left\{j\frac{\lambda^2\omega^2}{4\pi c}\left[D_{\text{ac}}(L)-D_{\text{ac}}(0)\right]\right\}- \\ j\gamma\int_0^L \mathcal{F}\left[u_{0,m}(t,z)\cdot u_{0,n}^*(t,z)\cdot u_{0,p}(t,z)\right] \\ \cdot\sqrt{\frac{g(L)}{g(z)}}\exp\left\{j\frac{\lambda^2\omega^2}{4\pi c}\left[D_{\text{ac}}(L)-D_{\text{ac}}(z)\right]\right\}\cdot dz\end{aligned} \tag{6.34}$$

The final result is obtained using the inverse Fourier transform:

$$\begin{aligned}\Delta u_{m,n,p}(L,t) = \mathcal{F}^{-1}\left\{\Delta\tilde{u}_{m,n,p}(0,\omega)\cdot\sqrt{\frac{g(L)}{g(0)}}\right. \\ \left.\cdot\exp\left[j\frac{\lambda_0^2\omega^2}{4\pi c}\left[D_{\text{ac}}(L)-D_{\text{ac}}(0)\right]\right]\right\}- \\ j\gamma\int_0^L \mathcal{F}^{-1}\left\langle\mathcal{F}\left[u_{0,m}(t,z)\cdot u_{0,n}^*(t,z)\cdot u_{0,p}(t,z)\right]\cdot\right. \\ \left.\sqrt{\frac{g(L)}{g(z)}}\exp\left\{j\frac{\lambda^2\omega^2}{4\pi c}\left[D_{\text{ac}}(L)-D_{\text{ac}}(z)\right]\right\}\right\rangle\cdot dz\end{aligned} \tag{6.35}$$

where $\mathcal{F}^{-1}(\cdot)$ denotes the inverse Fourier transform. The first term on the right hand side of (6.35) corresponds to the propagation of the nonlinear perturbation present at the input of the link to the output of the link. This term is often considered null when assumed that the transmission system starts at the beginning of the link under consideration. The second term represents the integral sum of the contributions for the nonlinear perturbation, generated at each coordinate z of the link and propagated linearly to the output of the link. The model presented by (6.35) will be used throughout this section to describe intra-channel nonlinearities. Nevertheless, one must first note that (6.35) allows only an estimate of the impact of such nonlinearities. As a consequence, it may be used to assess magnitude

and impact of the intra-channel nonlinearities in changing the phase and amplitude of the signal components but not its absolute influence on the original signal.

6.4.2.2. Application of the Small-Perturbations Model for Gaussian Impulses

The assumption of signals with gaussian impulses has the advantage of providing a closed form analytical formulation for the integrand term in (6.35). This allows a significant insight on the behavior of the nonlinear perturbation and is often used in the literature to justify the nonlinear phenomena observed. In the presented case, it will be considered that the components of the transmitted signal at the input of the link are given by:

$$\begin{aligned} u_i(0,t) &= A_p \cdot \exp\left(-\frac{(t-T_i)^2}{2\tau^2}\right), \quad i < M \\ u_M(0,t) &= A_z \end{aligned} \tag{6.36}$$

where A_p and A_z are the optical field amplitude of the gaussian impulses and the zero level, respectively, normalized in a way that:

$$\begin{aligned} A_p &= \sqrt{P_{peak}} \cdot \left(1 - 1/\sqrt{r}\right) \\ A_z &= \sqrt{P_{peak}/r} \end{aligned} \tag{6.37}$$

and $\tau = t_0/[4\cdot\ln(2)]^{0.5}$ with t_0 as the full width at half maximum of the transmitted impulses. T_i is the temporal location of the i-th impulse. The linearly transmitted components of the signal, $u_{0,i}(z,t)$ may be described by [Agrawal, 1997]:

$$\begin{aligned} u_{0,i}(z,t) &= \frac{A_p \tau \cdot \sqrt{g(z)}}{\sqrt{R(z)}} \cdot \exp\left[-\frac{(t-T_i)^2}{2 \cdot R(z)}\right], \quad i < M \\ u_{0,M}(z,t) &= A_z \cdot \sqrt{g(z)} \end{aligned} \tag{6.38}$$

with

$$R(z) = \tau^2 - j\,\lambda^2/(2\pi c)\cdot D_{\text{ac}}(z) \tag{6.39}$$

As such, the term $u_{0,m}(t,z)\cdot u_{0,n}^{*}(t,z)\cdot u_{0,p}(t,z)$ in (6.35) can be written in the forms presented in Table 6.2, depending on the choice for the values of *m*, *n*, and *p*. Note that the term corresponding to $m\neq M$, $n\neq M$ and $p\neq M$ is the only existing term in the case of signals with infinite extinction ratio. This corresponds to the interaction between three impulse components, generating a nonlinear perturbation located approximately at T_m-T_n+T_p. This interaction will generate the well know effects of IXPM, IFWM, and SPM [Essiambre, 2002]. Note that the interaction between three symbol components does not include the power of the zero component. This will be included when considering the five additional contributions to the nonlinear perturbation resulting from the interaction between two impulse components and the zero component, given by expressions (6.42) and (6.43); the interaction between a single impulse component and the zero component, given by expressions (6.44) and (6.45); and finally, the interaction of the zero component with itself, given by expression (6.46). The latter is constant and corresponds to SPM of the zero component. The interactions between a single impulse component and the zero component, corresponding to the combinations $m\neq M$, $n=M$, $p=M$; $m=M$, $n=M$, $p\neq M$; and $n\neq M$, $p=M$, $m=M$, generate contributions located at the corresponding symbol time slot, yielding the additional SPM of each component due to the zero level power. It will be shown that the degradation of signals with finite extinction ratio results from the interaction of two impulses with the zero component.

To analyze the additional nonlinear perturbations we begin by considering the case $m\neq M$, $n=M$, $p\neq M$. Replacing the corresponding expression (6.42) for $u_{0,m}(t,z)\cdot u_{0,n}^{*}(t,z)\cdot u_{0,p}(t,z)$ from Table 6.2 in (6.35) and considering $\Delta\tilde{u}_{m,n,p}(0,\omega)=0$ yields:

$$\Delta u_{m,n,p}(L,t) = \int_0^L \frac{-j\gamma A_p^2 A_z \tau^2 g(z)\sqrt{g(L)}}{\sqrt{R(z)}\sqrt{R(z)+2j\,\lambda^2/(\pi c)\left(D_{\text{res}}-D_{\text{ac}}(z)\right)}}\cdot \exp\left\{-\frac{\left(T_m-T_p\right)^2}{4R(z)}-\frac{\left[t-\left(T_m+T_p\right)/2\right]^2}{R(z)-j\,\lambda^2/(\pi c)\left(D_{\text{res}}-D_{\text{ac}}(z)\right)}\right\}\cdot \mathrm{d}z \tag{6.40}$$

	$u_{0,m}(t,z)\cdot u_{0,n}^{*}(t,z)\cdot u_{0,p}(t,z)$	
$m\neq M$, $n\neq M$ and $p\neq M$	$\frac{A_p^3\tau^3\cdot g^{3/2}(z)}{\lvert R(z)\rvert\sqrt{R(z)}}\cdot\exp\left[-\frac{(t-T_m)^2+(t-T_p)^2}{2\cdot R(z)}-\frac{(t-T_n)^2}{2\cdot R^{*}(z)}\right]$	(6.41)
$m\neq M$, $n=M$, $p\neq M$	$\frac{A_p^2A_z\tau^2\cdot g^{3/2}(z)}{R(z)}\cdot\exp\left[-\frac{(T_m-T_p)^2}{4R(z)}\frac{\left[t-(T_m+T_p)/2\right]^2}{R(z)}\right]$	(6.42)
$m=M$, $n\neq M$, $p\neq M$ or $m\neq M$, $n\neq M$, $p=M$	$\frac{A_p^2A_z\tau^2\cdot g^{3/2}(z)}{\lvert R(z)\rvert}\cdot\exp\left[-\frac{(t-T_{m,p})^2}{2\cdot R(z)}-\frac{(t-T_n)^2}{2\cdot R^{*}(z)}\right]$	(6.43)
$m\neq M$, $n=M$, $p=M$ or $m=M$, $n=M$, $p\neq M$	$\frac{A_pA_z^2\tau\cdot g^{3/2}(z)}{\sqrt{R(z)}}\cdot\exp\left[-\frac{(t-T_{m,p})^2}{2\cdot R(z)}\right]$	(6.44)
$m=M$, $p=M$, $n\neq M$	$\frac{A_pA_z^2\tau\cdot g^{3/2}(z)}{\sqrt{R^{*}(z)}}\cdot\exp\left[-\frac{(t-T_n)^2}{2\cdot R^{*}(z)}\right]$	(6.45)
$m=M$, $n=M$, $p=M$	$A_z^3\cdot g^{3/2}(z)$	(6.46)

Table 6.2. Nonlinear interactions between signal components.

Fig. 6.16-a) and -b) illustrate the nonlinear perturbation described by (6.40), under the conditions used to plot Fig. 6.14 with z_0=0 km, P_{peak} = 25 mW, and assuming $m=p$ and $m\neq p$, respectively. The different perturbations represented in Fig. 6.16 are identified by the trio (m,n,p), with M=3 considering two impulses and the zero symbol. The nonlinear perturbation described by (6.40) takes the form of an IFWM contribution between one or two symbol components and the zero component, which is centered at $(T_m+T_p)/2$. Hence for $m\neq p$, this corresponds to the instant between the two interfering symbols. Since there is no symbol located at this instant, it will generate a child impulse, similarly to the ghost impulses generated by IFWM in signals with infinite extinction ratio. For comparison purposes, Fig. 6.16-a) also presents the ghost impulses generated by IFWM with $m=p\neq n$. As shown, in the same conditions, the child impulse presents a significantly higher magnitude than the ghost impulse (approximately 5 dB higher), and spans over a longer time interval. The latter property implies that this perturbation also contributes to the tails of the impulses after transmission, as observed in Fig. 6.14-c).

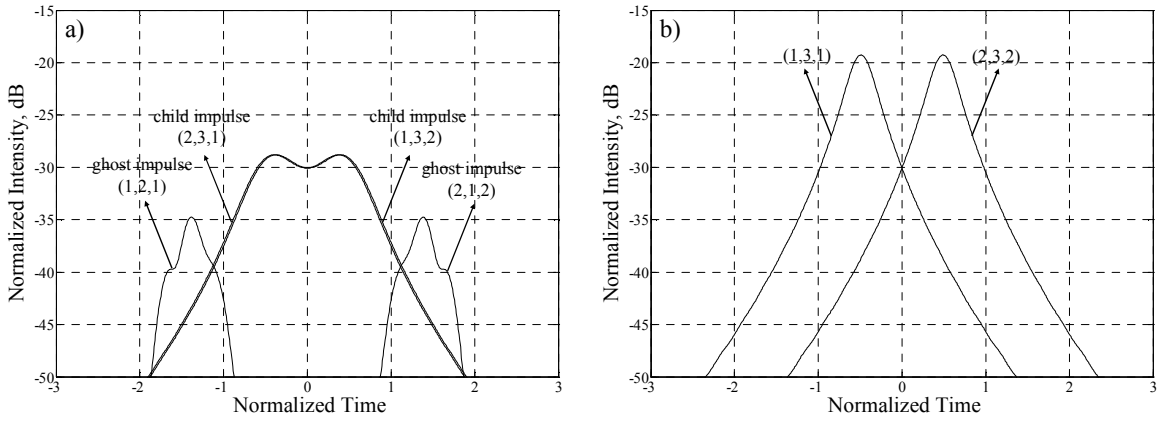

Fig. 6.16. Nonlinear perturbations resulting from the interaction of two impulse components with the zero component. The time axis is normalized to the symbol period and the intensity axis is normalized to the peak power. a) nonlinear perturbations resulting from the IFWM of two distinct impulses with the zero component as well as the IFWM ghost pulses for comparison purposes; b) nonlinear perturbations resulting from the IFWM of a single impulse with the zero component.

The perturbations observed in Fig. 6.16-b) for $m=p$ correspond to IFWM between a single impulse and the zero component and are approximately located in a time instant coincident with the generating impulse. As such, and similarly to what is observed with IFWM, these perturbations will mainly induce amplitude jitter on symbols. However, unlike the perturbations generated by conventional IFWM, these are significantly broader than the generating impulse. As such, these contributions will add with the previously described child impulses to form the tails of the impulses observed in Fig. 6.14-c).

The other important perturbation introduced by the nonlinear interaction between mark impulses and the zero symbol is described when considering the combinations $m=M$, $n\neq M$, $p\neq M$ or $m\neq M$, $n\neq M$, $p=M$. In this case, $\Delta u_{m,n,p}(L,t)$ becomes:

$$\Delta u_{m,n,p}(L,t)=\int_0^L \frac{A_p^2 A_z \tau g(z)\sqrt{g(L)}}{\sqrt{|R(z)|^2/\tau^2 - j\lambda^2/(\pi c)\cdot(D_{\text{res}}-D_{\text{ac}}(z))}}$$
$$\exp\left\{-\frac{(T_n-T_m)^2\tau^2}{4|R(z)|^2}+j\omega_f(z)\left(t-\frac{T_m+T_n}{2}+\omega_f(z)\frac{\lambda^2}{4\pi c}(D_{\text{res}}-D_{\text{ac}}(z))\right)\right\}\cdot \quad (6.47)$$
$$\exp\left\{-\frac{\left[t-\frac{T_m+T_n}{2}-\frac{\lambda^2\omega_f(z)}{2\pi c}(D_{\text{res}}-D_{\text{ac}}(z))\right]^2}{|R(z)|^2/\tau^2 - j\lambda^2/(\pi c)\cdot(D_{\text{res}}-D_{\text{ac}}(z))}\right\}\cdot dz$$

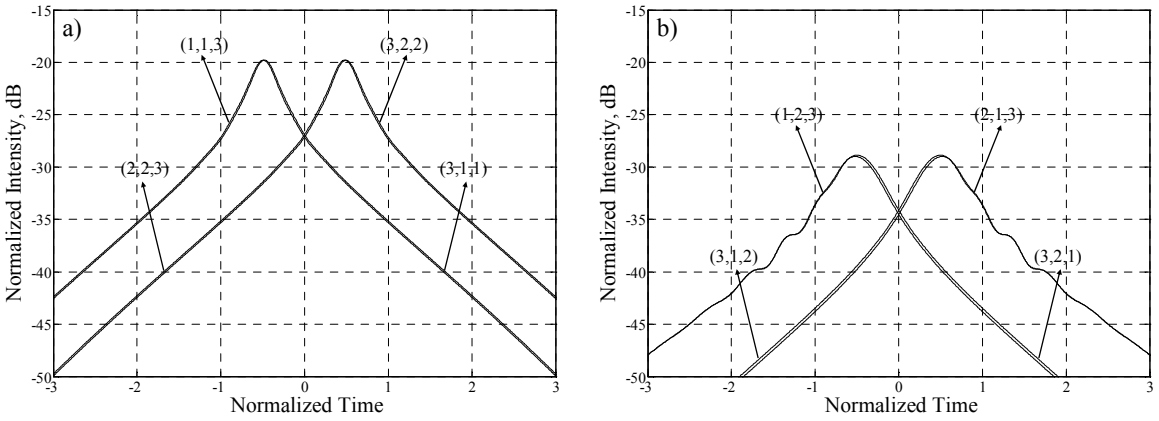

Fig. 6.17. Nonlinear perturbations resulting from the interaction of two impulse components with the zero component. The time axis is normalized to the symbol period and the intensity axis is normalized to the peak power. a) nonlinear perturbations resulting from IXPM of an impulse component with the zero component; b) nonlinear perturbations resulting from IFWM between two distinct symbol components and the zero component.

where $\omega_f(z)$ is a frequency shift of the nonlinear perturbation at the z coordinate of the fiber link, given by:

$$\omega_f(z) = \frac{\lambda^2}{2\pi c} \cdot \frac{T_m - T_n}{|R(z)|^2} \cdot D_{ac}(z) \tag{6.48}$$

Fig. 6.17-a) and -b) illustrate the nonlinear perturbation described by (6.47), under the conditions used to plot Fig. 6.14 with z_0=0 km and P_{peak} = 25 mW, and assuming m=p and $m \neq p$, respectively. Fig. 6.17-a) shows the nonlinear perturbations resulting from IXPM between each symbol and the zero component. Fig. 6.18 presents the frequency shift induced by these contributions, showing that these are shifted by approximately 6 GHz. This is a relatively weak shift in comparison with the 22 GHz frequency shift induced by conventional IXPM between the impulse components alone, also presented in the same figure. However, one must note that the IXPM generated by a symbol component on the zero component extends substantially from the time interval corresponding to the symbol duration. As a consequence, the zero component will suffer intensity fluctuations resulting from the phase-to-intensity conversion of the IXPM by GVD and SPM in the fiber.

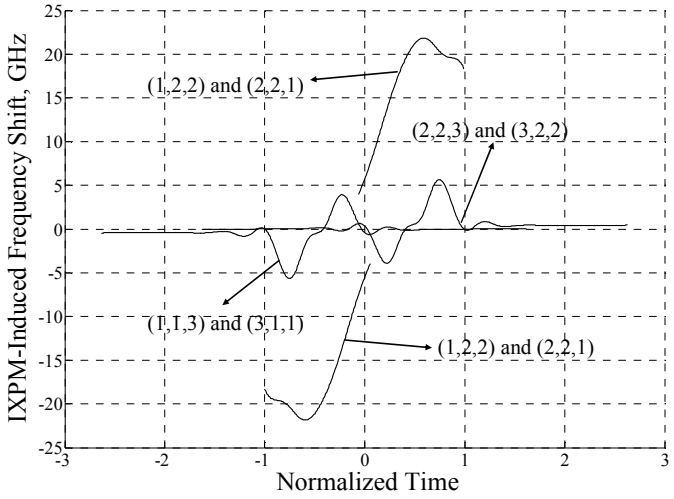

Fig. 6.18. IXPM-induced frequency shifts resulting from the interaction between a symbol and the zero component and the interaction between two symbol components. The time axis is normalized to the symbol period

Finally, Fig. 6.17-b) presents the nonlinear perturbations resulting from IFWM of two distinct symbol components with the zero component. These perturbations have approximately the same magnitude as the child impulses, yet are co-located with one of the generating impulses in the time instant T_m. As such, will contribute to amplitude jitter of that impulse.

6.4.3. Discussion

Sub-section 6.4.2 has demonstrated the existence of additional IFWM and IXPM components in signals with finite extinction ratio, presenting a small-perturbation analysis of these components. It has also been shown that the impact of these new components is a substantial degradation of the signal. Furthermore, optimum performance of such systems cannot be achieved using the rules for the optimum dispersion map derived by Killey et al. in [Killey, 2000: 2] and the principle for the cancellation of the impact of IXPM derived by Mecozzi et al. in [Mecozzi, 2001]. To justify the behavior of the nonlinear degradation of signals with finite extinction ratio, we may consider the principle for the cancellation of the impact of IXPM rewritten using the conventional model for XPM derived by Cartaxo in [Cartaxo, 1999:1]. The Fourier transform of the infinitesimal IXPM generated on the zero component in the z coordinate of the fiber due to the i-th impulse component may be approximated by [Cartaxo, 1999:1]:

$$d\tilde{\phi}_{\text{IXPM},i}(z,\omega) = -2\gamma \tilde{P}_i(z,\omega)\cdot dz \tag{6.49}$$

where $\tilde{P}_i(z,\omega) = \mathcal{F}\left[\left|u_i(z,t)\right|^2\right]$ represents the Fourier transform of the instantaneous power of the *i*-th impulse component, given by:

$$\tilde{P}_i(z,\omega) = \tilde{P}_i(0,\omega)\cdot C_{\text{IM-IM}}(z,\omega) \tag{6.50}$$

where $C_{\text{IM-IM}}(z,\omega)$ is the IM-IM conversion factor due to propagation from the input of the transmission system to the z coordinate. The infinitesimal IXPM will be converted in infinitesimal intensity fluctuations at the fiber output, which may be approximated by:

$$dP_{\text{IXPM},i}(z,\omega) = d\phi_{\text{IXPM},i}(z,\omega)\cdot C_{\text{PM-IM}}(L-z,\omega) \tag{6.51}$$

where $C_{\text{PM-IM}}(L\text{-}z,\omega)$ is the PM-IM conversion factor due to propagation from the z coordinate to the output of the transmission system. Expression (6.50) and (6.51) do not include the propagation delay because this is an intra-channel effect and such quantity is irrelevant. Replacing (6.49) and (6.50) in (6.51) yields:

$$dP_{\text{IXPM},i}(z,\omega) = -2\gamma \tilde{P}_i(0,\omega)\cdot C_{\text{IM-IM}}(z,\omega)\cdot C_{\text{PM-IM}}(L-z,\omega)\cdot dz \tag{6.52}$$

If we consider that the conversion factors $C_{\text{IM-IM}}(z,\omega)$ and $C_{\text{PM-IM}}(L\text{-}z,\omega)$ depend only on the impact of GVD, as usually assumed in the small perturbations model, we obtain [Cartaxo, 1999: 2]:

$$\begin{aligned} C_{IM-IM}(z,\omega) &= \cos\left[bD\cdot(z-z_0)\right] \\ C_{PM-IM}(L-z,\omega) &= -2\overline{P}_z \sin\left[b\left(D_{\text{res}} - D\cdot(z-z_0)\right)\right] \end{aligned} \tag{6.53}$$

where $\overline{P}_z$ is the average power of the zero component and $b=\lambda^2\cdot\omega^2/(4\pi c)$. Replacing (6.53) in (6.52) yields:

$$dP_{\mathrm{IXPM},i}(z,\omega) = 4\gamma\overline{P}_z \cdot \tilde{P}_i(0,\omega) \cdot \cos\left[bD \cdot (z - z_0)\right] \cdot \sin\left[b\left(D_{\mathrm{res}} - D \cdot (z - z_0)\right)\right] \cdot dz \tag{6.54}$$

Expression (6.54) provides a simple approximation to obtain the power fluctuations of the zero component, resulting from IXPM with the impulse components. Note that with D_{res}=0 ps/nm, (6.54) becomes anti-symmetric with respect to z_0. This implies the following condition:

$$dP_{\mathrm{IXPM},i}(z_0 - z,\omega) = -dP_{\mathrm{IXPM},i}(z_0 + z,\omega) \tag{6.55}$$

As such, if z_0 is set in the middle of the link, all the components generated in the z coordinates prior to z_0 are canceled by the symmetric contributions generated in the corresponding z coordinates after z_0. This conclusion was reached by Mecozzi et al. in [Mecozzi, 2001] in a distinct, and perhaps more complex way, for signals with infinite extinction ratio. However, it disagrees with the behavior observed for systems with finite extinction ratio, which do not show optimized performance for z_0 set in the middle of the link. To justify this discrepancy one may question the validity of (6.53) in considering only the impact of GVD on the IM-IM and PM-IM conversion factors. This validity stems from the principle used for the small-perturbations model applied in section 6.4.2. Expressions (6.53) may be improved by including the impact of SPM on the IM-IM and PM-IM conversion factors. In this case, $C_{\mathrm{IM\text{-}IM}}(z,\omega)$ and $C_{\mathrm{PM\text{-}IM}}(L\text{-}z,\omega)$ take the form [Cartaxo, 1999: 2]:

$$C_{IM-IM}(z,\omega) = \cos\left[bD \cdot (z - z_0)\right] - \frac{2\gamma\overline{P}_z}{bD} \cdot \left\{\cos\left[bD(z + z_0)\right] - \cos(bD \cdot z_0)\right\} + 2\gamma\overline{P}_z \cdot \sin(bD \cdot z_0) \tag{6.56}$$

$$C_{PM-IM}(L - z,\omega) = -2\overline{P}_z \left\langle \sin\left\{b\left[D_{\mathrm{res}} - D(z - z_0)\right]\right\} \cdot \left(1 - \frac{2\gamma\overline{P}_z}{bD}\right) + \frac{2\gamma\overline{P}_z}{bD} \cdot \sin\left\{b\left[D_{\mathrm{res}} - D(L - z_0)\right]\right\} + 2\gamma\overline{P}_z \cdot (L - z) \cdot \cos\left\{b\left[D_{\mathrm{res}} - D(L - z_0)\right]\right\} \right\rangle$$

Replacing (6.56) in (6.52) yields:

$$\begin{aligned} dP_{\mathrm{IXPM},i}(z,\omega) = &-4\gamma\overline{P}_z \cdot \tilde{P}_i(0,\omega) \cdot \Bigg\langle \cos\left[bD\cdot(z-z_0)\right] - \\ &\frac{2\gamma\overline{P}_z}{bD}\cdot\left\{\cos\left[bD(z+z_0)\right]-\cos(bD\cdot z_0)\right\} + 2\gamma\overline{P}_z\cdot\sin(bD\cdot z_0)\Bigg\rangle \cdot \\ &\Bigg\langle \sin\left\{b\left[D_{\mathrm{res}}-D(z-z_0)\right]\right\}\cdot\left(1-\frac{2\gamma\overline{P}_z}{bD}\right)+\frac{2\gamma\overline{P}_z}{bD}\cdot\sin\left\{b\left[D_{\mathrm{res}}-D(L-z_0)\right]\right\} + \\ &2\gamma\overline{P}_z\cdot(L-z)\cdot\cos\left\{b\left[D_{\mathrm{res}}-D(L-z_0)\right]\right\}\Bigg\rangle\cdot dz \end{aligned} \tag{6.57}$$

Expression (6.57) provides a simple approximation to obtain the power fluctuations of the zero component, resulting from IXPM with the impulse components, which includes the impact of SPM. Replacing (6.57) in (6.55) yields the condition:

$$2\cos(bD_{\mathrm{res}})\cdot\sin(bDz)\cdot\left(1-\frac{2\gamma\overline{P}_z}{bD}\right)+4\gamma\overline{P}_z\cdot z\cdot\cos\left\{b\left[D_{\mathrm{res}}-D(L-z_0)\right]\right\}=0 \tag{6.58}$$

Expression (6.58) shows that, for a given combination of z_0 and D_{res}, the anti-symmetry may only be achieved for specific frequency components and fiber coordinates. These results justify the breakdown of the Mecozzi approach, when considering signals with finite extinction ratio. Note that satisfying (6.58) only allows reducing the IXPM of the symbol components with the zero component, which does not necessarily means minimizing IFWM and IXPM between symbol components. It simply shows that these effects cannot be simultaneously minimized. The optimum performance in a pseudo-solitonic regime is given by a compromise between minimizing the intra-channel nonlinearities between different impulse components, as originally proposed in [Killey, 2000: 2], and minimizing the intra-channel nonlinearities between the impulses and the zero component, if present.

6.5. Conclusions

The results presented in this chapter have shown that, according to numerical simulations, optimization of the dispersion pre- and post-compensation of a 10 Gb/s RZ-SSB system without inline dispersion compensation allows a 3 dB increase of the maximum launch power in comparison with an simply electrically pre-compensated system. Under these conditions for single-channel transmission, intra-channel fiber nonlinearities have been identified as the main degradation source and the dependence of the system performance on the dispersion scheme resembles the one verified in a pseudo-linear transmission regime. In this case, the main differences are nonzero total residual dispersion and an asymmetric dispersion compensation map with the zero dispersion point shifted significantly forward from the middle of the link. It has been verified that this asymmetry varies abruptly with the modulation depth. The nonlinear characteristic of the SSB transmitter has been accounted for, showing that it limits modulation depth to 0.9 for the best performance, when using electrical pre-compensation.

In addition, a innovative pump-probe analysis of the XPM-degradation of DPSK signals due to nonlinear interaction with ASK signals was proposed. This technique allowed the distinction of the contributions of XPM-induced PM and IM and was validated by Monte-Carlo simulation. Application of the pump-probe analysis allowed identifying the XPM-induced IM as the dominant source of degradation, when using SSMF or TW with high residual dispersion. The presented results invalidate the application of previous techniques based on the sole analysis the XPM-induced PM to model this type of systems, such as the model proposed by Wei et al. in [Wei, 2003] and further developed by Hiew et al. in [Hiew, 2004]. Note that a rigorous treatment of the BER for DPSK systems may only be achieved with complex numerical computation, such as the *Karhunen-Löeve* series expansion [Gnauck, 2005]. Nevertheless, the analysis is carried out in a quite involved manner. The presented approach has the advantage of providing insight on the XPM-degradation, easily distinguishing the dominant system parameters with reduced computational effort. A novel analytical model for the estimation of the XPM degradation of DPSK signals due to the nonlinear interference with ASK signals has been proposed. The analytical model has been validated using Monte Carlo simulation. It has been shown that the proposed model allows a reasonable prediction of the dependence of the system

performance on the dispersion pre-compensation for a 20 sections transmission system using SSMF.

Finally, the intra-channel nonlinearities in signals with finite extinction ratio have been analyzed. It has been shown that the impact of the nonlinear interaction between impulse components and the zero component may exceed greatly the impact of nonlinear interactions between different impulses components in magnitude and temporal extension. A new form of IFWM ghost pulses has been identified and classified as child impulses. Unlike ghost impulses, which arise in the center of the time slots of the transmitted signal, the child impulses appear in-between consecutive impulses. Furthermore, it has been shown that the rule for the cancellation of IXPM derived in [Mecozzi, 2001] does not apply when assuming that the nonlinear perturbation propagates nonlinearly through the fiber, as initially assumed by these authors. By introducing the impact of SPM on the propagation of the nonlinear perturbation, it has been shown that the power fluctuations induced in the zero component will not cancel by setting a symmetric dispersion compensation map.

Chapter 7. Final Conclusions

7.1. Conclusions

This chapter presents the final conclusions obtained along the development of this work on the areas of optical monitoring, fiber XPM-based wavelength conversion and impact of fiber nonlinearities in systems employing advanced transmission techniques. The majority of the work was carried out using analytical modeling, which has been subsequently validated through numerical simulation. However, some experimental work was conducted for the development of OMS based on the analysis of asynchronous histograms.

Chapter 2 has presented a review of the main principles of optical monitoring. A form of classification has been proposed to distinguish OMS according to their purpose and form of analysis of optical performance and impairments. Particular emphasis has been given to the techniques for the analysis of asynchronous histograms available in the literature.

Chapter 3 has presented a study of the application of the analysis of asynchronous histograms to monitor Q-factor and OSNR. The first part of this study focused on the limitations imposed by non-ideal sampling. It has been shown that a finite sampling aperture may be modeled as an equivalent sampling filter with a bandwidth inversely proportional to the sampling aperture, positioned prior to an ideal sampling system. The

model has been used to demonstrate through numerical simulation that, for sampling apertures below the bit period, the non-ideal sampling system only affects the noise component of the signal under analysis by reducing its equivalent noise bandwidth. As a result, over-estimated Q-factor measurements using non-ideal sampling may be corrected with a simple correction factor, given by the ratio between the equivalent noise bandwidths with and without the equivalent sampling filter. In the case of sampling apertures exceeding the bit-period, it has been shown that the Q-factor is under-estimated as a consequence of the distortion of the acquired samples. As such, a novel technique has been developed to estimate the Q-factor based on the comparison of the histogram under analysis with a numerically computed histogram, which included the impact of non-ideal sampling. Application of this method using numerical simulation allowed extending the range of required sampling aperture to values exceeding the bit-period, with Q-factor measurement errors below 15%.

Chapter 3 has also presented and experimentally demonstrated a novel method to estimate OSNR based on the comparison of asynchronous histograms with reference histograms. This method allowed the estimation of OSNR values as high as 28 dB independently of physical restrictions imposed by the OMS. Optical pre-amplification has been used to increase the sensitivity of the OMS by as much as 10 dB and 20 dB, when using a SOA or an EDFA pre-amplifier, respectively. This was achieved at the cost of limiting the maximum measurable OSNR to values as low as 24 dB. Furthermore, the method has been proved resilient to GVD-induced distortion, as long as the reference histogram and histogram of the signal under analysis present similar distortion. Otherwise, it has been shown that the OMS under-estimates the OSNR by a factor corresponding to a GVD-induced OSNR penalty.

Chapter 4 has presented a review on the principles of fiber nonlinearity commonly used in fiber-based AOWC. This review consisted on the analysis of the operation principles of XPM-based AOWC using NOLM and detuned filters. Chapter 4 has also included a review on the principle of fiber FWM-based AOWC.

Chapter 5 has presented a novel analytical model for the characterization of the XPM-frequency limitations in fiber XPM-based AOWC. The model includes the impact of GVD and SPM, which allowed its application to modulation frequencies in the THz range. The XPM cut-off frequency has been introduced as a design parameter for wavelength

converters, presenting a logarithmic dependence on the maximum XPM-induced phase modulation. Application of the analytical model allowed comparing the aptitude of DSF, HN-DSF and BOF for AOWC. It has been shown that HN-DSF is the most appropriate fiber, with XPM-bandwidth above 1 THz, due to its low dispersion and dispersion slope characteristics. The analytical model was also applied to the design of fiber-NOLM wavelength converters. This allowed the derivation of approximate close-form expressions for the dimensioning of the loop length and the required input peak power, accounting for the XPM cut-off frequency. Furthermore, analytical and numerical simulation results demonstrated that the XPM frequency limitations ultimately impose a maximum loop length.

Chapter 5 has also presented a novel theoretical filter for PM-IM conversion. The design of this filter was based on the numerical computation of the amplitude and phase characteristics of an ideal PM-IM converting filter. Numerical simulations have shown that the improved filter allows a reduction of the required input peak power and increase of the maximum output peak power by factors of 2 and 3, respectively, in comparison to wavelength converters using detuned filters. It has been shown, through numerical simulation, that the signals converted using the proposed filter are degraded by pattern dependent power fluctuations. This leads to a power penalty of 2 dB in back-to-back configurations, against 1 dB when using detuned filters. Nevertheless, it has been shown that a signal converted using the proposed filter has low residual chirp increasing the dispersion tolerance when comparing to a signal obtained using a detuned filter.

Chapter 6 has presented a study of the dispersion management in transmission systems employing 10 Gb/s RZ-SSB modulation format and electrical dispersion compensation without inline optical dispersion compensation. Comparison with an equivalent system using optical dispersion pre-compensation has also been performed. This has shown that, with low modulation depths, both cases of optical or electrical dispersion pre-compensation have similar degradation. The main degradation of the single channel system results from intra-channel fiber nonlinearities and, similarly to systems operating in the pseudo-linear transmission regime, the required OSNR for a BER of 10^{-12} may be improved by as much as 3 dB, when using partial optical dispersion post-compensation. The main difference of the proposed system lies in an asymmetric optimum dispersion compensation map, with the zero dispersion compensation point shifted

forwards from the middle of the link by 20% of the link length. Extensive simulation has shown that the optimum dispersion compensation map varies abruptly with the modulation depth of the signal, becoming symmetric for high modulation depths.

Further analytical studies of the intra-channel fiber nonlinearities affecting signals with finite extinction ratio have shown that, besides the degradation resulting from IFWM and IXPM, the nonlinear interaction between mark and space symbols yields additional non-negligible degradation. This novel form of degradation takes the form of amplitude and timing jitter of the mark symbols, amplitude fluctuations in the space level, and a specific type of ghost impulses that rises between consecutive impulses. The latter have been referred as child impulses.

Chapter 6 has also presented a study of the nonlinear interactions between ASK and DPSK channels in WDM transmission systems using mixed modulation formats. Numerical simulations have been conducted using pump-probe analysis to compare the magnitude of the electrical current fluctuations present on the DPSK receiver as a result of XPM-induced IM and XPM-induced PM. In has been shown that the latter are only dominant in the cases of low accumulated dispersion and when using fibers with a low dispersion parameter. Otherwise the electrical current fluctuations resulting from XPM-induced IM are dominant. This result contradicts prior works on this topic, which neglect the XPM-induced IM. It has been shown that, for small XPM-degradation, these electrical current fluctuations may be assumed Gaussian. Based on this observation, a simplified approximate model to obtain the BER degradation of a DPSK signal due to XPM-induced by an interfering ASK channel has been derived. The model has been validated using the Monte Carlo method.

7.2. Suggestions for Future Work

This section presents a few suggestions for future works regarding the topics approached in this dissertation.

- Application of the techniques developed for optical monitoring using the analysis of asynchronous histograms with DPSK and DQPSK signals.
- Improvement of the technique for the analysis of asynchronous histograms using reference histograms to allow the distinction of the OSNR penalty resulting from different impairments, particularly dispersion and crosstalk.

- Development of a technique to estimate the signal degradation occurring within part of an optical path with OMS placed in the extremities of that section, using analysis of asynchronous histograms.
- Development of analytical models to characterize the impact of the XPM in fiber-NOLM wavelength converters, including the impact of counter-propagating XPM.
- Development of analytical models to characterize the frequency limitations of fiber FWM-based AOWC.
- Application of fiber FWM and parametric gain for optical processing of phase modulated signals.
- Analysis and optimization of WDM systems operating in links without inline dispersion compensation. Comparison of the performance of phase modulated and intensity modulated signals.
- Development of rigorous modeling of the BER degradation of DPSK signals due to XPM with ASK channels, including the impact on nonlinear phase noise.
- Improved analysis of the intra-channel fiber nonlinearities occurring in signals with finite extinction ratio. This involves including the impact of SPM on the propagation of the nonlinear perturbation using a small-signals approach.

Appendix A. Effects of finite aperture time in asynchronous sampling systems

A.1. Introduction

Optical or electrical, most real-life signals have a continuous and analog nature. In order to process these signals using digital circuitry, analog-to-digital conversion is required. However, a digital signal is discrete in amplitude and time. To obtain an amplitude and time discrete signal from an amplitude and time continuous signal a sampling process is required. The fundamental principal of sampling is the repeated quasi-instantaneous capture of a time-varying waveform by a sampling *gate* [Kahrs, 2003]. A train of narrow impulses controls the sampling gate. After a sample of the continuous sensor signal is obtained, an ADC circuit can be used to obtain a corresponding digital value.

The existing ADC circuits require a constant input for a certain amount of time, in order to obtain a correct digital output. Therefore, a sample obtained with a narrow impulse is usually not enough for the ADC to function properly. In order to retain the impulse amplitude an analog memory is used between the sampling circuit and the ADC. The simplest analog memory is a capacitor, known as *hold capacitor*. The charge accumulated when the gate is closed is proportional to the amplitude of the sample and can be used for

analog-to-digital conversion. The combination of the sampling circuit with the hold capacitor is known as a sample-and-hold (S&H) circuit. An example of a simplified S&H block diagram is presented in Fig. A.1.

When the sampling gate is closed, the input sensor signal current, $i_{in}(t)$, charges the hold capacitor. The time required for the sampling gate to open is known as the *aperture* time. After the gate is open, the capacitor discharges with a given fall-off rate, depending on the input impedance of the following circuitry. In most cases, a high input impedance amplifier is used to decrease the falloff rate. The time required for the hold capacitor to discharge should be sufficient for the ADC to produce a valid digital value for the acquired sample.

Some of the main limitations of S&H systems are listed below:

1. Finite aperture time. The S&H takes a period of time to capture a sample of the sensor signal. Since the signal will vary during this time, the sampled signal can be slightly off.
2. Sampling jitter. Temporal variations of the sampling frequency lead to uncertainty of the sampling instant. This problem is particularly hazardous in synchronous sampling systems.
3. Signal feedthrough. Due to construction limitations of the sampling gate, some current "bleeds" through the switch to the capacitor causing the voltage to change slightly.
4. Signal droop. The voltage being held on the capacitor starts to slowly decrease over time due to the limited input resistance of the following circuitry.
5. Aperture uncertainty. Variations from sample to sample of the aperture time lead to

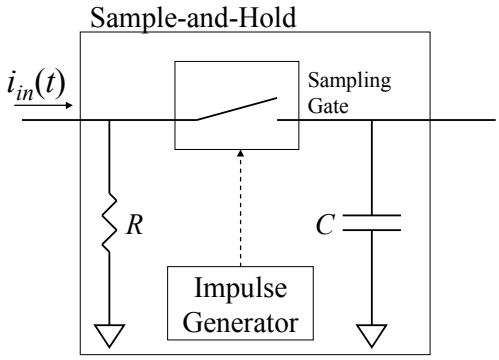

Fig. A.1 Block diagram of a sample and hold circuit.

additional sampling noise.

In this work, it is considered that the input impedance of the ADC is high enough to assume a constant voltage at the hold capacitor terminals. Additionally, the sampling gate is assumed to have no feedthrough. As so, limitations 3 and 4 will be neglected. Additionally, temporal variations of the aperture time (limitation 5) will also not be considered because the sampler characteristics are assumed perfect.

The sampling jitter leads to significant error in systems were the sampling frequency is related with the frequency of the sensor signal. These systems include all digital receivers, oscilloscopes and time-domain reflectometry devices. In this work, asynchronous sampling is considered. As such, the sampling frequency is not related to the frequency of the sensor signal. Therefore, sampling jitter does not affect significantly the overall accuracy of the system.

The study presented in this appendix will concentrate on the limitation 1 using asynchronous sampling systems. The main objective is to evaluate the consequences of finite aperture in the sampling process. Section A.2 presents theoretical considerations of this problem and an analytical model to estimate the sampling noise variance. Some applications of this model are presented in section A.3 comparing the analytical model with simulation results. Section A.4 presents the conclusions of this appendix.

A.2. Theory

The aperture time is the time required for the sampling gate to open after a sample is acquired. In an ideal situation, the aperture time is zero and the output signal of the S&H is proportional to the signal value immediately before the sampling instant. However, in a non-ideal situation, the sampling gate requires a finite time to switch. During this time, the

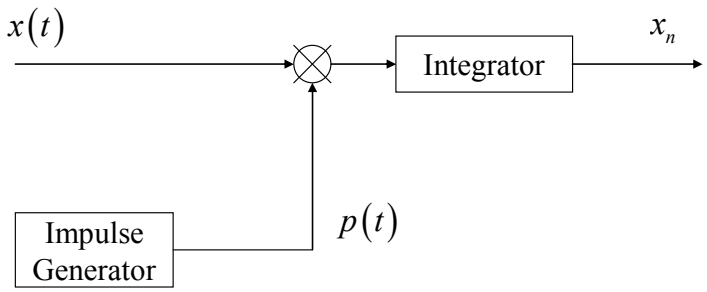

Fig. A.2 General block diagram of a S&H system.

input signal of the S&H is changed leading to sampling error. In order to evaluate the effects of finite aperture time in asynchronous sampling, a general model for a S&H system is presented in Fig. A.2.

The pulse generator creates a pulse train given by:

$$p(t) = \sum_{n=-\infty}^{+\infty} \psi(t - n \cdot T_a) \tag{A.1}$$

where T_a is the sampling period given by T_a=1/F_a with F_a the sampling frequency. The term $\psi(t)$ is the shape of the sampling impulse. It is considered that $\psi(t)$ is normalized in a way that $\int \psi(t) = 1$. The pulse train is multiplied by the sensor signal, $x(t)$, and the result is inserted in an integrator. This integrator is such that its output is a constant signal in each sampling period. The output value of the integrator for the k-th sampling interval, x_k, is given by:

$$x_k = \int_{-\infty}^{+\infty} x(t) \cdot \psi(t - k \cdot T_a) \cdot dt \tag{A.2}$$

The diagram presented in Fig. A.2 allows the use of different shapes for $\psi(t)$. In an ideal sampling system, the time required by the sampling gate to open is infinitesimal. In this case, the sampling impulse is given by:

$$\psi(t) = \delta(t) \tag{A.3}$$

where $\delta(t)$ is the dirac function. The value of the sample for the k-th sampling interval is obtained by replacing (A.3) in (A.2). As such, we obtain $x_k = x(k \cdot T_a)$ and the sampling error is null. In a non-ideal situation, $\psi(t) \neq \delta(t)$. Therefore, consider the Taylor series expansion of $x(t)$ around the sampling instant:

$$x(t) = \sum_{m=0}^{+\infty} \frac{(t - k \cdot T_a)^m}{m!} \cdot x^{(m)}(k \cdot T_a) \tag{A.4}$$

where $x^{(m)}(t)$ is the m-th order derivate of $x(t)$ with relation to t. By replacing (A.4) in (A.2) we have:

$$x_k = \int_{-\infty}^{+\infty} \sum_{m=0}^{+\infty} \frac{x^{(m)}\left(k \cdot T_a\right)}{m!} \cdot \left(t - k \cdot T_a\right)^m \cdot \psi\left(t - k \cdot T_a\right) \cdot dt \tag{A.5}$$

By swapping the integral with the infinite sum, we obtain:

$$x_k = \sum_{m=0}^{+\infty} \frac{x^{(m)}\left(k \cdot T_a\right)}{m!} \cdot \psi_m \tag{A.6}$$

where

$$\psi_m = \int_{-\infty}^{+\infty} t^m \cdot \psi\left(t\right) \cdot dt \tag{A.7}$$

The term of the infinite sum on the RHS of (A.6) corresponding to m=0 is identical to the ideal value of the sample if $\psi(t)$ is normalized. The remaining terms of the infinite sum on the RHS of (A.6) are contributions to the sampling error. The sampling error for the k-th sample, e_k, is then given by:

$$e_k = \sum_{m=1}^{\infty} \frac{x^{(m)}\left(k \cdot T_a\right)}{m!} \cdot \psi_m \tag{A.8}$$

Expression (A.8) shows that the sampling error depends mainly on the derivates of the sensor signal and the shape of the sampling function. An additional result is that, if $\psi(t)$ is an even function, the contribution of the even order derivates of $x(t)$ to the error is null [Sauerwald, 1994]. The overall sampling error can be considered as sampling noise and measured by its variance, σ_{SN}^2, given by:

$$\sigma_{SN}^2 = \frac{1}{N_s} \cdot \sum_{k=1}^{N_s} e_k^2 \tag{A.9}$$

where N_s is the number of acquired samples. Replacing (A.8) in (A.9) we obtain:

$$\sigma_{SN}^2 = \frac{1}{N_s} \cdot \sum_{k=1}^{N_s} \left[\sum_{m=1}^{\infty} \frac{\psi_m}{m!} \cdot x^{(m)}\left(k \cdot T_a\right) \right]^2 \tag{A.10}$$

Assuming that the main contribution for the sampling error results from the first order derivate and neglecting the contributions of the higher order derivates, σ_{SN}^2 can be approximated by:

$$\sigma_{SN}^2 \approx \psi_1^2 \cdot \sigma_{x,1}^2 \tag{A.11}$$

where $\sigma_{x,m}^2$ is the variance of the samples acquired from the m-th order derivate of $x(t)$, defined as:

$$\sigma_{x,m}^2 = \frac{1}{N_s} \cdot \sum_{k=1}^{N_s} \left[x^{(m)}\left(k \cdot T_a\right) \right]^2 \tag{A.12}$$

In the particular case that even sampling impulses are used, the odd order derivates of the sensor signal do not contribute to the error signal. As an approximation, only the contribution of the second order derivate will be considered. The contribution of the higher order derivates will be neglected. As so, σ_{SN}^2 can be approximated by:

$$\sigma_{SN}^2 \approx \frac{\psi_2^2}{4} \cdot \sigma_{x,2}^2 \tag{A.13}$$

Expressions (A.11) and (A.13) show that the sampling error may be characterized by a constant value, dependent of the sampling impulse shape, and the variance of the first and second order derivates of the sensor signal in the sampling instant. The validity of (A.10) is limited to the validity of the Taylor series expansion of the signal $x(t)$ around the sampling

point. Note that $x(t)$ is generally not an analytic function in the case of the considered optical systems. Therefore, it may not agree with its Taylor expansion in all points. For digital signals, the critical points are does were the derivates of the signal are not continuous in the neighborhood of the symbol transitions. If the integration time of the sampler or aperture time is long, it may include these instants, leading to a failure of the analytic model. This limitation implies that the model presented by (A.10) is valid only for small sampling aperture values when compared with the period of the sampled signal. As a limit, when the aperture value is very high, the value of the acquired samples converges to the average value of the signal, $\overline{x}$. Therefore, the sampling error is given by:

$$e_k = x\left(k \cdot T_a\right) - \overline{x} \tag{A.14}$$

By expression (A.14) we verify that, in this limit situation, the variance of the sampling error corresponds to the variance of the sensor signal in the sampling instants:

$$\sigma_{SN}^2 = \frac{1}{N_s} \cdot \sum_{k=1}^{N_s} \left[x\left(k \cdot T_a\right) - \overline{x} \right]^2 \tag{A.15}$$

The result presented by (A.15) has limited practical application since its validity implies very high aperture values. For these aperture values, the acquired samples are practically unrelated with the sampled signal shape and cannot be used for monitoring purposes.

A.3. Application Example

A.3.1. Theoretical Considerations

Consider an application where $x(t)$ is a binary NRZ signal with a raised cosine transition function. In these conditions, the signal is characterized by its binary sequence and its transition functions. The binary sequence, a_n, takes the values 1 or 0 for the n-th symbol. The transition functions are $x_{01}(t)$ and $x_{10}(t)$ for the transitions from "0" to "1" and "1" to "0", respectively. The normalized temporal evolution of $x(t)$ is given by:

$$x(t)=\begin{cases}1, & a_{n-1}=a_n=1\\ x_{10}\left(t-n\cdot T\right), & a_{n-1}=1\wedge a_n=0\\ x_{01}\left(t-n\cdot T\right), & a_{n-1}=0\wedge a_n=1\\ 0, & a_{n-1}=a_n=0\end{cases} \tag{A.16}$$

for $n\cdot T_a < t \leq (n+1)\cdot T_a$. In the case of a raised cosine binary signal $x_{10}(t)$ = 1- $x_{01}(t)$ and $x_{01}(t)$ is given by:

$$x_{01}\left(t\right)=\begin{cases}\frac{1}{2}-\frac{1}{2}\cdot\cos\left(\frac{\pi\cdot t}{t_r}\right), & 0\leq t\leq t_r\\ 1, & t<0\vee t>t_r\end{cases} \tag{A.17}$$

where t_r is the time required for the symbol transition and is proportional to the transition time. Considering expressions (A.16) and (A.17), it is possible to obtain expressions for the first and second order derivates of $x(t)$. These are given by:

$$x^{(1)}\left(t\right)=\begin{cases}0, & a_{n-1}=a_n\\ -x_{01}^{(1)}\left(t-n\cdot T\right), & a_{n-1}=1\wedge a_n=0\\ x_{01}^{(1)}\left(t-n\cdot T\right), & a_{n-1}=0\wedge a_n=1\end{cases} \tag{A.18}$$

and

$$x^{(2)}\left(t\right)=\begin{cases}0, & a_{n-1}=a_n\\ -x_{01}^{(2)}\left(t-n\cdot T\right), & a_{n-1}=1\wedge a_n=0\\ x_{01}^{(2)}\left(t-n\cdot T\right), & a_{n-1}=0\wedge a_n=1\end{cases} \tag{A.19}$$

respectively. $x_{01}^{(1)}\left(t\right)$ and $x_{01}^{(2)}\left(t\right)$ are given by:

$$x_{01}^{(1)}\left(t\right)=\begin{cases}\frac{\pi}{2\cdot t_r}\cdot\sin\left(\frac{\pi\cdot t}{t_r}\right), & 0\leq t\leq t_r\\ 0, & t<0\vee t>t_r\end{cases} \tag{A.20}$$

and

$$x_{01}^{(2)} = \begin{cases} \frac{1}{2} \cdot \left(\frac{\pi}{t_r} \right)^2 \cdot \cos\left(\frac{\pi \cdot t}{t_r} \right), & 0 \le t \le t_r \\ 0, & t < 0 \vee t > t_r \end{cases} \tag{A.21}$$

In order to determine the values of $\sigma_{x,1}^2$ and $\sigma_{x,2}^2$ we take expression (A.12), approximated by:

$$\sigma_{x,m}^2 \approx \frac{1}{T_o} \int_0^{T_o} \left[x^{(m)}(t) \right]^2 \cdot dt \tag{A.22}$$

This approximation assumes that the variance of a large number of samples acquired from a given function in the time interval of duration $T_o >> T$ is approximated by the variance of the sampled function during the same interval. Considering that the sampled function is given by (A.18) or (A.19), its variance corresponds to the sum of the variances of the different possible segments (depending on the type of symbol transition) balanced by their probability of occurrence. In the case of binary signals, all the transitions have an identical probability of 1/4 therefore $\sigma_{x,m}^2$ can be approximated by:

$$\sigma_{x,m}^2 \approx \frac{1}{4T} \cdot \int_0^T \left[x_{01}^{(m)}(t) \right]^2 \cdot dt + \frac{1}{4T} \cdot \int_0^T \left[-x_{01}^{(m)}(t) \right]^2 \cdot dt \tag{A.23}$$

Replacing (A.20) and (A.21) in (A.23) we obtain:

$$\sigma_{x,1}^2 = \frac{\pi^2}{16 \cdot T \cdot t_r} \tag{A.24}$$

and

$$\sigma_{x,2}^2 = \frac{\pi^4}{16 \cdot T \cdot t_r^3} \tag{A.25}$$

In order to characterize the sampling noise it is still necessary to evaluate the sampling impulse shape. For this application, a rectangular and triangular shape will be considered. In the first case, the following expression will be used for $\psi(t)$:

$$\psi(t) = \begin{cases} \frac{1}{a_p}, & |t| \le \frac{a_p}{2} \\ 0, & |t| > \frac{a_p}{2} \end{cases} \tag{A.26}$$

where a_p is the sampling aperture. In this case, the impulse shape is an even function. Therefore, only the influence of the second derivate of $x(t)$ for the sampling noise is evaluated. Replacing (A.26) in (A.7) and considering m=2, we obtain for ψ_2:

$$\psi_2 = \frac{a_p^2}{12} \tag{A.27}$$

Replacing (A.25) and (A.27) in (A.13) we have:

$$\sigma_{SN}^2 \approx \frac{\pi^4}{9216 \cdot T} \cdot \frac{a_p^4}{t_r^3} \tag{A.28}$$

In the following, a similar result is obtained for a non-symmetrical triangular sampling impulse given by:

$$\psi(t) = \begin{cases} \frac{2}{a_p} \cdot \left(\frac{t}{a_p} + 1 \right), & -a_p \le t \le 0 \\ 0, & t < -a_p \vee t > 0 \end{cases} \tag{A.29}$$

In this case, all the derivates of $x(t)$ contribute for the sampling noise. However, we consider only the influence of the first derivate. Replacing (A.29) in (A.7) and considering m=1 we obtain for ψ_1:

$$\psi_1 = -\frac{a_p}{3} \tag{A.30}$$

Replacing (A.24) and (A.30) in (A.11) we obtain:

$$\sigma_{SN}^2 \approx \frac{\pi^2}{144 \cdot T} \cdot \frac{a_p^2}{t_r} \tag{A.31}$$

Expressions (A.28) and (A.30) provide simple engineering rules for the dimensioning of S&H systems with the corresponding sampling impulses. In both cases, the sampling noise variance depends on the period and transition time of the sampled signal and the aperture time of the S&H. Note that both the triangular impulse and the rectangular impulse have identical aperture times. However, the triangle shaped sampling impulse is closer to the system presented in Fig. A.1. This shape assumes that the sampling gate reduces its current progressively until the circuit is open. In the case of a rectangular shape, the construction of the S&H system is significantly more demanding due to the requirement of sharp transitions.

A.3.2. Numerical Simulation and Analytical Results

In order to compare the performance of S&H systems using rectangular and triangular sampling impulse shapes and evaluate the accuracy of expressions (A.28) and (A.31) the sampling noise variance will be calculated analytically and by numerical simulation.

Consider the S&H system presented in Fig. A.2. The signal generator produces a binary NRZ signal composed by a periodical *deBruijn* sequence of 2^7 raised cosine symbols. The signal has a bit-rate of 10 Gb/s. For numerical simulation, each symbol of the transmitted sequence is composed by 512 samples. A high number of samples per symbol were required to minimize the interference between the sampling process required for the

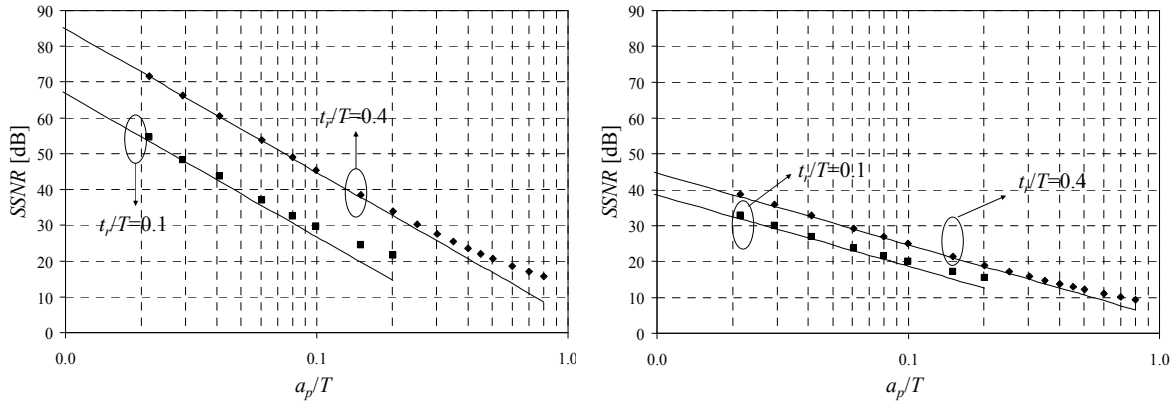

Fig. A.3. Signal-to-Sampling noise ratio as a function of the aperture time for different values of the transition time. Numerical simulation results: ■ - t_r/T=0.1; ♦ - t_r/T=0.4. Analytical results: continuous line.

numerical simulation and the actually simulated sampling system. In the latter case, a total of 2^{16} samples were acquired. To obtain the sampling error, each sample value is determined by calculating expression (A.2) numerically. After that, the sample values are compared with the actual signal values to obtain the sampling error. The sampling error variance is obtained using expression (A.9).

To obtain the sampling error variance analytically, expressions (A.28) and (A.31) are used. To evaluate the sampling noise we define the signal-to-sampling noise ratio (SSNR) as:

$$SSNR = 10 \cdot \log_{10}\left[\frac{P_s}{\sigma_{SN}^2}\right] \tag{A.32}$$

where P_s is the signal power. Fig. A.3 presents the SSNR as a function of the aperture time for different values of t_r. Both a_p and t_r are normalized to the period of the sensor signal. Fig. A.3-a) and -b) present the SSNR calculated for a S&H with rectangular and triangular sampling impulses, respectively.

As predicted by expressions (A.28) and (A.31), the sampling noise variance increases with the aperture time leading to a degradation of the SSNR. Fig. A.3-a) or b) show that, an increase of the transition time leads to a significant decrease of the sampling noise variance. This decrease is more evident for low values of the aperture time. Comparing Fig. A.3-a) with Fig. A.3-b), the advantage of using a rectangular sampling

impulse to a triangular sampling impulse becomes evident. The latter case presents a significant degradation of the SSNR due to the contribution of the first order derivate of the sensor signal. For the considered cases, the analytical values of the SSNR determined with expressions (A.28) and (A.31) allow a reasonable conservative estimate of the numerical simulation values.

A.4. Conclusions

In this appendix, an analytical evaluation of the noise caused by the sampling process was performed. This process assumed that the sampling noise depends on the shape of the sampling impulse and the derivates of the sampled signal. Simple expressions to estimate the variance of this noise have been presented and their values compared with results from numerical simulation. The signal-to-sampling noise ratio was introduced and proposed as a metric to evaluate the performance of a sampling system. It was verified that the sampling noise depends mainly on the aperture time of the sampling gate and the transition time of the sampled signal. Additionally, a very significant factor is the shape of the sampling impulses. It was verified that significant improvement of the S&H performance could be achieved by using symmetrical sampling impulses and suppressing the contribution of the odd order derivates of the sampled signal to the sampling noise.

Appendix B. On the Impact of Limited Histogram Resolution on the Q-Factor Estimation

B.1. Introduction

In order to perform quality measurements of optical signals using asynchronous histograms, it is necessary to consider the impact of the non-idealities of the histogram acquisition system. Among these non-idealities is the limited resolution of the ADC used to digitize the signal under analysis. To understand this impact consider, as an example, the histogram acquisition system presented in Fig. B.1 [Luís, 2004: 1]. Each input analog sample is converted to a digital value by an ADC. The ADC output is used to call up a

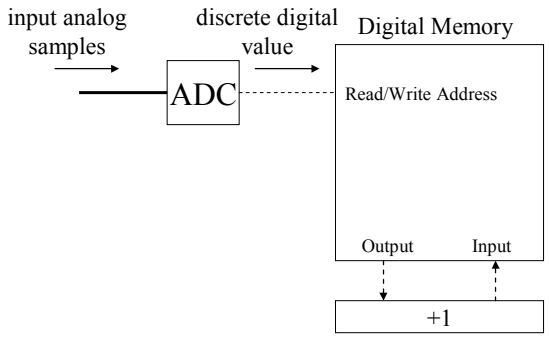

Fig. B.1. Block diagram of the proposed histogram counter.

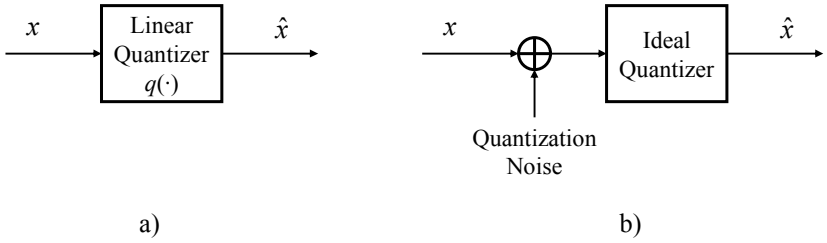

Fig. B.2. Simplified block diagram of the considered quantizer.
a) Non-ideal system; b) Equivalent non-ideal system.

memory address, which is incremented. After the desired number of samples is acquired, the contents of the memory correspond to the amplitude histogram. The amplitude resolution of a histogram calculator is determined by the ADC. This device acts as a quantizer and, as such, introduces quantization noise. It will be show, in this appendix, that this noise leads to the underestimation of the Q-factor, ultimately imposing a maximum limit for the measurable Q factor.

B.2. Theoretical Model for the Quantization Noise

In order to evaluate the distortion induced in the quantization process, the ADC can be characterized as being a uniform quantizer with step size Δ [Cover, 1991] (pp. 134). A uniform quantizer converts an input entry, x, into a discrete output $\hat{x} = q(x)$, where $q(x)$ is the quantizer function, as represented in Fig. B.2-a). The output of the quantizer function is given by [Cover, 1991] (pp. 139):

$$q(x) = \sum_{i=1}^{N_b} y_i \cdot S_i(x) \tag{B.1}$$

where $S_i(x)$ is given by:

$$S_i(x) = \begin{cases} 1, & y_i - \dfrac{\Delta}{2} < x < y_i + \dfrac{\Delta}{2} \\ 0, & \text{otherwise} \end{cases} \tag{B.2}$$

This defines a set of N_b identical cells of center y_i. $q(x)$ corresponds to the center of the cell that contains x. The statistical average of the distortion caused by the quantization process can be written as [Cover, 1991] (pp. 145):

$$D = \int_{-\infty}^{+\infty} d\left(x,\hat{x}\right)\cdot f_X\left(x\right)\cdot dx \tag{B.3}$$

where $f_X(x)$ is the PDF of x and $d\left(x,\hat{x}\right)$ is the a measure of distortion between x and $\hat{x}$. The most common measure of the distortion between two numbers is the squared error defined by [Cover, 1991] (pp. 144):

$$d\left(x,\hat{x}\right) = \left|x - q\left(x\right)\right|^2 \tag{B.4}$$

Replacing (B.4) and (B.1) in (B.3) and assuming real values for x and $q(x)$, the average distortion can be expressed as [Cover, 1991] (pp. 145):

$$D = \sum_{i=1}^{N}\int_{y_i-\Delta/2}^{y_i+\Delta/2}\left(x-y_i\right)^2\cdot f_X\left(x\right)\cdot dx \tag{B.5}$$

Expressions (B.5) requires previous knowledge of the PDF of the measured signal. However, this is usually not the case. In order to estimate the distortion caused by the quantization process will be assumed that the signal under analysis is a binary NRZ signal. As such, its PDF may be approximated by the superposition of two Gaussian PDFs centered at the levels μ_1 and μ_0 with the variances σ_1^2 and σ_0^2, corresponding to the mark and space symbols respectively:

$$f_X\left(x\right) = \frac{1}{2}\cdot\left[\frac{1}{\sqrt{2\pi}\sigma_0}\cdot\exp\left(-\frac{\left(x-\mu_0\right)^2}{2\sigma_0^2}\right)+\frac{1}{\sqrt{2\pi}\sigma_1}\cdot\exp\left(-\frac{\left(x-\mu_1\right)^2}{2\sigma_1^2}\right)\right] \tag{B.6}$$

Replacing (B.6) in (B.5) yields an average distortion given by:

$$D = \sum_{i=1}^{N} \int_{y_i-\Delta/2}^{y_i+\Delta/2} \frac{(x-y_i)^2}{2\sqrt{2\pi}} \cdot \left[\frac{1}{\sigma_0} \cdot \exp\left(-\frac{(x-\mu_0)^2}{2\sigma_0^2} \right) + \frac{1}{\sigma_1} \cdot \exp\left(-\frac{(x-\mu_1)^2}{2\sigma_1^2} \right) \right] \cdot dx \tag{B.7}$$

Expression (B.7) permits an estimation of the average distortion due to the quantization process. This allows the definition of a simplified model for the characterization of the impact of quantization noise on the performance monitoring, as presented in Fig. B.2-b). In this model, the signal under analysis is combined with additive quantization noise with a variance *D*, given by (B.7), and fed into an ideal quantizer with infinitesimal resolution. This model will be used in section B.3 to estimate the impact of the quantization noise on the Q-factor estimates.

B.3. Impact of the Quantization Noise on the Q-factor Estimation

Under the conditions described in section B.2, the Q-factor of the signal under analysis may be approximated by:

$$q = \frac{\mu_1 - \mu_0}{\sigma_1 + \sigma_0} \tag{B.8}$$

However, after the quantization process, we must account for the impact of the quantization noise. For this purpose, the quantization noise will be approximated by a Gaussian distribution, with null average and variance *D*. As such, the equivalent Q-factor of the quantized signal under analysis may be approximated by:

$$q_q = \frac{\mu_1 - \mu_0}{\sqrt{\sigma_1^2 + D} + \sqrt{\sigma_0^2 + D}} \tag{B.9}$$

Expression (B.9) shows that a Q-factor monitoring system placed after the quantizer will underestimate the quality of the signal under analysis due to the impact of the quantization

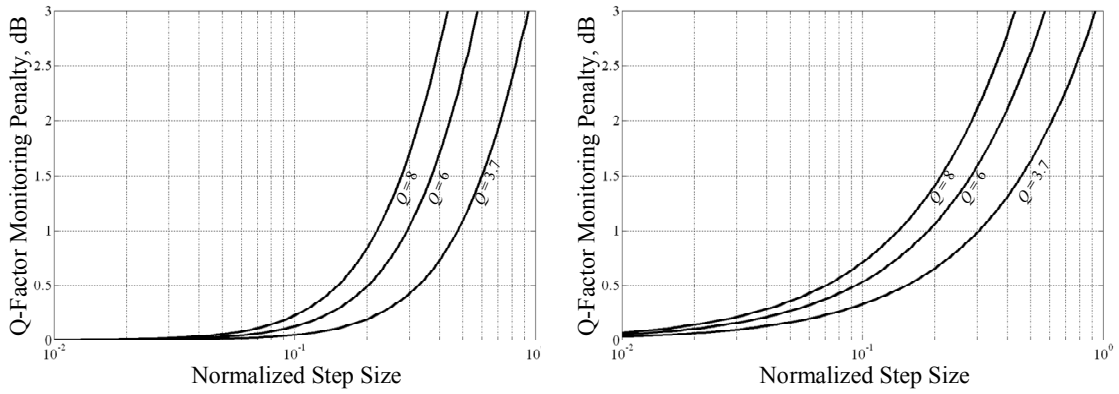

Fig. B.3. Dependence of the Q-factor monitoring penalty on the normalized step size, for Q-factor values of 3.7, 6, and 8. a) The signal is degraded by Gaussian noise;
b) The signal is degraded by signal-noise beat terms.

noise. Taking (B.8) and (B.9), we may define the Q-factor monitoring penalty due to the quantization noise as:

$$\Delta Q_q = 20 \cdot \log_{10}\left(\frac{q}{q_q}\right) \tag{B.10}$$

To illustrate the application of (B.10), consider that the signal under analysis presents an infinite extinction ratio ($\mu_0 = 0$) and is impaired by additive Gaussian noise with variance σ^2. This corresponds to the case of optical signals without optical amplification. Under these conditions the noise component is independent on the signal under analysis, yielding $\sigma_1 = \sigma_0 = \sigma$. Fig. B.3-a) plots the dependence of the Q-factor monitoring penalty on the normalized step size of the quantizer, defined as:

$$\Delta_n = \frac{2\Delta}{\mu_1 - \mu_0} \tag{B.11}$$

It was assumed that the Q-factor of the signal under analysis takes the values 3.7, 6 and 8, corresponding to the bit-error rates 1×10^{-4}, 1×10^{-9}, and 1×10^{-15}, respectively. As shown, the Q-factor monitoring penalty increases rapidly with the normalized step-size. Furthermore, increasing the Q-factor of the signal under analysis requires a more demanding step size to

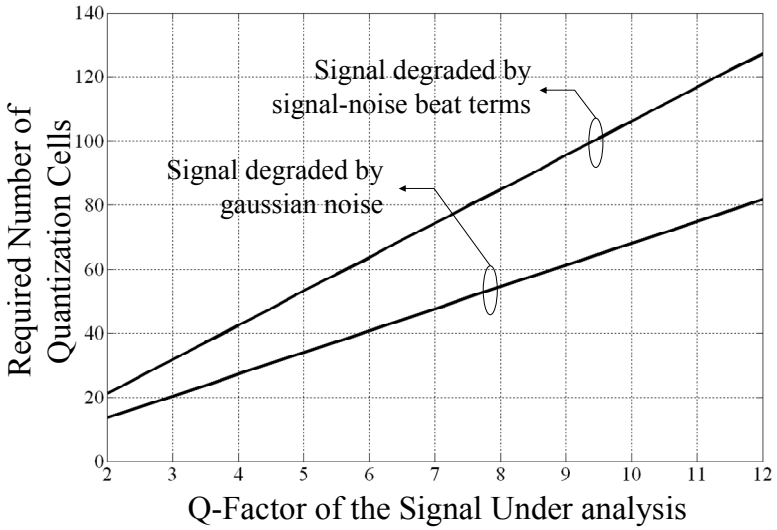

Fig. B.4. Dependence of the required number of quantizer cells on the Q-factor of the signal under analysis assuming signals degraded by Gaussian noise and signal-noise beat terms.

achieve the same monitoring penalty. Assuming a maximum allowable penalty of 1 dB leads to normalized step sizes of 0.48, 0.3, and 0.21, for the Q-factor values of 3.7, 6, and 8, respectively.

A more realistic approach must take into consideration the impact of the nonlinear characteristic of the photodetector used to signal under analysis. In this case, one must take into account that the dominant noise components are dependent on the signal, altering significantly the variances of the noise associated with the mark and space symbols. To simplify this analysis, it will be assumed that the variance of the noise associated with the space symbol is null. As a result, the Q-factor of the signal under analysis depends only on the variance of the noise degrading the mark symbol as $Q=\mu_1/(2\sigma_1)$ and the dependence of the Q-factor monitoring penalty may be calculated directly by using (B.7), (B.9), and (B.10). This dependence is presented in Fig. B.3-b). It is shown that the analysis of under these conditions is substantially more demanding than the previous case. A maximum allowable penalty of 1 dB leads to normalized step sizes of 0.3, 0.18, and 0.13, for the Q-factor values of 3.7, 6, and 8, respectively. These values correspond to a decrease with respect to the previous case by a factor of 1.6.

The values of the maximum allowable step size, $\Delta_{n,max}$, may be related with the required number of quantization cells, $N_{b,req}$, using a simple empirical relation $N_{b,req} > 12/\Delta_{n,max}$. Fig. B.4 presents the required number of quantization cells as a function of the

Q-factor of the signal under analysis. It can be seen that the required number of cells evolves linearly with the Q-factor of the signal under analysis. Considering a maximum measurable Q-factor of 8, it may be seen that the minimum number of quantization cell is approximately 85. This value will provide acceptable levels of quantization noise for both the considered cases of noise.

B.4. Conclusions

This appendix has presented a simplified method to estimate the impact of quantization noise on Q-factor estimates using histograms. It has been shown that the required number of quantization cells is directly proportional to the maximum value of Q-factor intended to estimate. In addition, it was demonstrated that a minimum number of 85 cell, or histogram bins, is required to analyze signals with a Q-factor as high as 8, corresponding to a bit-error-rate of 1×10^{-15}, considered error-free.

Appendix C. Distortion Resilient OSNR Monitoring Technique Based on Evaluation of Asynchronous Histograms

C.1. Introduction

Several techniques have been proposed to evaluate signal quality using asynchronous histograms [Hanik, 1999], [Teixeira, 2002], [Rasztovits-Wiech, 1999], and [Shake, 2002: 2]. In most cases, negligible signal distortion must be assumed or, in the case of [Teixeira, 2002], previous knowledge of the measured signal power PDF is required. This work proposes to solve these two limitations by estimating with high accuracy the OSNR from asynchronous histograms using an experimental calibration based on a RAH. The RAH is previously acquired by monitoring the signal under analysis at low noise conditions. The proposed process numerically includes the influence of optical noise in the RAH until it matches the MAH that is to be evaluated. The result of this fitting is an estimate of the optical noise power spectral density, which can be used to determine the OSNR. The advantage of the proposed technique is that distorted signals can be assessed, as long as the RAH presents similar distortion. A detailed description of the proposed technique and its principal limitations is presented in section C.2. Section C.3 presents experimental results that validate the presented technique. Main conclusions are

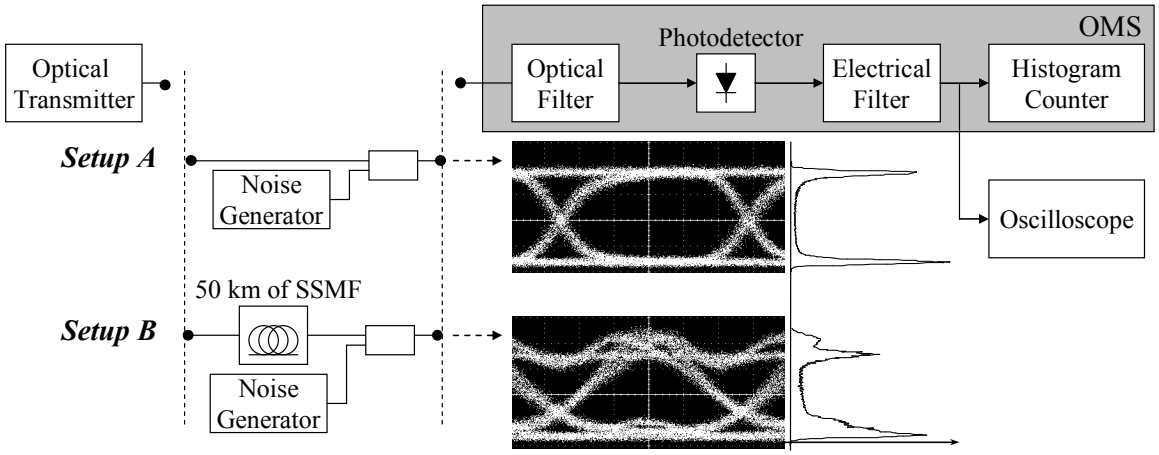

Fig. C.1. Block diagram of the considered system. Insets: eye patterns acquired in the absence of optical noise and corresponding asynchronous histogram.

outlined in section C.4. The work presented in this appendix has been published in [Luís, 2004: 1], [Luís, 2004: 5], [Luís, 2005: 2], [Luís, 2005: 3], and [Luís, 2006: 2].

C.2. OSNR Monitoring Technique

A block diagram of the considered system is presented in Fig. C.1, where setup *A* is assumed. The optical transmitter produces an optical signal, which is combined with optical noise by an optical coupler. The optical signal and noise are inserted in the OMS, composed by an optical filter with bandwidth B_o, followed by a p-i-n photodetector with responsivity R_s. The generated current is filtered by an electrical filter with bandwidth B_e, and processed by a histogram counter. To evaluate the signal distortion, a digital oscilloscope is placed in parallel with the histogram counter.

In the case of a constant optical signal with average power, P_s, the PDF of the generated current at the photodetector output conditioned to the signal power, $p_n(\mu|P_s)$, can be assumed gaussian [Bergano, 1993]:

$$p_n\left(\mu \mid P_s\right) = \frac{1}{\sqrt{2\pi \cdot \sigma^2\left(P_s\right)}} \cdot \exp\left\{-\frac{\left(\mu - I_s\right)}{2\sigma^2\left(P_s\right)}\right\} \tag{C.1}$$

where $I_s=R_s \cdot P_s$ is the average current. The term $\sigma^2(P_s)$ is the variance, approximated by [Agrawal, 1997] (pp. 404):

$$\sigma^2\left(P_s\right) = 4R_s \cdot P_s \cdot N_{sp}B_e + 4R_s^2 \cdot N_{sp}^2 \cdot B_e B_o \tag{C.2}$$

where N_{sp} is the power spectral density of the optical noise. Note that only the signal-spontaneous emission and the spontaneous emission-spontaneous emission beat noises are considered. In practical systems, the remaining contributions can usually be neglected [Rasztovits-Wiech, 1999]. To obtain the PDF of the electrical current at the histogram counter input, $p_{EST}(\mu)$, it is necessary convolve $p_n(\mu \mid P_s)$ with the PDF of the additive noise generated in the OMS, $p_{OMS}(\mu)$ [Teixeira, 2002]. The latter is assumed gaussian, with variance σ_{OMS}^2. If the optical transmitter is producing a modulated optical signal with instantaneous power, $s(t)$, and average optical power P_s, the PDF of the signal under analysis may be approximated by removing the conditioning of $p_n(\mu \mid s)$ and convolving the result with the PDF of the OMS noise:

$$p_{EST}\left(\mu\right) = \left[\int_{-\infty}^{+\infty} p_{SIG}\left(s\right) \cdot p_n\left(\mu \mid s\right) \cdot ds\right] * p_{OMS}\left(\mu\right) \tag{C.3}$$

where $p_{SIG}(s)$ is the PDF of the optical signal's instantaneous power. It is assumed than the electrical and optical filters' bandwidths are large enough to neglect signal distortion due to filtering. Equation (C.3) can be used to obtain an estimated histogram using the method presented in [Teixeira, 2002] if $p_{SIG}(s)$ is known. Assuming that $p_{SIG}(s)$ is unknown, we propose an approximation of (C.3) assuming that the OMS noise is added to the signal before the optical beat noise components are generated. In this case, (C.3) becomes:

$$p_{EST}\left(\mu\right) \approx \int_{-\infty}^{+\infty} \left[p_{SIG}\left(s\right) * p_{OMS}\left(s\right)\right] \cdot p_n\left(\mu \mid s\right) \cdot ds \tag{C.4}$$

Note that expressions (C.3) and (C.4) become identical if the OMS noise is suppressed. The validity of the proposed approximation is limited to cases where the signal's contribution to the detected electrical current, $R_s \cdot s(t)$, is larger that the OMS noise. The approximation allows the isolation of the term $p_{SIG}(s) * p_{OMS}(s)$, which can be measured by

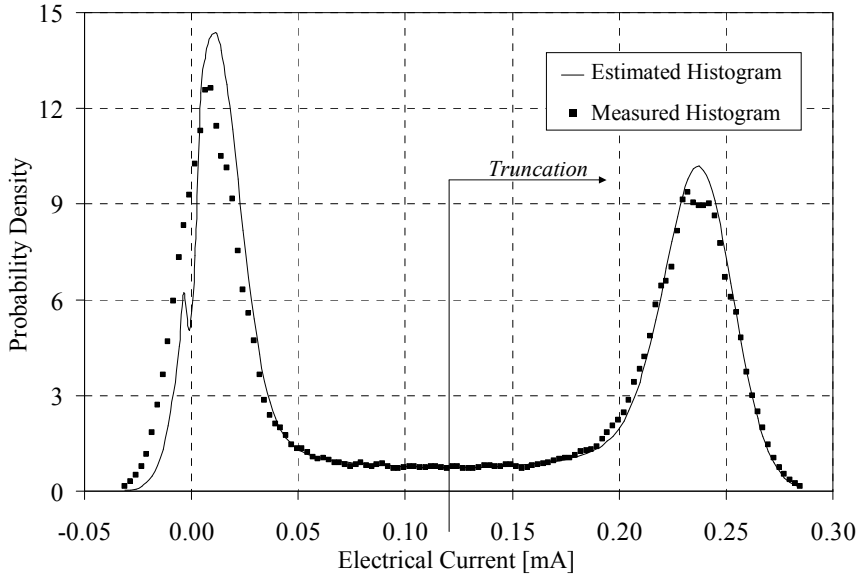

Fig. C.2. Block diagram of the considered system. Insets: eye patterns acquired in the absence of optical noise and corresponding asynchronous histogram.

acquiring a histogram of the signal in the absence of optical noise. This histogram corresponds to the RAH and must be acquired from a signal with the same distortion has the signal that is to be monitored. No significant limitations are imposed concerning the shape of the monitored signal. In this work, binary NRZ signals will be used. However, application to other modulation formats is straightforward.

To assess the validity of the proposed approximation, Fig. C.2 presents a MAH of a signal with an OSNR of 22 dB and the corresponding estimated histogram, obtained using (C.4). The optical transmitter produces a 10 Gb/s NRZ signal and bandwidths of 20 GHz and 72 GHz are used for the electrical and optical filters, respectively. An average power at the photodetector input of –9 dBm is used. The photodetector presents unitary responsivity and the OMS generates noise with a variance of 126 μA^2. The MAH and RAH are produced by collecting 2×10^6 samples at a rate of 200 ksamples/s. The RAH was obtained by performing a measurement without the main contributor to optical noise. Fig. C.2 shows that the accuracy of the estimated histogram increases with the electrical current level. Discrepancies are verified in the area around the space symbol whereas the area around mark symbol is accurately estimated, except for small discrepancies resulting from limited number of collected samples. This shows that only the areas of the numerically calculated AH corresponding to high amplitude levels should be used for comparison with the

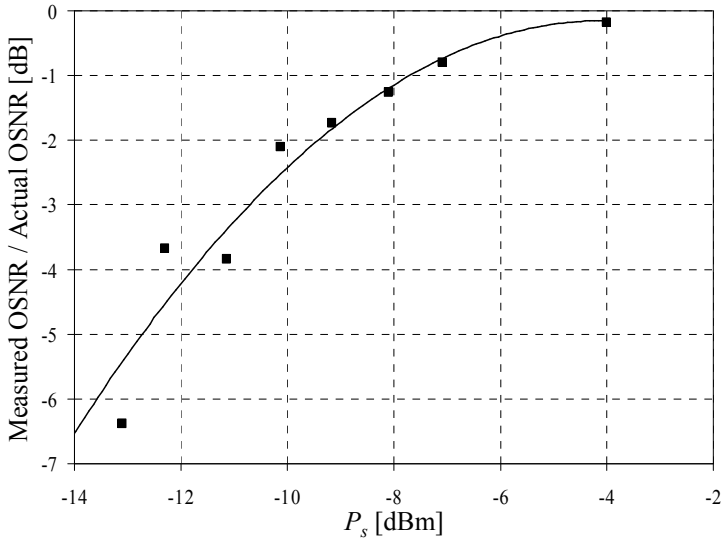

Fig. C.3. OSNR measurement error in dB, as a function of P_s for $OSNR$ = 22 dB. The trendline is a visual guide.

measured histogram. However, this is not a limitation for the OSNR evaluation since these areas are more affected by optical noise than areas corresponding to low amplitude levels.

The procedure used to measure the OSNR consists in adjusting the estimated value of N_{sp}, in order to minimize the mean squared error between the estimated histogram and the MAH. Before the comparison, the histograms are truncated from the mean amplitude level upwards, as shown in Fig. C.2. After finding the best value of N_{sp} using a nonlinear minimization algorithm, the OSNR can be calculated by $OSNR=10\cdot\log_{10}(P_s/(2N_{sp}\cdot B_o))$ [Bergano, 1993].

C.3. Experimental Results

The accuracy of the proposed method depends on the relation between the average power at the photodetector input, and the OMS noise power generated in the receiver. To evaluate this dependence, we have performed OSNR measurements with the proposed method, maintaining an OSNR of 22 dB and reducing the total optical power at the photodetector input. Fig. C.3 presents the dependence of the measurement error as a function of P_s. The remaining system parameters are identical to the ones used at Fig. C.2.

Fig. C.3 shows that, as P_s decreases, the measurement error increases significantly. Nevertheless, the OSNR estimates are always conservative. The measurement errors result from the discrepancies between estimated histogram and the MAH, mainly due to the

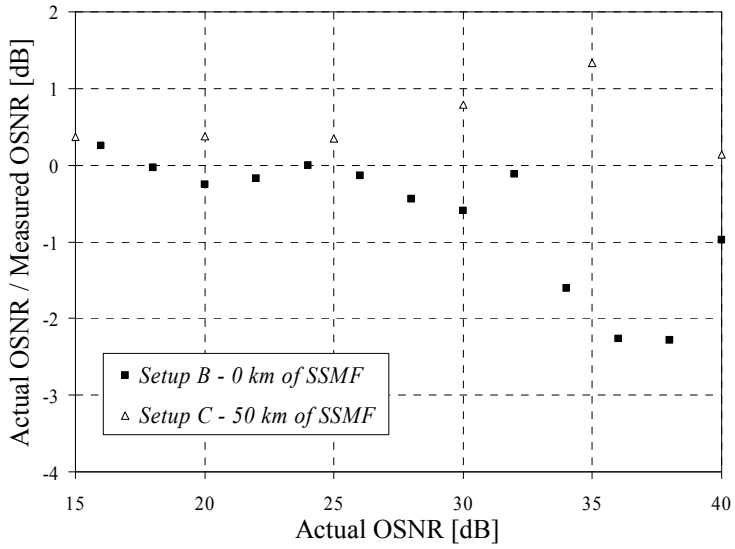

Fig. C.4. OSNR measurement error in dB, as a function of the actual OSNR. An optical power at the photodetector input of -4 dBm was used.

approximation used to obtain (C.4) but also, as verified in Fig. C.2, from a limited number of acquired samples. Values of P_s above −7.5 dBm are required to obtain measurement errors bellow 1 dB. In a more generic form, we verify a minimum ratio I_s/σ_{OMS} of 15. To reduce the minimum input power level it is necessary to reduce the electrical noise power generated in the receiver. This can be achieved by reducing the electrical filter bandwidth. As a consequence, the range of bit-rates that can be evaluated is decreased. A compromise must be found between the desired range of signal's bit-rates to evaluate and the measurement accuracy.

To assess the validity range of the proposed monitoring method, Fig. C.4 presents the measurement error as a function of the actual OSNR, using setup *A*. The system parameters are identical to the ones used for Fig. C.2, except for P_s=-4 dBm. Errors below 1 dB are verified for OSNR values below 32 dB. Above this value, it becomes difficult for the minimization algorithm to find an appropriate value of N_{sp} because the variance of the optical beat noise components becomes comparable to the variance of the electrical noise. This limitation is usually negligible since for OSNR values larger than 32 dB, the noise power becomes too low to induce significant degradation.

To test the robustness of the proposed method to signal distortion induced by GVD, 50 km of SSMF with a dispersion parameter of 17 ps/nm/km are placed before the optical coupler, constituting setup *B*. To assess the GVD-induced distortion, the insets of Fig. C.1

show the measured eye patterns and AH of the signal with and without the transmission fiber. Noticeable ISI is present when the transmission fiber is inserted. To measure the OSNR, a new RAH of the distorted signal was acquired. The OSNR was measured in the same range as presented for setup *A*. The measurement error as a function of the actual OSNR is presented in Fig. C.4. It is shown that the evolution of the measurement error follows a similar pattern as obtained for setup *A*, with measurement errors below 1 dB for OSNR values below 32 dB. This validates the proposed monitoring method, even in conditions of significant signal distortion.

C.4. Conclusions

An OSNR monitoring method using asynchronous histograms has been proposed and validated experimentally for 10 Gb/s signals. This method consists in using a previous calibration that produces a RAH, obtained in conditions of low optical noise, in order to obtain the asynchronous histograms that would be expected in conditions of optical noise-induced degradation. Measurement errors below 1 dB have been verified for OSNR values below 32 dB. The proposed method shows resilience to GVD-induced distortion, maintaining the same 1 dB error margins verified without signal distortion. The principal limitation of the proposed method is a minimum average optical power required at the input of the monitoring device. In the case of the tested system, a minimum input power of -7.5 dBm was verified. It is shown that electrical bandwidth limitations may be required to reduce this value. This indicates that a compromise between minimum input power and maximum evaluated bit-rate must be found.

Appendix D. Evaluation of Intra-Band Crosstalk Using Asynchronous Histograms

D.1. Introduction

This appendix proposes a technique to evaluate intra-band crosstalk based on the numerical computation an estimated histogram of the signal and intra-band crosstalk under analysis. By comparing the estimated histogram with the corresponding MAH, conclusions about the affecting crosstalk power can be drawn. The estimated histogram computation is based on transforming an amplitude histogram of the signal in the absence of crosstalk, in order to match the MAH. The amplitude histogram of the signal in the absence of crosstalk is referred in this work as RAH. The work presented in this appendix has been published in [Luís, 2004: 2], and [Luís, 2004: 5].

D.2. Numerical Model for Intra-band Crosstalk

The intra-band crosstalk generally results from imperfect isolation in optical add&drop multiplexers or optical cross-connectors and can be classified as homodyne or heterodyne if the signal and crosstalk components have or not closely valued carrier frequencies, respectively [Monroy, 2002] (see page 24). In the case of homodyne crosstalk, we can still consider the crosstalk coherent if the delay between the crosstalk and signal

components is below the coherence delay of the laser used to produce the signal. In that case, the consequence of the crosstalk is a fading effect and will not be considered in this work. If the delay between the signal and crosstalk components is in excess of the laser's coherence delay, the homodyne crosstalk is considered incoherent and generates a noise-like effect [Monroy, 2002] (see page. 24)]. Incoherent homodyne and heterodyne crosstalk induce similar degradation [Monroy, 2002] (see page 24).

Consider the detection of an optical signal with constant power P_s, affected by intra-band crosstalk with constant power P_c. Assuming that the electrical receiver bandwidth is large, when compared with the signal bandwidth, the PDF of the detected photocurrent, conditioned to the signal and crosstalk powers, $p_c(\mu|P_s,P_c)$, can be approximated by [Monroy, 2002] (see page 66):

$$p_{XTK}(\mu \mid P_s, P_c) = \begin{cases} \dfrac{1}{2R \cdot \pi \cdot \sqrt{1-\left[(\mu - P_s)/(2R)\right]^2}} & -2R < \mu - P_s < 2R \\ 0 & \text{elsewhere} \end{cases} \qquad R = \sqrt{P_s \cdot P_c} \tag{D.1}$$

where the pin responsivity is assumed unitary. Expression (D.1) only takes into account the signal-crosstalk beat component. The crosstalk-crosstalk beat component can usually be neglected due its low magnitude. ASE noise will not be considered in this work. The PDF of the electrical current, $p_{EST}(\mu)$, can be obtained by convolving $p_{XTK}(\mu \mid P_s,P_c)$, with the PDF of the OMS noise, $p_{OMS}(\mu)$. The latter is assumed gaussian, with variance σ^2_{OMS} [Teixeira, 2002]. In the case of modulated signal and crosstalk components, the PDF of the electrical current can be approximated by removing the conditioning of $p_{XTK}(\mu \mid P_s,P_c)$ and convolving the result with the electrical noise PDF:

$$p_{EST}(\mu) = \left[\int_{-\infty}^{+\infty} \int_{-\infty}^{+\infty} p_{XTK}(\mu \mid s,c) \cdot p_{SIG,XTK}(s,c) \cdot ds \cdot dc \right] * p_{OMS}(\mu) \tag{D.2}$$

where $p_{SIG,XTK}(s,c)$ is the joint PDF of the signal and crosstalk components' instantaneous power, s and c, respectively. Assuming that the signal and crosstalk components are

uncorrelated, we have $p_{SIG,XTK}(s,c) = p_{SIG}(s) \times p_{XTK}(c)$. The terms $p_{SIG}(s)$ and $p_{XTK}(c)$ are the PDFs of the signal and crosstalk components' instantaneous power, respectively. For simplicity, it will be assumed that the crosstalk component has only two levels with identical probability of occurrence, corresponding to the mark and space symbols. In that case, (D.2) can be written as:

$$p_{EST}(\mu) = \frac{1}{2}\left[\int_{-\infty}^{+\infty} p_{XTK}(\mu \mid s, c_0) \cdot p_{SIG}(s) \cdot ds + \int_{-\infty}^{+\infty} p_{XTK}(\mu \mid s, c_1) \cdot p_{SIG}(s) \cdot ds\right] * p_{OMS}(\mu) \quad \text{(D.3)}$$

where c_0 and c_1 are the crosstalk component's power levels corresponding to the space and mark symbols, respectively. Expression (D.3) constitutes a simplified model to calculate the PDF of the received electrical current. The corresponding histogram, normalized to the number of acquired samples, is given by:

$$h_{c,n} = \int_{\mu_n - \Delta/2}^{\mu_n + \Delta/2} p_c(\mu) \cdot d\mu \approx \Delta \cdot p_c(\mu_n) \quad \text{(D.4)}$$

where $\mu_n = n \times \Delta$ is the center of the n-th bin of the histogram and Δ is the bin amplitude.

Fig. D.1 presents an example of asynchronous histograms calculated using (D.3) and (D.4) for different signal-to-crosstalk ratio (SCR) levels. Note that, in this work, the SCR is given by: $SCR=P_s/(c_0+c_1)\times 2$. $p_{SIG}(s)$ was obtained using the method presented in Chapter 3, for raised cosine signals with a transition time of 50% of the bit period, an average power of -9 dBm and an extinction ratio of 15 dB.

Fig. D.1 shows that the principal changes due to crosstalk occur in the peak corresponding to the mark symbol. Changes in the space symbol are negligible for SCR equal or above 20 dB. Therefore, it is only necessary to consider the part of the PDF corresponding to the mark symbol in order to evaluate the crosstalk of a given signal, for low crosstalk levels. Note that the histograms presented in Fig. D.1 are in agreement with [Hanik, 1999].

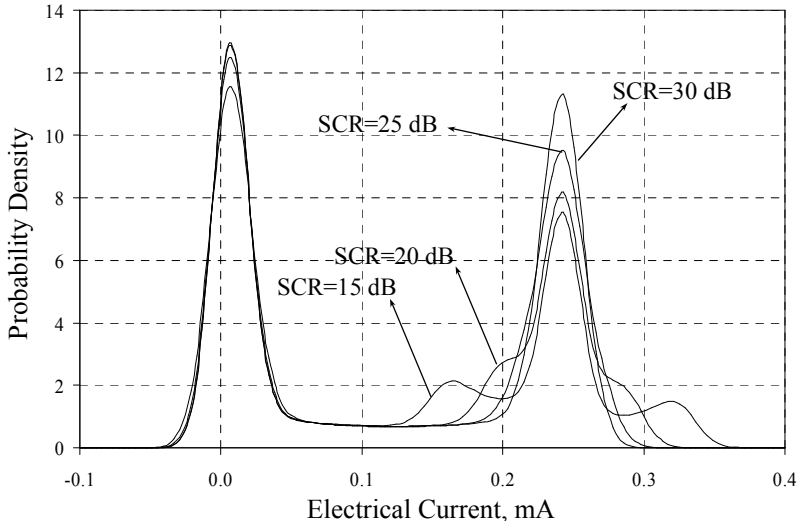

Fig. D.1. Asynchronous histograms of a signal degraded by different levels of SCR.

In real systems it is not always possible to obtain the PDF of the monitored signal's instantaneous power due to the large number of parameters that condition the signal shape. Nevertheless, the PDF of the signal's instantaneous power can be approximated by a RAH, acquired experimentally in the monitoring point. The RAH contains the PDF of the monitored signal's instantaneous power and the influence of the OMS noise. Therefore, the error of the performed approximation will depend on the rate between the signal power and the electrical noise. The PDF that corresponds to the RAH, $p_{REF}(\mu)$, is given by $p_{REF}(\mu) = p_{SIG}(\mu) * p_{OMS}(\mu)$. Using the reference PDF, (D.3) can be approximated by:

$$p_{EST}(\mu) \approx \frac{1}{2} \cdot \int_{-\infty}^{+\infty} p_{XTK}(\mu \mid s, c_0) \cdot p_{REF}(s) \cdot ds + \frac{1}{2} \cdot \int_{-\infty}^{+\infty} p_{XTK}(\mu \mid s, c_1) \cdot p_{REF}(s) \cdot ds \quad \text{(D.5)}$$

Expression (D.5) assumes that the electrical noise is added to the signal before the signal-crosstalk beat component is generated. Note that expressions (D.5) and (D.3) are identical if the electrical noise is neglected. The validity of the proposed approximation is limited to cases where the signal's contribution to the detected electrical current is much larger that the electrical noise. This is generally true for the mark symbol, which also corresponds to the area of greatest interest in the evaluation of intra-band crosstalk. The error of (D.5) with relation to (D.3) depends mainly on the OMS noise power. Expression (D.5) can be further simplified assuming that $c_0 \approx 0$:

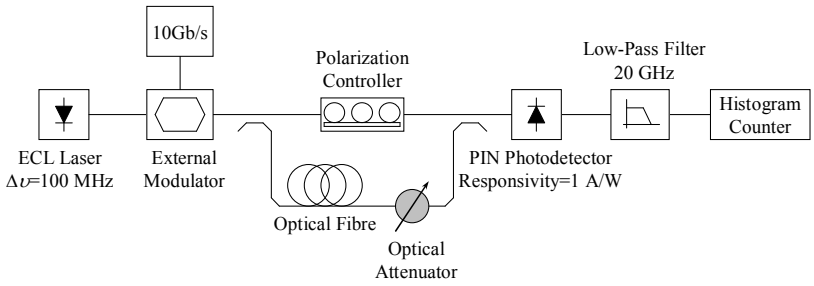

Fig. D.2. Block diagram of the experimental setup.

$$p_{EST}(\mu) \approx \frac{1}{2} \cdot p_{REF}(\mu) + \frac{1}{2} \int_{-\infty}^{+\infty} p_{XTK}(\mu \mid s, c_1) \cdot p_{REF}(s) \cdot ds \tag{D.6}$$

Expression (D.6) comprises a simplified model to obtain the PDF of the electrical current resulting from the direct detection of an intra-band crosstalk affected signal. The corresponding histogram can be obtained using (D.4). This model will be experimentally validated in section D.3.

D.3. Experimental Validation

Consider the block diagram of the experimental setup, presented in Fig. D.2. The light produced by an external cavity laser (ECL) with a linewidth of $\Delta\upsilon$=100 MHz is externally modulated to produce a binary pseudo-random non-return to zero signal with 2^{23}-1 symbols at 10 Gb/s. After the transmitter, the signal is split to form a signal path and a crosstalk path. In the signal path, a polarization controller adjusts the signal's polarization to maximize the crosstalk-induced degradation. A fiber segment and an optical attenuator compose the crosstalk path. The fiber segment is long enough to introduce a delay in excess of the laser's coherence length. The optical attenuator controls the rate between the signal power and the crosstalk power at the pin photodetector input. The response of the receiver presents a –3 dB cut-off frequency of 20 GHz, considered enough to neglect signal distortion due to electrical filtering. For histogram acquisition purposes, it is assumed that the pin presents a unitary responsivity. After detection and filtering, the signal is sent to a histogram counter, which samples the signal at a rate of 200 ksamples/s. Each histogram results from acquiring 2^6 samples.

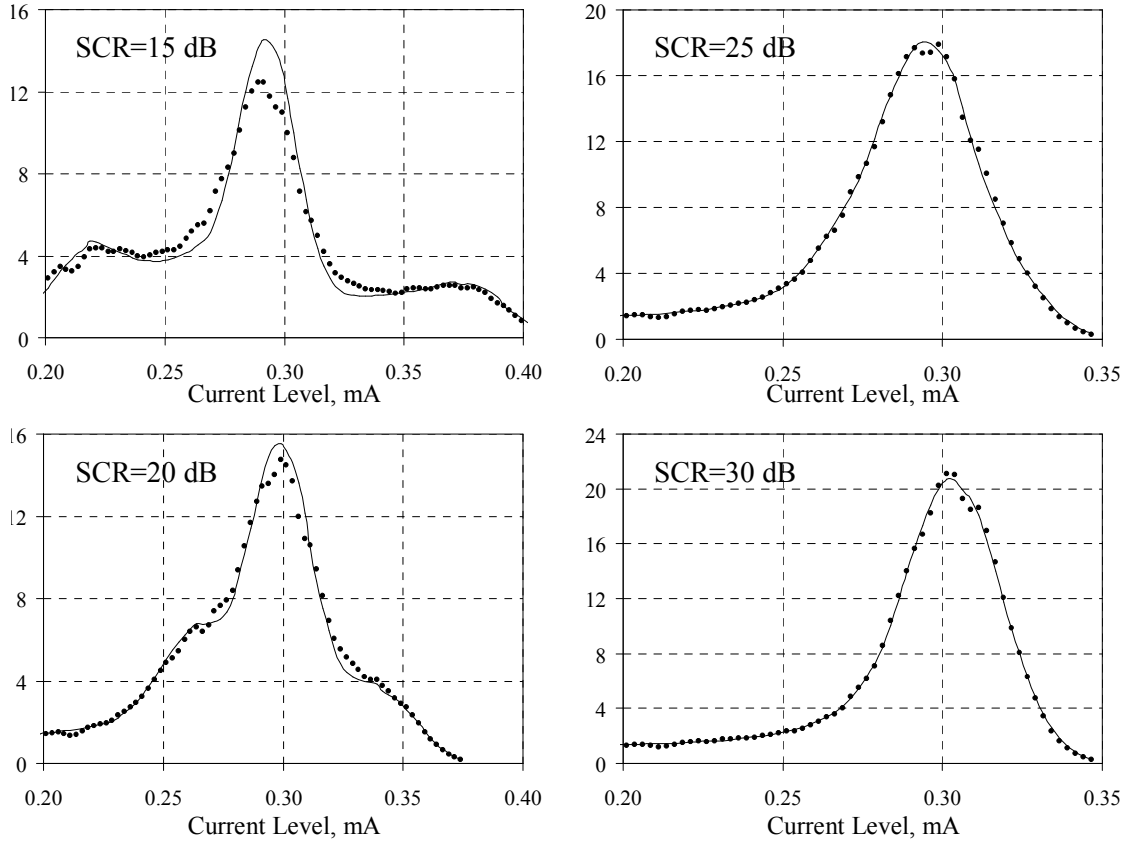

Fig. D.3. Comparison between MAH (dots) and corresponding EAH (lines) for different SCR levels. Amplitude levels below the average current are not considered.

To assess the validity of (D.6), Fig. D.3 presents a comparison between MAH and the corresponding estimated histograms for different SCR values. Only the region corresponding to the mark symbol is considered. An average optical power at the photodetector input of –7 dBm and OMS noise variance of 125 μA^2 are considered. The RAH used to produce the estimated histograms was acquired by first canceling the crosstalk component. Fig. D.3 shows a good agreement of the MAHs with the corresponding EAHs, validating the proposed method. The accuracy of the numerically estimated curves decreases for lower SCR values due to the approximation performed from expressions (D.5) to (D.6). More rigorous estimated histograms can be obtained using expression (D.5) with the cost of an increased computation time. Using the presented model allowed a reasonable histograms estimation for SCR values above 20 dB, corresponding to power penalties bellow 3 dB [Teixeira, 2002]. Therefore, expression (D.6) is sufficiently accurate.

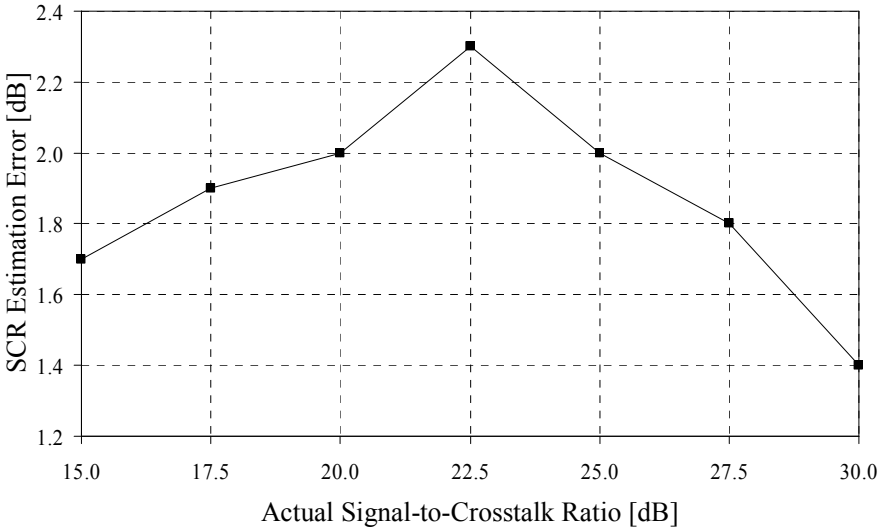

Fig. D.4. SCR estimation error of the proposed monitoring technique, as a function of the actual SCR.

D.4. SCR Measurement Technique

To perform SCR measurements, we perform the curve fitting of an EAH to a MAH by adjusting the estimated value of SCR with a nonlinear minimization algorithm. In each iteration, the nonlinear minimization algorithm varies the estimated SCR to minimize the error function, *e*, given by:

$$e = \sum_{n=n_t}^{N_b} h_{EST,n}^2 - h_{MEA,n}^2 \tag{D.7}$$

where $h_{EST,n}$ and $h_{MEA,n}$ are the estimated histogram and the MAH, respectively. N_b is the number of bins in the histograms and n_t is such that $\mu_{n_t} \geq I_s$. The term I_s is the average current. This limitation corresponds to the truncation of the histograms. The result of the fitting process is an estimate of the actual SCR of the measured signal. Fig. D.4 presents the ratio between the estimated and actual SCR levels as a function of the latter. Due to the fact that the used RAH contains the influence of the OMS noise and the limited number of samples, the minimization algorithm tends to over-estimate the SCR. Measurement errors under 2.4 dB are verified along the observed range of SCR values. A non-zero average measurement error of 1.9 dB suggests the use of a corrective factor.

D.5. Conclusions

In this work, a novel technique has been derived to evaluate intra-band crosstalk induced by a single source, using asynchronous histograms. A numerical model to obtain an estimate of the PDF of a signal affected by intra-band crosstalk is derived. The model proposes the approximation of the PDF of the signal in the absence of intra-band crosstalk using a previously acquired RAH. The influence of intra-band crosstalk is then numerically included. Therefore, accurate knowledge of the signal's PDF is not required.

By comparing the measured and estimated histograms it is possible to determine the SCR. The application of the proposed technique and corresponding numerical estimation model is tested experimentally. SCR estimation errors under 2.4 dB are obtained, validating the proposed model for the evaluation of intra-band crosstalk.

Appendix E. Passive PM-IM Converter Filter for High Capacity Systems

E.1. Introduction

Fiber wavelength converters (FWC) using XPM have been considered as key elements in future wavelength or time division multiplexing optical networks. These can support ultra-high bit-rates (above 160 Gb/s [Rau, 2004]), due to the Kerr nonlinearity fentosecond response. Generically, a XPM-FWC consists of a nonlinear medium, where the input data and a CW signals are injected and interact, followed by a PM-IM converter, as shown in Fig. E.1-a). In the nonlinear medium, the input signal will induce XPM on the CW, resulting in modulation sidebands. Afterwards, the PM-IM converter transforms the PM of the CW in IM. A band-pass filter may be used afterwards, to suppress the original signal.

In this work we propose a filter that induces a phase shift in the carrier component of the phase modulated CW signal. Shifting the phase of the CW carrier component will cause it to interfere constructively or destructively with the modulation sidebands, acting as a PM-IM converter. An additional attenuation of the CW carrier component will allow reducing its DC level, improving the extinction ratio. If properly dimensioned, this filter may become a PM-IM converter, implemented as a linear filter. This filter will be referred

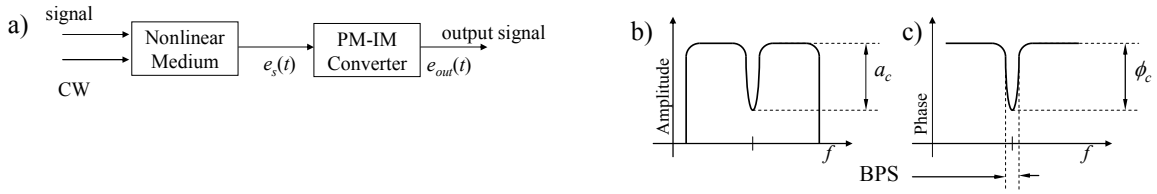

Fig. E.1. Scheme of a) a XPM-based wavelength converter and b) amplitude and c) phase characteristics of a CPSF.

here as CPSF. A schematic transfer function of the CPSF is presented in Fig. E.1-b) and c). Unlike interferometric PM-IM converters, which usually switch off the output power in the zero symbols or sideband filter PM-IM converters, which select only a fraction of the CW sidebands, the CPSF only attenuates the average CW power, allowing the peak power of the output pulses to be significantly higher than the CW power. The work presented in this appendix has been partially published in [Luís, 2006: 1]

E.2. Principle

Consider the FWC presented in Fig. E.1–a), where a CPSF replaces the PM-IM converter. It can be assumed that the complex envelope of the electrical field at the CPSF input, $u_s(t)$, is purely phase modulated, taking the form $u_s(t) = \sqrt{P_{CW}} \cdot e^{j\phi_s(t)}$, where P_{CW} is the average CW power at the CPSF input and $\phi_s(t)$ is the XPM-induced PM. Ideally, the equivalent low-pass transfer function of the proposed CPSF can be given by:

$$H_{CPSF}(f) = 1 + \left(e^{j\phi_c} / \sqrt{a_c} - 1\right) \cdot \delta(f) \tag{E.1}$$

where ϕ_c and a_c are the carrier phase shift and attenuation, respectively, and $\delta(f)$ is the Dirac function. $H_{CPSF}(f)$ is represented schematically in Fig. E.1–b) and –c), where $\delta(f)$ is replaced by a finite bandwidth of phase shift (BPS). The Fourier transform of the complex envelope of the electrical field at the CPSF output, $\tilde{u}_{out}(f)$, is given by:

$$\tilde{u}_{out}(f) = \tilde{u}_s(f) \cdot H_{CPSF}(f) = \tilde{u}_s(f) - \left(1 - e^{j\phi_c} / \sqrt{a_c}\right) \cdot \tilde{u}_s(f) \cdot \delta(f) \tag{E.2}$$

where $\tilde{u}_s(f)$ is the Fourier transform of $u_s(t)$. Converting (E.2) to the time domain yields:

$$u_{out}(t) = u_s(t) - \left(1 - e^{j\phi_c} \Big/ \sqrt{a_c}\right) \cdot \xi, \qquad \text{where} \quad \xi = \tilde{u}_s(0) \cdot \tag{E.3}$$

The dimensioning of ξ by appropriate choice of ϕ_c and a_c, may allow destructive or constructive sum for the zero and one symbols, respectively, similar to what would be obtained in an interferometer. Note that the phase modulated CW must present a valid carrier, i. e. $\tilde{u_s}(0) \neq 0$. For proof of principle simulation, the physical aspects of implementing a CPSF will initially be disregarded, assuming that the amplitude and phase profiles of the filter have the shape presented in Fig. E.1-b) and –c), respectively. However, simulation of a CPSF implemented using fiber Bragg gratings (FBG) will be presented in section E.4.

E.3. Simulation Results

Consider the nonlinear medium as a 1.3 km highly nonlinear dispersion shifted fiber with nonlinearity coefficient of 17 $W^{-1} \cdot km^{-1}$, attenuation of 0.25 dB/km and dispersion slope of 20 $fs/nm^2/km$ and the CPSF with a BPS of 0.4 GHz. The CW and data signal channels are transmitted 5 nm bellow and above the zero dispersion wavelength of 1550 nm, respectively. The XPM-induced IM and PM will be calculated using the analytical models presented in [Cartaxo, 1999:1] and [Luís, 2005: 4], which is described in Appendix F. respectively, and validated by numerical simulation using the split step Fourier method [Agrawal, 1995]. Coupling losses are neglected and the input signal is a 2^{12}-1 pseudo-random bit sequence at 160 Gbit/s with gaussian shaped impulses and pulsewidths of 2 ps and 3 ps. Consider, at this point, that the CPSF presents a fixed setting of ϕ_c=-140º and a_c = 3 dB. Fig. E.2-a) shows the minimum and maximum eye openings of the output pulses, as a function of the input peak power, using a CW input power of 12 dBm (~16 mW). Fig. E.2-b) and –c) present the converted signal eye diagrams for an input peak power of 60 mW.

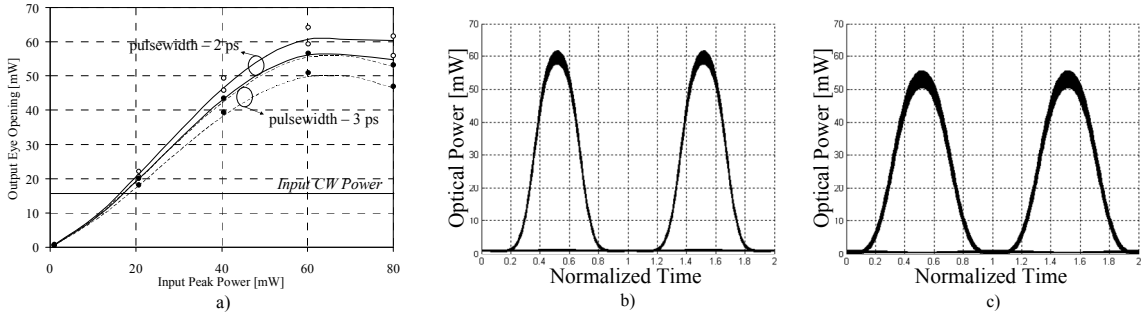

Fig. E.2. Transmission characteristic of the wavelength converter. a) maximum and minimum eye openings, lines – analytical results, circles – numerical simulation;
b) and c) signal eye diagrams with 2 ps and 3 ps pulsewidths respectively.

As can be seen in all cases, a valid output signal can be obtained using the CPSF. Furthermore, the difference of the transmission characteristics for signals with 2 ps and 3 ps pulse-widths, is small up to input peak powers of 60 mW. These results indicate that the CPSF is fairly tolerant to variations of the input signal pulse-width. Unlike interferometric PM-IM converters, which usually switch off the output power in the zero symbols or sideband filter PM-IM converters, which select only a fraction of the CW sidebands, the CPSF only attenuates the average CW power by a_c. As a consequence, the output peak power can be significantly higher than the average CW probe power. Fig. E.2-a) shows that, for an input peak power of 60 mW and CW power of 16 mW, the CPSF presents conversion efficiencies of 100% (identical input and output peak powers) and 83% for the signals with 2 ps and 3 ps pulse-widths, respectively. Preliminary studies indicate that using CPSF with ultra-high nonlinear fibers or Raman assisted XPM may allow reducing

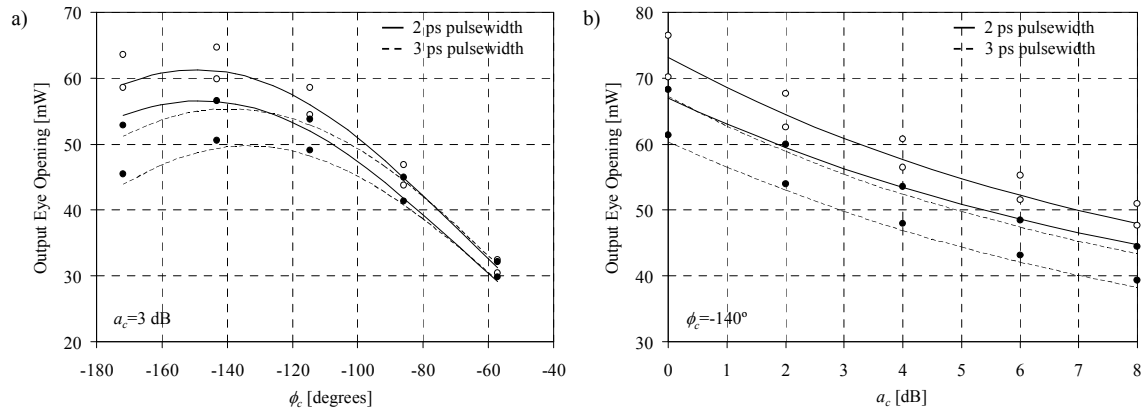

Fig. E.3. Eye opening variation with the CPSF parameters. a) variation of a_c b) variation of ϕ_c. Lines – Analytical results; Circles – Numerical simulation.

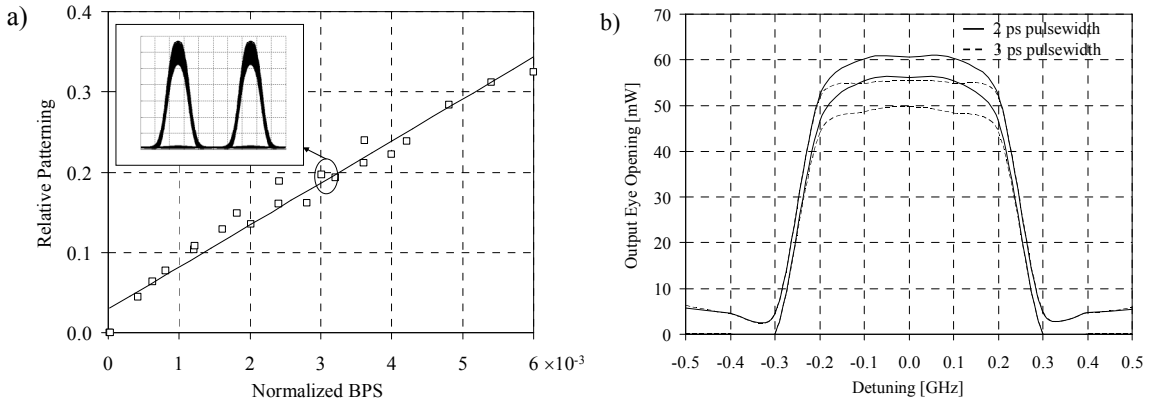

Fig. E.4. Limitations of the CPSF. a) Relative patterning as a function of the normalized BPS (squares). The trendline is a visual guide and the inset is an eye diagrams of the output signal. b) Eye opening as a function of the CPSF detuning.

the required CW power bellow the stimulated Brillouin scattering threshold, eliminating the need to modulate the CW before injecting it in the fiber.

To assess the sensitivity of the CPSF to variation of the filter parameters, Fig. E.3-a) and –b) present the dependence of the minimum and maximum output signal eye opening on ϕ_c and a_c. As can be seen, setting ϕ_c to values between -180º and -120º yields a relatively small variation of the output eye opening (less than 10%) and corresponds to the area of maximum eye opening. On the other hand, varying a_c always affects the eye opening, since the attenuation is reflected directly on the CPSF output power. As such, a_c should be kept at a minimum, in order to obtain the desired extinction ratio while maximizing the output power. A limitation of the CPSF is that the output signal presents a low frequency patterning, which results from the non-ideal characteristics of the CPSF.

Fig. E.4-a) presents the dependence of the relative patterning on the BPS. The relative patterning is defined as the difference between the minimum and maximum eye openings, normalized by the average eye opening. To compare the results obtained with different pulse-widths, the BPS has also been normalized by the inverse of the impulse pulse-widths. As can be seen in Fig. E.4-a), the normalized patterning increases linearly with the normalized BPS, regardless of the used signal pulse-width. The inset shows an eye diagram of the output signal with a pulse-width of 2 ps and a normalized BPS of 3×10^{-3}. As a design rule, we can consider that a normalized BPS of 1.2×10^{-3} is required to have a normalized patterning bellow 0.1. As such, the maximum BPS is 0.6 GHz and 0.4 GHz for pulse-widths of 2 ps and 3 ps, respectively. Note that, as the signal bandwidth becomes

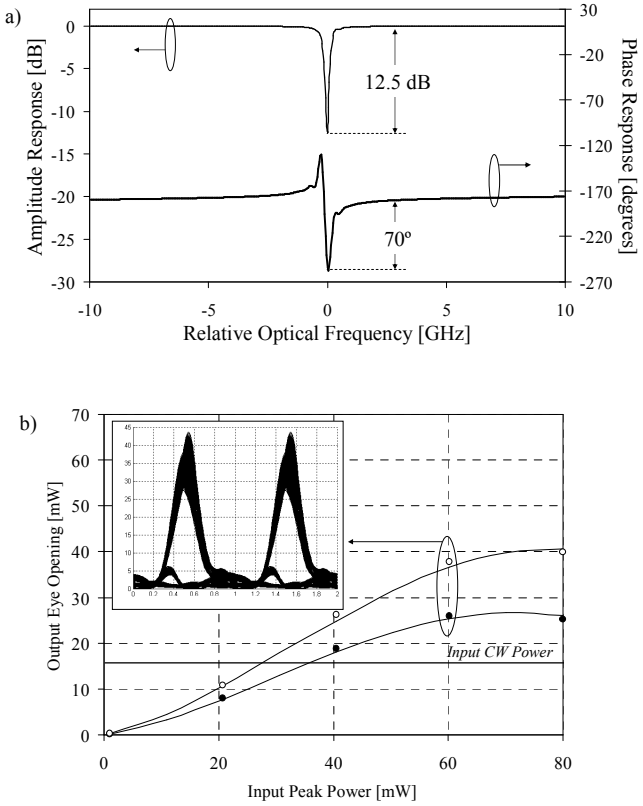

Fig. E.5. Implementing a CPSF using a FBG. a) Phase and amplitude response of the CPSF; b) transmission characteristic. Lines – Analytical results; Circles – Numerical simulation.

larger (by reducing the pulse-width), the low BPS requirement becomes less demanding and the output signal quality increases. The impact of detuning of the CPSF or the CW source must also be considered. Fig. E.4-b) presents the eye opening of the output signal as a function of the CPSF detuning. It is shown that a significant drop on the eye opening occurs outside a 0.4 GHz bandwidth around the central frequency. It can be shown that the maximum detuning is directly related with BPS. As such, it becomes important to find a compromise between low patterning, reducing BPS, and stability of the system, increasing BPS.

E.4. Implementation Using FBG

A simple way to implement a CPSF is using a FBG designed to present the desired phase and amplitude characteristics. In the case of the CPSF, one can obtain such characteristics using two FBG with length L separated by a distance d, shorter than the grating period. The correct phase shift is selected by adjusting d, where half the grating

period corresponds to a π phase shift in the reflection band. Usually, a grating with these parameters has a high rejection deep in the reflection band at the same wavelength of the phase shift. In order to reduce the deep rejection and, therefore, reduce a_c to a few dB, the FBG must have short L (less than 3 mm) and a high modulation amplitude ($\approx 10^{-3}$). The combination of these two conditions greatly widens the FBG reflection spectrum, which results in reducing the attenuation at the deep and extending the bandwidth of the filter. The gratings simulation was performed using the transfer matrix method. Fig. E.5-a) and presents the resulting amplitude and phase profiles, respectively. Unlike the characteristics presented before, it does not have an ideal amplitude deep and phase shift at the carrier frequency. Nevertheless, it can be used as a PM-IM converter. Fig. E.5-b) presents the simulated transmission characteristic for a pulse-width of 2 ps, under the same conditions as Fig. E.2. The inset presents an eye pattern of the output signal, for an input peak power of 60 mW. Due to the filter imperfections, a significant patterning and a limited efficiency of 40% are observed. This results from the low value of ϕ_c (-70º) and excessive a_c (12.5 dB). Nevertheless, it illustrates the principle of the CPSF and its potential application in highly efficient wavelength converters for ultra-high bit-rate signals. Throughout this work, the analytical model for characterization of XPM was used, showing a good agreement with numerical simulation and the advantage of a significantly lower computer processing time.

E.5. Conclusions

This appendix presented the applications of a CPSF for the wavelength conversion of signals at 160 Gb/s. It has been shown that the filter potentially allows a 100% conversion efficiency. The main limitations of the filter have also been addressed, presenting limits for the required BPS. In addition, the application of FBG for the implementation of CPSF has been considered using numerical simulation. It has been shown that, despite a significant degradation induced by patterning effects, the proposed filter still allows a substantial efficiency.

Appendix F. A Short Theoretical Study on the XPM Frequency Limitations in NOLM based Wavelength Converters

F.1. Introduction

AOWC have often been proposed has key systems for future transparent optical networks, being subject to intense research. Among the most promising techniques for all-optical wavelength conversion is the use of a NOLM to replicate the intensity coded information of an optical channel. These systems have the potential for attaining terabits per second switching operation [Yu, 2000: 1] while maintaining a high efficiency [Man, 1998] and low noise [Olsson, 2000].

The operation of a NOLM is based on using XPM in a DSF segment to modulate the phase of a CW probe with the intensity signal of a control channel. The PM is afterwards converted into IM. The XPM process is very efficient, as long as the probe and control channels travel together in the optical fiber. This is not always possible due to walkoff between channels [Jinno, 1992], [Man, 1998]. As such, the design of NOLM wavelength converters has been based on minimizing the walkoff between the interfering channels, neglecting the impact of other effects such as GVD and SPM. This approximation if usually valid since the fibers used have very low dispersion values in the

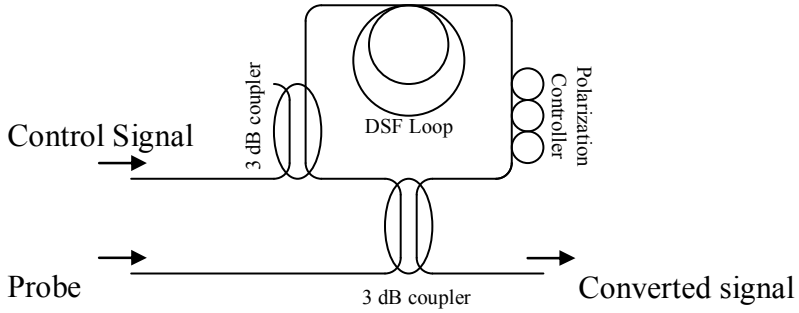

Fig. F.1. Schematic diagram of the considered nonlinear optical loop mirror.

wavelengths typically used. However, when signals with pulse widths of tens of picoseconds or less are used, even the lowest amount of dispersion may already have significant impact. This appendix presents a short theoretical study of the XPM in NOLMs, taking into account the impact of GVD. In section F.2, an analytical model is used to evaluate the XPM frequency limitations due to GVD. Unlike numerical simulation, the analytical model allows a fast evaluation of the XPM efficiency while remaining reasonably accurate. Nevertheless, the limitations of the analytical model are also assessed in this section. In section F.3, the relation between the XPM frequency limitations, the conversion ratio and the converted signal pulse-width is assessed analytically and validated by numerical simulation. Section F.4 presents the main conclusions and outline of this work. The work presented in this appendix has been partially published in [Luís, 2005: 4].

F.2. Frequency Limitations of XPM in a NOLM

Fig. F.1 presents the considered structure for a NOLM for wavelength conversion. The probe CW is injected in both directions of the DSF loop by a 50:50 polarization maintaining coupler. The control signal is injected in one of the loop directions, to interfere with the probe traveling in the same direction. A polarization controller is used to adjust the SOP of the signals in the loop.

To evaluate the bandwidth limitations of the XPM in the NOLM, consider the copolarized propagation, in the DSF of the CW probe and the IM control signal, centered on the wavelengths λ_c and λ_s, respectively. The relation between the Fourier transforms of the control signal IM at the fiber input, $\tilde{P}_p(\omega)$, and the probe channel XPM-induced PM at

the fiber output, $\tilde{\phi}_s(\omega)$, can be approximated by [Cartaxo, 1999:1], [Bononi, 1998], and [Luís, 2005: 1]:

$$\tilde{\phi}_s(\omega) = \tilde{P}_s(\omega) \cdot H_{XPM}(\omega) \tag{F.1}$$

where $H_{XPM}(\omega)$ is the transfer function of an equivalent linear model (ELM) for the XPM-induced PM and ω is the angular frequency. It can be shown that the ELM is approximated by:

$$\begin{aligned} H_{XPM}(\omega) = & -\frac{\gamma}{a_{sp}^2 + (b+q)^2} \cdot \left[a_{cs} \cdot \cos(bL) + (b+q) \cdot \sin(bL) \right. \\ & \left. - e^{-a_{sp}L} \left(a_{sp} \cdot \cos(qL) - (b+q) \cdot \sin(qL) \right) \right] \\ & - \frac{\gamma}{a_{sp}^2 + (b-q)^2} \cdot \left[a_{sp} \cdot \cos(bL) + (b-q) \cdot \sin(bL) \right. \\ & \left. - e^{-a_{sp}L} \left(a_{sp} \cdot \cos(qL) + (b-q) \cdot \sin(qL) \right) \right] \end{aligned} \tag{F.2}$$

where γ, and α are the fiber nonlinearity and attenuation coefficients; $a_{sp} = \alpha - j\omega d_{sp}$, where $d_{sp} = (v_{gs})^{-1} - (v_{gp})^{-1}$ is the walkoff parameter, defined as the difference between the group velocities of the probe and signal waves, respectively; $b = \omega^2 \cdot \lambda_s^2 \cdot D_s/(4\pi c)$ and $q = \omega^2 \cdot \lambda_s^2 \cdot D_s/(4\pi c)$, where D_s and D_p are the dispersion parameters at the probe and signal channel wavelengths and c is the speed of light in vacuum. The derivation of (F.2) is presented in Chapter 5, considering only the impact of GVD in the transmission of the probe and control signals. Nevertheless, this derivation is somewhat extensive and irrelevant to the purpose of this appendix. As such, it will not be presented here.

Fig. F.2-a) presents the PM index defined as $|H_{XPM}(f)|$, calculated analytically using (F.2) for a DSF assuming λ_p = 1545 nm and different values for λ_s. The DSF parameters are: length, L = 8 km; zero dispersion wavelength, λ_0 = 1550 nm; dispersion slope, S = 0.08 ps/km/nm^2; attenuation coefficient, α=0.25 dB/km; nonlinearity coefficient, γ= 2.17 W^{-1}·km^{-1}. To validate the analytical results, we have simulated the transmission of the control signal intensity modulated by a sinusoidal signal, superimposed on a constant power level. By changing the control signal modulation frequency, it is possible to

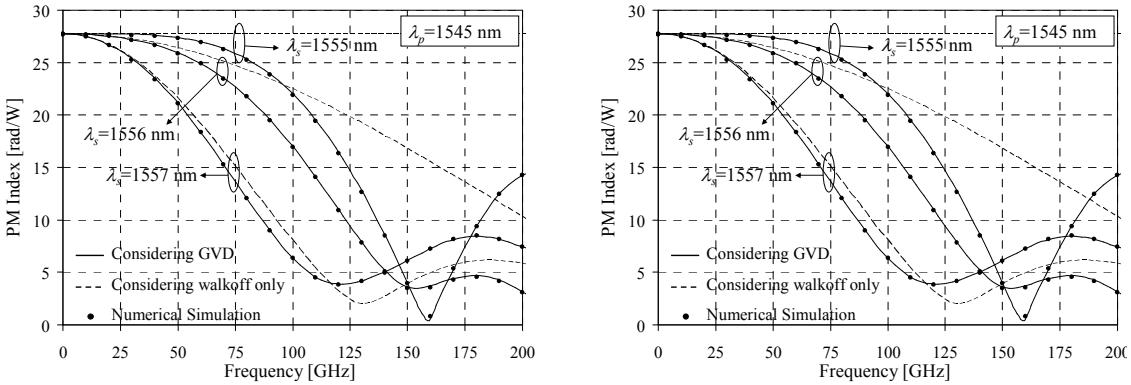

Fig. F.2. XPM-induced PM index. a) Frequency dependence of the PM index for different values of the probe wavelength; b) Wavelength dependence of the PM index bandwidth.

determine the frequency response of the probe channel XPM-induced PM [Cartaxo, 1999:1], and [Luís, 2005: 1]. Numerical simulation was performed by solving the coupled nonlinear Schrödinger equations for the control signal and probe channels with the symmetrized split-step Fourier method. Additionally, for comparison purposes, results using a similar analytical model by [Bononi, 1998] are presented. This model considers only the impact of walkoff in the XPM-induced PM.

Setting λ_p = 1555 nm validates the condition λ_s-λ_0 = λ_0-λ_p for minimum walkoff [Jinno, 1992]. As such, considering only the impact of walkoff in the XPM-induced PM yields no frequency limitations, as shown in Fig. F.2. However, including the impact of GVD on the signal and probe channels yields a significant frequency dependence of the PM index, which resembles that of a low-pass filter. Numerical simulation results have shown an excellent agreement with the analytical model given by (F.2). When varying λ_s, the impact of walkoff starts to impose significant frequency limitations on the XPM-induced PM.As shown in Fig. 2-a), even though the impact of GVD is still dominant for λ_p = 1556 nm, it becomes almost negligible for λ_p = 1557 nm.

To allow a swift evaluation of the XPM-induced PM frequency limitations as a function of the probe wavelength, we introduce the PM index cut-off frequency, B_{XPM}, defined as $|H_{XPM}(B_{XPM})/H_{XPM}(0)|=1/2$. As an approximation, B_{XPM} can be considered as the maximum control signal bandwidth for negligible distortion of the corresponding XPM-induced PM. Fig. F.2-b) presents the wavelength dependence of B_{XPM}, calculated analytically for λ_p values of 1545 nm and 1548 nm. From Fig. F.2-b) it becomes clear that, when setting the probe wavelength away from the minimum walkoff point, the main

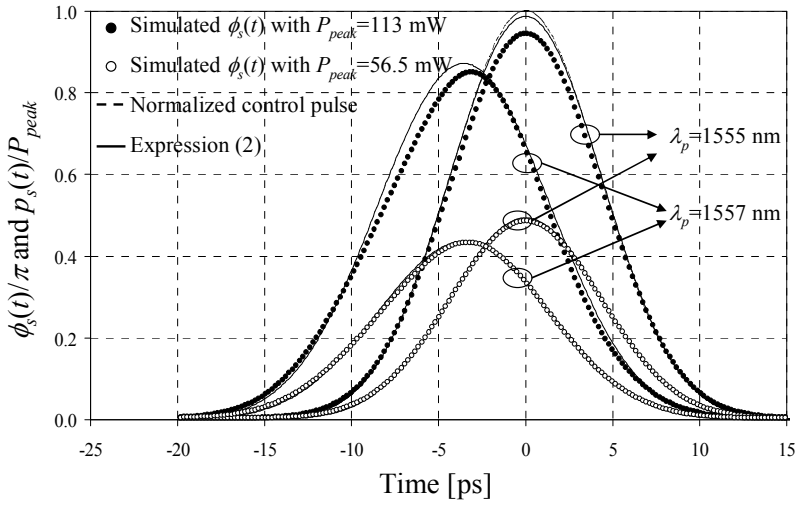

Fig. F.3. Normalized probe XPM-induced PM for a gaussian control pulse with a FWHM of 10 ps.

frequency limitation of the XPM-induced PM is imposed by walkoff. However, for wavelengths close to the minimum walkoff condition, which are typically used in XPM-based wavelength converters and optical switches [Jinno, 1992], the impact of GVD becomes dominant, and ultimately limits the bandwidth of the XPM-induced PM. The case of λ_p = 1548 nm is a typical configuration used in wideband XPM-based wavelength converters [Yu, 2000: 1]. This setting has the advantage of providing a large continuous wavelength range for the probe channel with high bandwidth, as shown in Fig. F.2-b).

As shown in Fig. F.2-a), expression (F.2) allows a good estimate of the XPM-induced PM, in the case of sinusoidal modulation. However, for large signals, the validity of (F.2) becomes conditioned to the impact of SPM on the probe or control signal channels, which is not considered in the model. This factor can be particularly limiting in the latter case, as high power control pulses are often used to obtain strong XPM-induced phase shifts on the probe channel. To illustrate the limitations of (F.2), Fig. F.3 presents the temporal evolution of the XPM-induced PM, $\phi_s(t)$, normalized to π for a gaussian control pulse with a FWHM of 10 ps and peak powers of P_{peak} = 113 mW and P_{peak} = 56.5 mW. As can bee observed from Fig. F.3, with P_{peak} = 113 mW the simulated and analytical evolutions of $\phi_s(t)$ have some discrepancies, which are particularly evident for the maximum XPM-induced phase shift, $\phi_{\max}$. When the peak power of the control pulses is reduced to half, the discrepancies become negligible, which indicates that the validity of (F.2) is conditioned by the control signal power, and consequently the presence of SPM in

the control channel. Further studies using modified coupled nonlinear Schrödinger equations that do not include the SPM terms, have confirmed this statement.

F.3. Impact of the XPM frequency limitations on the NOLM conversion characteristics

As shown previously in Fig. F.3, the main consequences of XPM frequency limitations are the broadening of the XPM-induced phase pulses and a reduction of the maximum XPM-induced phase shift on the probe channel. However, the impact of these limitations on the NOLM output signal is often unclear due to the nonlinear PM to IM conversion characteristic of this device. Assuming ideal couplers, negligible counter-propagating XPM, and optimized polarization controller adjustment this characteristic can be approximated by [Kolleck, 1997]:

$$p_{out}(t) = \frac{P_{CW}}{2} \cdot \left[1 - \cos\left(\phi_s(t)\right)\right] \tag{F.3}$$

where $p_s(t)$ is the instantaneous power of the output signal and P_{CW} is the average probe channel power. From (F.2), it can be noted that the maximum output peak power is P_{CW}. Therefore, we can define the switching efficiency as the ratio between output signal peak power with the probe power, given by $\eta = \sin^2(\phi_{\max}/2)$. Note that this is not the conversion efficiency, as defined in [Man, 1998]. The term $\phi_{\max} \leq \pi$ is the maximum XPM-induced phase shift which, in the absence of XPM frequency limitations, is given by $\phi_{\max} = -2\gamma \cdot P_{peak} \cdot L_{eff}$. The term $L_{eff} = (1-e^{-\alpha L})/\alpha$ is the effective length of the fiber. Considering the system used for illustration in F.3, in the absence of XPM frequency limitations we would obtain $\phi_{\max} = \pi$ for $P_{peak} = 113$ mW. Nevertheless, the actual values of $\phi_{\max}$ are below π and vary with the probe wavelength, resulting in $\eta < 1$. Fig. F.4-a) presents the dependency of η on the probe wavelength, calculated analytically and by numerical simulation with $P_{peak} = 113$ mW and several values of the control signal pulse FWHM, T_o.

Fig. F.4-a) shows a good agreement between numerical simulation results and the analytical estimates. The existing discrepancies are consistent with the results obtained in section F.2. When comparing the results from Fig. F.4-a) and Fig. F.2-b) for $T_o = 10$ ps, it

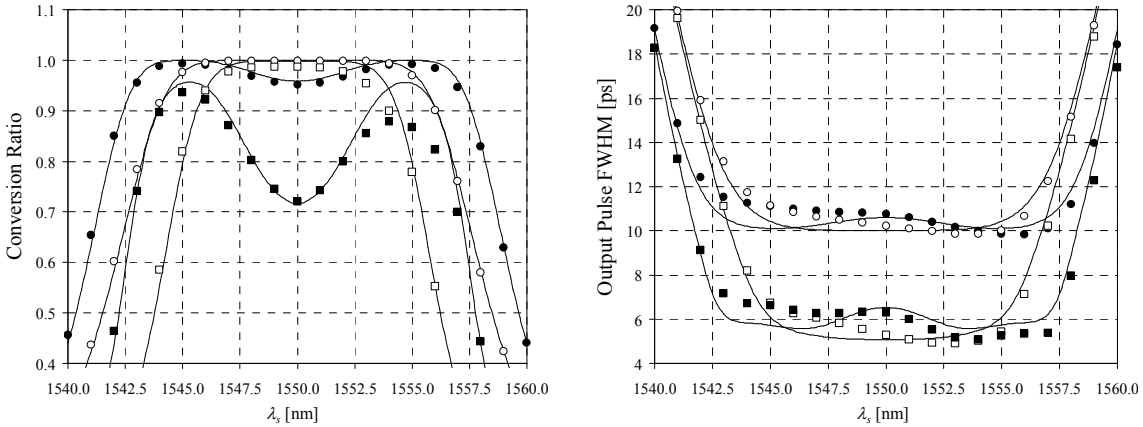

Fig. F.4. Conversion ratio as a function of the probe wavelength, a); Output pulse FWHM, b).
● - Control pulse FWHM 10 ps, λ_p=1545 nm; ○ - Control pulse FWHM 10 ps, λ_p=1548 nm
■ - Control pulse FWHM 5 ps, λ_p=1545 nm; □ - Control pulse FWHM 5 ps, λ_p=1548 nm.

can be seen that the wavelength range for maximum conversion ratio corresponds approximately to the wavelength range for which $B_{XPM} > 1/T_o = 100$ GHz, in this case. In the case of $T_o = 5$ ps, maximum conversion ratio is never reached, which corresponds to having $B_{XPM} < 1/T_o = 200$ GHz, in this case, for the entire wavelength range. As such, it has been shown that B_{XPM} can be used for a quick assessment of the conversion ratio achievable with the corresponding wavelength converter.

To evaluate the impact of the XPM frequency limitations on the FWHM of the output signal we must consider that the nonlinear PM to IM conversion characteristic of the NOLM provides some pulse compression. In fact, it has been shown elsewhere that the pulse compression factor increases with the reduction of the conversion ratio [Yu, 2000: 1]. This means that, if the conversion ratio is reduced due to the XPM bandwidth limitations, the pulse compression factor increases, which may generate shorter output pulses. This property tends to equalize the FWHM of the output pulses when varying the probe wavelength, as shown in Fig. F.4-b). The tilt of the numerical simulation results is produced by SPM, which has different properties for normal and anomalous dispersion.

F.4. Conclusions

A novel analytical method to evaluate the design parameters of wavelength converters based on XPM has been presented. This method was based on an analytical model of the XPM in the DSF loop, considering the impact of GVD in the probe and

control signals. It has been shown that the XPM presents non-negligible frequency limitations due to GVD when the probe and control signals wavelength have low walkoff. Furthermore, the frequency limitations resemble a low-pass filter characteristic. As such, the bandwidth of the XPM-induced PM has been introduced as a parameter for quick evaluation of the wavelength converter bandwidth. It has been qualitatively shown that the XPM cut-off frequency is related with the conversion ratio. Additionally, it has been shown that the FWHM of the output pulses can also be accurately estimated using the presented analytical model.

The analytical model was shown to have some limitations when the control signal power is high. Further studies have shown that this behavior results from neglecting the impact of SPM on the control signal. To include this effect on the presented model, a large signal model for the impact of SPM would be required. However, to the author's knowledge, such a model as not been derived yet.

Appendix G. Description of a Dual-Mach-Zehnder Modulator to Implement a Single Sideband Transmitter

G.1. Introduction

Optical SSB transmission has been considered over the years as a means to reduce and even compensate for the impact of GVD on optical transmission systems while at the same time, the reduced spectral occupation of the signal allows a more efficient use of the available optical bandwidth, suitable for dense WDM systems [Sieben, 1997], [Sieben, 1999], among others.

Several techniques for the generation of SSB signals have been proposed in the literature. The most popular have been optical filtering of the undesired sideband, and the phase shift technique (see [Fonseca, 2007: 3]). In this work, only carrier-unsupressed intensity modulation formats have been considered, for which, according to the results presented by Fonseca et al. in [Fonseca, 2007: 3], the phase shift technique provides enhanced suppression near the optical carrier for such modulation formats. From the different transmitters based on the phase shift technique, the scheme proposed in [Fonseca, 2006: 3], has been selected for this work since it has been experimentally shown to outperform alternative methods such as [Sieben, 1997], [Sieben, 1999] with improved sideband suppression. The SSB transmitter proposed by Fonseca consists of a dual MZM

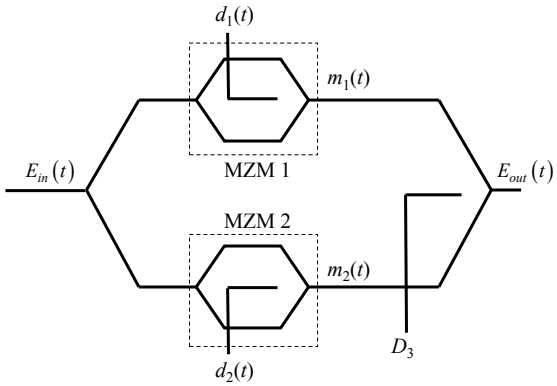

Fig. G.1. Structure of the dual Mach-Zehnder used to generate SSB signals from [Higuma, 2001].

driven by the signal component and its corresponding Hilbert transform. This appendix presents a summarized description of the SSB transmitter proposed by Fonseca. Section G.2 describes the simulation model and final remarks are presented in section G.3.

G.2. Dual Mach-Zehnder Single-Sideband Modulator

The optical transmitter used to generate SSB signals is shown in Fig. G.1 [Higuma, 2001]. Internally, the transmitter is composed by an outer MZM with a MZM in each arm (MZM 1 and MZM 2). Each internal MZM is used to obtain an amplitude modulation of the optical carrier according to the signal applied to its electrode.

The analytical signal of the electrical output field of the SSB transmitter, $E_{out}(t)$, is given by [Fonseca, 2006: 3] [1]:

$$E_{out}(t) = \frac{E_{in}(t)}{2} \cdot \left\{ \exp\left(j \frac{\pi \cdot D_3}{2 \cdot V_{\pi,3}} \right) \cdot m_1(t) + \exp\left(-j \frac{\pi \cdot D_3}{2 \cdot V_{\pi,3}} \right) \cdot m_2(t) \right\} \qquad \text{(G.1)}$$

where t is time and $E_{in}(t)$ is the input electrical field. $E_{in}(t)$ is given by $\sqrt{P} \cdot \exp(j \cdot \omega_o \cdot t)$, where P is the optical power of the input electrical field and ω_o is the optical carrier angular frequency ($\omega_o = 2 \cdot \pi \cdot \nu_o$, where ν_o is the optical carrier frequency). $m_1(t)$ and $m_2(t)$ are the normalized optical fields at the output of the internal MZM 1 and MZM 2, respectively.

[1] Considering ideal scaling factors and null phase differences (obtained assuming identical phase modulator lengths) in all MZM structures.

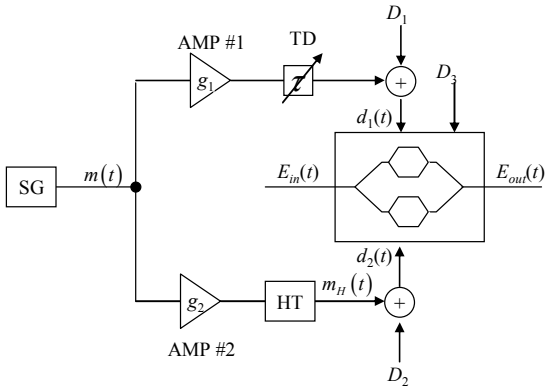

Fig. G.2. SSB transmitter including optical transmitter, from [Fonseca, 2006: 3].

D_3 is the DC voltage used to control the phase shift between the optical signals provided by MZM 1 and MZM 2. $V_{\pi,3}$ is the switching voltage of the outer MZM. $m_1(t)$ and $m_2(t)$ are given by [Fonseca, 2006: 3]:

$$m_1(t) = \frac{1}{2} \cdot \exp\left[j \frac{\pi \cdot d_1(t)}{2 \cdot V_{\pi,1}} \right] + \frac{1}{2} \cdot \exp\left[-j \frac{\pi \cdot d_1(t)}{2 \cdot V_{\pi,1}} \right] = \cos\left[\frac{\pi \cdot d_1(t)}{2 \cdot V_{\pi,1}} \right] \tag{G.2}$$

$$m_2(t) = \frac{1}{2} \cdot \exp\left[j \frac{\pi \cdot d_2(t)}{2 \cdot V_{\pi,2}} \right] + \frac{1}{2} \cdot \exp\left[-j \frac{\pi \cdot d_2(t)}{2 \cdot V_{\pi,2}} \right] = \cos\left[\frac{\pi \cdot d_2(t)}{2 \cdot V_{\pi,2}} \right] \tag{G.3}$$

where $d_1(t)$ and $d_2(t)$ are the electrical signals applied to the MZM 1 and MZM 2, respectively. $V_{\pi,1}$ and $V_{\pi,2}$ are the switching voltages of MZM 1 and MZM 2, respectively.

The optical transmitter setup proposed to generate the SSB modulation is shown in Fig. G.2, where SG is the signal generator and HT is a Hilbert filter [Fonseca, 2006: 1]. A variable time delay (TD) is used to match the delay propagation of the electrical components used to obtained $d_1(t)$ and $d_2(t)$. AMP1 #1 and #2 are electrical amplifiers, with electrical gains g_1 and g_2, respectively. The electrical amplifiers are used to guarantee the correct drive voltage at the input of the optical modulator. $d_1(t)$ and $d_2(t)$ can be expressed by:

$$d_1(t) = g_1 \cdot m(t) + D_1 \tag{G.4}$$

$$d_2(t) = g_2 \cdot m_H(t) + D_2 \tag{G.5}$$

D_1 and D_2 are DC voltages used to bias MZM 1 and MZM 2, respectively. $m(t)$ is the AC coupled version of the signaling format used ($-1 \leq m(t) \leq 1$ for AMI and $-0.5 \leq m(t) \leq 0.5$ for unipolar binary). $m_H(t)$ is the Hilbert transform of $m(t)$, obtained filtering $m(t)$ by an ideal HT. The ideal HT transfer function is given by:

$$H(f) = -j \cdot \mathrm{sgn}(f) \tag{G.6}$$

where f represents the frequency and sgn(·) is the signum function [2]. Such ideal transfer function is impossible to obtain experimentally as it would require a device with unlimited impulse time response. Nevertheless, an ideal transfer function is assumed for the analytical assessments presented within this appendix. Consider identical switching voltages for all MZMs as all structures are integrated on the same substrate ($V_{\pi,1}=V_{\pi,2}=V_{\pi,3}=V_{\pi}$). Under these circumstances, expression (G.1) yields [Fonseca, 2006: 3]:

$$\begin{aligned} E_{out}(t) = {} & \frac{E_{in}(t)}{2} \cdot \exp\left(j \frac{\pi \cdot D_3}{2 \cdot V_\pi} \right) \cdot \cos\left[\frac{\pi \cdot d_1(t)}{2 \cdot V_\pi} \right] + \\ & \frac{E_{in}(t)}{2} \cdot \exp\left(-j \frac{\pi \cdot D_3}{2 \cdot V_\pi} \right) \cdot \cos\left[\frac{\pi \cdot d_2(t)}{2 \cdot V_\pi} \right] \end{aligned} \tag{G.7}$$

In expression (G.7), the first term on the right-hand side represents the optical modulation obtained in MZM 1, whereas the second term represents the optical modulation obtained in MZM 2. Both modulations are combined by a Y-junction at the output of the optical modulator. To generate an OSSB signal at the output, one of the internal MZM is used to obtain an optical signal modulated by the information signal whereas the other internal

[2] The signum function is defined as: $\mathrm{sgn}(x) = \begin{cases} 1, & x > 0 \\ 0, & x = 0 \\ -1, & x < 0 \end{cases}$

MZM is used to obtain an optical signal modulated by the Hilbert transform of the information signal.

G.2.1. Optimization of the Modulator Bias Voltages

To obtain the several bias voltages used by the transmitter, the polarity of the desired optical fields at the output of MZM 1 and MZM 2 and phase mismatch between both optical fields must be considered [Fonseca, 2006: 3]. A SSB signal, $x_{OSSB}(t)$, can be written in the form:

$$x_{OSSB}(t) \propto x(t) \pm j \cdot x_H(t) \tag{G.8}$$

where $x(t)$ is the electrical envelope of the optical signal carrying the information signal and $x_H(t)$ is the electrical envelope of the optical signal carrying the Hilbert transform of $x(t)$. The – (+) is used to define if the SSB signal has the upper (lower) sideband suppressed. D_1 must bias MZM 1 guaranteeing $m_1(t)$ modulated according to the chosen signaling format. This work considers only return-to-zero signaling formats, which may be coded as an intensity modulated carrier-unsuppressed signal, obtained by setting D_1 at the transmission midpoint of MZM 1 ($D_1=3\cdot V_\pi/2$) and keeping $g_1 \cdot m(t)$ within the range [$-V_\pi/2$, $V_\pi/2$]. [Fonseca, 2006: 3]. Similar to D_1, D_2 must bias MZM 2 guaranteeing $m_2(t)$ modulated according to the Hilbert transform of the chosen signaling format. The Hilbert transform of a unipolar signal is given by polar signals, so D_2 must be set at the minimum transmission of MZM 2 ($D_2=V_\pi$) and $g_2 \cdot m_H(t)$ must be kept within the range [$-V_\pi$, V_π] [Fonseca, 2006: 3]. Finally, D_3 must guarantee a phase mismatch of $\pm k \cdot \pi/2$ (k odd) between the output fields of MZM 1 (modulated by the data signal) and MZM 2 (modulated by the Hilbert transform of the data signal). Along this work, k=1 is considered. As a consequence, D_3 must be set to $V_\pi/2+k \cdot V_\pi$, where k is an integer. Along this chapter, we consider $D_3= -V_\pi/2$.

An important aspect to analyze when using external optical modulators which require specific operating conditions, namely prescribed bias voltages, is the performance degradation when the optimum bias voltages do not hold [Yacoubian, 2002]. In the

following section, a brief study of the impact of bias voltage detuning on the transmitter performance is presented.

G.2.2. Optimization of the Modulator Drive Voltages

In this sub-section, the impact of the electrical amplifier gains on the performance of the OSSB transmitter is assessed. The tests conducted within this section are related to a 10 Gb/s system. At the end of the sub-section, a description on the results obtained by such OSSB transmitter at 40 Gb/s is delivered. For the theoretical assessment, the amplifiers and electrodes of the optical modulator have their combined frequency responses modeled by third order Bessel filter with a -3 dB cut-off frequency equal to the bit rate. The HT is modeled from experimental data of a commercial hybrid coupler, having a passband between 1 and 18 GHz. Using the bias voltages obtained for the return-to-zero format in expression (G.7) and developing in the Taylor series expansion, the output field of the optical transmitter, $E_{out,rz}(t)$, is given by [Fonseca, 2006: 3]:

$$E_{out,rz}(t) = -\frac{E_{in}(t)\cdot\exp\left(-j\frac{\pi}{4}\right)}{2}\cdot \left\{\frac{\sqrt{2}}{2}\cdot\left(1+\frac{\pi\cdot g_1\cdot m(t)}{2\cdot V_\pi}-\frac{1}{2!}\cdot\left[\frac{\pi\cdot g_1\cdot m(t)}{2\cdot V_\pi}\right]^2-\frac{1}{3!}\cdot\left[\frac{\pi\cdot g_1\cdot m(t)}{2\cdot V_\pi}\right]^3+\ldots\right)\right. \\ \left. +j\cdot\left(\frac{\pi\cdot g_2\cdot m_H(t)}{2\cdot V_\pi}-\frac{1}{3!}\cdot\left[\frac{\pi\cdot g_2\cdot m_H(t)}{2\cdot V_\pi}\right]^3+\frac{1}{5!}\cdot\left[\frac{\pi\cdot g_2\cdot m_H(t)}{2\cdot V_\pi}\right]^5+\ldots\right)\right\} \quad \text{(G.9)}$$

Retaining only the first-order terms, valid for small g_1 and g_2, $E_{out,rz}(t)$ yields [Fonseca, 2006: 3]:

$$E_{out,rz}(t) = -\frac{E_{in}(t)\cdot\exp\left(-j\frac{\pi}{4}\right)}{2}\cdot\left\{\frac{\sqrt{2}}{2}\cdot\left[1+\frac{\pi\cdot g_1\cdot m(t)}{2\cdot V_\pi}\right]+j\cdot\frac{\pi\cdot g_2\cdot m_H(t)}{2\cdot V_\pi}\right\} \quad \text{(G.10)}$$

Note that unbalanced electrical gains must be used to guarantee an OSSB signal with a form similar to (G.8). The required gain coefficient is given by $g_2/g_1 = \sqrt{2}/2$. This condition has been experimentally validated in [Fonseca, 2006: 3].

G.3. Conclusions

The basic model of an optical SSB transmitter based on a dual-Mach-Zehnder modulator has been presented along with the derivation of the modulator bias and drive voltages has been described, according to results by other authors. Note that this description is merely a summary of the work by Fonseca et al., and further details may be found in the aforementioned references.

Appendix H. Analysis of the Dispersion Management in Systems Employing SSB Modulation Formats and Electrical Dispersion Post-Compensation

H.1. Introduction

To complete the results presented in section 6.2 of Chapter 6, this appendix presents the simulation results obtained from the optimization of the dispersion compensation map assuming a 10 Gb/s RZ-SSB system using electrical dispersion post-compensation (C_{pos}) and electrical or optical dispersion pre-compensation (C_{pre}). All the presented results were obtained from numerically simulating the system presented in section 6.2 of Chapter 6, with identical simulation parameters as the ones indicated in that section.

H.2. Numerical Simulation Results

Fig. H.1-a) and -b) present the dependence of the EOP on the amount of C_{pre} (electrical and optical) and C_{pos} (electrical) for an average launched power of 7 dBm. It is clearly shown that using electrical dispersion post-compensation yields a minimum degradation around 4 dB higher than the results obtained for optical dispersion post-compensation presented in Chapter 6. The dependence of the EOP on the amount of C_{pre}

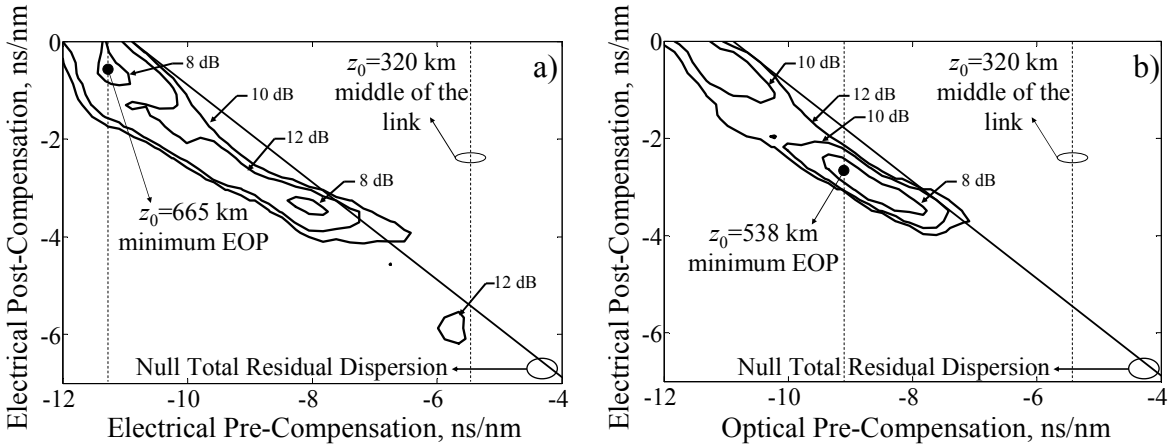

Fig. H.1. Dependence of the EOP on C_{pre} [electrical (a) or optical (b)] with electrical C_{pos}.

and C_{pos} is also substantially altered with the optimized value of z_0 shifted significantly towards the end of the link. This shift results from the degradation of the signal by the beating of the SSB signal components at the receiver, which is enhanced by electrical dispersion post-compensation. As result, the optimum dispersion compensation map tends to the case of a full dispersion pre-compensation. Although the shift of z_0 to higher values occurs when using electrical or optical C_{pre}, it is not as evident in the latter case. This results from the influence of fiber nonlinearities, whose impact becomes significant when the distortion of the dispersion pre-compensating SSB transmitter is removed by using optical C_{pre}.

H.3. Conclusions

A short study of the optimization of dispersion compensation in 10 Gb/s RZ-SSB systems using electrical dispersion post-compensation considering electrical or optical pre-compensation has been presented. It has been shown that such systems present a minimum EOP at least 4 dB higher than its electrical dispersion pre-compensated counterparts. It was also shown that the degradation resulting from the beating of the SSB signal components in the receiver is dominant when using electrical dispersion pre-compensation. However, when using optical dispersion pre-compensation, the impact of fiber nonlinearities becomes dominant, leading to a less predominant shift of z_0 towards the end of the link.

Appendix I. Comparison of the XPM-Induced Degradation due to Single and Double Sideband Signals

I.1. Introduction

The recent developments in advanced modulation formats have provided techniques to mitigate the impact of fiber dispersion in long distance transmission links, particularly in the case of systems employing optical SSB modulation formats with electrical dispersion compensation [Fonseca, 2007: 3]. Assuming transmission in standard single-mode fibers, it can be expected that the most detrimental effect in such systems is XPM. In conventional IM-DD systems, dispersion management is the preferential way to avoid the XPM-degradation [Sano, 2000]. Alternatively, other means could be used to reduce the XPM-degradation of individual channels, such as controlling each individual channel's group delay [Bellotti, 2000]. Without the need for optical dispersion management to control GVD, a SSB multi-section system becomes similar to the cases presented in [Marcuse, 1994] and [Cartaxo, 1999:1], among others, where the XPM-degradation limits considerably the system performance and consequently, the maximum reach. The difference here is the use of spectrally efficient modulation formats with a greater resilience to fiber dispersion. Additionally, the transmitted signals are submitted to very high accumulated dispersion (several nanoseconds per nanometer), which may lead to

effects that have not been thoroughly investigated so far. Among these is the pattern dependent degradation observed in [Essiambre, 2005: 1], and [Essiambre, 2005: 2].

This appendix focuses on comparing the impact of XPM on the performance of multi-channel systems at 10 Gbit/s, employing SSB- and double sideband (DSB) -NRZ modulation formats in standard single-mode fiber. The impact of XPM on IM-DD systems has been extensively studied in the past. Nevertheless, SSB signals have not been considered so far, to the author's knowledge. Section I.2 presents the definition of the XPM-induced power penalty used in this appendix. Section I.3 presents the simulated system and a comparison of the XPM-degradation in transmission systems using DSB and SSB modulation formats without dispersion compensation. The impact of the modulation depth on the XPM-degradation is also considered. Section I.3 also includes a study of the figure of merit of the XPM-degradation, relating the maximum number of reachable sections with the average transmission power. Final conclusions are outlined in section I.4.

I.2. XPM-Induced Power Penalty

Due to the Kerr nonlinearity, the IM of the interfering channels (pumps) will induce infinitesimal XPM on the interfered channel (probe) along the transmission fiber. This XPM will be converted in IM and PM at the receiver input by GVD and SPM [Luís, 2005: 1]. Since square-law direct-detection receivers are considered, only the XPM-induced IM plays a role on the system performance [Marcuse, 1994], leading to electrical current fluctuations that degrade the eye pattern of the interfered signal. This behavior in SSB signals is identical to conventional IM-DD systems. As such, the XPM-induced power penalty is defined as the ratio between the required average power at the receiver input with and without XPM degradation for a prescribed Q-factor, Q. Assuming zero inter-symbol interference, dominant signal-spontaneous emission beat noise, Gaussian distribution for the XPM-induced IM, and XPM degradation only in the symbol "1", it can be shown that the XPM-induced power penalty is given by [Luís, 2005: 1]:

$$P_P = -20\log_{10}\left[\frac{\sqrt{r}}{\sqrt{r}-1}\cdot\sqrt{1-\frac{r}{r-1}\sigma_n^2\cdot Q^2}-\frac{1}{\sqrt{r}-1}\right] \tag{I.1}$$

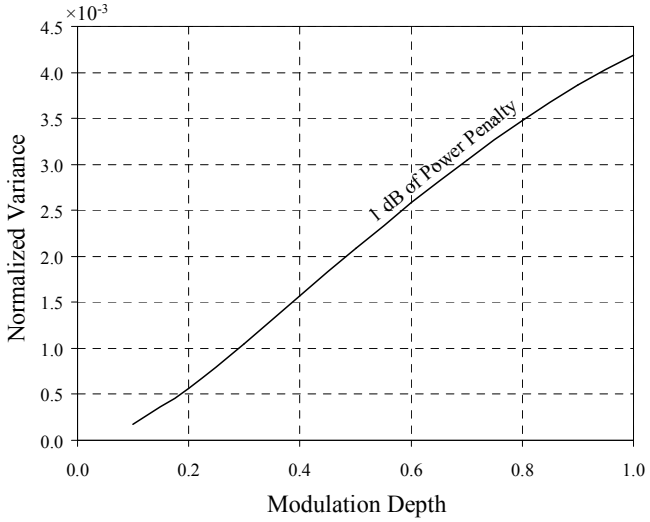

Fig. I.1. Dependence of the maximum allowable normalized variance for 1 dB of power penalty on the modulation depth.

where σ^2_n is the variance of the XPM-induced IM in the symbol "1", normalized to the square of the symbol "1" signal power, P_1. Considering infinite extinction ratio, a power penalty of 1 dB is obtained for σ^2_n=4.2×10^{-3}, for Q=7 [Luís, 2005: 1]. However, SSB signals typically present low extinction ratios, to reduce signal distortion at the receiver [Sieben, 1999]. Furthermore, it is common to use the modulation depth, z_m, defined here between 0 and 1, instead of the extinction ratio. Therefore, considering that the signal is produced using a push-pull MZM biased in the mid-point of the power characteristic, we can consider the relation between modulation depth and extinction ratio given by:

$$r = \frac{1+\sin\left(z_\mathrm{m}\pi/2\right)}{1-\sin\left(z_\mathrm{m}\pi/2\right)} \tag{I.2}$$

Fig. I.1 presents the maximum value of σ^2_n for a power penalty of 1 dB. As can be seen, the maximum allowable normalized variance is strongly reduced when decreasing the modulation depth. For a typical modulation depth of 0.4 [Sieben, 1999], the maximum allowable σ^2_n for a power penalty of 1 dB is 1.6×10^{-3}. The estimate of σ^2_n may be performed from a pump-probe analysis [Thiele, 2002]. In the latter, the average power of

the probe channel is set to P_1. Therefore, the IM of the probe channel corresponds to the XPM-induced IM of the symbol "1" in normal operation.

I.3. Pump-Probe Analysis

I.3.1. Simulation Parameters

This section presents an investigation on the impact of XPM on SSB signals transmitted in systems using electrical dispersion compensation through pump-probe analysis. In this case, the pump is a modulated signal whereas the probe is a CW. The pump-probe analysis allows assessing the XPM-degradation independently of the degradation induced by other impairments such as GVD, SPM and FWM [Thiele, 2002].

The considered transmission system is a typical optically amplified multi-section point-to-point link, presented in Fig. I.2-a). The proposed system consists of *N* identical sections. Each section is composed by a segment of transmission fiber with length *L*=80 km, followed by an EDFA to compensate for the section losses. Simulation of the optical transmission will be performed by solving the corresponding generalized coupled nonlinear Schödinger equations using the SSFM.

The transmitter of the pump channel is a SSB modulator using the phase modulation technique proposed by Villard [Hahn, 1996]. This is simulated using the setup proposed in [Sieben, 1999] with a push-pull MZM and an optical phase modulator, as shown in Fig. I.2-b). The MZM is used to intensity modulate a CW signal coming from a laser source, which is assumed noiseless. The phase modulator is driven by an electrical signal with the shape of the original signal's Hilbert transform. As such, the electrical field at the OSSB transmitter output is given by [Sieben, 1999]:

$$E_p(t) = E_{in} \cdot \cos\left[\pi \cdot z_{\mathrm{m}} \cdot m(t) - \pi/4\right] \cdot \exp\left[j\pi \cdot z_{\mathrm{m}} \cdot m_H(t)\right] \tag{I.3}$$

where $m(t)$ is the AC coupled version of the information, with $-0.5 \le m(t) \le 0.5$, and $m_H(t)$ is the corresponding Hilbert transform. The frequency limitations of the electrical terminals of the MZM and phase modulator are simulated by a 3rd order Butterworth filter with a bandwidth of 65% of the bit-rate [Sieben, 1999]. The simulated Hilbert transformer is

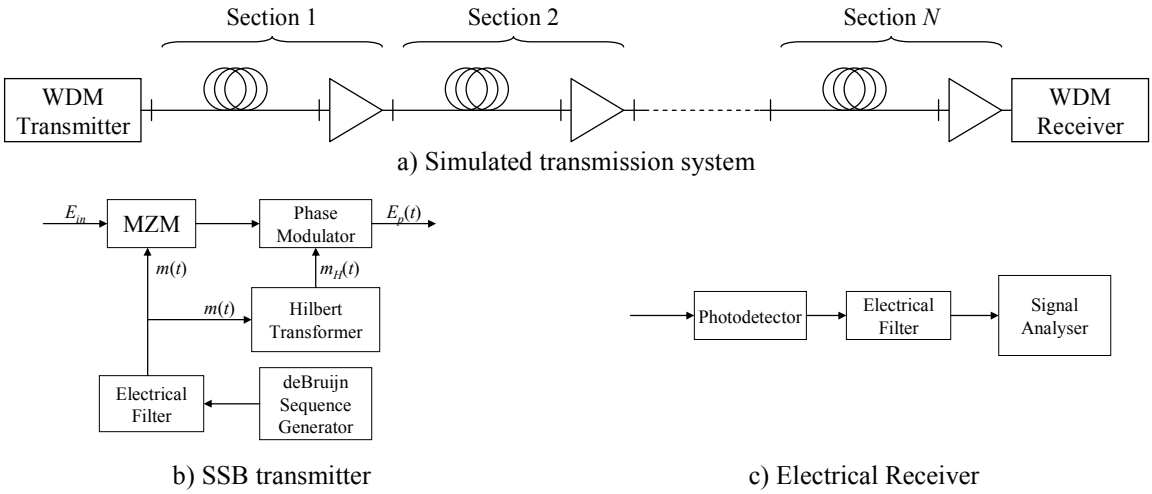

Fig. I.2. Block diagrams of the a) transmission system, b) SSB transmitter and c) electrical receiver.

based on the characteristics obtained from a real hybrid coupler presented in [Fonseca, 2006: 2]. For all considered simulations, the pump channel transmits a pseudo-random deBruijn sequence of 2^9 symbols at a bit-rate of 10 Gb/s.

The receiver for each channel is presented in Fig. I.2-c). This is modeled by an ideal square-law photodetector with unitary responsivity. An electrical 3rd order Butterworth filter with a bandwidth of 65% of the bit-rate simulates the frequency limitations of the electrical circuit. The value of σ^2_n will be estimated using the pump-probe analysis by considering [Bellotti, 2000]:

$$\sigma_n^2 = \frac{\sum_{n=1}^{N_S} \left\{ i[n] - I_s \right\}^2}{N_S \cdot I_s^2} \tag{I.4}$$

where N_S, $i[n]$ and $\overline{I}_s$ are the number, succession of simulated samples and average of the electrical current after electrical filtering. The impact of optical noise will not be considered.

I.3.2. XPM-Degradation in Non-Dispersion Managed Systems

This sub-section presents a study on the impact of XPM when using SSB signals without dispersion compensation. The presented results provide insight on the effects that

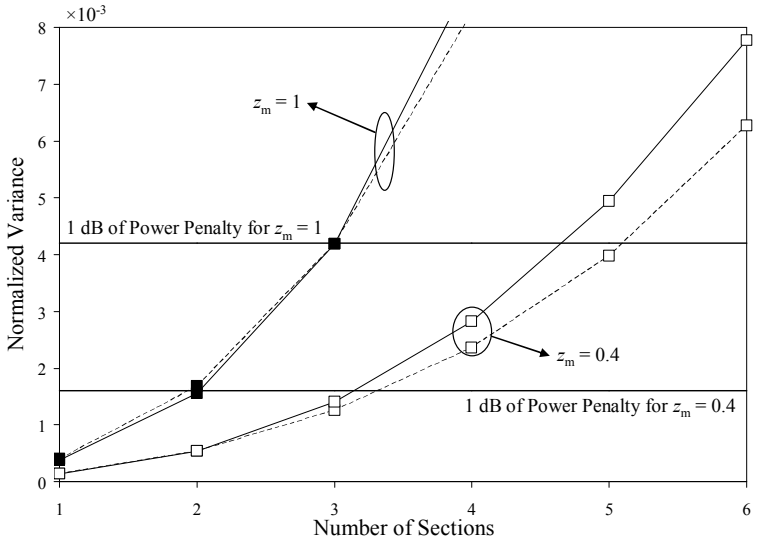

Fig. I.3. Dependence of the normalized variance of the XPM-induced IM on the number of sections without electrical or optical dispersion compensation for modulation depths of 0.4 (hollow symbols) and 1 (filled symbols). DSB (dashed line) and SSB (continuous line) signals are considered.

condition the XPM-degradation on SSB systems with very high accumulated dispersion. The results are compared with the ones obtained with an equivalent DSB system.

Consider transmission of the pump and probe channels along the presented transmission system, without the use of optical or electrical dispersion compensation. The pump channel is transmitted with an average power of 6 dBm at the input of each section. The probe channel will be transmitted with an average power corresponding to the power of the symbol "1" in the pump channel, depending on the modulation depth. Fig. I.3 presents the dependence of σ^2_n on the number of sections. The SSB and DSB pump signals are considered with the latter obtained by removing the HT from the transmitter. The channel spacing is 0.8 nm, corresponding to 100 GHz. Modulation depths of 1 and 0.4 are considered and the maximum normalized variances for 1 dB of power penalty are indicated in both cases. As shown in Fig. I.3, the value of σ^2_n increases rapidly with the number of sections for all cases, due to the strong GVD and SPM-induced PM-IM conversion of XPM along the transmission path [Marcuse, 1994]. Reducing the modulation depth from 1 to 0.4 leads to a significant decrease of the XPM-degradation, resulting from the smaller amplitude of the power transitions of the pump channels. Nevertheless, reducing the modulation depth also leads to a lower limit for 1 dB of power penalty, as shown in Fig. I.1. Therefore, it is verified that reducing the modulation depth brings little advantage in terms of XPM-degradation when comparing the reachable number of sections. Comparing

the values of σ^2_n obtained using DSB and SSB pumps, it can be seen that the latter generally present a worst performance. Although, with z_m=1, the values of σ^2_n obtained for 3 or less than 3 sections are almost the same with SSB or DSB pumps. The differences observed between SSB and DSB pumps would be, in principle, unexpected since the XPM is mostly generated by intensity fluctuations of the pump, which are identical for both DSB and SSB pumps, at the transmitter output. More accurately, it can be considered that the main contribution to the XPM-induced IM results from the intensity of the high-frequency components of the pump signal [Cartaxo, 1999:1], which in turn result from the impulse transitions. However, one must consider that without dispersion management, the intensity fluctuations of the pump channel will change significantly with the transmission distance, due to the impact of GVD and SPM. As such, it can be assumed that the reduced bandwidth of the SSB pump leads to a smaller impact of GVD, maintaining the original pulse shapes for a longer distance. Therefore, the sharp symbol transitions of the signal at the transmission output are retained for a longer fiber length, unlike the DSB signal, where these transitions are reduced by GVD.

To verify this behavior, Fig. I.4-a) and –b) present traces of the SSB and DSB pump intensities at the output of the first, second and fourth sections, considering a modulation depths of 1 and 0.4, respectively. Considering only the pump signals at the output of the first section, it can be seen that the intensity shape of the SSB pump is less degraded than the DSB pump, which in turn becomes completely degraded at the output of the second and fourth sections. It can be seen from Fig. I.4-a) and –b) that, in the case of the DSB pump, several power peaks arise in the areas with two or more consecutive "1" symbols. These result from collisions between the NRZ impulses due to GVD and have been observed previously by Essiambre and Winzer in [Essiambre, 2005: 1] and [Essiambre, 2005: 2].

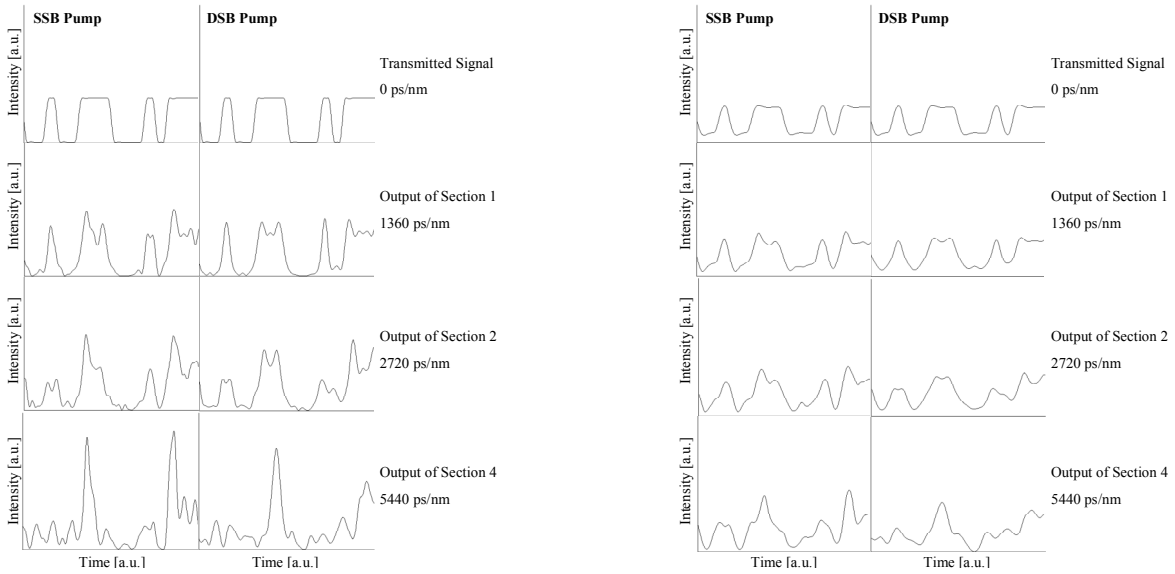

Fig. I.4. Traces of the SSB (upper) and DSB (lower) pump channel intensity at the output of the 1st, 2nd and 4th sections for a) z_m=1 and b) z_m=0.4.

In the case of the SSB signal, similar power peaks are also observed. However, in this case the power peaks become noticeable immediately after the first transmission section. This may result from the fact that the power peaks of the SSB pump are due not only to NRZ impulse collision but also to PM-IM conversion of the phase modulation imposed on the SSB pump by the transmitter. Note that this phase modulation corresponds to the Hilbert transform of the information signal. Therefore, it typically presents very rapid phase transitions coinciding with the rising and falling edges of the information impulses. To illustrate the strength of the contribution of the PM-IM conversion of the SSB pump phase modulation, we have considered transmission of the SSB pump without the intensity modulation component. This was performed by removing the MZM of the SSB transmitter from Fig. I.2. As a result, the transmitted pump is only phase modulated with the Hilbert transform of the information signal. Fig. I.5 presents traces of the pump intensity at the output of the transmitter and sections 1, 2 and 4, considering z_m=0.4 and z_m=1. Fig. I.5 clearly shows significant power fluctuations of the pump channel due to PM-IM conversion, immediately after the first transmission section for both modulation depths. The power fluctuations are more intense for z_m=1 because in this case the phase shifts of the pump channel have higher amplitude.

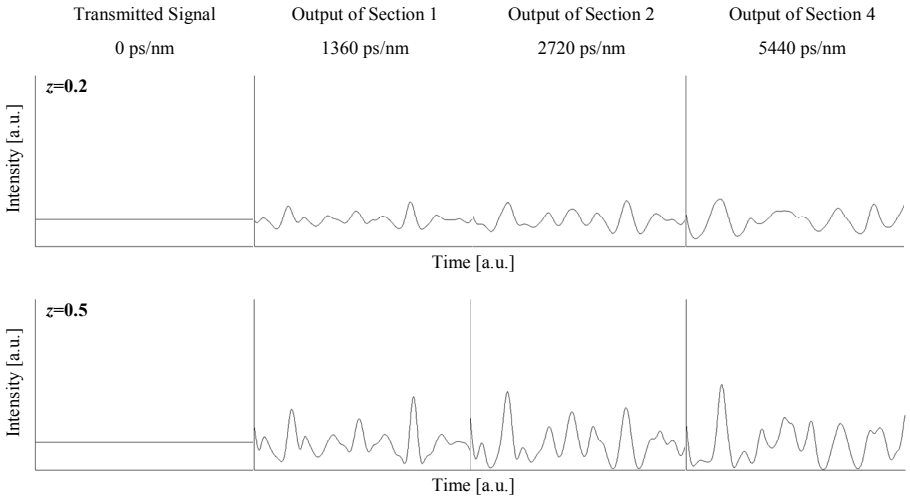

Fig. I.5. Traces of the pump channel's intensity at the transmitter, 1st, 2nd and 4th sections output, considering that the pump channel is phase modulated with the Hilbert transform of the information signal.

In summary, it is verified that an SSB pump signal in a non-dispersion managed system generally induces higher XPM than a DSB pump due to: i) higher tolerance to GVD-induced pulse broadening and ii) power peaks resulting from PM-IM conversion of the phase modulated component of the SSB pump. Considering a maximum XPM-induced power penalty of 1 dB, a two channel SSB system with 0.8 nm of channel spacing barely reaches 3 sections when using a modulation depth of 1. Reducing the modulation depth reduces significantly the XPM-degradation. However, it also reduces the maximum limit for 1 dB of XPM-induced power penalty. Therefore, the limit of 3 sections holds even for a modulation depth of 0.4. Note that the maximum number of sections obtained for the SSB system is the same for the DSB system. However, one can expect that, after 3 sections (240 km) the DSB signal is completely degraded due to GVD and SPM whereas the SSB signal may still be successfully detected [Sieben, 1999].

I.3.3. Figure of Merit of the XPM-Degradation

The results presented so far were obtained for a fixed average pump power of 6 dBm and a channel spacing of 0.8 nm. When varying these parameters it is expected that the XPM degradation will also vary accordingly, i. e. increasing the power or decreasing the channel spacing will lead to stronger XPM-degradation and vice-versa. However, a simpler approach has been proposed for DSB dispersion managed systems by Fürst et al. in [Fürst, 2001]. It as been observed that, for a given channel spacing and considering a

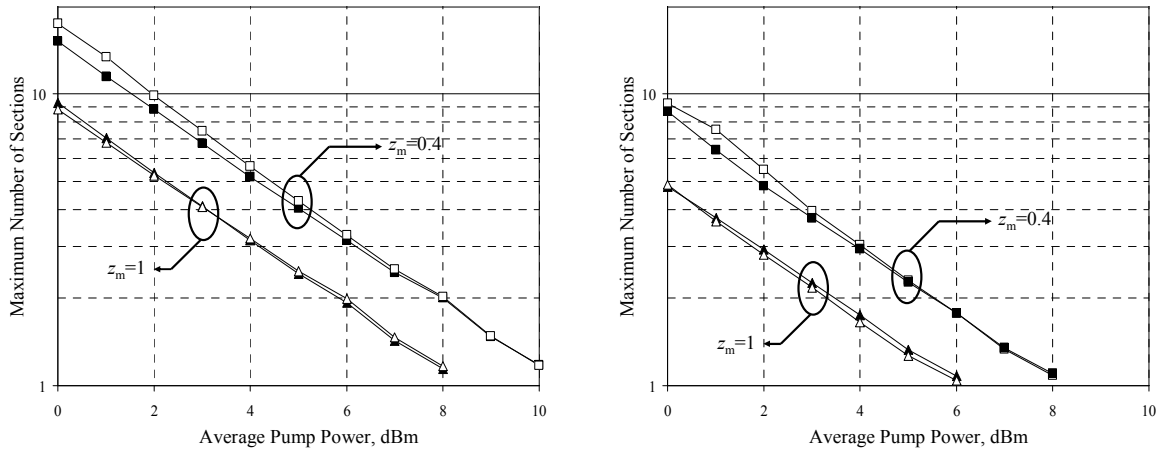

a) Channel Spacing of 0.8 nm b) Channel Spacing of 0.4 nm

Fig. I.6. Maximum number of sections for 1 dB of XPM power penalty as a function of the pump channel power considering a channel spacing of 0.8 nm (a) and 0.4 nm (b).
Hollow symbols: DSB pump; Filled symbols: SSB pump.

maximum XPM-degradation, the product of the maximum number of sections and the average pump power is approximately constant [Fürst, 2001].

To verify if this behavior holds in SSB systems without dispersion compensation, simulations have been performed to determine the maximum number of sections with a power penalty of less than 1 dB. Fig. I.6 presents the maximum number of sections for 1 dB of XPM-induced power penalty as a function of the average pump power for modulation depths of 0.2 and 0.5 and considering SSB and DSB signals. The non-integer values were obtained by interpolation. As shown in Fig. I.6 for all considered cases, the maximum number of sections decreases almost linearly with the average pump power (in logarithmic units). This indicates a relation between average power and maximum number of sections similar to the ones obtained for dispersion managed systems [Fürst, 2001]:

$$\overline{P}_p \cdot N = P_{\max} \tag{I.5}$$

where $\overline{P}_p$ is the average pump power and $P_{\max}$ is a figure of merit corresponding to the maximum pump channel power in a single section for 1 dB of degradation. The value of $P_{\max}$ is a characteristic of the considered system. Table I.1 presents the values of the figure of merit calculated for the cases presented in Fig. I.6. As can be seen, for z_m=1 there is little difference when using an SSB or DSB pump. For z_m=0.4, the system using an SSB pump tends to perform slightly worse, which justifies the lower values for the figure of

Case	Figure of Merit [mW]
SSB signal with z_m=0.4, considering $\Delta\lambda$=0.4 nm	7.4
DSB signal with z_m=0.4, considering $\Delta\lambda$=0.4 nm	7.8
SSB signal with z_m=0.4, considering $\Delta\lambda$=0.8 nm	13.1
DSB signal with z_m=0.4, considering $\Delta\lambda$=0.8 nm	14.0
SSB signal with z_m=1, considering $\Delta\lambda$=0.4 nm	4.4
DSB signal with z_m=1, considering $\Delta\lambda$=0.4 nm	4.4
SSB signal with z_m=1, considering $\Delta\lambda$=0.8 nm	8.0
DSB signal with z_m=1, considering $\Delta\lambda$=0.8 nm	8.1

Table I.1. Figure of merit for SSB and DSP signals impaired by XPM.

merit obtained. However, this difference is negligible, considering the limited accuracy of the pump-probe analysis.

I.4. Conclusions

A comparison of the XPM-degradation of systems employing DSB and SSB modulation formats has been performed. The analysis has been conducted using pump-probe analysis. It has been shown that the impact of the phase modulation component of the SSB signal yields a strong contribution to the overall XPM-induced IM as a result of its conversion to IM along the fiber by GVD and SPM. However, estimations of the figure of merit for SSB and DSB systems have revealed that, despite the differences between both systems, the impact of XPM-degradation remains similar, with approximately the same maximum number of reachable sections for 1 dB of degradation.

Appendix J. On the XPM-Degradation of Dispersion Pre-compensated IM-DD Systems Without Inline Dispersion Compensation

J.1. Introduction

Recent developments of 10 Gb/s WDM optical transmission systems allowed electronic pre-distortion [Killey, 2005] and brought the possibility of completely eliminating inline optical dispersion compensation [Chadrasekhar, 2006]. Despite their advantage in cost and flexibility, such systems are strongly degraded by fiber nonlinearities such as SPM and XPM [Essiambre, 2006]. Although the first may be mitigated using electronic pre-distortion, the random behavior of XPM prevents an effective pre-compensation [Essiambre, 2006]. Predicting the XPM-degradation in such systems requires the use of analytical tools to avoid the prohibitive computation times usually required for numerical simulation, particularly of signals with intense dispersion precompensation.

This appendix addresses the XPM-degradation in dispersion pre-compensated systems without inline dispersion compensation, using the analytical model presented and validated in [Luís, 2005: 1]. It will be shown that the XPM-degradation depends mainly on the relation between the XPM-resonance [Nelson, 1999], and the shape of the power and

phase spectral densities of the intensity and phase components of the precompensated interfering channels, respectively. This relation will be used to derive design rules for optimizing the dispersion precompensation with respect to the XPM-degradation. The presented analytical results will be validated using numerical simulation.

J.2. System Description and XPM Modeling

The XPM-degradation will be addressed using the XPM power penalty in decibel, $P_{XPM}=-10\cdot\log_{10}(1-\sigma^2_{XPM}\cdot Q^2)$, defined for NRZ signals without ISI for a prescribed Q-factor, Q, [Luís, 2005: 1] The term σ^2_{XPM} is the variance of the XPM-induced IM at the electrical receiver for a mark symbol normalized by the squared of that power. Setting a limit of 1 dB for P_{XPM} yields a maximum σ^2_{XPM} of -18.3 dB for Q=3.7, corresponding to a bit-error ratio of 10^{-4}, which is correctable using forward-error-correction. Analytically, σ^2_{XPM} may be estimated integrating the power spectral density (PSD) of the XPM-induced IM of the probe channel, $S_{XPM}(f)$ as:

$$\sigma^2_{XPM}=\frac{1}{P_1^2}\int_{-\infty}^{+\infty}S_{XPM}(f)\cdot df \tag{J.1}$$

where P_1 is the power of the mark symbol. Optical dispersion precompensation will be considered, assuming an equivalence to electronic dispersion precompensation in the case of ideal waveform generation without electronic limitations [Essiambre, 2006]. As such, $S_{XPM}(f)$ may be approximated using an equivalent linear model for the XPM as [Luís, 2005: 1]:

$$\begin{aligned}S_{XPM}(f)=\big|&H_{XPM,P}(f)\cdot C_{IM\text{-}IM}(f)+\\&H_{XPM,\phi}(f)\cdot C_{IM\text{-}PM}(f)\big|^2\cdot S_{p,0}(f)\end{aligned} \tag{J.2}$$

where $S_{p,0}(f)$ is the PSD of the pump IM prior to dispersion precompensation. The terms $H_{XPM,P}(f)$ and $H_{XPM,\phi}(f)$ are the equivalent linear transfer functions for the XPM-induced IM due to the pump IM and PM, respectively, defined between the input of the first transmission fiber to the input of the electrical receiver. Closed-form analytical expressions

for these terms were derived and validated in [Luís, 2005: 1], taking into account the impact of GVD and SPM on the propagation of the probe and pump channels. The terms $C_{\text{IM-IM}}(f)$ and $C_{\text{IM-PM}}(f)$ are small-signals approximation of the IM-IM and PM-IM conversion factors due to the dispersion precompensation given by [Luís, 2005: 1]:

$$C_{\text{IM-IM}}(f) = \cos\left(\pi C_{\text{pre}} \frac{\lambda_{\text{p}}^2 f^2}{c}\right) \tag{J.3}$$

$$C_{\text{IM-IM}}(f) = -\frac{1}{2\overline{P}_p} \cdot \sin\left(\pi C_{\text{pre}} \frac{\lambda_{\text{p}}^2 f^2}{c}\right) \tag{J.4}$$

with C_{pre}, λ_{p}, c, and $\overline{P}_{\text{p}}$ as the amount of dispersion precompensation, the pump wavelength, the speed of light in vacuum, and the average launched pump power. Although this approximation has a limited validity, it has been previously shown to allow a reasonable estimation of the XPM-degradation [Luís, 2005: 1]. Note that (J.2) is dependent only on the pump IM prior to precompensation. As such, the contributions of the pump IM and PM may be separated as:

$$\begin{aligned} S_{\text{XPM}}(f) \approx & \left|H_{\text{XPM},P}(f)\right|^2 \cdot S_{p,1}(f) + \\ & \left|H_{\text{XPM},\phi}(f)\right|^2 \cdot S_{\phi,1}(f) \end{aligned} \tag{J.5}$$

where $S_{p,1}(f)$ and $S_{\phi,1}(f)$ are the power and phase spectral densities of the pump PM and IM, respectively, at the input of the first TF given by:

$$S_{p,1}(f) = \left|C_{\text{IM-IM}}(f)\right|^2 \cdot S_{p,0}(f) \tag{J.6}$$

$$S_{\phi,1}(f) = \left|C_{\text{IM-PM}}(f)\right|^2 \cdot S_{p,0}(f) \tag{J.7}$$

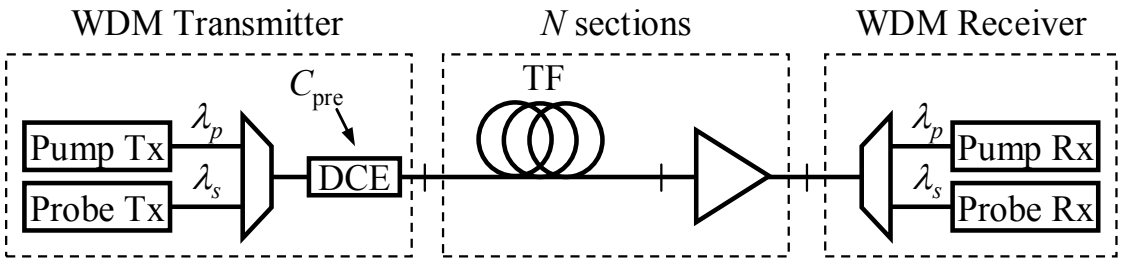

Fig. J.1. Transmission system without inline dispersion compensation.

Note that (J.5) disregards the cross-spectral density resulting from the correlation between the pump IM and PM at the input of the first TF. However, it may be used merely to address the relative magnitude of the contributions from the pump PM and IM.

To compute $H_{XPM,P}(f)$ and $H_{XPM,\phi}(f)$, consider the transmission system depicted in Fig. J.1. A WDM transmitter (Tx) generates and multiplexes a continuous waveform probe and a 10 Gb/s NRZ pump at the wavelengths λ_s=1550 nm and λ_p=1550.4 nm, respectively. A linear DCE will be used to model dispersion precompensation. The transmission is performed through N optically amplified sections of transmission fiber (TF) with length L=80 km, attenuation parameter of 0.22 dB/km, nonlinearity coefficient 1.37 $W^{-1}\cdot km^{-1}$, and dispersion parameter D_s=17 ps/nm/km, for the probe wavelength. The WDM receiver is composed by a demultiplexer and the channel receivers (Rx). Simulation of the system will be carried out using *deBruijn* sequences of 2^{14} symbols, to reduce the patterning effects observed in [Essiambre, 2006] and transmission through the TF will be governed by the generalized coupled nonlinear Schrödinger equations.

J.3. Impact of Dispersion Precompensation on the XPM-Degradation

To address the impact of dispersion precompensation consider that the XPM contributions of the individual sections only add constructively at the end of the link for specific modulation frequencies, referred as XPM resonances, f_{res}, given by [Nelson, 1999]:

$$f_{res} = \frac{m}{d_{sp} \cdot L} \tag{J.8}$$

where $d_{sp} \approx D_s \cdot (\lambda_s - \lambda_p)$ is the walkoff parameter and m is positive integer. As such, the main contribution to the XPM-degradation results from frequency components of the pump IM and PM located around f_{res}. On the other hand, from the small-signals model for $C_{IM\text{-}IM}(f)$ and $C_{IM\text{-}PM}(f)$ one may deduce that the precompensation leads to deeps in the spectral densities of the pump IM and PM, located at the frequencies:

$$f_{\min,IM}^2 = c\left(k + 1/2\right) \Big/ \left(\lambda_p^2 \left| C_{pre} \right|\right) \tag{J.9}$$

and

$$f_{\min,PM}^2 = c \cdot k \Big/ \left(\lambda_p^2 \left| C_{pre} \right|\right) \tag{J.10}$$

respectively, with integer k. Therefore, we may assume that the XPM-contributions due to the pump IM and PM are minimized when the deeps $C_{IM\text{-}IM}(f)$ and $C_{IM\text{-}PM}(f)$ match the XPM resonances. This occurs for the values of C_{pre}:

$$C_{pre,IM}^{(k,m)} = \pm c \frac{d_{sp}^2 L^2}{\lambda_p^2} \cdot \frac{k + 1/2}{m^2} \quad \text{and} \quad C_{pre,PM}^{(k,m)} = \pm c \frac{d_{sp}^2 L^2}{\lambda_p^2} \cdot \frac{k}{m^2} \tag{J.11}$$

To illustrate this relation, Fig. J.2 presents a comparison between the theoretical $S_{p,1}(f)$ and $S_{\phi,1}(f)$ with the corresponding transfer functions for the XPM-induced IM, assuming fully pre-compensated systems with various section counts. As shown, the contributions of the pump IM and PM vary, according to the amount of pre-compensation. Furthermore, the XPM transfer function becomes narrower around the resonance frequency. To illustrate the limitations of the small-signals model used in (J.2) and (J.5), Fig. J.2 also presents numerically computed $S_{p,1}(f)$ and $S_{\phi,1}(f)$, respectively. It is shown that, despite the evident limitations of the small-signals approach, there is a fair agreement of the deeps of the analytically computed $S_{p,1}(f)$ and $S_{\phi,1}(f)$ with the relative minimums of the corresponding numerically computed spectral densities.

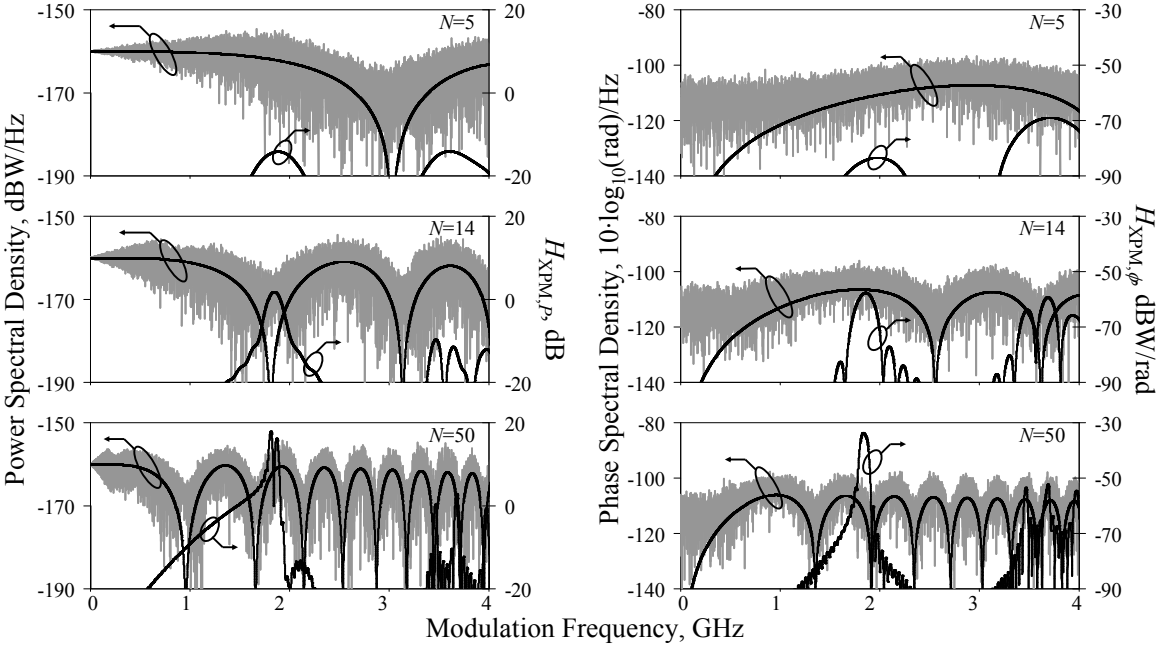

Fig. J.2. Comparison of the theoretical and numerically computed power and phase spectral densities of the precompensated probe IM (left column) and PM (right column) for a system with 5, 14, and 50 sections, with the corresponding XPM transfer functions $H_{XPM,p}(f)$ and $H_{XPM,\phi}(f)$.

To address the impact of dispersion precompensation on the XPM-degradation, Fig. J.3 presents the dependence of σ^2_{XPM} on the section count and corresponding value of C_{pre} assuming full dispersion precompensation, for $\bar{P}_p$=-4 dBm and $\bar{P}_p$=0 dBm. The presented values where obtained analytically using (J.2) and validated using numerical simulation. Fig. J.3 also presents the isolated contributions of the pump PM and IM at the input of the first TF. Each PM or IM contribution was obtained using (J.5) and canceling the remaining IM or PM component, respectively. As shown for both considered pump powers, the contributions of the pump PM and IM are alternatively dominant as the section count and corresponding pre-compensation are increased. Note that for $\bar{P}_p$=-4 dBm and N<60 or P_p=0 dBm and N<30, the most prominent local minima of the contributions of the pump IM and PM approximate the values of $C^{(k,m)}_{pre,IM}$ and $C^{(k,m)}_{pre,PM}$, respectively. For higher section counts, we verify a deviation from the values predicted by (J.11), due to the impact of SPM. Note also that the rate of growth of the total XPM-degradation tends to decrease with the section count. This results from the compression of the power and phase spectral densities of the pump PM and IM by pre-compensation and the narrowing of the XPM-resonance, as previously observed.

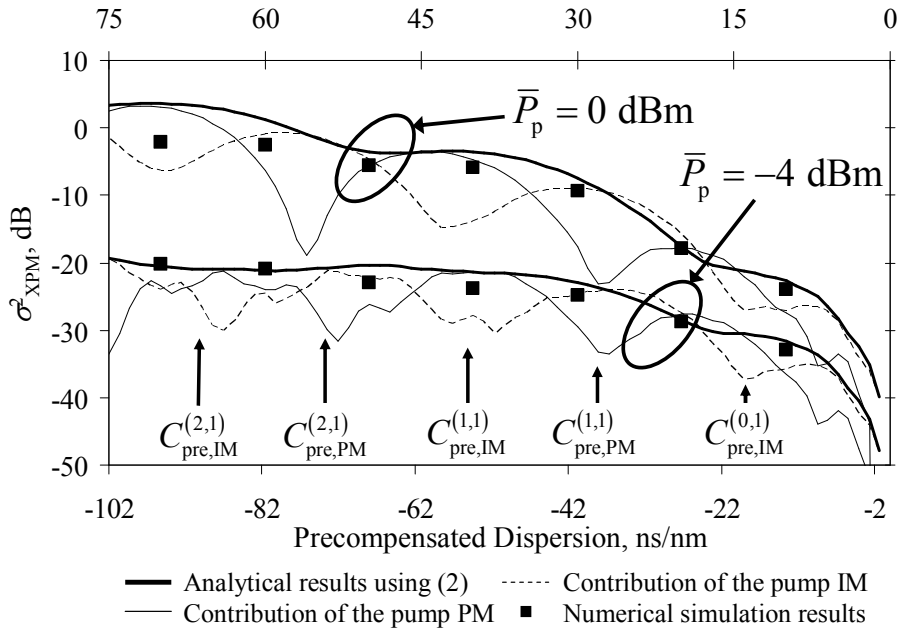

Fig. J.3. Dependence of the normalized XPM variance on the section count in a pre-compensated system.

To complete this study, Fig. J.4 presents the dependence of the XPM-degradation on C_{pre}, for a fixed section count of 20 and $\overline{P}_p$=0 dBm. The remaining conditions are identical to Fig. J.3. It is shown that σ^2_{XPM} varies periodically with C_{pre}, as a consequence of the periodic variation of the contributions of the pump IM and PM described above. Fig. 4 shows that the minimum values of σ^2_{XPM} occur when the contributions of the pump IM and PM have roughly the same value. From (J.6) and (J.7), this observation may be expressed as the condition $S_{p,1}(f) = S_{\phi,1}(f)$. Taking (J.3) and (J.4), the latter may be re-written as:

$$\cos\left[\pi\lambda_p^2 C_{pre}/\left(d_{sp}^2 L^2 c\right)\right] = -\sin\left[\pi\lambda_p^2 C_{pre}/\left(d_{sp}^2 L^2 c\right)\right] \tag{J.12}$$

which results in the value of C_{pre} for minimum XPM-degradation as:

$$C^{(l)}_{pre,opt} = -\left(l + 3/4\right) c \cdot d_{sp}^2 L^2 / \lambda_p^2 \tag{J.13}$$

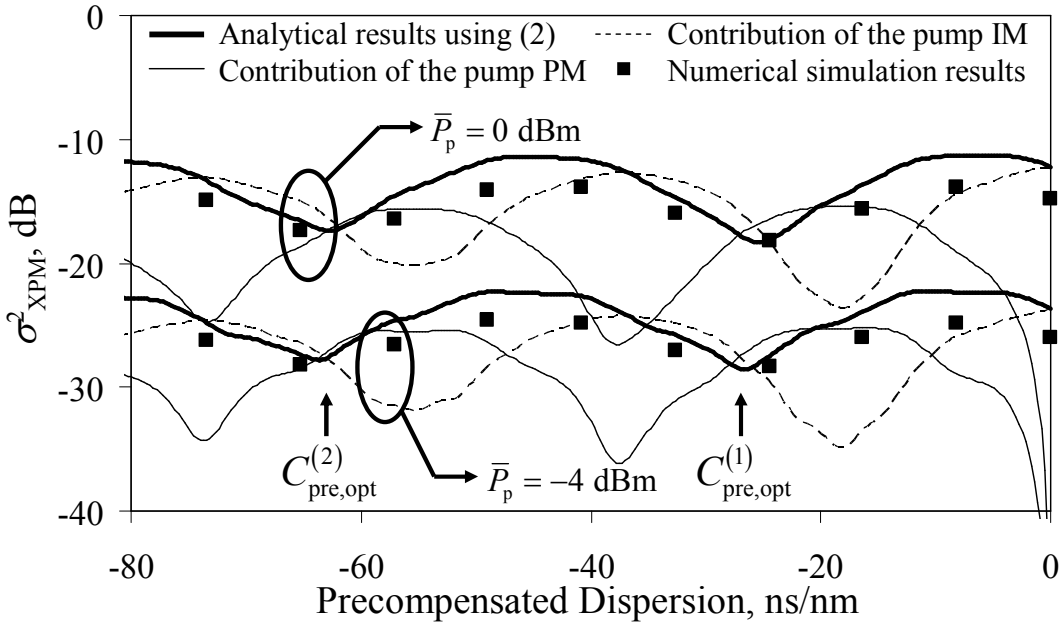

Fig. J.4. Dependence of the XPM-degradation on the dispersion precompensation for a fixed section count of 20.

with integer l. Fig. 4 indicates the values of $C^{(l)}_{pre,opt}$ for l=1 and 2. Fig. J.4 shows that, apart from the previously described SPM-induced deviation, the values of $C^{(l)}_{pre,opt}$ constitute a reasonable approximation of the optimum values of C_{pre}.

J.4. Conclusions

Analytical estimations and numerical simulations have shown that the XPM-degradation in multi-section systems using intense dispersion pre-compensation depends strongly on the relation between the XPM resonance and the power and phase spectral densities of the intensity and phase components of the pre-compensated interfering signals. Using a simplified analysis, we have derived engineering rules to determine the dominant component of the interfering channel and optimize the dispersion pre-compensation with respect to the XPM-degradation. These rules have been validated by analytical and numerical simulation results.

Appendix K. Pump-Probe Analysis of the XPM-Degradation of DPSK Signals Due to ASK Signals

K.1. Introduction

The pump-probe analysis of the XPM-degradation of DPSK signals due to nonlinear interference with ASK signals performed in Chapter 6 has shown, for a limited number of cases, that the impact of XPM-induced IM is dominant when compared with the impact of XPM-induced PM. This appendix presents a more extensive set of results that support this claim, assuming various dispersion compensation schemes. All presented results have been obtained using pump-probe simulation.

K.2. Simulated Transmission System

Consider the simulated transmission scheme presented in Fig. K.1, which is similar to the one considered in Fig. 6.6 of chapter 6. An ASK pump and a CW probe are multiplexed and transmitted through an optically amplified and dispersion managed multi-section transmission system. Each section is composed by a segment of transmission fiber with a length of L=80 km, followed by a linear DCE and an optical amplifier to compensate the losses in that section. The amount of dispersion compensated by each DCE, C_{inline}, is identical except for the last DCE, which is set to leave a given amount of

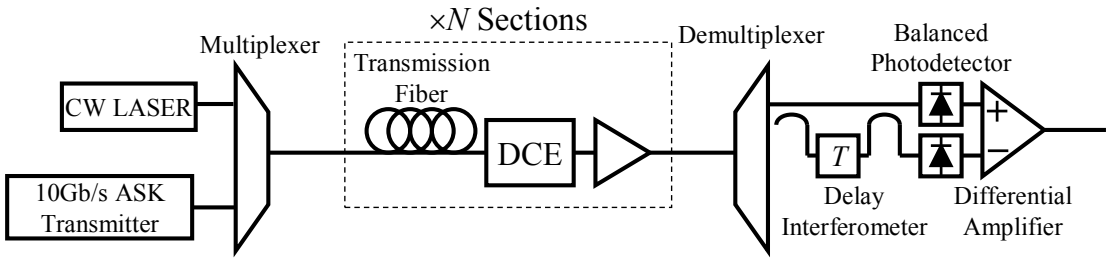

Fig. K.1. Simulated transmission system for the pump-probe analysis of the XPM-degradation in mixed DPSK and ASK Systems.

uncompensated dispersion in the link, D_{res}. Fig. K.2 presents the considered dispersion compensation scheme. We define D_u as the residual dispersion per section as $D_u=L\cdot D+C_{inline}$, where D it the dispersion parameter of the transmission fiber.

At the receiver side, the probe channel is demultiplexed and sent to a direct-detection DPSK receiver. The latter is composed by a delay interferometer, with a delay of 25 ps, followed by a balanced photodetector and a differential amplifier. It is assumed that the combined gain of the balanced photodetectors and the differential amplifier is unitary. All simulations presented in this appendix assume a link with 20 sections, a channel spacing of 0.4 nm, and identical average pump and probe power values of P_s=0 dBm or P_s=2 dBm. The transmission fiber parameters correspond to the SSMF and TW, presented in Table 6.1.

K.3. Pump-Probe Simulation Results

K.3.1. Impact of the Total Residual Dispersion

Fig. K.3-a) to -d) present the dependence of the variances of the electrical current

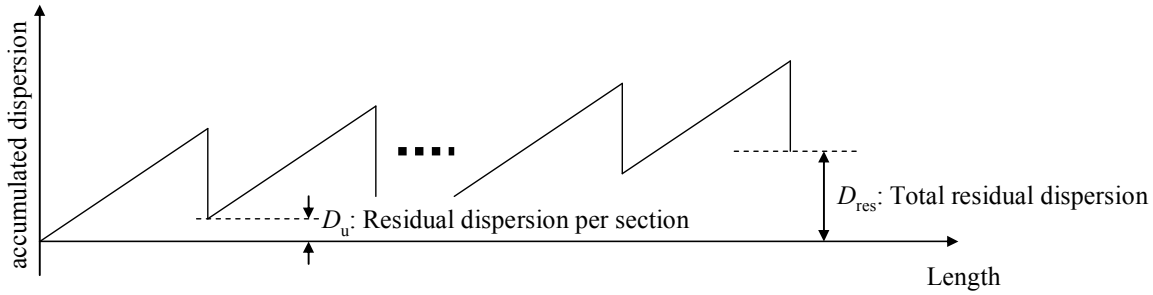

Fig. K.2. Dispersion compensation scheme used for pump-probe simulations.

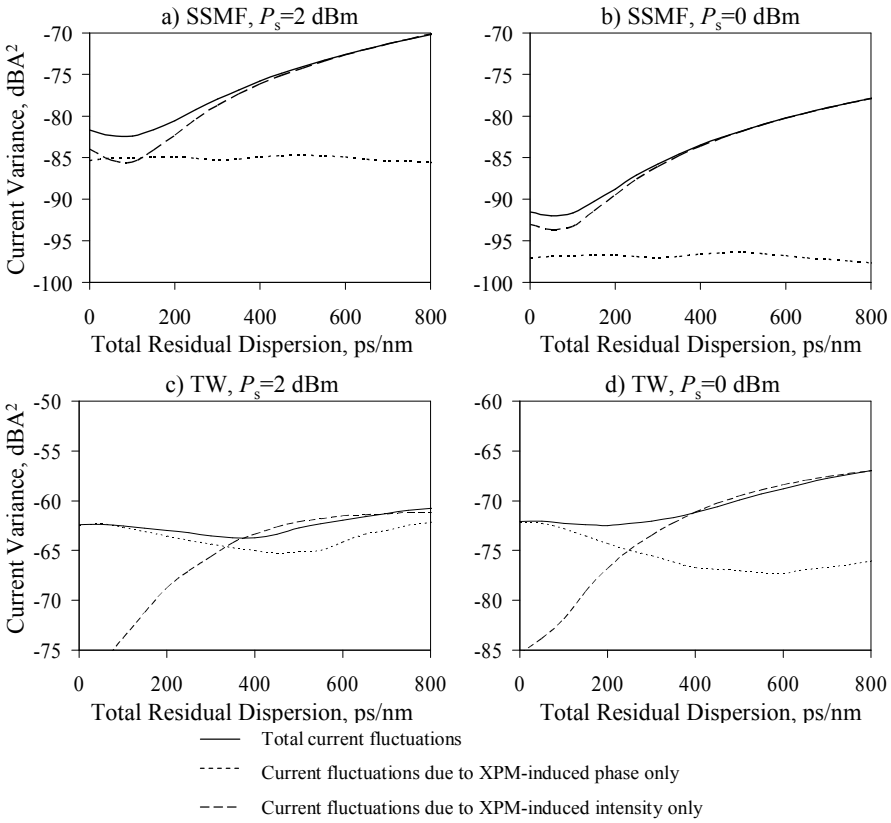

Fig. K.3. Variances of the electrical current fluctuations at the DPSK receiver due to XPM-induced IM and PM as a function of the residual dispersion for a null residual dispersion per section.

fluctuations resulting from the XPM-induced IM, PM and the overall current fluctuations at the DPSK receiver, as a function of the residual dispersion when using SSMF and TW as transmission fiber. Null residual dispersion is assumed in all cases. Fig. K.3-a) and -b) show that when using SSMF, the XPM-induced IM is dominant for values of D_{res} above 200 ps/nm. This behavior is particularly evident for a launched power of 0 dBm, where the impact of XPM-induced PM is only noticeable for low residual dispersion values. In the examples presented for TW fiber in Fig. K.3-c) and -d), it is shown that the XPM-induced PM plays a significant role as it is dominant for residual dispersion values below 300 ps/nm. In the case of Fig. K.3-c), for a launched power of 2 dBm, it is shown that even for residual dispersion values above 300 ps/nm the impacts of XPM-induced PM and IM are comparable, although the latter present a stronger contribution to the overall XPM-induced current fluctuations.

Fig. Fig. K.3-a) and -b) also show that the value of residual dispersion that yields minimum XPM-degradation is approximately 100 ps/nm and varies negligibly with the launched power within the considered range. The value of optimum total residual

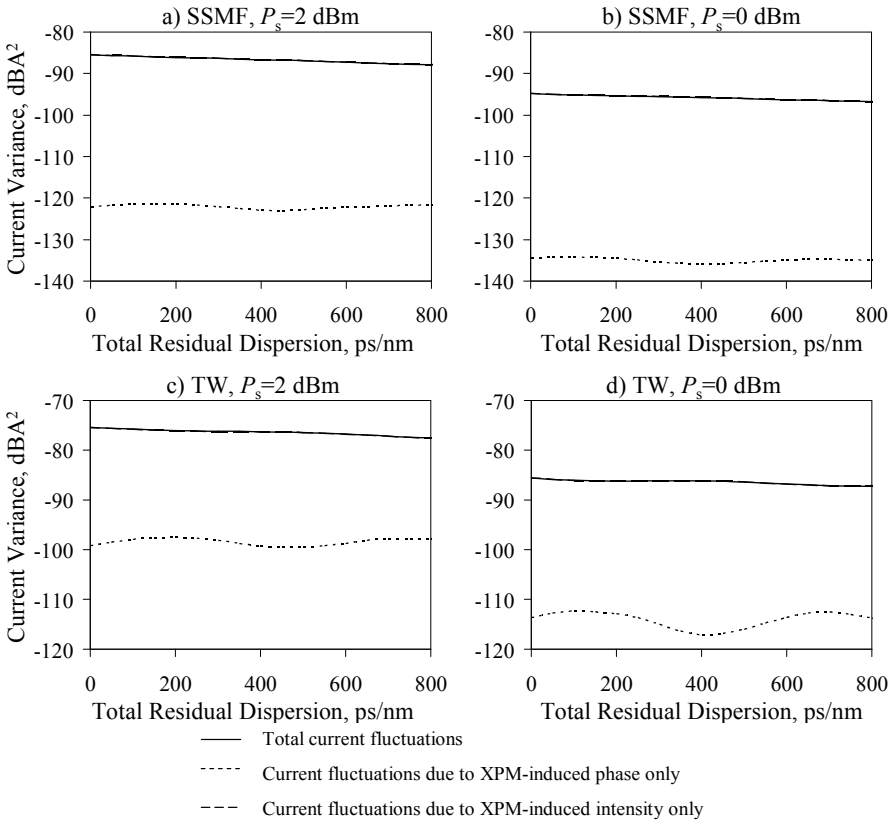

Fig. K.4. Variances of the electrical current fluctuations at the DPSK receiver due to XPM-induced IM and PM as a function of the total residual dispersion for a residual dispersion per section of 170 ps/nm.

dispersion is increased to approximately 300 ps/nm and 400 ps/nm when using the TW fiber with launched powers of 0 dBm and 2 dBm, respectively, as a consequence of the increase of the contribution of the XPM-induced PM by a factor of approximately 20 dB.

Fig. K.4-a) to d) present the dependence of the variances of the electrical current fluctuations resulting from the XPM-induced IM, PM and the overall current fluctuations at the DPSK receiver, as a function of the residual dispersion when using SSMF and TW as transmission fiber in the same conditions used for Fig. K.3-a) to -d), but considering a residual dispersion per section of 170 ps/nm. In all presented cases and all considered values of power and total residual dispersion, the contribution of XPM-induced IM exceeds the contribution of XPM-induced PM by an excess of 20 dB. To further substanciate this observation, it is clear that the contribution of the XPM-induced IM is coincident with the variance of the overall XPM-induced electrical current fluctuations, indicating that the XPM-induced PM plays a negligible role in this system. Fig. K.4-a) to d) also show that for the considered values of residual dispersion per section, the XPM-degradation varies negligibly with the total residual dispersion. This indicates that for

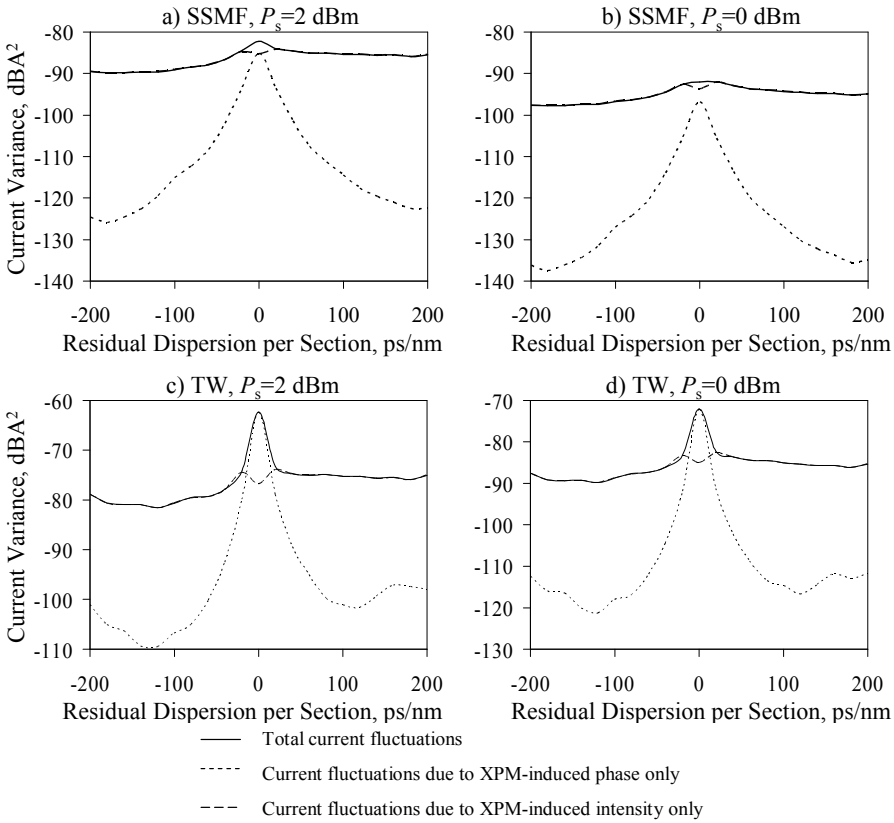

Fig. K.5. Variances of the electrical current fluctuations at the DPSK receiver due to XPM-induced IM and PM as a function of the residual dispersion per section for a null total residual dispersion.

dispersion managed systems under these conditions, one may choose freely the total residual dispersion with negligible impact on the XPM-degradation of the DPSK channel.

K.3.2. Impact of the Residual Dispersion per Section

Fig. K.5-a) to d) present the dependence of the variances of the electrical current fluctuations resulting from the XPM-induced IM, PM and the overall current fluctuations at the DPSK receiver, as a function of the residual dispersion per section, when using SSMF and TW as transmission fiber in the same conditions used for Fig. K.3-a) to -d) and considering a null total residual dispersion. As shown in all cases, the impact of XPM-induced PM is only significant for a low residual dispersion per section. This particularly evident when using TW fiber, where the XPM-induced PM is dominant for residual dispersion values between -50 ps/nm and +50 ps/nm. For residual dispersion values outside this interval, the XPM-induced IM becomes dominant in all cases. This results from the inline PM-IM conversion of XPM occurring in each section as a result of the residual dispersion.

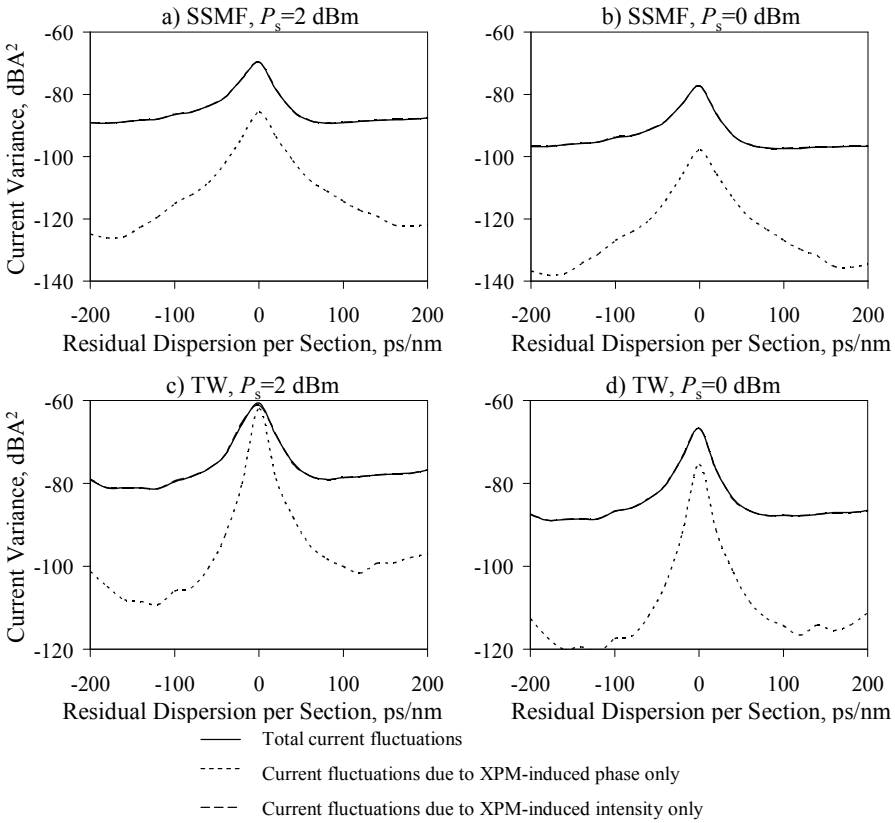

Fig. K.6. Variances of the electrical current fluctuations at the DPSK receiver due to XPM-induced IM and PM as a function of the residual dispersion per section for a null total residual dispersion.

Finally, Fig. K.6-a) to d) present the dependence of the variances of the electrical current fluctuations resulting from the XPM-induced IM, PM and the overall current fluctuations at the DPSK receiver, as a function of the residual dispersion per section, when using SSMF and TW as transmission fiber in the same conditions used for Fig. K.5-a) to -d) but considering a total residual dispersion of 850 ps/nm. Total residual dispersion values of this magnitude are often used in 10 Gb/s IM-DD transmission systems to reduce the SPM-degradation [Elbers, 2000]. Fig. K.6-a) to d) show in all considered cases a dominant XPM-induced IM with the sole exception of the TW fiber when considering very low residual dispersion per section and a launched power of 2 dBm.

K.4. Conclusions

Results of the comparison between the contributions of XPM-induced PM and IM to the XPM-degradation of DPSK signals due to ASK signals have been presented. Dispersion compensation schemes employing residual dispersion per section and total

residual dispersion have been considered. It has been shown that the XPM-induced PM is only significant when assuming a low total residual dispersion or TW transmission fiber. In the latter case, for low total residual dispersion values and low residual dispersion per section, the XPM-induced PM is dominant. Otherwise, it has been shown that the XPM-induced IM is dominant.

Appendix L. Publications and Communications Resulting From the Work Presented in this Dissertation

L.1. Peer Reviewed Journals and Letters

- R. Luís, P. André, A. Teixeira, and P. Monteiro, "Performance monitoring in optical networks using asynchronously acquired samples with nonideal sampling systems and intersymbol interference," *IEEE/OSA J. Lightwave Technol.,* vol. 22, no. 11, pp. 2452-2459, November 2004.
- R. Luís, A. Teixeira, P. André, and P. Monteiro, "Novel distortion resilient OSNR monitoring technique based on evaluation of asynchronous histograms," *Microwave and Optical Technol. Lett.,* vol. 48, no. 7, pp. 1369-1372, July 2006.
- R. Luís, A. Teixeira, and P. Monteiro, "Cross-phase modulation bandwidth in ultrafast fiber wavelength converters," *OSA Optics Letters,* vol. 31, no. 23, pp. 3408-3410, December 2006.
- R. Luís, A. Teixeira, and P. Monteiro, "Design of optical filter for increased efficiency of wavelength converters based on fiber XPM," *Optical Communications,* no. 271, pp. 100-104, January 2007.

- R. Luís, D. Fonseca, A. Teixeira, P. Monteiro, "Dispersion management of electrically precompensated RZ single-sideband signals at 10 Gb/s without inline dispersion compensation," *IEEE Photon. Technol. Lett.,* vol. 19, no. 14, pp. 1039-1041, July 15, 2007.
- R. Luís, B. Clouet, A. Teixeira, and P. Monteiro, "Pump-probe analysis of the cross-phase modulation degradation induced by 10 Gbit/s amplitude-shift-keyed signals on 40 Gbit/s DPSK signals," *OSA Optics Letters,* vol. 32, no. 19, pp. 2786-2788, October 2007.

L.2. Peer Reviewed Communications

- R. Luís, A. Teixeira, P. André, P. Monteiro, "Evaluation of Intra-Band Crosstalk Using Asynchronous Histograms," in Proc. *European Conference on Networks & Optical Communications* 2004 (NOC2004), pp. 374-381, June 2004.
- R. Luís, P. André, A. Teixeira, and P. Monteiro, "Asynchronous histogram analysis for evaluation of Q-factor, OSNR or crosstalk," in Proc. *E-Photon One Winterschool* 2004, Aveiro, Portugal, November, 2004.
- R. Luís, A. Teixeira, P. André, and P. Monteiro, "OSNR monitoring technique based on evaluation of asynchronous histograms," in Proc. *Conf. Nac. Telecomunicações* 2005 (ConfTele 2005), Tomar, Portugal, April 2005.
- R. Luís, A. Teixeira, P. André, and P. Monteiro, "Optical signal-to-noise ratio estimation using reference amplitude histograms," in Proc. *Symposium on Enabling Optical Networks and Sensors,* (SEON 2005), Aveiro, Portugal, June 2005.
- R. Luís, A. Teixeira, A. Cartaxo, and P. Monteiro, "A short theoretical study on the XPM frequency limitations in NOLM based wavelength converters," in Proc. *International Conference on Transparent Optical Networks* 2005 (ICTON 2005), vol. 2, pp. 109-112, July 2005.
- R. Luís, R. Nogueira, A. Teixeira, and P. Monteiro, "Highly efficient fiber wavelength converter based on a passive PM-IM converter filter for high capacity systems," in Proc. *Conf. on Lasers and Electro-Optics* 2006 (CLEO 2006), paper PS3 - JThC, May 2006.

- R. Luís, A. Teixeira, and P. Monteiro, "Monitoring of amplified spontaneous emission and nonlinear phase noise in DPSK systems", in Proc. *Conf. Nac. Telecomunicações* (ConfTele 2007), Peniche, Portugal, vol. 1, June 2007.
- R. Luís, B. Clouet, A. Teixeira, and P. Monteiro, "Analytical modelling of the cross-phase modulation-induced degradation in mixed DPSK and ASK transmission systems," in Proc. *International Conference on Transparent Optical Networks* 2007 (ICTON 2007), paper Mo.P.17, July 2007.

L.3. Other Publications by the Author

- R. Luís, A. Teixeira, P. André, P. Monteiro, "Method to estimate optical signal-to-noise ratio in transparent optical networks using asynchronous histograms," *Siemens Invention Disclosure,* no. 2003E08776, May 2004.
- R. Luís, A. Teixeira, P. André, P. Monteiro, "Asynchronous Optical Monitoring System based on Optical Sampling," *Siemens Invention Disclosure,* no. 2004E11638, June 2004.
- R. Luís, A. Teixeira, P. André, P. Monteiro, "OSNR monitoring method based on experimental calibration," *Siemens Invention Disclosure,* no. 2004E13420, June 2004.
- P. André, A. Teixeira, M. Lima, R. Luís, and D. Fonseca, "Asynchronous sampled amplitude histogram models for optical performance monitoring in high-speed networks," *OSA J. of Optical Networking,* vol. 3, no. 8, pp. 636-642, August 2004.
- R. Luís, and A. Cartaxo, "Analytical Characterization of SPM Impact on XPM-Induced Degradation in Dispersion-Compensated WDM Systems," *IEEE/OSA J. Lightwave Technol.,* vol. 23, no. 3, pp. 1503-1513, March 2005.
- A. Cartaxo, J. Rebola, N. Pavlovic, P. Charrua, D. Fonseca, J. Morgado, R. Luís, and M. Leiria, "Overview of DWDM/ODC project", *Fiber and Integrated Optics* , vol. 24, no. 3-4, pp. 331-352, April 2005.
- A. Cartaxo, and R. Luis, "Cross-phase modulation in WDM systems," in Proc. *Conf. Nac. Telecomunicações* (ConfTele 2005), Tomar, Portugal, April 2005.

- R. Luis, and A. Cartaxo, "Equivalent linear model of XPM-induced degradation in dispersion compensated WDM systems taking into account the SPM-influence," in Proc. *Conf. Nac. Telecomunicações* (ConfTele 2005), Tomar, Portugal, April 2005.
- P. Monteiro, D. Fonseca, A. Ferreira, T. Silveira, N. Garcia, M. Hajduczenia, C. Santiago, J. Pedro, R. Luís, and L. Pellegrino, "Optical communications research activities at COM RD1 Siemens S.A," *Fiber and Integrated Optics*, vol. 24, no. 4-5, pp. 395-410, June 2005.
- R. Luís, and A. Cartaxo, "Impact of dispersion slope on SPM degradation in WDM systems with high channel count," *IEEE/OSA J. Lightwave Technol.,* vol. 23, no. 11, pp. 3764-3772, November 2005.
- S. Pato, R. Luis, P. Monteiro, and H. Silva, "On the impact of nonlinear effects in 10 Gbit/s ethernet passive optical networks," in Proc. *Conf. Nac. Telecomunicações* (ConfTele 2007), Peniche, Portugal, pp. 577 - 580, May 2007.
- D. Fonseca, R. Luis, A. Cartaxo, and P. Monteiro, "Near pseudo-linear transmission regime in 10 Gb/s single sideband-alternate mark inversion systems using electrical dispersion pre-compensation," *IEEE Photon. Technol. Lett.,* vol. 19, no. 15, pp. 1127-1129, August 2007.

Annex I. Invention Disclosure: Method to Estimate OSNR in Transparent Optical Networks Using Asynchronous Histograms

I.1. Technical Problem

This annex presents a reproduction of the internal Siemens disclosure proposed in [Luís, 2004: 1]. The extensive use of wavelength division multiplexing systems and complex optical network structures is a reality. Optical networks are used to transmit signals with an increasing variety of bit-rates, frame structures and modulation formats. OMS are required to quantify and distinguish different transmission impairments. Optical noise is considered as a main impairment of optical transmission systems. Therefore, optical noise and/or OSNR monitoring techniques are of great interest for present and future optical transmission networks. Currently used in-service OSNR monitoring techniques involve complex and expensive equipments, such as optical spectrum analyzers, that are difficult to integrate in commercial optical transmission systems. Simplified techniques to measure OSNR are highly desirable.

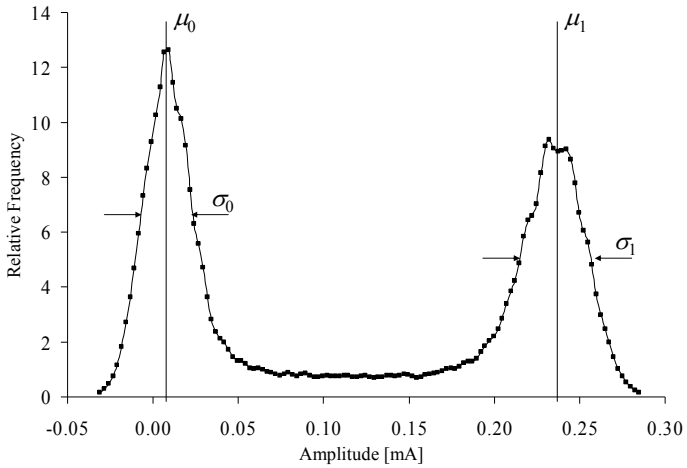

Fig. I.1. Typical asynchronous amplitude histogram of an NRZ signal.

I.2. State-of-the-Art

Techniques based on acquiring amplitude histograms of the analyzed signals are less costly and have been proposed to evaluate signal degradation. The amplitude histograms are obtained by optically or electrically sampling the signal to analyze at a sampling rate that may be synchronous or asynchronous with the monitored signal. Fig. I.1 presents an example of a measured asynchronous histogram, acquired from a binary NRZ signal. The diagram presents two relative maximums at amplitudes μ_0 and μ_1, corresponding to the symbols "0" and "1", respectively. The influence of electrical and optical noise in the signal can be evaluated by determining the standard deviations, σ_0 and σ_1, of the samples around the symbols "0" and "1", respectively.

Asynchronous histogram acquisition systems do not require clock recovery circuits therefore are less costly than synchronous systems. A low frequency independent clock generator can replace the clock recovery circuit. Nevertheless, synchronous histogram acquisition systems can be integrated in the signal receiver at the end of the optical path,

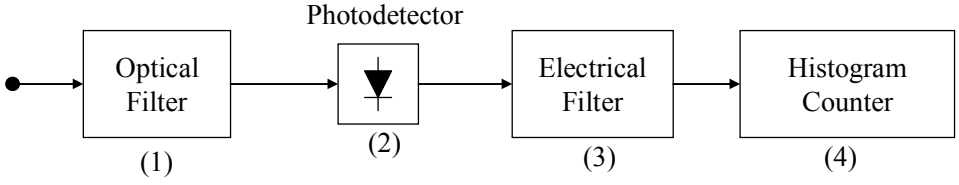

Fig. I.2. Histogram acquisition system.

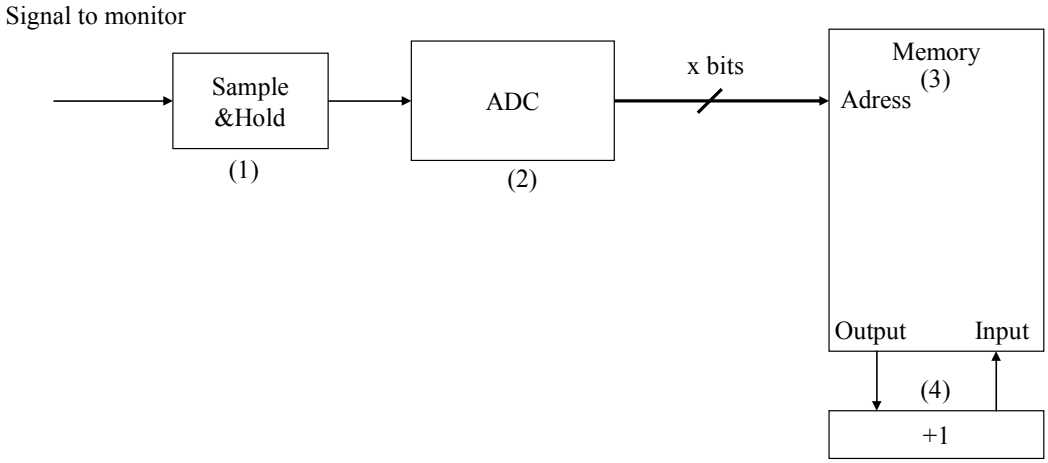

Fig. I.3. Histogram counting sub-system.

becoming cost effective. Asynchronous histogram acquisition systems are applicable in intermediate points of the optical network, where 3R regeneration is not desirable.

A possible block diagram for a histogram acquisition system is presented in Fig. I.2. The incoming optical signal is optically filtered (1) and converted to the electrical domain by a photodetector (2). An electrical filter (3) models bandwidth limitations of the electrical receiver. After filtering, the current is sent to a histogram counter (4), which produces the amplitude histogram. Fig. I.3 presents a possible structure for a histogram counter. A sample&hold (1) isolates samples of the monitored current in time. Each analog sample is converted to a digital value by an ADC (2). The ADC output is used to call up a memory address (3), which is incremented (4). After the desired number of samples is acquired, the contents of the memory correspond to the amplitude histogram. Another possible histogram counter is described in patent no. [Elbers, 2002].

Several methods to analyze and evaluate signal quality that use asynchronous and/or synchronous amplitude histograms have been proposed in [Bischoff, 2004], [Elbers, 2002], and [Shake, 2002: 1]. These methods are generally based on obtaining μ_0, μ_1, σ_0 and σ_1 in order to extract information about the signal quality.

I.3. Proposed Solution

The proposed method accurately estimates the OSNR of a signal using an experimental calibration based on a RAH. The RAH is previously acquired by sampling the signal to monitor at low noise conditions. The proposed process numerically includes

the influence of optical noise in the RAH until it matches the MAH that is to be evaluated. The result of this fitting is an estimated asynchronous histogram (EAH) and an estimate of the OSNR. This technique can be applied to non-conventionally modulated signals or distorted signals, as long as the RAH presents similar modulation or distortion. The numerical fitting technique is a nonlinear minimization algorithm, such as the "Nelder-Mead Simplex Method" [Lagarias, 1998].

To understand how the EAH is calculated, we assume that the probability density function (PDF) of the electrical current at the histogram counter input is approximated by:

$$p_i(\mu) = \left[\int_{-\infty}^{+\infty} p_s(s) \cdot p_n(\mu \mid s) \cdot ds \right] * p_e(\mu) \tag{I.1}$$

where $p_s(\mu)$ is the PDF of the optical signal's power and $p_e(\mu)$ is the PDF of the electrical noise generated at the electrical receiver, assumed gaussian with standard deviation σ_e. The term $p_n(\mu \mid s)$ is the PDF of the electrical current at the photodetector output, taking into account the presence of optical noise, conditioned to a given signal power, s. $p_n(\mu \mid s)$ is approximated by:

$$p_n(\mu \mid s) = \frac{1}{\sqrt{2\pi \cdot \sigma^2}} \cdot \exp\left\{ -\frac{(\mu - R_s \cdot s)}{2\sigma^2} \right\} \tag{I.2}$$

where R_s is the photodetector responsivity and σ^2 is the variance, given by [Agrawal, 1997] (pp. 404), and [Elbers, 2002]:

$$\sigma^2 = \frac{2R_s^2 \cdot s^2 \cdot B_e}{OSNR \cdot B_o} + R_s^2 \cdot \frac{s^2}{OSNR^2 \cdot B_o^2} \cdot B_e B_o \tag{I.3}$$

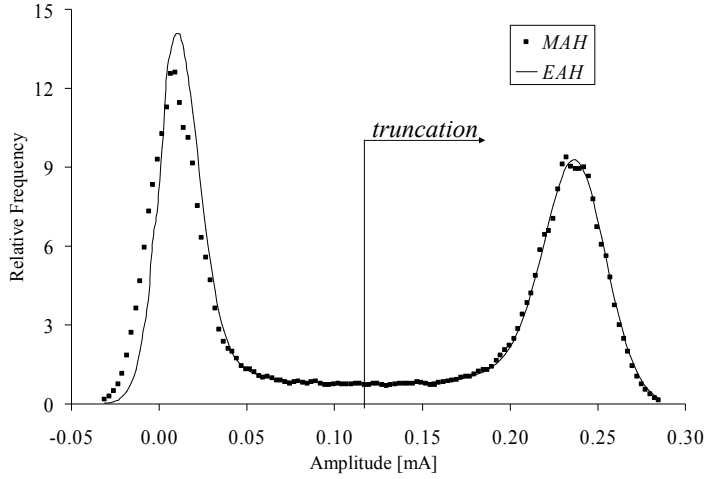

Fig. I.4. Comparison between a measured and estimated histograms.

where the shot noise is neglected. B_e and B_o are the electrical and optical filters' bandwidth, respectively. Expression (I.1) can be used to obtain the EAH as a function of the OSNR, as long as B_e, B_o, R_s, σ_e and $p_s(s)$ are known. The main problem is to obtain $p_s(s)$, which varies with the signal's shape. Therefore, we approximate (I.1) by:

$$p_i(\mu) \approx \int_{-\infty}^{+\infty} \left[p_s(s) * p_e(s) \right] \cdot p_n(\mu, s) \cdot ds \tag{I.4}$$

Note that expressions (I.1) and (I.4) become identical if the electrical noise is suppressed. The validity of the proposed approximation is limited to cases where the signal's contribution to the detected electrical current, $R_s \times s$, is much larger that the electrical noise. The approximation allows the isolation of the term $p_s(s)*p_e(s)$, which can be measured by acquiring a histogram of the signal in the absence of optical noise. This histogram corresponds to the RAH and must be acquired from a signal with the same distortion has the signal that is to be monitored. No significant limitations are imposed concerning the shape of the monitored signal. Fig. I.4 presents the MAH of Fig. I.1, compared with the EAH, using the proposed method. Due to the influence of electrical noise in the RAH, the EAH presents error for low amplitudes but a good accuracy for high amplitudes. Therefore, a truncation of the EAH and the MAH is performed, as shown in

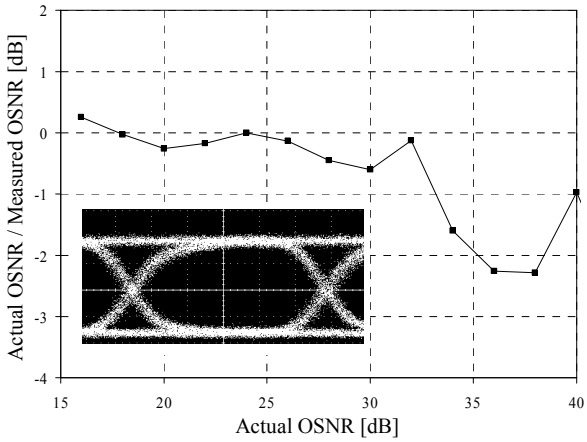

Fig. I.5. Dependence of the OSNR estimation error on the OSNR of the monitored signal. The inset presents an eye-diagram of the signal under analysis without the impact of optical noise.

Fig. I.4. Only the histogram points located above the average current are taken into account for the numerical fitting.

The proposed method was evaluated experimentally. Fig. I.5 presents the dependence of the OSNR measurement error on the actual OSNR. The presented values were obtained using a non-distorted 10 Gb/s NRZ signal carrying optical noise. The inset of Fig. I.5 presents an eye pattern of the signal in the absence of optical noise. The latter signal was used to obtain the RAH. Fig. I.6 presents the dependence of the OSNR measurement error on the actual OSNR obtained using a 10 Gb/s NRZ signal distorted by 50 km of standard fiber. The inset of Fig. I.6 presents an eye pattern of the signal in the absence of optical noise. The latter signal was used to obtain the RAH. Measurement errors

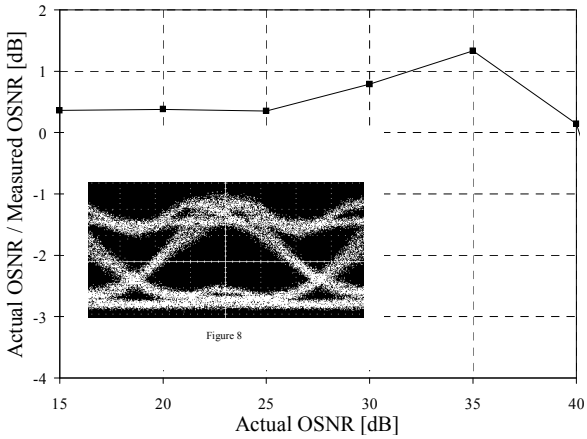

Fig. I.6. Dependence of the OSNR estimation error on the OSNR of the monitored signal impaired by GVD. The inset presents an eye-diagram of the signal under analysis without the impact of optical noise.

bellow 1 dB were obtained for OSNR values under 32 dB. Improvements can be made by enhancing the histogram acquisition system.

I.4. Advantages of the Proposed Solution

The advantages of the proposed method are:

- Direct evaluation of OSNR without the need for correction factors
- Independence of distortion and modulation format of the monitored signal
- Algorithms to evaluate other transmission impairments can be included
- Measurement of histogram moments like μ_0, μ_1, σ_0 and σ_1 is not necessary.

The disadvantages of the proposed method are:

- Complex chip programming is required, in order to implement the fitting algorithm.
- Low noise receiver is required
- Previous acquisition of the RAHs is required

Annex II. Invention Disclosure: Asynchronous Optical Monitoring Based on Optical Sampling

II.1. Technical Problem

This annex presents a reproduction of the internal Siemens disclosure proposed in [Luís, 2004: 3]. The recent developments in optical communications networks have lead to increasing efforts to minimize the costs of optical transmission systems. However, technological advances have allowed the widespread use of multiple signal formats and bit-rates, increasing the demand for network flexibility. Therefore, a compromise between cost effective and technologically advanced systems must be found. Some of the required demands concern optical monitoring systems. The use of temporal sampling based optical monitoring systems has been strongly conditioned by the high cost of the sampling and clock recovery circuits. The cost of sampling circuits increases with the bandwidth requirements, invalidating their use to acquire samples with pico-second or tens of pico-second resolutions. The cost of clock recovery circuits is also strongly dependent on the bit-rate of the monitored signal. Additionally, the use of fixed clock recovery circuits does not allow transparent signal monitoring.

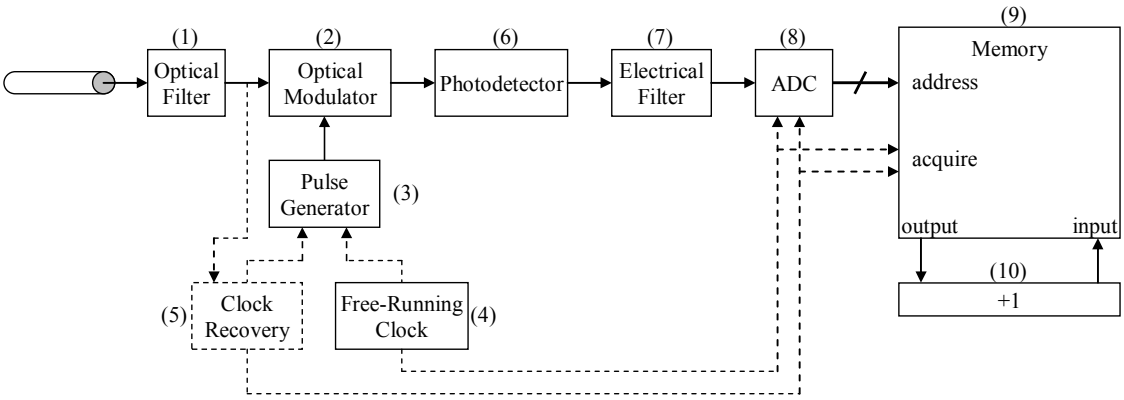

Fig. II.1. Block diagram of an optical sampling based optical monitoring system using synchronous or asynchronous histograms.

II.2. State-of-the-Art

Asynchronous sampling of the monitored signal has been also proposed as a method to evaluate signal quality. In this case, correlation between acquired samples and the monitored signal's bit-rate is not required. Therefore, a clock recovery circuit is not necessary. This technique produces asynchronous histograms of the signal and is less accurate than synchronous sampling due the contribution of samples acquired during cross-over instants that do not contribute to the signal's performance. However, asynchronous sampling can be used to evaluate the influence of different transmission impairments. Therefore, it may be important for future intelligent networks that react accordingly to different transmission impairments.

This report concerns monitoring systems based on optical monitoring. Fig. II.1 presents a possible diagram for such a system. The incoming optical signal is filtered by an optical filter (1) and is inserted in an optical modulating device (2). This device is activated by a pulse generator (3), which is controlled by a clock signal generated by a free-running clock (4) or a synchronized clock recovery circuit (5). In the latter case, additional elements are required to synchronize the clock recovery circuit. However, these elements will not be considered here. The optical modulating device isolates short optical pulses of the incoming signal that are then detected by a photodetector (6). The resulting electrical pulses are filtered by an electrical filter (7) that models bandwidth limitations of the electrical receiving circuit. The electrical pulses are captured by an ADC (8). The ADC

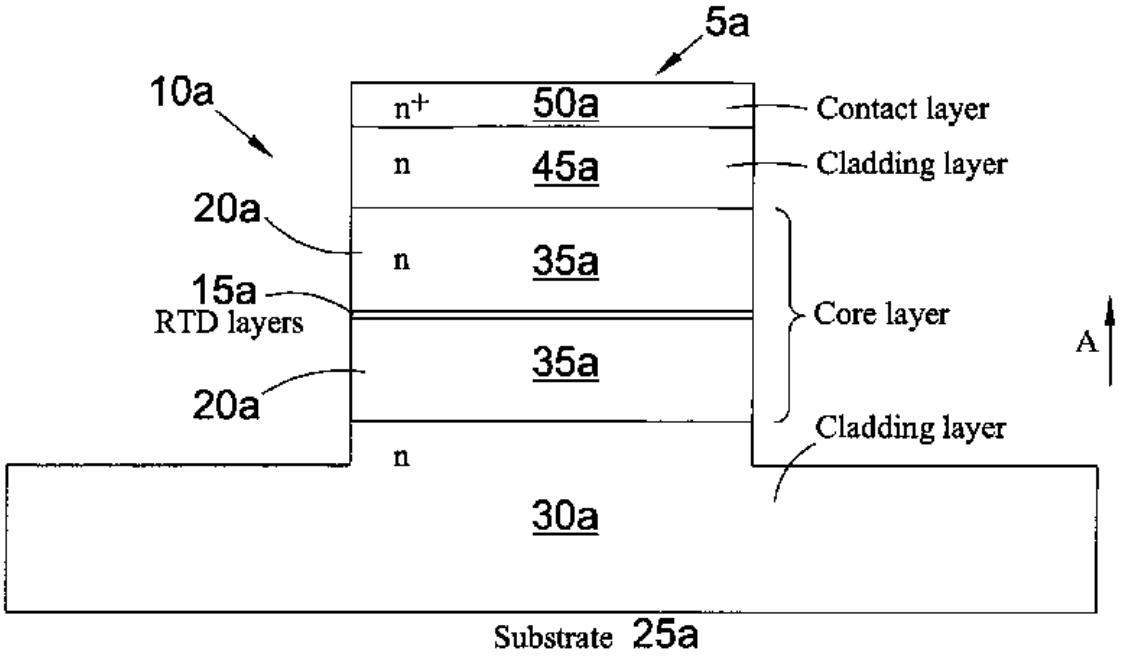

Fig. II.2. Schematic sectional end view of a RTD-EAM, extracted from [Ironside, 2000].

output is used to call up a memory address (9), which is incremented (10). Both the ADC and the memory are controlled by the used clock. After the desired number of samples is acquired, the contents of the memory correspond to the amplitude histogram. Note that, the required bandwidth of the electrical receiver is of the same order or one order above the sampling frequency, (tens of MHz) which is significantly lower than the case of an electrical sampling system. The high bandwidth requirements are in the optical sampling device and pulse generator. Several proposals have been made to optically modulate short pulses [Otani, 2002]. These systems are usually of some complexity and still require short pulse generators, which are complex and expensive equipments. These constitute the main impairment to the application of such systems in transmission equipment. However, commercial optical measurement equipments such as optical oscilloscopes are starting to use, in a general way, optical sampling.

II.3. Proposed Solution

The proposed invention consists in using the properties of a resonant tunnelling diode (RTD) as a fast electro-absorption modulator (EAM) to produce a low-cost optical

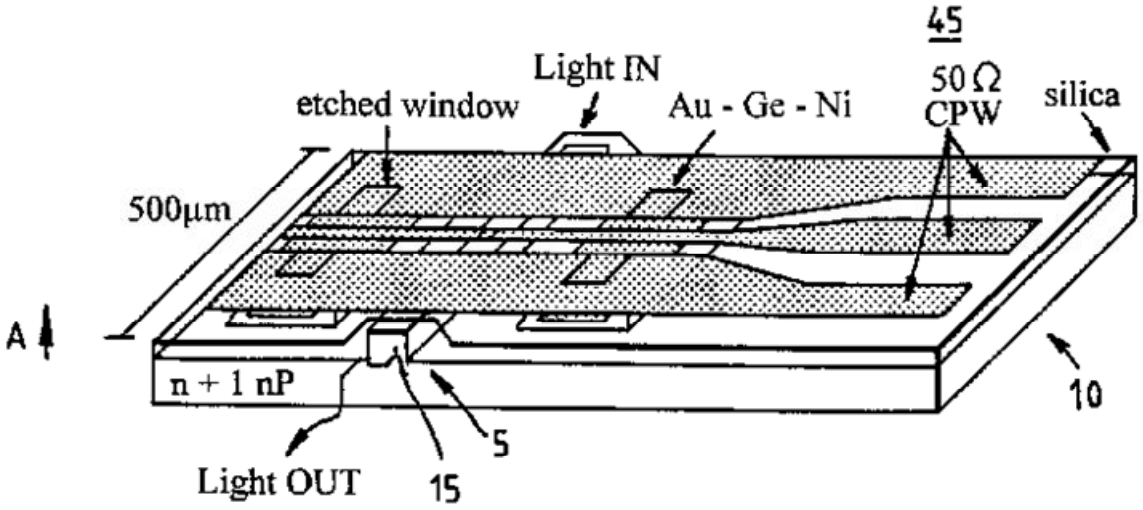

Fig. II.3. Diagram of a packaged RTD-EAM, extracted from [Ironside, 2000].

sampling system. The generated optical pulses are converted to the electrical domain by a waveguide photodetector (WPD) integrated with the RTD-EAM.

Essentially, an RTD-EAM is a unipolar device, which consists of a double barrier RTD embedded in an optical waveguide. This optoelectronic device is claimed in [Ironside, 2000] and [Ironside, 2002] and Fig. II.2 presents the corresponding schematic structure. Fig. II.3 presents a diagram of the packaged RTD-EAM.

The typical current-voltage (I-V) characteristic is presented in Fig. II.4 [Figueiredo, 2001]. When polarized in the negative differential resistance area of the I-V characteristic, the RTD presents the ability of amplifying an injected signal. The proposed invention

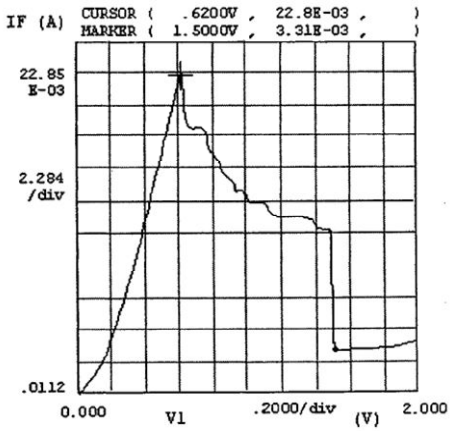

Fig. II.4. Typical I-V characteristic of a 2mm × 100 mm active area RTD-EAM, extracted from [Figueiredo, 2001].

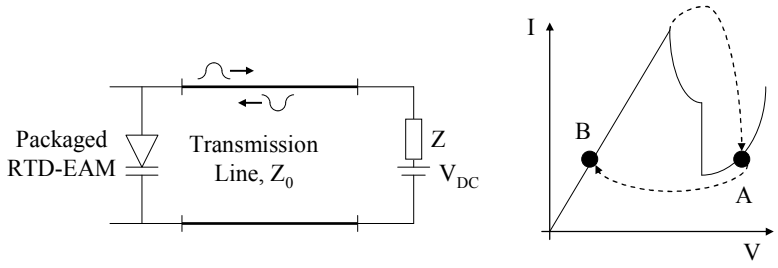

Fig. II.5. Schematic diagram of the electrical circuit for the RTD-EAM used as a relaxation oscillator.

intends to use this property to produce a relaxation oscillator with the setup presented in Fig. II.5 [Figueiredo, 1999]. In this setup, an RTD-EAM is placed in one end of a transmission line with impedance Z_0. On the other end is an impedance $Z<Z_0$, leading to a negative reflection coefficient. A power supply ensures energy for the oscillator and proper polarization of the RTD-EAM. A pulse incident on the RTD is amplified and retransmitted due to the device's negative differential resistance. The negative reflection coefficient of the impedance inverts the polarity of any pulse transmitted by the RTD to the impedance [Figueiredo, 2000]. The oscillation process is initiated by noise in the circuit.

When operating at point A of the characteristic presented in figure 5, the transmission is low. A negative current return pulse will switch the operating point directly to point B, causing the RTD capacitance to discharge. This allows high transmission along the waveguide for a short period. Some transmission exists when operating at point B. The following positive current pulse incident in the RTD shifts the operating point back to A, reinitializing the cycle. The sampling frequency depends on the length of the transmission line. The width of the optical sampling pulses depends on the physical characteristics of the RTD [Figueiredo, 2000]. Fig. II.6 presents a temporal diagram of a generated pulse, considering a constant input light [Figueiredo, 1999]. A temporal width of 33 ps was verified, which would be sufficient to analyse 10 Gb/s signals. The repetition rate of the optical pulse depends on the length of the transmission line. In the presented example, the repetition rate was of 166 MHz. Therefore, the time scale used only allows visualization of a single pulse.

To further integrate the proposed monitoring system, the photodetector can be fabricated in the same chip as the RTD-EAM. For this purpose, the ideal is the use of a WPD, sharing the waveguide with the RTD-EAM. This would eliminate coupling loss between the optical modulator and the photodetector and reduce the fabrication cost.

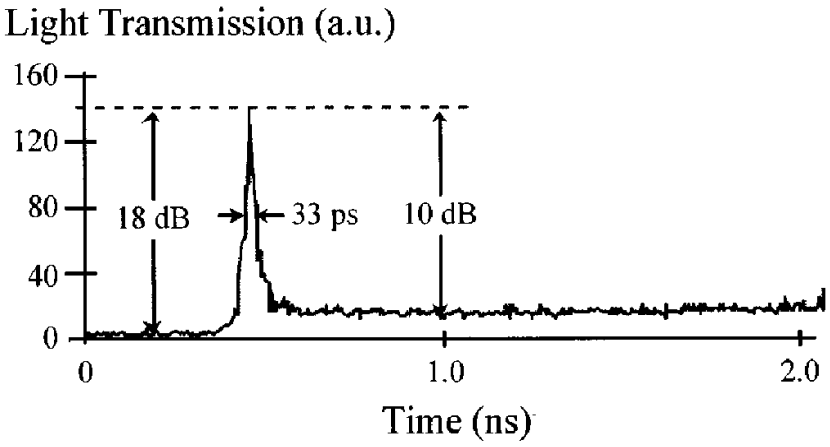

Fig. II.6. Measurement of the optical pulse generated by relaxation oscillation of the RTD , extracted from [Figueiredo, 1999].

The proposed system of this invention report is presented in Fig. II.7. After filtering, the optical signal is inserted in the packaged RTD-EAM/WPD device where it is sampled by the RTD-EAM and detected by the WPD. The transmission line connected to the RTD-EAM transmits the electrical current pulses and the input impedance of the electrical amplifier constitutes the impedance $Z<Z_0$. The electrical amplifier is required to produce the acquisition pulses for the ADC and the memory.

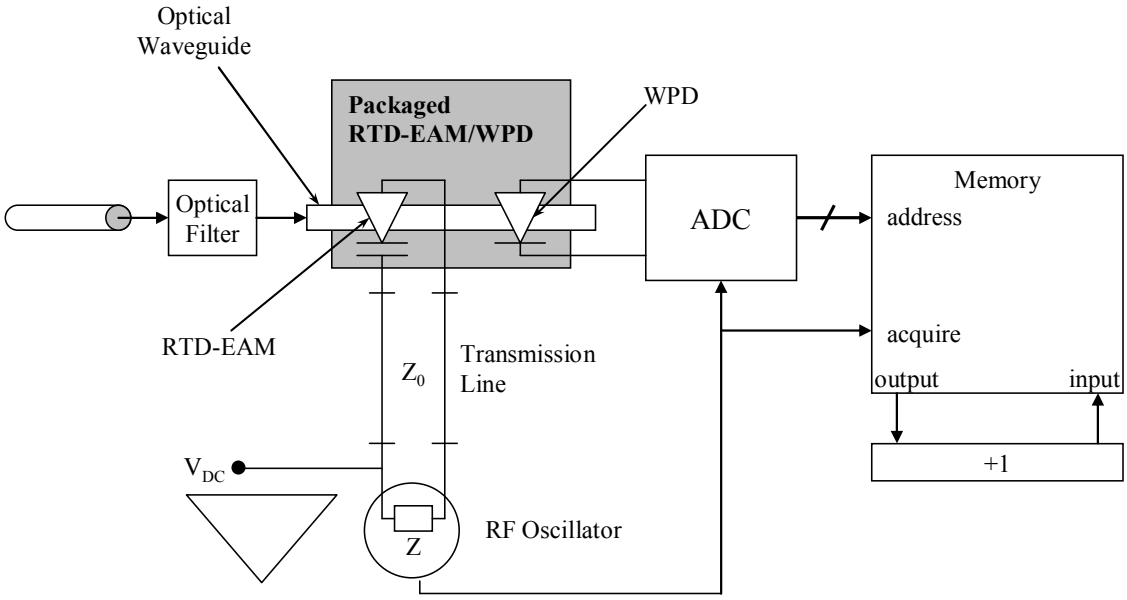

Fig. II.7. Block diagram of the proposed asynchronous optical monitoring system.

II.4. Advantages of the Proposed Solution

The proposed system dramatically reduces the cost of an optical asynchronous sampling system. The devices (2), (3) and (4) are replaced by a single RTD-EAM and a transmission line with the corresponding power source. With further integration of the WPD, a single chip would perform short optical pulse sampling and photo-detection. The low bandwidth requirements of the photodetector allow the use of a high sensibility device, which may increase the sensitivity of the monitoring system. The latter would not be possible with electrical sampling, where the photo-detection and sampling circuitry is required to have very large bandwidth (larger than the signal to monitor).

The dimensions and cost of the proposed system are small enough to allow its integration in any transmission equipment without significant impact in its size or cost.

Current monitoring techniques based on asynchronous sampling already allow reasonable estimates of the signal quality. Additionally, recent in-house developments allow accurate evaluation of transmission impairments such as optical signal-to-noise ratio [Luís, 2004: 1] and intra-band crosstalk [Luís, 2004: 2].

Annex III. Invention Disclosure: OSNR Monitoring Method Based On Experimental Calibration

III.1. Technical Problem

This annex presents a reproduction of the internal Siemens disclosure proposed in [Luís, 2004: 4]. Asynchronous amplitude histogram analysis has been proposed as an efficient and low cost method to monitor and identify different optical transmission impairments [Hanik, 1999]. The main problem of using asynchronous histograms to recognize different transmission impairments is to derive techniques to quantify and distinguish these impairments. Optical noise is considered as a major impairment of optical transmission systems. Therefore, optical noise and/or OSNR monitoring techniques are of great interest for present and future optical transmission networks. This invention report regards monitoring OSNR using asynchronous histograms.

III.2. State-of-the-Art

The most common way to monitor the OSNR in an optical transmission system uses an OSA. This device is sensitive to transmission phenomena that influence the power spectrum of the signal under analysis. However, an OSA is a complex and costly device and its integration cost in an optical transmission system to simply monitor optical noise is

often unpractical. Instead, it is common to perform spectral analysis during the system commissioning stage and assure OSNR margins that are large enough to sustain the lifetime of the link.

Asynchronous amplitude histogram analysis is a reasonable solution to perform monitoring of optical signals in intermediate points of an optical path. Several techniques have been developed to extract information from asynchronous histograms about the Q-factor [Shake, 2002: 2], GVD [Shake, 2003: 2] and pulse rise-time [Chen, 2004], among others. However, when different transmission impairments accumulate, it becomes difficult to distinguish them. [Luís, 2004: 1] proposed and experimentally demonstrated a technique to evaluate the OSNR of an optical signal suffering from GVD-induced distortion. In theory, this technique can be extended to signals affected by any type of amplitude distortion that remains unaltered in time, such as self-phase modulation. An asynchronous histogram monitoring system using this technique simultaneously with other techniques already developed to monitor other transmission impairments, could become a powerful performance monitoring tool.

The main limitation of the technique presented in [Luís, 2004: 1] is the difficulty in obtaining a RAH of the signal to monitor in low noise conditions. The invariability of the RAH with random varying transmission impairments such as PMD is also a limitation. This invention report proposes an evolution of the technique presented in [Luís, 2004: 1] to allow the use of a RAH with an arbitrary OSNR. The new technique requires only an initial calibration to obtain the RAH and an OSNR measurement using an external device to obtain the reference OSNR.

III.3. Proposed Solution

Several systems have been proposed to obtain the asynchronous histogram of an optical signal. These systems can be based on optical or electrical sampling of the signal under analysis. The OSNR monitoring technique proposed in this invention report will be applied to systems based on electrical sampling. However, its application to systems based in optical sampling is straightforward. Fig. III.1 presents a possible structure for the OMS. The optical signal under analysis is optically filtered and detected by a photodetector. The resulting electrical current follows to an asynchronous electrical sampler. Each sample is

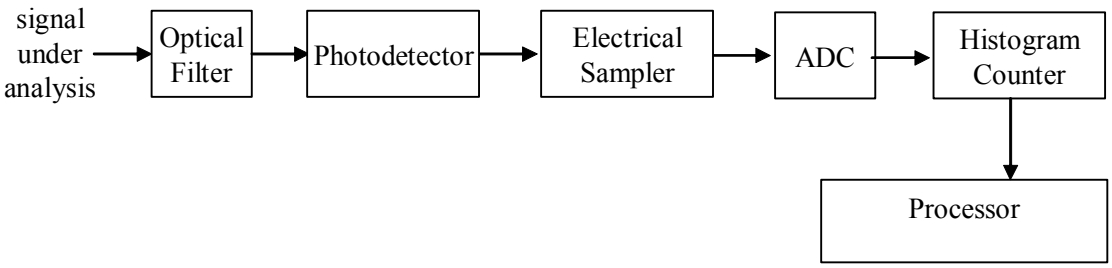

Fig. III.1. Block diagram of an optical sampling based optical monitoring system using asynchronous histograms.

converted to a digital value by an ADC and counted to obtain the asynchronous histogram. The histogram is then processed to evaluate the OSNR of the signal under analysis.

The proposed OSNR evaluation technique consists in estimating the OSNR of a signal using a MAH and an experimental calibration based on a RAH with an arbitrary reference OSNR, $osnr_R = P_s / N_R$, in linear units. P_s and N_R are the reference optical signal and noise power levels at the photodetector input. The RAH and $osnr_R$ can be obtained by previously acquiring a histogram of the signal under analysis and measuring its OSNR with an external device, such as an OSA. It is assumed that the measured and reference histograms were acquired from signals with the same power. Initially, consider that the optical noise power affecting the signal under analysis, N_M, is higher than N_R. We propose to use the numerical process described in [Luís, 2004: 1] to add an optical noise to the RAH until it matches the MAH. The histogram that results from adding the influence of optical noise to the RAH will be referred here as EAH. If a reasonable similarity between the EAH and the MAH is achieved, we can consider that $N_M \approx N_R + N_E$, where N_E is the added optical noise power. Consequently, the OSNR of the signal under analysis, $osnr_M$, is approximated by:

$$osnr_M^{-1} \approx osnr_R^{-1} + osnr_E^{-1} \tag{III.1}$$

where $osnr_M = P_s / N_M$ and $osnr_E = P_s / N_E$, in linear units. This method will be referred as *method A*.

If the noise power affecting the signal under analysis is lower than N_R it is not possible to add the influence of additional optical noise to the RAH in order to match the

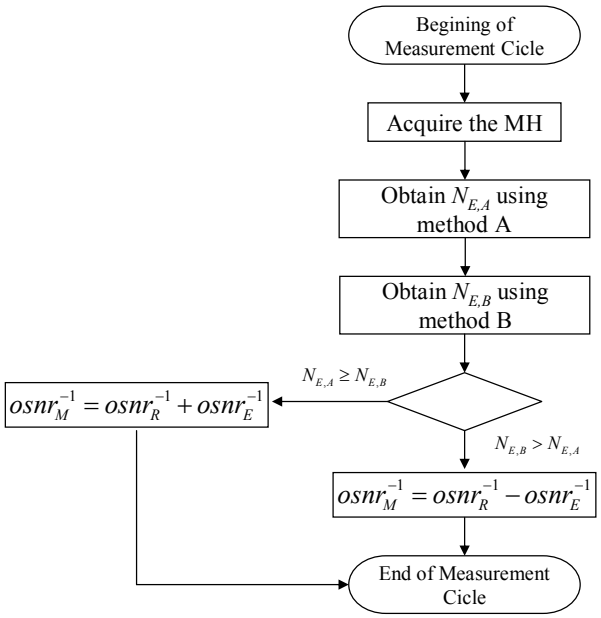

Fig. III.2. Flow chart of the measurement cycle.

MAH. Therefore, we propose to do the opposite: add the influence of additional optical noise to the MAH in order to match the RAH. In this case, if a good similarity between the RAH and the EAH is achieved we can consider that $N_R \approx N_M + N_E$. Consequently, the OSNR of the signal under analysis is approximated by:

$$osnr_M^{-1} \approx osnr_R^{-1} - osnr_E^{-1} \tag{III.2}$$

This method will be referred as *method B*.

Fig. III.2 presents a possible flow chart for the measurement cycle. It begins by acquiring a histogram of the signal under analysis. Initially, it is not possible to directly determine which method (A or B) should be used. However, if we apply method A when $N_M < N_R$, the best match between the RAH with added noise and the MAH is found for null added noise. Similarly, if we apply method B when $N_M > N_R$, the best match between the MAH with added noise and the RAH is for null added noise. This means that, if the incorrect method is applied, the result of the fitting is zero or close to zero N_E. Therefore, to determine which method should be used, we apply both methods and use only the one that with the highest value of N_E.

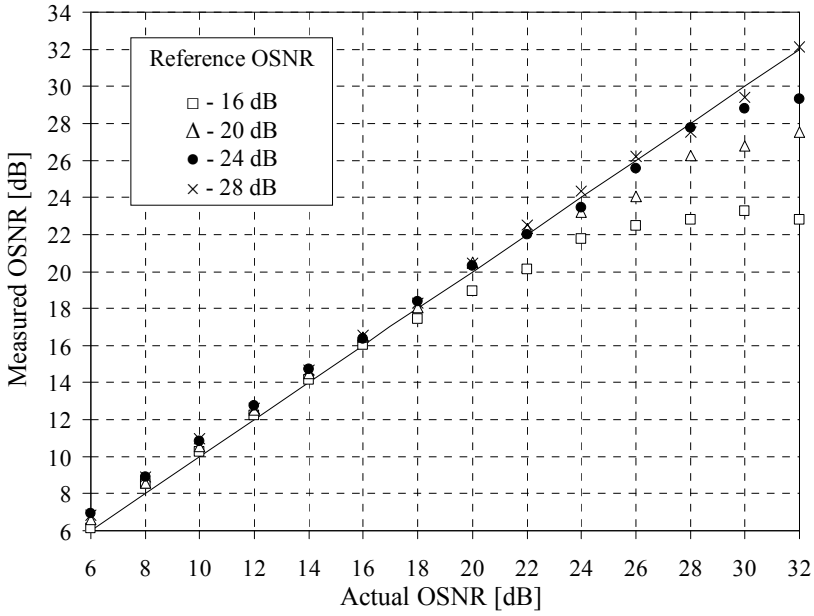

Fig. III.3. Flow chart of the measurement cycle.

To evaluate the proposed technique, we have simulated a 10 Gb/s non-return to zero optical signal that was combined with optical noise and injected in the OMS. The OMS uses an optical filter with a bandwidth of 72 GHz and the electrical receiving circuit and sampler presented a combined bandwidth of 20 GHz. Fig. III.3 presents the OSNR measurements obtained using the flowchart presented in Fig. III.2, as a function of the actual OSNR of the signal under analysis. Several values of $osnr_R$ were considered. The numerical process used to add the influence of optical noise power in the MH to match the RAH underestimates the value of N_E due to approximations performed in the calculations and the presence of electrical noise in the RAH and MAH. Therefore, we verify a small overestimation of the OSNR in the cases where $osnr_M < osnr_R$, which corresponds to having $N_M > N_R$ and applying the method A. Similarly, in the cases where $osnr_M > osnr_R$, which is equivalent to having $N_M < N_R$ and applying method B, there is an underestimation of the actual OSNR. Unlike the previous case, this underestimation increases significantly with the actual OSNR because, when $osnr_M$ is large, small variations of N_E lead to large variations of $osnr_M$. We consider that the influence of the N_E estimation error is small if $N_M > N_E$. Therefore, reasonable estimates can be achieved

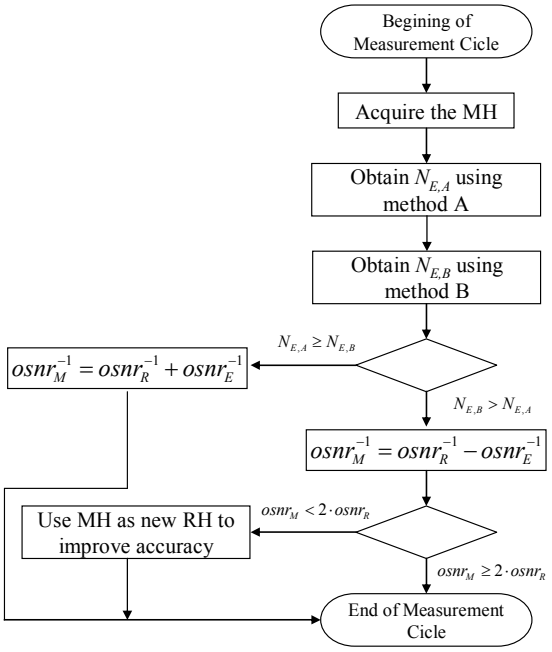

Fig. III.4. Flow chart of the measurement cycle for the OSNR Learning System.

if the actual OSNR is bellow $2 \cdot osnr_R$ (or +3 dB in Fig. III.3). A similar behavior was obtained when analyzing signals affected by GVD-induced distortion.

Fig. III.3 shows that the range of OSNR values that can be measured increases with $osnr_R$. Ideally, $osnr_R$ would be infinite, corresponding to the case presented in [Luís, 2004: 1]. Because this is not always feasible, we propose three possibilities to measure signals with a high OSNR:

III.3.1. OSNR Learning System

This approach takes advantage of the fact that the OSNR of the signal under analysis may vary in time and that signals with an OSNR within a margin of 3 dB above the reference OSNR can still be accurately measured. Such histograms can be used as RH for posterior measures. A simple adaptation on the flow chart of the measurement cycle is required to include the learning function, which is presented in Fig. III.4. In the new cycle, if a MAH presents an OSNR within a margin of 3 dB above the reference OSNR the system will memorize the MAH and use it as a RAH for posterior measurements. In this way, the monitoring system will improve its accuracy with new measurements whenever

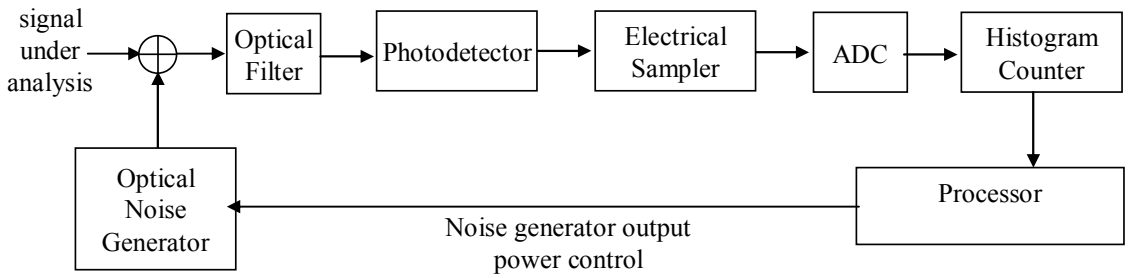

Fig. III.5. Block diagram of an optical sampling based optical monitoring system using asynchronous histograms with artificial noise introduction.

possible. The limitation of this method results from the error introduced when estimating the reference OSNR.

III.3.2. Noise Introduction

If the system is required to evaluate signals with an OSNR higher than the reference OSNR, we can introduce optical noise on the signal under analysis until the MH matches the RAH. This corresponds to a direct implementation of method B and can be performed using the setup presented in Fig. III.5. This setup is identical to the one presented in Fig. III.1 but includes an optical noise generator with a controlled output power. The optical noise is added to the signal under analysis prior to optical filtering until the MAH matches the RAH. The generated noise power required to match the MAH with the RAH corresponds directly to N_E and expression (III.2) can be used to estimate $osnr_M$. Note that, because the total power available for monitoring is typically low, the output power of the noise generator required to obtain the match is low. Therefore, the quality requirements for this component are low, reducing its price. In fact, the noise generator can be build with a simple LED. In this approach, the method A remains as proposed before in this invention report.

III.3.3. Learning System with Artificial Noise Introduction

This is a combination of approaches 1 and 2. If a signal with an OSNR higher than the reference OSNR is monitored, we initially memorize the MAH to use as a RAH in posterior measurements. After that, we use approach 2 to determine the OSNR of the signal under analysis. The measured OSNR becomes the reference OSNR.

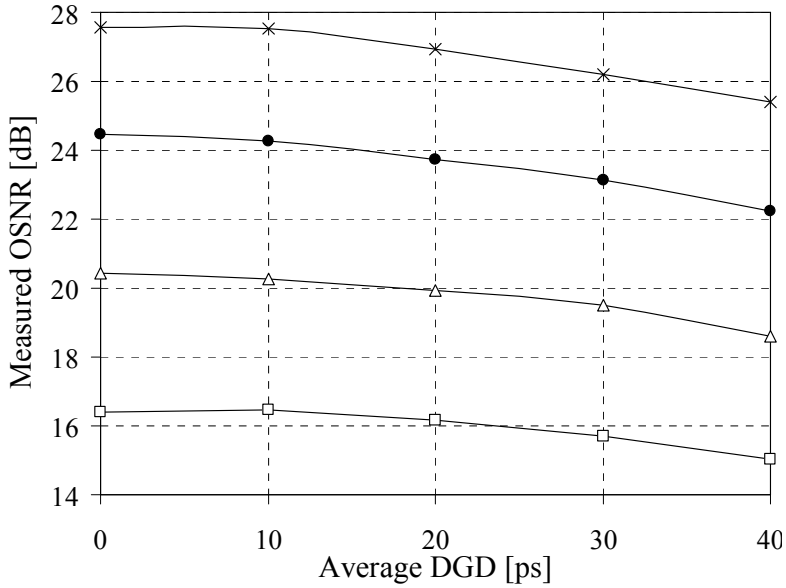

Fig. III.6. Measured OSNR as a function of the average DGD for different values of the actual OSNR. A reference OSNR of 28 dB was used. Actual OSNR values: □ - 16 dB; Δ - 20 dB; ● - 24 dB; × - 28 dB.

III.3.4. Influence of PMD on the OSNR measurements

Similarly to [Luís, 2004: 1], the technique proposed in this invention report is not sensitive to signal shape distortion, as long as the RAH is acquired from a signal with similar distortion. However, if the signal suffers from additional distortion due to PMD that was not present at the time of the RAH acquisition, measurement errors may occur. To evaluate the impact of PMD on the OSNR measurement, we consider the system used to obtain Fig. III.3, but with a signal affected by a given average DGD. Fig. III.6 presents the variation of the estimated OSNR with the DGD for different values of the actual OSNR. The RAH was acquired from a signal with an OSNR of 28 dB. Each point was obtained averaging 10 simulations.

Fig. III.6 shows that as the average DGD is increase, the measured OSNR decreases. This occurs because the fitting process interprets the PMD-induced signal distortion as additional noise. However, the variation of the measured OSNR with the average DGD is negligible up to a given value of DGD. In fact, maintaining the average DGD under 20 ps yields OSNR variations, with respect to the point of null DGD, bellow 1 dB. Fig. III.7 presents the maximum allowable DGD for a 1 dB OSNR variation as a function of the actual OSNR for different values of the reference OSNR. It is shown that,

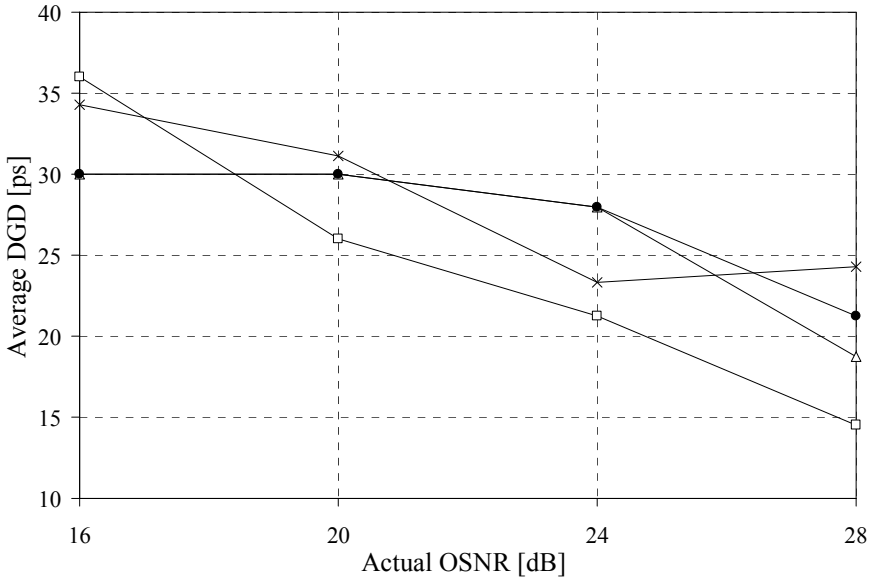

Fig. III.7. Maximum allowable DGD for a 1 dB variation of the measured OSNR as a function of the actual OSNR. Reference OSNR values: □ - 16 dB; Δ - 20 dB; ● - 24 dB; × - 28 dB.

for average DGD values bellow 15 ps, the measured OSNR variations are under 1 dB. The most limiting cases were observed for a reference OSNR of 16 dB.

The results presented in Fig. III.6 and Fig. III.7 suggest that the proposed OSNR estimation technique can be used with 10 Gb/s signals affected by average DGD values up to 15 ps. Note that, with average DGD values above 12% the bit period, the outage probability due to PMD becomes intolerable [Sunnerud, 2001]. In these conditions, it is not so important to measure the OSNR because the main degradation of the signal results from PMD.

III.4. Advantages of the Proposed Solution

The advantages of the proposed method are:

- Direct evaluation of OSNR without the need for correction factors.
- Independence of distortion and modulation format of the monitored signal.
- Algorithms to evaluate other transmission impairments can be included in parallel with the proposed technique.
- Measurement of histogram moments like μ_0, μ_1, σ_0 and σ_1 is not necessary.
- Resilience to PMD within acceptable limits.

- Combined use of the proposed technique with other histogram analysis techniques is possible.

The disadvantages of the proposed method are:

- Low noise receiver is required but significant improvements can be obtained using optical sampling.

- Low accuracy for OSNR measurements above the reference OSNR.

References

A

[Adams, 2006] R. Adams, M. Rochette, T. Ng, B. Eggleton, "All-optical in-band OSNR monitoring at 40 Gb/s using a nonlinear optical loop mirror," *IEEE Photon. Technol. Lett.*, vol. 18, no. 3, pp. 469-471, February 1, 2006.

[Agrawal, 1995] G. Agrawal, *Nonlinear fiber optics*, 2nd Edition, Academic Press, New York, 1995.

[Agrawal, 1997] G. Agrawal, *Fiber-Optic Communication Systems*, 2nd Ed. Wiley-Interscience, New York, 1997.

[André, 2002: 1] P. André, "Optoelectronic components for high bitrate photonic networks," Ph.D. Thesis, Dept. Elect. and Telecom. Eng., Univ. of Aveiro, Aveiro, Portugal, 2002.

[André, 2002: 2] P. André, J. Pinto, A. Teixeira, J. Rocha, T. Almeida, and M. Pousa, "Optical-signal-quality monitor for bit-error-ratio assessment in transparent DWDM networks based on asynchronously sampled amplitude histograms," *OSA J. of Optical Networking*, vol. 1, no. 3, pp. 118-128, March 2002.

[André, 2002: 3] P. André, and J. Pinto, "Bit error rate assessment in DWDM transparent networks using optical performance monitor based in asynchronous sampling," in Proc. *Optical Fiber Communication Conf.* 2002 (OFC 2002), pp. 749 – 750, March 2002.

[André, 2004] P. André, A. Teixeira, M. Lima, R. Luís, and D. Fonseca, "Asynchronous sampled amplitude histogram models for optical performance monitoring in high-speed networks," *OSA J. of Optical Networking*, vol. 3, no. 8, pp. 636-642, August 2004.

B

[Bellotti, 2000] G. Bellotti and S. Bigo, "Cross-phase modulation suppressor for multispan dispersion-managed WDM transmissions," *IEEE Photon. Technol. Lett.*, vol. 12, no. 6, pp. 726-728, June 2000.

[Benlachtar, 2003] Y. Benlachtar, R. Killey, and P. Bayvel, "Identification of sources of degradation in optical channels using deconvolution technique," in Proc. *Optical Fiber Communications Conf.*2003, (OFC 2003), vol. 1, pp. 109-110, March 2003.

[Bergano, 1993] N. Bergano, F. Kerfoot, and C. Davidson, "Margin measurements in optical amplifier systems," *IEEE Photon. Technol. Lett.*, vol. 5, no. 3, pp. 304-306, March 1993.

[Bischoff, 2004] M. Bischoff, "Method for monitoring the signal quality in transparent optical networks," US Patent no. US 6,836,620 B1, December 2004.

[Blow, 1990] K. Blow, N. Doran, B. Nayar, and B. Nelson, "Two-wavelength operation of the nonlinear fiber loop mirror," *OSA Optics Letters*, vol. 15, no. 4, pp. 248-250, February 1990.

[Bogoni, 2004] A. Bogoni, P. Ghelfi, M. Scaffardi, and L. Optì, "All-optical regeneration and demultiplexing for 160-Gb/s transmission systems using a NOLM-based three-stage scheme," *IEEE J. of Selected Topics in Quantum Electron.*, vol. 10, no. 1, pp. 192-196, January-February 2004.

[Bononi, 1998] A. Bononi, C. Francia, and G. Bellotti, "Impulse response of cross-phase modulation filters in multi-span transmission systems with dispersion compensation," *Optical Fiber Technol.*, Vol. 4, No. 4, pp. 371–383, October 1998.

[Bosco, 2005] G. Bosco, and P. Poggiolini, "The impact of receiver imperfections on the performance of optical direct-detection DPSK," *IEEE/OSA J. of Lightwave Technol.*, vol. 23, no. 2, pp. 842-848, February 2005.

C

[Carlson, 1986] A. B. Carlson, *Communication systems*, 3ª ed., McGraw-Hill, 1986.

[Cartaxo, 1998] A. Cartaxo, “Impact of modulation frequency on cross-phase modulation effect in intensity modulation-direct detection WDM systems,” *IEEE Photon. Technol. Lett*., vol. 10, no. 9, pp. 1268-1270, September 1998.

[Cartaxo, 1999:1] A. Cartaxo, “Cross-phase modulation in intensity modulation-direct detection WDM systems with multiple optical amplifiers and dispersion compensators,” *IEEE/OSA J. of Lightwave Technol.*, vol. 17, no. 2, pp. 178-190, February 1999.

[Cartaxo, 1999: 2] A. Cartaxo, "Small-signal analysis for nonlinear and dispersive optical fibres, and its application to design of dispersion supported transmission systems with optical dispersion compensation", *IEE Proc.-Optoelectron.*, vol. 146, no. 5, pp. 213-222, October 1999.

[Chan, 1998] V. Chan, K. Hall, E. Modiano, and K. Rauschenbach, “Architectures and technologies for high-speed optical data networks,” *IEEE/OSA J. of Lightwave Technol.*, vol. 16, no. 12, pp. 2146-2168, December 1998.

[Chadrasekhar, 2006] S. Chandrasekhar, C. R. Doerr, and L. L. Buhl, “Demonstration of 100% precompensated DWDM transmission over 1280 km of SSMF with no inline dispersion compensation using interconnected recirculating loops,” *IEEE Photon. Technol. Lett.*, vol. 18, no. 1, pp. 256–258, January 1, 2006.

[Charlet, 2003] G. Charlet, J. Lazaro, E. Corbel, P. Tran, A. Klekamp, T. Lopez, H. Mardoyan, W. Idler, A. Konczykowska, J.-P. Thiery, R. Dischler, and S. Bigo, “One-hundred WDM-channel transatlantic transmission experiment at 43 Gbit/s using Raman repeaters with large 65-km spacing,” in Proc. *Eur. Conf. Optical Communication* 2003, (ECOC 2003), Postdeadline paper Th4.3.3, September 2003.

[Chen, 2003] H. Chen, A. Poon, and X. Cao, “Amplitude histogram-based method for inline pulse rise time monitoring without eye-diagram,” in Proc. *Conf. on Lasers and Electro-Optics* 2003, (CLEO 2003), pp. 1511 – 1513, June 2003.

[Chen, 2004] H. Chen, A. Poon and X. Cao, “Transparent monitoring of rise time using asynchronous amplitude histograms in optical transmission systems,” *IEEE/OSA J. of Lightwave Technol.*, vol. 22, no. 7, pp. 1661-1667, July 2004.

[Chiang, 1996] T. Chiang, N. Kagi, M. Marhic and L. Kazovsky, "Cross-phase modulation in fiber links with multiple optical amplifiers and dispersion compensators," *IEEE/OSA J. of Lightwave Technol.*, vol. 14, no. 3, pp. 249-260, March 1996.

[Chinn, 1996] S. Chinn, D. Boroson, and J. Livas, "Sensitivity of optically preamplified DPSK receivers with Fabry-Perot filters," *IEEE/OSA J. of Lightwave Technol.*, vol. 14, no. 3, pp. 370-376, March 1996.

[Chraplyvy, 1990] A. Chraplyvy, "Discussion at Optical Fiber Communication Conf. (OFC) Sunday rump session in early 1990s ," unpublished.

[Ciaramella, 2000] E. Ciaramella, and S. Trillo, "All-optical signal reshaping via four-wave mixing in optical fibers," *IEEE Photon. Technol. Lett.*, vol. 12, no. 7, pp. 849–851, July, 2000.

[Correia, 1996] J. Correia, A. Cartaxo, "Rigorous assessment of the impact of intersymbol interference on the performance of optically preamplified receivers", in Proc. *Lasers and Electro-Optics Society* 1996 (LEOS 1996), vol. 2, pp. 252-253, November 1996.

[Cover, 1991] T. Cover and J. Thomas, *Elements of Information Theory*, Elements of Information Theory, 1st Ed. Wiley Interscience, New Jersey, 1991.

D

[Desurvire, 1994] E. Desurvire, *Erbium-Doped Fiber Amplifiers - Principles and Applications*, 1st Edition, Wiley-Interscience, New York, 1994.

[Devgan, 2006] P. Devgan, R. Tang, V. Grigoryan, and P. Kumar, "Highly efficient multichannel wavelength conversion of DPSK signals," *IEEE/OSA Journal of Lightwave Technol.*, vol. 24, no. 10, pp. 3677-3682, October 2006.

[Ding, 2004] L. Ding, W. Zhong, C. Lu, Y. Wang, "New bit-error-rate monitoring technique based on histograms and curve fitting," *OSA Optics Express*, vol. 12, no. 11, pp. 2507-2511, May 2004.

[Doran, 1988] N. Doran, and D. Wood, "Nonlinear-optical loop mirror," *OSA Optics Letters*, vol. 13, no. 1, pp. 56-58, January 1988.

[Duelk, 2005] M. Duelk, "Next-generation 100G ethernet," in Proc. *Eur. Conf. Optical Communication* 2005 (ECOC 2005), paper Tu 3.1.2, September 2005.

E

[Elbers, 2000] J. Elbers, A. Färbert, C. Scheerer, C. Glingener, and G. Fischer, "Reduced model to describe SPM-limited fiber transmission in dispersion managed lightwave systems," *IEEE J. of Selected Topics in Quantum Electron.*, vol. 6, no. 2, pp. 276–281, March/April 2000.

[Elbers, 2002] J. Elbers, A. Faerbert, C. Glingener, "Verfahren zur ermittlung der signalqualität bei optischen übertrangungssystemen," Deutsches Patent no. DE 101 11 497, September 2002.

[Elmirghani, 2000] J. Elmirghani and H. Mouftah, "All-optical wavelength conversion: Technologies and applications in DWDM networks," *IEEE Comm. Mag.*, vol. 38, no. 3, pp. 86–92, March 2000.

[Essiambre, 1999] R. Essiambre, B. Mikkelsen, and G. Raybon, "Intra-channel cross-phase modulation and four-wave mixing in high-speed TDM systems," *IEE Electronics Lett.*, vol. 35, no. 18, pp. 1576-1578, September 1999.

[Essiambre, 2002] R. Essiambre, G. Raybon, and B. Mikkelsen, "Pseudo-linear transmission of highspeed signals: 40 and 160 Gbit/s," in *Optical Fiber Telecommunications IVB*, I. P. Kaminow, and T. Li, Editors. New York: Academic Press, 2002

[Essiambre, 2005: 1] R. Essiambre, and P. Winzer, "Impact of fiber nonlinearities on advanced modulation formats using electronic pre-distortion," in Proc. *Optical Fiber Communications Conf.* 2005, (OFC 2005), paper OWB1, March 2005.

[Essiambre, 2005: 2] R. Essiambre, and P. Winzer, "Fibre nonlinearities in electronically pre-distorted transmission," in Proc. *Eur. Conf. Optical Communication* 2005 (ECOC 2005), vol. 2, pp. 191-192, September 2005.

[Essiambre, 2006] R. Essiambre, P. Winzer, X. Wang, W. Lee, C. White, and E. Burrows, "Electronic predistortion and fiber nonlinearity," *IEEE Photon. Technol. Lett.*, vol. 18, no. 17, pp. 1804-1806, September 2006.

[Evangelides, 1999] S. Evangelides, "Cross phase modulation resonances in WDM systems," in Proc. *Optical Fiber Communications Conf.* 1999, (OFC 1999), vol. 3, pp. 240-242, March 1999.

F

[Figueiredo, 1999] J. Figueiredo, C. Stanley, A. Boyd and C. Ironside, "Optical modulation in a resonant tunneling relaxation oscillator", *Applied Physics Lett.*, vol. 74, no. 9, pp. 1197-1199, March 1999.

[Figueiredo, 2000] J. Figueiredo, "Optoelectronic properties of resonant tunnelling diodes", PhD. Thesis, University of Aveiro, April 2000.

[Figueiredo, 2001] J. Figueiredo, C. Ironside and C. Stanley, "Electric field switching in a resonant tunneling diode electroabsorption modulator", *IEEE J. of Quantum Electr.*, vol. 37, no. 12, pp. 1547-1552, December 2001.

[Fonseca, 2006: 1] D. Fonseca, A. Cartaxo, and P. Monteiro, "Optical single sideband transmitter for various electrical signaling formats," *IEEE/OSA Journal of Lightwave Tech.*, vol. 24, no. 5, pp. 2059-2069, May 2006.

[Fonseca, 2006: 2] D. Fonseca, A. Cartaxo, and P. Monteiro, "On the use of electrical precompensation of dispersion in optical single-sideband transmission systems," *IEEE J. of Selected Topics in Quantum Electron.*, vol. 12, no. 4, pp. 603-614, July/August 2006.

[Fonseca, 2006: 3] D. Fonseca, A. Cartaxo, and P. Monteiro, "Modeling and experimental validation of an x-cut 4 phase modulators structure", *IET Proc. Optoelectron.*, vol. 153, no. 4, pp. 145-151, August 2006.

[Fonseca, 2007: 1] D. Fonseca, A. Cartaxo, and P. Monteiro, "Influence of the extinction ratio on the intrachannel nonlinear distortion of 40-Gb/s return-to-zero transmission

systems over standard fiber," *IEEE/OSA J. of Lightwave Technol.*, vol. 25, no. 6, pp. 1447-1457, June 2007.

[Fonseca, 2007: 2] D. Fonseca, R. Luis, A. Cartaxo, and P. Monteiro, "Near pseudo-linear transmission regime in 10 Gb/s single sideband-alternate mark inversion systems using electrical dispersion pre-compensation," *IEEE Photon. Technol. Lett.*, vol. 19, no. 15, pp. 1127-1129, August 2007.

[Fonseca, 2007: 3] D. Fonseca, A. Cartaxo, and P. Monteiro, "Topics on OSSB modulation for 40 Gb/s transmission systems," to be published in *Advanced Technologies for High-Speed Optical communications*, editor Lei Xu, Research Signpost, 2007.

[Funabashi, 2004] M. Funabashi, H. Nasu, T. Mukaihara, T. Kimoto, T. Shinagawa, T. Kise, K. Takaki, T. Takagi, M. Oike, T. Nomura, A. Kasukawa, "Recent advances in DFB lasers for ultradense WDM applications," *IEEE J. of Selected Topics in Quantum Electron.*, vol. 10, no. 2, pp. 312-320, March/April 2004.

[Fürst, 2001] C. Fürst, C. Scheerer, G. Mohs, J. Elbers, and C. Glingener, "Influence of the dispersion map on limitations due to cross-phase modulation in WDM multispan transmission systems," in Proc. *Optical Fiber Communication Conf.* 2001 (OFC 2001), vol. 1, pp. MF4-1–MF4-3, March 2001.

G

[Galili, 2005] M. Galili, L. Oxenløwe, D. Zibar, A. Clausen, H. Deyerl, N. Plougmann, M. Kristensen, and P. Jeppesen, "160 Gb/s notch-filtered Raman assisted XPM wavelength converter," in Proc. *Eur. Conf. Optical Communication* 2005 (ECOC 2005), vol. 1, pp. 113-114, September 2005.

[Gnauck, 2005] A. Gnauck, and P. Winzer, "Optical phase-shift-keyed transmission," *IEEE/OSA J. of Lightwave Technol.*, vol. 23, no. 1, pp. 115-130, January 2005.

[Goeger, 2004] G. Goeger, M. Wrage, and W. Fischler, "Cross-phase modulation in multispan WDM systems with arbitrary modulation formats," *IEEE Photon. Technol. Lett.*, vol. 16, no. 8, pp. 1858-1860, August 2004.

[Griesser, 2005] H. Griesser, and J. Elbers, "Influence of cross-phase modulation induced nonlinear phase noise on DQPSK signals from neighbouring OOK channels," in *Proc. 31st Eur. Conf. Optical Communication* 2005 (ECOC 2005), vol. 2, pp. 123-124, September 2005.

H

[Hahn, 1996] S. Hahn, *Hilbert transforms in signal processing*, Artch House Publisher, Boston, 1996

[Hanik, 1999] N. Hanik, A. Gladisch, C. Caspar and B. Strebel, "Application of amplitude histograms to monitor performance of optical channels," *IEE Electronics Lett.*, vol. 35, no. 5, pp. 403-404, March 1999.

[Herrera, 2005] J. Herrera, F. Ramos, and J. Marti, "Small-signal analysis of wavelength converters based on cross-phase modulation in dispersion-shifted fibers," *IEEE Photon. Technol. Lett*., vol. 17, no. 11, pp. 2370-2372, November 2005.

[Hiew, 2004] C. Hiew, F. Abbou, H. Chuah, S. Majumder, and A. Hairul, "BER estimation of optical WDM RZ-DPSK systems through the differential phase Q," *IEEE Photon. Technol. Lett*., vol. 16, no. 12, pp. 2619-2621, December 2004.

[Higuma, 2001] K. Higuma, S. Oikawa, Y. Hashimoto, H. Nagata, and M. Izutsu, "X-cut lithium niobate optical single-sideband modulator," *IEE Electronics Lett.*, vol. 37, no. 8, pp. 515-516, April 2001.

[Ho, 2004] K. Ho, "Error probability of DPSK signals with cross-phase modulation induced nonlinear phase noise," *IEEE J. of Selected Topics in Quantum Electron.*, vol. 10, no. 2, pp. 421-427, March-April 2004.

[Ho, 2006] K. Ho, and H. Wang, "Cross-phase modulation-induced crosstalk for RZ-DPSK signals in dispersive transmission systems," *IEEE/OSA J. of Lightwave Technol.*, vol. 24, no. 1, pp. 396-403, January 2006.

[Holmes, 1995] M. Holmes, D. Williams, and R. Manning, "Highly nonlinear optical fiber for all optical processing applications," *IEEE Photon. Technol. Lett*., vol. 7, no. 9, pp. 1045-1047, September 1995.

I

[Inoue, 1992: 1] K. Inoue, and H. Toba, "Wavelength conversion experiment using fiber four-wave mixing," *IEEE Photon. Technol. Lett*., vol. 4, no. 1, pp. 69-72, January 1992.

[Inoue, 1992: 2] K. Inoue, "Four-wave mixing in an optical fiber in the zero-dispersion wavelength region," *IEEE/OSA J. of Lightwave Technol.*, vol. 10, no. 11, pp. 1553-1561, November 1992.

[Inoue, 1995] K. Inoue, and H. Toba, "Fiber four-wave mixing in multi-amplifier systems with nonuniform chromatic dispersion," *IEEE/OSA J. of Lightwave Technol.*, vol. 13, no. 1, pp. 88-93, January 1995.

[Ironside, 2000] C. Ironside, C. Stanley and J. Figueiredo, "Improved optoelectronic device," International Patent no. WO 00/72383 A1, November 2000.

[Ironside, 2002] C. Ironside, and J. Figueiredo, "Improved optoelectronic device," International Patent no. WO 02/088834 A2, November 2002.

[Ishida, 2002] K. Ishida, T. Mizuochi, and T. Sugihara, "Demonstration of PMD mitigation in long-haul WDM transmission using automatic control of input state of polarization," in Proc. *Eur. Conf. Optical Communication* 2002 (ECOC 2002), vol. 4, pp. 1-2, September 2002.

[ITU G.707, 2003] Network node interface for the synchronous digital hierarchy (SDH), ITU-T G. 707, 2003.

[ITU G.709, 2003] Interfaces for the Optical Transport Network (OTN), ITU-T G.709, (2003).

J

[Jacobsen, 1994] G. Jacobsen, *Noise in digital optical transmission systems*, Artech House Inc., Boston, 1994.

[Jiang, 2003] Z. Jiang, and C. Fan, "A comprehensive study on XPM- and SRS-induced noise in cascaded IM-DD optical fiber transmission systems," *IEEE/OSA J. Lighwave Technol*., vol. 21, no. 4, pp. 953-960, April 2003.

[Jinno, 1992] M. Jinno, "Effects of group velocity dispersion on self/cross phase modulation in a nonlinear sagnac interferometer switch," *IEEE/OSA J. Lighwave Technol*., vol. 10, no.8, pp. 1167-1178, August 1992.

[Jinno, 1994] M. Jinno, and M. Abe, "All-optical regenerator based on nonlinear fiber Sagnac interferometer," *IEE Electronics Lett.*, vol. 28, no. 4, pp. 1350-1352, July 1994.

K

[Kahrs, 2003] M. Kahrs, "50 Years of RF and microwave sampling", *IEEE Transactions on Microwave Theory and Techniques*, vol. 51, no. 6, pp. 1787-1805, June 2003.

[Kazousky, 1996] L. Kazousky, S. Benedetto e A. Willner, *Optical Fiber Communication*s, Artech House, London, 1996.

[Killey, 2000: 1] R. Killey, H. Thiele, V. Mikhailov, and P. Bayvel, "Prediction of transmission penalties due to cross-phase modulation in WDM systems using a simplified technique," *IEEE Photon. Technol. Lett.*, vol. 12, no. 7, pp. 804-806, July 2000.

[Killey, 2000: 2] R. Killey, H. Thiele, V. Mikhailov, and P. Bayvel, "Reduction of intrachannel nonlinear distortion in 40-Gb/s-based WDM transmission over standard fiber," *IEEE Photon. Technol. Lett.*, vol. 12, no. 12, pp. 1624-1625, December 2000.

[Killey, 2005] R. Killey, P. Watts, V. Mikhailov, M. Glick, and P. Bayvel, "Electronic dispersion compensation by signal predistortion using digital processing and a dual-drive Mach-Zehnder modulator," *IEEE Photon. Technol. Lett.*, vol. 17, no. 3, pp. 714-716, March 2005.

[Kilper, 2003] D. Kilper, W. Weingartner, "Monitoring optical network performance degradation due to amplifier noise," *IEEE/OSA J. Lightwave Technol.*, vol. 21, no. 5, pp. 1171-1178, May 2003.

[Kilper, 2004] D. Kilper, R. Bach, D. Blumenthal, D. Einstein, T. Landolsi, L. Ostar, M. Preiss, and A. Willner, "Optical performance monitoring," *IEEE/OSA J. Lightwave Technol.*, vol. 22, no. 1, pp. 294-304, January 2004.

[Klekamp, 2006] A. Klekamp, F. Buchali, M. Audoin, and H. Bülow, "Nonlinear limitations of electronic dispersion pre-compensation by intrachannel effects," in Proc. *Optical Fiber Communication Conf.* 2006 (OFC 2006), paper OWR1, March 2006.

[Kolleck, 1997] C. Kolleck and U. Hempelmann, "All-optical wavelength conversion of NRZ and RZ signals using a nonlinear optical loop mirror," *IEEE/OSA J. Lightwave Technol.*, vol. 5, no. 10, pp. 1906-1913, October 1997.

L

[Lagarias, 1998] J. Lagarias, J. Reeds, M. Wright, P. Wright, "Convergence properties of the Nelder-Mead simplex method in low dimensions", *SIAM J. of Optimization*, vol. 9, no. 1, pp. 112-147, 1998

[Lee, 2001] J. Lee, D. Jung, C. Kim, and Y. Chung, "ONSR monitoring technique using polarization-nulling method," *IEEE Photon. Technol. Lett.*, vol. 13, no. 1, pp. 88-90, January 2001.

[Lee, 2003] J. Lee, W. Belardi, K. Furusawa, P. Petropoulos, Z. Yusoff, T. Monro, and D. Richardson, "Four-wave mixing based 10-Gb/s tunable wavelength conversion using a holey fiber with a high SBS threshold," *IEEE Photon. Technol. Lett.*, vol. 15, no. 3, pp. 440-442, March 2003.

[Lee, 2005: 1] J. Lee, T. Tanemura, and K. Kikuchi, "Use of 1-m Bi_2O_3 nonlinear fiber for 160-Gbit/s optical time division demultiplexing based on polarization rotation and a wavelength shift induced by cross-phase modulation," *OSA Optics Letters*, vol. 30, no. 11, pp. 1267-1269, June 2005.

[Lee, 2005: 2] J. Lee, T. Nagashima, T. Hasegawa, S. Ohara, N. Sugimoto, and K. Kikuchi, "Four-wave-mixing-based wavelength conversion of 40-Gb/s nonreturn-to-zero signal using 40-cm bismuth oxide nonlinear optical fiber," *IEEE Photon. Technol. Lett.*, vol. 17, no. 7, pp. 1474-1476, July 2005.

[Lee, 2005: 3] J. Lee, T. Nagashima, T. Hasegawa, S. Ohara, N. Sugimoto, and K. Kikuchi, "Wavelength conversion of 160 Gbit/s OTDM signal using bismuth oxide-based ultra-high nonlinearity fibre," *IEE Electronics Lett.*, vol. 41, no. 16, pp. 918-919, August 2005.

[Lee, 2005: 4] J. Lee, K. Kikuchi, T. Nagashima, T. Hasegawa, S. Ohara, and N. Sugimoto, "All fiber-based 160-Gbit/s add/drop multiplexer incorporating a 1-m-long bismuth oxide-based ultra-high nonlinearity fiber," *OSA Optics Express*, vol. 13, no. 18, pp. 6864-6869, September 2005.

[Lenihan, 2005] A. Lenihan, G. Tudury, W. Astar, and G. Carter, "XPM-induced impairments in RZ-DPSK transmission in a multi-modulation format WDM system," in Proc. *Conf. on Lasers and Electro-Optics* 2005 (CLEO 2005), vol. 2 pp. 1500-1502, May 2005.

[Leuthold, 1999] J. Leuthold, P. Besse, E. Gamper, M. Dülk, S. Fischer, G. Guekos, and H. Melchior, "All-optical Mach-Zehnder interferometer wavelength converters and switches with integrated data- and control-signal separation scheme," *IEEE/OSA J. Lightwave Technol.* vol. 17, no. 6, pp. 1056-1066, June 1999.

[Leuthold, 2003] J. Leuthold, D. Marom, S. Cabot, R. Ryf, P. Bernasconi, F. Baumann, J. Jaques, D. Neilson, and C. Giles, "All-optical wavelength converter based on a pulse reformatting optical filter," in Proc. *Optical Fiber Communications Conf.* 2003 (OFC 2003), vol. 3, pp. PD41-P1-3, March 2003.

[Leuthold, 2004] J. Leuthold, D. Marom, S. Cabot, J. Jaques, R. Ryf, and C. Giles, "All-optical wavelength conversion using a pulse reformatting optical filter," *IEEE/OSA J. Lightwave Technol.* vol. 22, no. 1, pp. 186-192, January 2004.

[Li, 2006] Z. Li, and G. Li, "Chromatic dispersion and polarization-mode dispersion monitoring for RZ-DPSK signals based on asynchronous amplitude-histogram evaluation," *IEEE/OSA J. Lightwave Technol.* vol. 24, no. 7, pp. 2859-2866, July 2006.

[Lizé, 2007] Y. Lizé, J. Yang, L. Christen, X. Wu, S. Nuccio, T. Wu, A. Willner, R. Kashyap, and F. Séguin, "Simultaneous and independent monitoring of OSNR, chromatic and polarization mode dispersion for NRZ-OOK, DPSK and duobinary," in Proc. *Optical Fiber Communications Conf.* 2007 (OFC 2007), vol. 2, paper OThN2, March 2007.

[Liu, 2007] Y. Liu, E. Tangdiongga, Z. Li, H. Waardt, A. Koonen, G. Khoe, X. Shu, I. Bennion, and H. Dorren, "Error-free 320-Gb/s all-optical wavelength conversion using a single semiconductor optical amplifier," *IEEE/OSA J. Lightwave Technol.*, vol. 25, no. 1, pp. 103-108, January 2007.

[Luís, 2004: 1] R. Luís, A. Teixeira, P. André, P. Monteiro, "Method to estimate optical signal-to-noise ratio in transparent optical networks using asynchronous histograms," *Siemens Invention Disclosure*, no. 2003E08776, May 2004.

[Luís, 2004: 2] R. Luís, A. Teixeira, P. André, P. Monteiro, "Evaluation of Intra-Band Crosstalk Using Asynchronous Histograms," in Proc. *European Conference on Networks & Optical Communications* 2004 (NOC2004), pp. 374-381, June 2004.

[Luís, 2004: 3] R. Luís, A. Teixeira, P. André, P. Monteiro, "Asynchronous Optical Monitoring System based on Optical Sampling," *Siemens Invention Disclosure*, no. 2004E11638, June 2004.

[Luís, 2004: 4] R. Luís, A. Teixeira, P. André, P. Monteiro, "OSNR monitoring method based on experimental calibration," *Siemens Invention Disclosure*, no. 2004E13420, June 2004.

[Luís, 2004: 5] R. Luís, P. André, A. Teixeira, and P. Monteiro, "Asynchronous histogram analysis for evaluation of Q-factor, OSNR or crosstalk," in Proc. *E-Photon One Winterschool* 2004, Aveiro, Portugal, November, 2004.

[Luís, 2004: 6] R. Luís, P. André, A. Teixeira, and P. Monteiro, "Performance monitoring in optical networks using asynchronously acquired samples with nonideal sampling systems and intersymbol interference," *IEEE/OSA J. Lightwave Technol.*, vol. 22, no. 11, pp. 2452-2459, November 2004.

[Luís, 2005: 1] R. Luís, and A. Cartaxo, "Analytical Characterization of SPM Impact on XPM-Induced Degradation in Dispersion-Compensated WDM Systems," *IEEE/OSA J. Lightwave Technol.*, vol. 23, no. 3, pp. 1503-1513, March 2005.

[Luís, 2005: 2] R. Luís, A. Teixeira, P. André, and P. Monteiro, "OSNR monitoring technique based on evaluation of asynchronous histograms," in Proc. *Conf. Nac. Telecomunicações* 2005 (ConfTele 2005), Tomar, Portugal, April 2005.

[Luís, 2005: 3] R. Luís, A. Teixeira, P. André, and P. Monteiro, "Optical signal-to-noise ratio estimation using reference amplitude histograms," in Proc. *Symposium on Enabling Optical Networks and Sensors*, (SEON 2005), Aveiro, Portugal, June 2005.

[Luís, 2005: 4] R. Luís, A. Teixeira, A. Cartaxo, and P. Monteiro, "A short theoretical study on the XPM frequency limitations in NOLM based wavelength converters," in Proc. *International Conference on Transparent Optical Networks* 2005 (ICTON 2005), vol. 2, pp. 109-112, July 2005.

[Luís, 2005: 5] R. Luís, and A. Cartaxo, "Impact of dispersion slope on SPM degradation in WDM systems with high channel count," *IEEE/OSA J. Lightwave Technol.*, vol. 23, no. 11, pp. 3764-3772, November 2005.

[Luís, 2006: 1] R. Luís, R. Nogueira, A. Teixeira, and P. Monteiro, "Highly efficient fiber wavelength converter based on a passive PM-IM converter filter for high capacity systems," in Proc. *Conf. on Lasers and Electro-Optics* 2006 (CLEO 2006), paper PS3 - JThC, May 2006.

[Luís, 2006: 2] R. Luís, A. Teixeira, P. André, and P. Monteiro, "Novel distortion resilient OSNR monitoring technique based on evaluation of asynchronous histograms," *Microwave and Optical Technol. Lett.*, vol. 48, no. 7, pp. 1369-1372, July 2006.

[Luís, 2006: 3] R. Luís, A. Teixeira, and P. Monteiro, "Cross-phase modulation bandwidth in ultrafast fiber wavelength converters," *OSA Optics Letters*, vol. 31, no. 23, pp. 3408-3410, December 2006.

[Luís, 2007: 1] R. Luís, A. Teixeira, and P. Monteiro, "Design of optical filter for increased efficiency of wavelength converters based on fiber XPM," *Optical Communications*, no. 271, pp. 100-104, January 2007.

[Luís, 2007: 2] R. Luís, D. Fonseca, A. Teixeira, P. Monteiro, "Dispersion management of electrically precompensated RZ single-sideband signals at 10 Gb/s without inline dispersion compensation," *IEEE Photon. Technol. Lett.*, vol. 19, no. 14, pp. 1039-1041, July 15, 2007.

[Luís, 2007: 3] R. Luís, B. Clouet, A. Teixeira, and P. Monteiro, "Analytical modelling of the cross-phase modulation-induced degradation in mixed DPSK and ASK transmission systems," in Proc. *International Conference on Transparent Optical Networks* 2007 (ICTON 2007), paper Mo.P.17, July 2007.

[Luís, 2007: 4] R. Luís, B. Clouet, A. Teixeira, and P. Monteiro, "Pump-probe analysis of the cross-phase modulation degradation induced by 10 Gbit/s amplitude-shift-keyed signals on 40 Gbit/s DPSK signals," *OSA Optics Letters*, vol. 32, no. 19, pp. 2786-2788, October 2007.

[Luo, 2004] T. Luo, Z. Pan, S. Nezam, L. Yan, A. Sahin, and A. Willner, "PMD monitoring by tracking the chromatic-dispersion-insensitive RF power of the vestigial sideband," *IEEE Photon. Technol. Lett.*, vol. 16, no. 9, pp. 2177-2179, September 2004.

M

[Madsen, 1999] C. Madsen and J. Zhao, *Optical Filter Design and Analysis*, Wiley-Interscience, New York, 1999.

[Mamyshev, 1999] P. Mamyshev, and N. A. Mamysheva, "Pulse-overlapped dispersion-managed data transmission and intrachannel four-wave missing," *OSA Optics Letters*, vol. 24, no. 21, pp. 1454-1456, November 1999.

[Man, 1998] W. Man, H. Tam and S. Demokan, "Optimal loop length of a nonlinear optical loop mirror in switching solitons," *IEEE/OSA J. Lighwave Technol.,* vol. 16, no. 1, pp. 100-105, January 1998.

[Marcuse, 1994] D. Marcuse, A. Chraplyvy, and R. Tkach, "Dependence of cross-phase modulation on channel number in fiber WDM systems," *IEEE/OSA J. of Lightwave Technol*., vol. 12, no. 5, pp. 885-890, May 1994.

[Matsumoto, 2007] M. Matsumoto, A fiber-based all-optical 3R regenerator for DPSK signals," *IEEE Photon. Technol. Lett.*, vol. 19, no. 5, pp. 273-275, March 1, 2007.

[Matera, 2000] F. Matera and M. Settembre, "Role of Q-factor and of time jitter in the performance evaluation of optically amplified transmission systems," *IEEE J. of Selected Topics in Quantum Electron.*, vol. 6, no. 2, pp. 308-316, March-April 2000.

[Mecozzi, 2000] A. Mecozzi, C. Clausen, and M Shtaif, "Analysis of intrachannel nonlinear effects in highly dispersed optical pulse transmission," *IEEE Photon. Technol. Lett.*, vol. 12, no. 4, pp. 392-394, April 2000.

[Mecozzi, 2001] A. Mecozzi, C. Clausen, M. Shtaif, S. Park, and A. Gnauk, "Cancelation of timing and amplitude jitter in symmetric links using highly dispersed pulses," *IEEE Photon. Technol. Lett.*, vol. 13, no. 5, pp. 445-446, May 2001.

[Meloni, 2005] G. Meloni, M. Scaffardi, P. Ghelfi, A. Bogoni, L. Potì, and N. Calabretta, "Ultrafast all-optical ADD-DROP multiplexer based on 1-m-long bismuth oxide-based highly nonlinear fiber," *IEEE Photon. Technol. Lett.*, vol. 17, no. 12, pp. 2661-2663, December 2005.

[Mizuochi, 2006] T. Mizuochi, "Recent progress in forward error correction and its interplay with transmission impairments," *IEEE J. of Selected Topics in Quantum Electronics*, vol. 12, no. 4, pp. 544-554, July/August 2006.

[Mobilon, 2005] E. Mobilon, M. Barros, and A Lopes, "Experimental verification of an eye diagram reconstruction technique based on asynchronous undersampling," in Proc. *International Conf. on Microwave and Optoelectronics* 2005, pp. 603-606, July 2005.

[Monroy, 2002] I. Monroy and E. Tangdiongga, *Crosstalk in WDM Communication Networks*, Kluwer Academic Publishers, 2002.

[Mueller, 1998] K. Mueller, N. Hanik, A. Gladisch, H. Foisel, C. Caspar, "Application of amplitude histograms for quality of service measurements of optical channels and fault identification," in Proc. *Eur. Conf. Optical Communication* 1998 (ECOC 1998), vol. 1, pp. 707-708, September 1998.

N

[Nakamura, 2006] H. Nakamura, H. Suzuki, and K. Iwatsuki, "Scalability of carrier-distributed WDM-PON for ethernet services; GbE to future 100 GbE," in Proc. *Optical Fiber Communication Conference* 2006 (OFC 2006), paper OFE3, March 2006.

[Nakazawa, 2000] M. Nakazawa, T. Yamamoto, and K. Tamura, "1.28Tbit/s-70km OTDM transmission using third and fourth-order simultaneous dispersion compensation with a phase modulator," *IEE Electronics Lett.*, vol. 36, no. 24, pp. 2027-2079, November 2000.

[Nelson, 1999] L. Nelson, R. Jopson, A. Gnauk, and A. Chraplyvy, "Resonances in cross-phase modulation impairment in wavelength-division-multiplexed lightwave transmission," *IEEE Photon. Technol. Lett.*, vol. 11, no. 7, pp. 907-909, July 1999.

[Ng, 2005] T. Ng, J. Blows, M. Rochette, J. Bolger, I. Littler, and B. Eggleton, "In-band OSNR and chromatic dispersion monitoring using a fibre optical parametric amplifier," *OSA Optics Express*, vol. 13, no. 14, pp. 5542-5552, July 2005.

[Noirie, 2002] L. Noirie, F. Cérou, G. Moustakides, O. Audouin, and P. Peloso, "New transparent optical monitoring of the eye and ber using asynchronous under-sampling of the signal," in *Proc. European Conf. on Optical Communication* 2002 (ECOC 2002), vol. 5, pp. 1-2, September 2002.

O

[Öhlén, 2000] P. Öhlén, B. Olsson and D. Blumenthal, "Wavelength dependence and power requirements of a wavelength converter based on XPM in a dispersion-shifted optical fiber," *IEEE Photon. Technol. Lett.*, vol. 12, no. 5, pp. 522-524, May 2000.

[Olsson, 2000] B. Olsson, P. Öhlén, L. Rau and D. Blumenthal, "A simple and robust 40-Gb/s wavelength converter using fiber cross-phase modulation and optical filtering," *IEEE Photon. Technol. Lett.* vol. 12, no. 7, pp. 846-848, July 2000.

[Onishi, 1997] M. Onishi, T. Okuno, Tm. Kashiwada, S. Ishikawa, N. Akasaka, and M. Nishimura, "Highly nonlinear dispersion shifted fiber and its application to broadband wavelength converter," in Proc. *Eur. Conf. Optical Communication* 1997 (ECOC 1997), vol. 2, pp. 115-118, September, 1997.

[Ooi, 2002] H. Ooi, K. Nakamura, Y. Akiyama, T. Takahara, T. Terahara, Y. Kawahata, H. Isono, and G. Ishikawa, "40-Gb/s WDM transmission with virtually imaged phased array (VIPA) variable dispersion compensators," *IEEE/OSA J. of Lightwave Technol*., vol. 20, no. 12, pp. 2196-2203, December 2002.

[Otani, 2002] A. Otani, and T. Otsubo, "Optical pulse generation system for generating optical pulses having high duty ratio," US Patent no. US 6,483,624 B1, November, 2002

P

[Pachnicke, 2006] S. Pachnicke, T. Gravemann, M. Windmann, and E. Voges, "Physically constrained routing in 10-Gb/s DWDM networks including fiber nonlinearities and polarization effects," *IEEE/OSA J. of Lightwave Technol*., vol. 24, no. 9, pp. 3418-3426, September 2006.

[Pan, 2001] Z. Pan, Q. Yu, Y. Xie, S. Havstad, A. Willner, D. Starodubov, and J. Feinberg, "Chromatic dispersion monitoring and automated compensation for NRZ and RZ data using clock regeneration and fading without adding signaling," in Proc. *Optical Fiber Communication Conf.* 2001 (OFC 2001), vol. 3, pp. WH5-1 - WH5-3, March 2001.

[Park, 2002: 1] E. Park, "Error monitoring for optical metropolitan network services," *IEEE Comm. Magazine*, vol. 40, no. 2, pp. 104-109, February, 2002.

[Park, 2002: 2] K. Park, J. Lee, C. Youn, and Y. Chung "A simultaneous monitoring technique for polarization-mode dispersion and group-velocity dispersion," in Proc. *Optical Fiber Communication Conference*, 2002 (OFC 2002), pp. 199 – 200, March 2002.

[Park, 2002: 3] K. Park, C. Youn, J. Lee, and Y. Chung, "Chromatic dispersion monitoring technique in WDM network," in Proc. *Optical Fiber Communication Conf.* 2002 (OFC 2002), pp. 735 – 737, March 2002.

[Park, 2002: 4] K. Park, C, Youn, J. Lee, and Y. Chung, "Effect of sel-phase modulation on group-velocity dispersion measurement technique using PM-AM conversion," *IEE Electronics Lett.*, vol. 38, no. 21, pp. 1247-1248, October 2002.

[Park, 2003] K. Park, C. Youn, J. Lee, and Y. Chung, "Performance comparisons of chromatic dispersion-monitoring techniques using pilot tones," *IEEE Photon. Technol. Letters*, vol. 15, no. 6, pp. 873-875, June 2003.

[Perlin, 2002] V. Perlin, and H. Winful, "All-fiber wavelength conversion using cross-phase modulation and Bragg gratings," *IEEE Photon. Technol. Letters*, vol. 14, no. 2, pp. 176-178, February 2002.

R

[Rasztovits-Wiech, 1998] M. Rasztovits-Wiech, M. Danner, and W. Leeb, "Optical signal-to-noise ratio measurement in WDM networks using polarization extinction," in Proc. *Optical Fiber Communication Conf.* 1998 (OFC 1998), vol. 1, pp. 549-550, September, 1998.

[Rasztovits-Wiech, 1999] M. Rasztovits-Wiech, K. Studer and W. Leeb, "Bit error probability estimation algorithm for signal supervision in all-optical networks," *IEE Electronics Lett.*, vol. 35, no. 20, pp. 1754-1755, September 1999.

[Rau, 2004] L. Rau, W. Wang, S. Camatel, H. Poulsen, and D. Blumenthal, "All-optical 160-Gb/s phase reconstructing wavelength conversion using cross-phase modulation (XPM) in dispersion-shifted fiber," *IEEE Photon. Technol. Letters*, vol. 16, no. 11, pp. 2520-2522, November 2004.

[Rebola, 2001] J. Rebola, A. Cartaxo, "Gaussian approach for performance evaluation of optically preamplified receivers with arbitrary optical and electrical filters", *IEE Proc. Optoelectron.*, vol. 148, pp. 135-142, June 2001.

[Rebola, 2002] J. Rebola and A. Cartaxo, "Power penalty assessment in optically preamplified receivers with arbitrary optical filtering and signal-dependent noise dominance," *IEEE*/*OSA J. of Lightwave Technol.*, vol. 20, no. 3, pp. 401-408, March 2002.

[Rohde, 2000] M. Rohde, C. Caspar, N. Heimes, M. Konitzer, E. Bachus, and N. Hanik, "Robustness of DPSK direct detection transmission format in standard fiber WDM systems," *IEE Electronics Lett.*, vol. 36, no. 17, pp. 1483-1484, August 2000.

S

[Sakamoto, 2001] T. Sakamoto, F. Futami, K. Kikuchi, S. Takeda, Y. Sugaya, and S. Watanabe, "All-optical wavelength conversion of 500-fs pulse trains by using a nonlinear-optical loop mirror composed of a highly nonlinear DSF," *IEEE Photon. Technol. Letters*, vol. 13, no. 5, pp. 502-504, May 2001.

[Sano, 2000] A. Sano, Y. Miyamoto, S. Kuwahara, and H. Toba, "A 40-Gb/s/ch WDM transmission with SPM/XPM suppression through prechirping and dispersion management," *IEEE/OSA J. of Lightwave Technol.*, vol. 18, no. 11, pp. 1519-1527, November 2000.

[Sauerwald, 1994] M. Sauerwald, "Effects of aperture time and jitter in a sampled data system," *in National Semiconductor Application Note AD-03*, http://www.national.com, May 1994

[Shake, 1998] I. Shake, H. Takara, S. Kawanishi, and Y. Yamabayashi, "Optical signal quality monitoring method based on optical sampling," *IEE Electronics Lett.*, vol. 32, no. 22, pp. 2152-2154, October 1998.

[Shake, 2000] I. Shake, E. Otani, H. Takara, K. Uchiyama, Y. Yamabayashi, and T. Morioka, "Bit rate flexible quality monitoring of 10 to 160Gbit/s optical signals based on optical sampling technique," *IEE Electronics Lett.*, vol. 36, no. 25, pp. 2087-2088, December 2000.

[Shake, 2001] I. Shake, H. Takara, K. Uchiyama, and Y. Yamabayashi, "Quality monitoring of optical signals influenced by chromatic dispersion in a transmission fiber using averaged Q-factor evaluation," *IEEE Photon. Technol Lett.*, vol. 13, no. 4, pp. 385-387, April 2001.

[Shake, 2002: 1] I. Shake, H. Takara, K. Uchiyama, "Method and system for determining origin of optical signal quality degradation," European Patent no. EP 1 276 253, June 2002.

[Shake, 2002: 2] I. Shake and H. Takara, "Averaged Q-factor method using amplitude histogram evaluation for transparent monitoring of optical signal-to-noise ratio degradation in optical transmission system," *IEEE/OSA J. of Lightwave Technol.*, vol. 20, no. 8, pp. 1367-1373, August 2002.

[Shake, 2002: 3] I. Shake, and H. Takara, "Transparent and flexible performance monitoring using amplitude histogram method," in Proc. *Optical Fiber Communication Conf.* 2002 (OFC 2002), pp. 19 – 21, March 2002.

[Shake, 2002: 4] I. Shake, H. Takara, and T. Morioka, "Determination of the origin of BER degradation utilizing asynchronous amplitude histograms," in Proc. *Pacific Rim Conf. on Lasers and Electro-Optics*, 2001, (CLEO/Pacific 2001), vol. 2, pp. II-560 – II-561, July 2002.

[Shake, 2003: 1] I. Shake, H. Takara, and S. Kawanishi, "Simple Q factor monitoring for BER estimation using opened eye diagrams captured by high-speed asynchronous electroopical sampling," *IEEE Photon. Technol. Lett.*, vol. 15, no. 4, pp. 620-622, April 2003.

[Shake, 2003: 2] I. Shake, H. Takara, "Chromatic dispersion dependence of asynchronous amplitude histogram evaluation of NRZ signal," *IEEE/OSA J. Lightwave Technol.*, vol. 21, no. 10, pp. 2154-2161, October 2003.

[Sieben, 1997] M. Sieben, J. Conradi, D. Dodds, B. Davies, and S. Walkin, "10Gbit/s optical single sideband system," *IEE Electronics Lett.*, vol. 33, no. 11, pp. 971-973, May 1997.

[Sieben, 1999] M. Sieben, J. Conradi, and D. Dodds ,"Optical single sideband transmission at 10 Gb/s using only electrical dispersion compensation," *IEEE/OSA J. of Lightwave Technol.,* vol. *17*, no. 10, pp. 1742–1749, October 1999.

[Spinnler, 2004] B. Spinnler, N. Hecker-Denschlag, S. Calabrò, M. Herz, C. Weiske, E. Schmidt, D. Borne, G. Khoe, H. Waardt, R. Griffin, and S. Wadsworth, "Nonlinear tolerance of differential phase shift keying modulated signals reduced by XPM," in Proc. *Optical Fiber Communication Conf.* 2004 (OFC 2004), vol. 1, paper TuF3, March 2004.

[Stuart, 2003] H. Stuart, "Signal-to-noise ratio monitoring of optical data using narrowband RF analysis at the half-clock frequency," in Proc. *Optical Fiber Communication Conf.* 2003 (OFC2003), vol. 1, pp. 407-409, March 2003.

[Sugihara, 2002] T. Sugihara, K. Shimomura, K. Shimizu, Y. Kobayashi, K. Matsuoka, M. Hashimoto, T. Hashimoto, T. Hirai, S. Matsumoto, T. Ohira, M. Takabayashi, K. Yoshiara, and T. Mizuochi, "Automatically tracked dispersion compensation with penalty-free

tunable dispersion equalizer for 40 Gbit/s systems," in Proc. *Optical Fiber Communication Conf.* 2004 (OFC 2004), vol. 2, pp. 577-578, March 2002.

[Sugimoto, 2004] N. Sugimoto, T. Nagashima, T. Hasegawa, and S. Ohara, "Bismuth-based optical fiber with nonlinear coefficient of $1360W^{-1}km^{-1}$," in Proc. *Optical Fiber Communication Conf.* 2004 (OFC 2004), paper PDP26, March 2004.

[Sunnerud, 2001] H. Sunnerud, M. Karlsson, and P. Andrekson, "A comparison between NRZ and RZ data formats with respect to PMD-induced system degradation," *IEEE Photon. Technol. Letters*, vol. 13, no. 5, pp. 448-4450, May 2001.

T

[Tanemura, 2004] T. Taneura, C. Goh, K. Kikuchi, and S. Set, "Highly efficient arbitrary wavelength conversion within entire C-band based on nondegenerate fiber four-wave mixing," *IEEE Photon. Technol. Lett.*, vol. 16, no. 2, pp. 551-553, February 2004.

[Teixeira, 2002] A. Teixeira, P. André, M. Lima, J. da Rocha, J. Pinto, "Characterization of high bit rate optical signals by low rate asynchronous sampling", in Proc. *Lasers and Electro-Optics Society* 2002 (LEOS 2002), vol. 2, pp. 625-626, November 2002.

[Thiele, 2002] H. Thiele, R. Killey and P. Bayvel, "Investigation of cross-phase modulation-induced transmission penalties using the pump-probe technique", *Optical Fiber Technol*., vol. 8, no. 1, pp. 71-81, 2002.

[Tomkos, 2004] I. Tomkos, D. Vogiatzis, C. Mas, I. Zacharopoulos, A. Tzanakaki, E. Varvarigos, "Performance engineering of metropolitan area optical networks through impairment constraint routing," *IEEE Communications Magazine*, vol. 42, no. 8, pp. S40-S47, August 2004.

[Tsuji, 2006] K. Tsuji, T. Yamaguchi, N. Onodera, and M. Saruwatari, "Filter-free wavelength converter using sagnac loop and delayed interferometer," *OSA Optics Express*, vol. 14, no. 2, pp. 575-580, January 2006.

W

[Wang, 1992] J. Wang, and K. Petermann, "Small signal analysis for dispersive optical fiber communication systems", *IEEE/OSA J. of Lightwave Technol.*, vol. 10, no. 1, pp. 96-100, January 1992.

[Wang, 2005] W. Wang, H. Poulsen, L. Rau, H. Chou, J. Bowers, and D. Blumenthal, "Raman-enhanced regenerative ultrafast all-optical fiber XPM wavelength converter," *IEEE*/*OSA J. Lightwave Technol.*, vol. 23, no. 3, pp. 1105-1115, March 2005.

[Watanabe, 1998] S. Watanabe, S. Takeda, and T. Chikama, "Interband wavelength conversion of 320 Gb/s (32×10 Gb/s) WDM signal using a polarization-insensitive fiber four-wave mixer," in Proc. *Eur. Conf. Optical Communication* 1998 (ECOC 1998), vol. 3, pp. 85-87, September, 1998.

[Weber, 2005] H. Weber, S. Ferber, M. Kroh, C. Langhorst, R. Ludwig, V. Marembert, C. Boemer, F. Futami, S. Watanabe, and C. Schubert, "Single channel 1.28 Tbit/s and 2.56 Tbit/s DQPSK transmission," in Proc. *Eur. Conf. Optical Communication* 2005 (ECOC 2005), vol. 6, pp. 25-29, September, 2005.

[Weber, 2006] H. Weber, R. Ludwig, S. Ferber, C. Langhorst, M. Kroh, V. Marembert, C. Boerner, and C. Schubert, "Ultrahigh-speed OTDM-transmission technology," *IEEE*/*OSA J. Lightwave Technol.*, vol. 24, no. 12, pp. 4616-4627, December 2006.

[Wei, 2003] X. Wei, X. Liu, and C. Xu, "Numerical simulation of the SPM penalty in a 10-Gb/s RZ-DPSK system," *IEEE Photon. Technol. Lett.*, vol. 15, no. 11, pp. 1636-1638, November 2003.

[Weinert, 2000: 1] C. Weinert, C. Caspar, M. Konitzer, and M. Rohde, "Histogram method for identification and evaluation of crosstalk," in Proc. *Optical Fiber Communication Conf.* 2000, (OFC 2000), vol. 3, pp. 56-58, March 2000.

[Weinert, 2000: 2] C. Weinert, C. Caspar, M. Konitzer, and M. Rohde, "Histogram method for identification and evaluation of crosstalk," *IEE Electronics Lett.*, vol. 36, no. 6, pp. 558-559, March 2000.

[Weinert, 2001] C. Weinert, C. Schmidt, H. Weber, "Application of asynchronous amplitude histograms for performance monitoring of RZ signals," in Proc. *Optical Fiber Communication Conf.* 2001 (OFC 2001), vol. 3, pp. WDD41-1 – WDD41-3, March 2001.

[Weinert, 2004] C. Weinert, "Gaussian deconvolution method for identification of impairments in optical signal transmission," *OSA J. Optical Networking*, vol. 3, no. 6, pp. 361-387, June 2004.

[Wiesmann, 2000] R. Wiesmann, O. Bleck, H. Heppner, "Cost effective performance monitoring in WDM systems," in Proc. *Optical Fiber Communication Conference*, 2000 (OFC 2000), vol. 2, pp. 171-173, March 2000.

[Willner, 2006] A. Wilner, "The optical network of the future: Can optical performance monitoring enable automated intelligent and robust systems?" *Optics and Photonics News*, pp. 30-35, March 2006.

[Winzer, 2005] P. Winzer, R. Essiambre, "Electronic pre-distortion for advanced modulation formats," in Proc. *Eur. Conf. Optical Communication* 2005 (ECOC 2005), vol. 2, pp. 257-258, September, 2005.

Y

[Yacoubian, 2002] A. Yacoubian, "A mechanically biased electrooptic polymer modulator," *IEEE Photon. Technol. Lett.*, vol. 14, no. 5, pp. 618-620, May 2002.

[Yang, 2002] W. Yang, "Sensitivity issues of optical performance monitoring," *IEEE Photon. Technol. Lett.*, vol. 14, no. 1, pp. 107-109, January 2002.

[Yang, 2004] C. Yang, S. Lee, and J. Wu, "Wavelength Control of Tunable Dense Wavelength-Division Multiplexing Sources by Use of a Fabry-Perot Etalon and a Semiconductor Optoelectronic Diode," *OSA Applied Optics*, vol. 43, no. 9, pp. 1914-1921, 2004.

[Ye, 2007] D. Ye, and W. Zhong, "Improved BER monitoring based on amplitude histogram and multi-gaussian curve fitting," *OSA J. of Optical Networking*, vol. 6, no. 6, pp. 584-598, June 2007.

[Yoo, 1996] S. Yoo, "Wavelength conversion technologies for WDM network applications," *IEEE/OSA J. Lightwave Technol.*, vol. 14, no. 6, pp. 955-966, June 1996.

[Yoshihiro, 2002] S. Yohihiro, K. Makoto, S. Yasuyuki, and O. Kenji, "WD200 WDM Monitor," *Yokogawa Technicar Reports English Edition*, no. 34, 2002.

[Yu, 2000: 1] J. Yu, X. Zheng, C. Peucheret, A. Clausen, H. Poulsen, and P. Jeppesen, "All-optical wavelength conversion of short pulses and NRZ signals based on a nonlinear optical loop mirror," *IEEE/OSA J. Lightwave Technol.*, vol. 18, no. 7, pp. 1007-1017, July 2000.

[Yu, 2000: 2] J. Yu, X. Zheng, C. Peucheret, A. Clausen, H. Poulsen, and P. Jeppesen, "40-Gb/s All-optical wavelength conversion based on a nonlinear optical loop mirror," *IEEE/OSA J. Lightwave Technol.*, vol. 18, no. 7, pp. 1001-1006, July 2000.

[Yu, 2000: 3] J. Yu, Y. Qian, A. Clausen, H. Poulsen, P. Jeppesen, and S. Knudsen, "40Gbit/s pulsewidth-maintained wavelength conversion based on a high-nonlinearity DSF-NOLM," *Electronics Lett.*, vol. 36, no. 19, pp. 1633-1635, October 1998.

[Yu, 2001] J. Yu, Y. Qian, P. Jeppesen, and S. Knudsen, "Broad-band and pulsewidth-maintained wavelength conversion based on a high-nonlinearity DSF nonlinear optical loop mirror," *IEEE Photon. Technol. Letters*, vol. 13, no. 4, pp. 344-346, April 2001.

[Yu, 2002] Q. Yu, Z. Pan, L. Yan, and A. Willner, "Chromatic dispersion monitoring technique using sideband optical filtering and clock phase-shift detection," *IEEE/OSA J. Lightwave Technol.*, vol. 20, no. 12, pp. 2267-2271, December 2002.

Z

[Zang, 2000] H. Zang, J. Jue, and B. Mukherjee, "A review of routing and wavelength assignment approaches for wavelength-routed optical WDM networks," *Optical Networks Mag.*, pp. 47-60, January, 2000.

[Zhang, 2005] A. Zhang, and M. Demokan, "Broadband wavelength converter based on four-wave mixing in a highly nonlinear photonic crystal fiber," *OSA Optics Letters*, vol. 30, no. 18, pp. 2375-2377, September 15, 2005.